
Large Amplitude Fish Swimming

Simon John Hill

Submitted in accordance with the requirements for the degree of PhD

The University of Leeds
Department of Applied Mathematics

September 1998

The candidate confirms that the work submitted is his own and that appropriate credit has been given where reference has been made to the work of others

Abstract

A fish swims by stimulating its muscles and causing its body to “wobble”, which in turn generates the thrust required for propulsion. The relationship between the forces generated by the fish muscles and the observed pattern of movement is governed by the mechanics of the internal structure of the fish, and the fluid mechanics of the surrounding water. The mathematical modelling of how fish swim involves coupling the external “biofluidynamics” to the body’s internal solid mechanics.

The best-known theory for the hydrodynamics of fish swimming is Lighthill’s elongated body theory (Lighthill, 1975). In Lighthill’s theory the curvature of the fish is assumed small and the effect on the fish of the vortex wake is neglected. Cheng *et al.* (1991) did not make these simplifications in developing their vortex lattice panel method, but the fish was assumed to be infinitely thin and its undulations of small amplitude.

Lighthill’s “recoil correction” is the addition of a solid-body motion to ensure that an imposed “swimming description” satisfies the conservation of momentum and angular momentum. A real fish is expected to minimize such sideways translation and rotation to avoid wasteful vortex shedding. Cheng and Blickhan (1994) found that the panel method model required a smaller recoil than did Lighthill’s model. Our approach is to extend Cheng’s model to large amplitude. Thus we include the effect of the wake on the fish, and the self-induced deformation of the wake itself.

In studying the internal mechanics of the body we model the fish as an active bending beam. Using the equations of motion of cross-sectional slices of the body we can form a set of coupled differential equations for the bending moment distribution. At large amplitude the bending moment equations involve the tangential forces acting on the body (which may be neglected in the small amplitude version). Consequently we include the boundary layer along the fish in order to estimate the viscous drag directly.

The panel method has been used successfully for the fluid mechanical calculations associated with large-amplitude fish swimming. We are able to use its results as input to calculate the bending moment distribution. The boundary layer calculations are based on a crude model; solutions to the large amplitude bending moment equations should also be considered in this light.

Acknowledgements

I would like to thank my supervisor, Tim Pedley, for all his help and encouragement over the last four years (and even before that). Thanks also to Owen Tutty, and to Mike Wilson for the programs that they allowed me to use; and to Nick Hill and Lew Hildyard who were always interested in my progress and happy to offer help. Who could do anything around here without the unwavering, 24-hour support of Tim Hainsworth? Thanks Tim!

I would like to gratefully acknowledge the support of the Wellcome Trust, who funded this research.

Also, a quick thanks to my ultimate team-mates in “Catch 22”, and the GB squad, who put up with my poor fitness this season.

I have benefitted from a great deal of support from my family over the past few months: thanks especially to Mum and Dad.

Most of all, I would like to thank Jack, my wife; and say sorry for the last few months. You always say you don't know how to help. But you do.

Contents

Abstract	i
Acknowledgements	ii
Contents	iii
List of Figures	viii
List of Tables	xviii
<i>Nomenclature</i>	xx
1 Introduction	1
1.1 Introduction	1
1.2 Basic fish biology	4
1.2.1 Neutral buoyancy	4
1.2.2 Fish muscle	5
1.3 The study of fish swimming	6
1.3.1 Description of swimming kinematics	6
1.3.2 Mathematical modelling of swimming	8
1.3.3 Fish-water interactions	18
1.4 A model for large amplitude swimming	20
1.5 Outline of the thesis	22

2	Two-dimensional panel method	24
2.1	Introduction	24
2.2	The lumped vortex element	26
2.3	The two-dimensional panel method	27
2.3.1	Non-dimensionalisation	27
2.3.2	Description of the motion.	27
2.3.3	Discretisation of the body and the wake	28
2.3.4	The induced velocity due to a point vortex	30
2.3.5	Forming the boundary condition equations	30
2.4	The pressure distribution	32
2.5	A flat plate moving with constant speed	36
2.6	The suction force	38
2.7	The wake	43
2.7.1	Wake rollup	43
2.7.2	Simplification of the wake model	44
2.7.3	Numerical instability in the discretisation of a continuous vortex sheet	46
2.8	Summary	48
2.9	A flat plate at constant small angle of incidence started impulsively from rest.	49
2.10	The sideforce and pressure distribution on a flat plate undergoing small-amplitude pitching and heaving motion.	55
2.10.1	Analytic solution	55
2.10.2	Results	57
2.11	Pitching and heaving flat plate model of lunate-tail propulsion	59

2.11.1	Small amplitude	61
2.11.2	Large amplitude	63
2.12	Conclusions	65
3	Two-dimensional Swimming	67
3.1	Introduction	67
3.2	Motion of a waving plate	67
3.3	The recoil correction	70
3.4	Small amplitude two-dimensional swimming	75
3.4.1	Testing the recoil correction	80
3.5	Large amplitude two-dimensional swimming	85
3.6	Conclusion	90
4	Three-dimensional panel method	92
4.1	Introduction	92
4.2	The three-dimensional panel method	93
4.2.1	Geometry and non-dimensionalisation of the model	93
4.2.2	Discretisation of the body and the wake	95
4.2.3	The induced velocity due to a finite vortex line segment.	96
4.2.4	Forming the boundary condition equations	98
4.2.5	The unsteady Kutta condition: shedding vortex rings	100
4.3	Calculating the pressure distribution	102
4.4	The suction force	105
4.5	Motion of a flat plate	106

4.5.1	Impulsively started flat plate	106
4.5.2	Pitching and heaving flat plate	107
4.6	Small amplitude steady state swimming	109
4.6.1	Large aspect ratio	109
4.6.2	Varying the panel method parameters	112
4.7	The recoil correction	116
4.8	A large amplitude example	116
4.9	Conclusions	123
5	The boundary layer	126
5.1	Introduction	126
5.2	The boundary layer equations	128
5.3	The numerical method	130
5.3.1	The finite difference equations and Newton method	132
5.3.2	The initial conditions	137
5.3.3	The outer velocity condition	138
5.4	Oscillating free stream example	139
5.5	An example involving large amplitude swimming	143
5.6	The “full” recoil correction	147
5.7	Conclusions	149
6	The bending moment distribution	152
6.1	Introduction	152
6.2	Derivation of the bending moment equations	153

6.2.1	The boundary conditions and recoil correction	157
6.2.2	The angular momentum	160
6.3	Small amplitude swimming	163
6.4	Large amplitude swimming	165
6.5	Conclusions	169
7	Conclusions	171
	Appendix	176
A	The computer program	176
A.1	Introduction	176
A.2	Program costs	176
B	Improving the code	179
	Bibliography	180

List of Figures

1.1	Variations of the lunate tail. Reading from left to right down the page: lateral views of wahoo, tunnyfish, striped marlin, louvar, sailfish, swordfish, whale shark, and porbeagle; ventral views of the sei whale, and a dolphin; an impression of <i>Ichthyosaurus</i> (taken from Lighthill, 1975).	15
2.1	Variable length panels are produced from equally spaced angles around a semi-circle.	29
2.2	Graph of bound vortex strength for uniform panels for various values of N , the number of panels. Angle of attack is $\alpha = 5^\circ$	37
2.3	Graph of bound vortex strength for variable panels for various values of N , the number of panels. Angle of attack is $\alpha = 5^\circ$	38
2.4	Graph showing the variation of a used in the suction approximation, as the number of panels N is increased. Both uniform and variable panels are shown and the result is significantly different for the two methods.	42
2.5	The shape of the vortex sheet at $t^* = 1.0$. In this example, $M = 50$ and $\Delta t^* = 10^{-2}$. The core radius is given by $r_c \approx a/M$	48
2.6	Flowchart of the basic procedures to be performed at each time step. The elements in the dashed box can be thought of as a single procedure when more complexity is added to the problem later on.	50

-
- 2.7 Graph of the lift coefficient divided the steady state value of the lift coefficient $C_L(t)/C_L(t = \infty)$: a comparison of Wagner's result with the numerical method for uniform panels. Using $\Delta t = l/NU$ to set the time step, the graph shows that the method converges with increasing N 51
- 2.8 Graph of $C_L(t)/C_L(t = \infty)$ against time showing the effect of changing Δt for $N = 50$ (cosine spacing). The boxes mark the values from (Wagner, 1925). . . . 52
- 2.9 Graph of $C_L(t)/C_L(t = \infty)$ against time showing the effect of changing Δt at small t , ($N = 50$). The box at $t = 0.25$ marks a data point from (Wagner, 1925). 53
- 2.10 Graph of $C_L(t)/C_L(t = \infty)$ against time. The parameter k is the position of the latest shed vortex, as a fraction of the distance back along the path travelled by the trailing edge over the latest time step. This example was done using $N = 50$ (cosine spacing) and $\Delta t = 0.02$ 54
- 2.11 Graph of the lift coefficient against time for small amplitude pitching-heaving flat plate. Results are shown for a varying number of panels, from $N = 10$ to $N = 40$. As explained in the text the parameter values of the pitching-heaving motion were: $U = 3$, $A = 0.05$, $B = 0.1$, $b = 0.5$ 58
- 2.12 The lift coefficient against time for the same parameter values as the results in Fig. 2.11. In this case the analytic solution (solid line) is compared with the numerical result (broken line) for $N = 30$ 59
- 2.13 Graphs of the pressure jump coefficient against distance s along the body. The graphs come from four instances in the first half-period, ($T = 1$). 60
- 2.14 Graph showing the variation in the thrust coefficient C_T over one period. The results of the full solution including the wake rollup and compared with the small-amplitude approximation that neglects the deformation of the wake. This example is for a reduced frequency of $\sigma = 1.0$; the "feathering parameter" is $\theta = UB/\omega A = 0.4$ 61

-
- 2.15 The mean thrust coefficient, \bar{C}_T , plotted against the reduced frequency σ for three values of the feathering parameter θ . Lighthill's results are plotted as continuous curves, with the discrete numerical results shown by different symbols for each value of θ 62
- 2.16 A graph of the mean thrust coefficient against the heaving amplitude. The panel method results are plotted with squares. The data read off from the graph in Chopra (1976) is plotted by crosses. The results in this case are for $\alpha_0 = 0.24$. The upper set of points is for $\sigma = 0.2$, the lower for $\sigma = 0.1$ 64
- 3.1 Sketch of the waving plate (the solid line) including the displacement and rotation due to the recoil parameters $R(t)$ and $\Theta(t)$. The X, Y axes represent the "lab frame"; the dashed axes represent the "body frame" in which the waving motion is defined. 73
- 3.2 Graph showing the variation of mean thrust against the reduced frequency σ . The solid line is the full thrust, with the broken line indicating the contribution to the thrust due to the suction force. The amplitude envelope is constant, $A = 0.05$, $B = 0.0$, and the wavenumber is $k = \pi$ 77
- 3.3 Graph showing the variation of mean thrust against the reduced frequency for linearly varying amplitude, $A = 0.1$, $B = 0.01$, $k = \pi$. The solid line is the full thrust, with the broken line indicating the contribution to the thrust due to the suction force. 78
- 3.4 Graph showing the variation of mean thrust against the wavenumber k for linearly varying amplitude, $A = 0.0$, $B = 0.1$, $\omega = 5.0$. The solid line is the full thrust, with the broken line indicating the contribution to the thrust due to the suction force. 79

-
- 3.5 Graph showing the convergence of the panel method solution for mean thrust with varying N and Δt for both uniform and variable panelling. In this case $\omega = 5$, $k = \pi$, $A = 0.05$, $B = 0.0$. The solid line shows Wu's analytic solution, and the broken line shows the suction force. The crosses mark the computed suction force for each experimental run. The plus signs and the triangles plot the mean thrust for variable and uniform panelling respectively with the time step chosen such that $U\Delta t \approx l/N$. The asterisks and squares plot the results for variable and uniform panelling respectively, with $\Delta t = 0.0025$ 80
- 3.6 Curves plotting L_R (dotted) and M_R (dashed) over first four periods of the swimming motion. At time $t = 3T$ the recoil calculation is started, and both values go to zero. 82
- 3.7 Variation in the recoil parameters depending on the time $t = t_r$ at which the recoil correction is "switched on" In each case, the solid line is R , with the dashed line being Θ which is an angle in radians. The graphs correspond to t_r as follows: (a) $t_r = 3.11T$, (b) $t_r = 3.25T$, (c) $t_r = 3.5T$, (d) $t_r = 3.61T$ 83
- 3.8 Graph of the pressure jump distribution at several different times. The solid line for which $\Delta p \leq 0$ for all s corresponds to a time $t = t_0$, say, before the recoil correction is included. The other (three) solid lines correspond to times $t = t_0 + nT$ where n is an integer $2 \leq n \leq 4$. The remaining lines correspond to time steps close to the time, $t = t_0 + T$, at which the recoil calculation was switched on. These are described in detail in the text. 84
- 3.9 Graph of the pressure jump distribution (once a steady state has been reached) for simulations involving different recoil switch-on times $t = t_r$. The results are given at two different times, one-third of a period apart. 85
- 3.10 The amplitude envelope of the body, formed by plotting the body shape over one period in a frame of reference where the nose of the fish does not advance. The top picture is before the recoil correction is included; and the lower picture is after the recoil has been included, and a steady state has been reached. 86

-
- 3.11 The body and wake at $t = 7T$. The solid line indicates the position of the body. The squares each represent a point vortex that has been shed from the trailing edge. The figure shows that the wake is not free of instabilities, but that the macroscopic behaviour that we expect is still in evidence. In particular we see counter-rotating, large-scale vortices (as opposed to the actual point vortices) behind the tail in a “vortex street”. The sense of the rotation in the fluid generated by these vortices is indicated by the arrows. Note that far from the body, the point vortices are amalgamated; and the furthest point vortex from the tail has resulted from many amalgamated vortices and now represents one of the vortices in the vortex street. 88
- 3.12 Graphs to show the pressure jump distribution against position along the body at four distinct moments in the period. The graphs on the right hand side show the body shape that corresponds to each pressure distribution. 89
- 3.13 Graph of the thrust against time over one period. The solid line is simply the total hydrodynamic thrust due to the pressure jump along the body and suction force at the leading edge. The broken line is the combination of the hydrodynamic thrust and the body inertia. If the nose is to move at constant speed the force indicated by the solid line must be balanced by the viscous drag. 90
- 4.1 An example of variable panelling, with $N = 32$. The dashed lines show the position of a single vortex ring, with the cross marking the collocation point. . . . 95
- 4.2 Sketch of a finite length vortex line segment, AB . In order to calculate the induced velocity at P we require the position vectors of the line segment’s end-points relative to P : $\mathbf{r}_1, \mathbf{r}_2$. The vortex line segment has strength Γ , defined positive for clockwise rotations about the vector \mathbf{r}_0 97
- 4.3 Two adjacent rings of strengths Γ_1 and Γ_2 coincide at the vortex line segment connecting the nodes $(k, l - 1), (k, l)$: the strength of this segment is $\Gamma_2 - \Gamma_1$. . . 99

-
- 4.4 Schematic representation of vortex rings initially attached to the body and subsequently shed from the trailing edge. Solid lines represent the panels, dashed lines the actual vortex line segments. The body is moving to the left with speed U , and we assume a constant time step Δt . The line AB and its continuation represents the starting vortex. The vortex line segment CD has strength $\Gamma_{N_x, j}^{(1)} - \Gamma_{N_x, j}^{(2)}$, and the vortex line segment EF has strength $\Gamma_{N_x, j}^{(2)} - \Gamma_{N_x, j+1}^{(2)}$ 101
- 4.5 The effect of aspect ratio on the lift coefficient on an impulsively started rectangular flat plate held at a constant angle of attack $\alpha = 5^\circ$ 107
- 4.6 The mean thrust coefficient plotted against reduced frequency of pitching-heaving motion for a flat plate of aspect ratio 8, with pitching axis at the trailing edge. The crosses mark the data read from the graph in Fig. 6(c), Chopra (1974). The upper points (triangles) are for $\theta = 0$, with the lower points (diamonds) plotting $\theta = 0.8$. 108
- 4.7 Comparison of the pressure distribution along (a) the centreline of a large aspect ratio waving plate with that on (b) a two-dimensional waving plate. In each case the variation in time is shown by overplotting the curves for various times. Exact agreement between two-dimensional and three-dimensional results is not expected. 110
- 4.8 Comparison between results for large aspect ratio three-dimensional waving plate and the two-dimensional waving plate: (a) thrust, (b) suction force (c) sideforce (d) moment about mean position of the nose ("a fixed axis"). The quantities are all per unit span. The results for three dimensions are given by dotted lines, with those for two dimensions given by dashed lines. We should expect (and indeed obtain) reasonable agreement between the two methods for these quantities. 111

4.9	Comparison of results for a large aspect ratio three-dimensional waving plate and the two-dimensional waving plate. The graphs plot (a) the lateral hydrodynamic force per unit span on the plate, and (b) the total hydrodynamic moment per unit span about the mean position of the nose. The inertia of the body has been included in the calculations, so that these are the quantities that should be zero in order to satisfy the recoil conditions. The three dimensional results are given by the dotted line, and the two-dimensional results are given by the dashed line. As with the results excluding the inertia, in Fig. 4.8, the agreement is very good.	112
4.10	Graph of mean thrust per unit span against the number of chordwise panels used for that run. The number of spanwise panels is fixed at $N_Y = 10$. The crosses (x's) indicate the effect of increasing the number of chordwise panels with the time step chosen so that the body and wake panels are of similar dimension: $\Delta t \approx l_X/N_X$. The plus signs (at $N_X = 40, N_X = 60$) show the effect of changing the time step. In each case reducing Δt results in a lower mean thrust. At $N_X = 40$ we have plotted results for $\Delta t = 0.05, 0.025, 0.01$. At $N_X = 60$ we have plotted results for $\Delta t = 0.05, 0.03, 0.02, 0.01$	113
4.11	Graphs showing the pressure jump distribution along the centreline of the waving plate for four different examples; (the kinematic parameters are given by Table 4.1, $AR = 0.2$). The only parameter to be changed between the examples shown is the time step Δt . The variation in the pressure distribution over one period is indicated by superimposing results upon one another at different times. Our interest lies near the trailing edge, where the pressure jump should tend to zero. Evidently the time step size has some effect on our ability to obtain a pressure jump distribution that tends to zero near the trailing edge.	114
4.12	Graph of mean thrust per unit span against the number of spanwise panels. The results are for fixed $N_X = 60, \Delta t = 0.02$; kinematic parameters are given in Table 4.1, $AR = 0.2$	115
4.13	Graphs showing the mean thrust on the waving plate against variations in (a) the number of chordwise panels, (b) the time step, and (c) the number of spanwise panels.	117

4.14	Three-dimensional surface plots of the data representing the body (shown in blue) and its wake (shown in red). Symmetry in the $Y = 0$ plane allows us to plot just half of the solution space. Three different “views” of the same run (B) are displayed. Graphics software used with permission from Dr Mike Wilson.	119
4.15	Graphs of the two-dimensional velocity field (in the plane of symmetry $Y = 0$) over four consecutive time steps. The solid line is the body; each square represents a wake-node lying along the $Y = 0$ plane; and the arrows indicate the velocity field.	121
4.16	Graphs of the projection of the velocity field in the plane $X = X(s = 0.5, t)$ onto that plane. The last four plots correspond to those in Fig. 4.15. The solid line indicates the position of the “slice” of body lying in the “scanned” plane.	122
4.17	Graphs to show the variation over a single period of the thrust, sideforce and moment about the mean position of the nose. All the quantities are displayed “per unit span”. (a) compares the total hydrodynamic thrust with the contribution to thrust due to suction. In (b), the total hydrodynamic thrust is compared with the (thrust – inertia). This latter quantity gives a panel-method based estimate of the what the viscous drag would have to be to allow the fish to swim at the imposed constant speed. In (c) and (d) the solid line indicates the sideforce, and the hydrodynamic moment about the mean lateral position of the nose, respectively. In both cases the broken line plots the same quantity, but with the inclusion of body inertia.	124
5.1	Sketch of the three-dimensional grid used for the finite difference equations in the boundary layer solver. The grid spacing is not necessarily uniform in the s and ζ directions.	133
5.2	Graphs of the reduced skin friction coefficient ($E\sqrt{s}$ in our notation) against the reduced frequency, $\omega s/U_0$, for (a) small reduced frequency, and (b) large reduced frequency; $B = 0.01$. The solid lines denote the analytic solution; the dotted lines denote the numerical solution (which is valid for intermediate values of the reduced frequency).	140

-
- 5.3 Graphs of the reduced skin friction coefficient, $E\sqrt{s}$, against the reduced frequency, $\omega s/U_0$, for (a) $B = 0.1$, (b) $B = 0.15$. The range of the reduced frequency was chosen on the basis of being relevant to fish swimming. 141
- 5.4 Velocity profiles of the boundary layer at three different values of $\omega s/U_0$. The quasi-steady Blasius solution is included (broken curves) to act as a reference. The variation in time is shown using times corresponding to the curves in Fig. 5.3(a). 142
- 5.5 Figure to show the shape of the swimming motion of the eel, using a frame of reference in which the x -coordinate of the nose remains fixed. 144
- 5.6 Plot of the swimming body (solid line) and its vortex wake. Each square indicates the position of a point vortex that was previously shed from the trailing edge (tail fin). As we expect, the wake rolls up into an arrangement of counter-rotating vortices. 145
- 5.7 Series of graphs plotting the non dimensional drag per unit length along the body. The broken lines give the value on each side of the body, with the solid line being the sum of these two. The graphs should be read top to bottom, then left to right. 146
- 5.8 Graph showing the variation in streamwise forces acting on the fish. The solid line is the hydrodynamic thrust. The dotted line is this thrust minus the body inertia. The dashed line is the viscous drag as calculated by the boundary layer method. . 147
- 5.9 Graph of the total streamwise force (ie thrust minus drag) on the body against time. In this example conservation of momentum was not enforced. 148
- 5.10 Graph to indicate the variation of the recoil parameters for the eel example including the full recoil correction (switched on at $t = 2T$). Note in particular that the streamwise recoil parameter is extremely small relative to the body length 1. 149
- 5.11 Graph of the resultant streamwise force (ie thrust minus drag) on the body against time. In contrast to Fig.5.9, for this example conservation of momentum was enforced. 150

-
- 6.1 Sketch of forces and moments acting on element δs of the bending fish, modelled using the Bernoulli-Euler beam theory. F and G are the components of the internal force, with M being the bending moment. Δp and D_{\pm} are the normal and tangential components of the hydrodynamic force per unit length (as functions of s_X only, having been integrated across the span). 155
- 6.2 Sketch of an element of the body's bending centreline. We require an expression for the angular velocity ω at O 161
- 6.3 Graphs to show (a) the bending moment $M(s, t)$, and (b) the internal force $F(s, t)$ against position along the body. The curves are plotted for a number of equally spaced time steps. The time-interval between the plotted curves has been arranged so that the graphs are not simply symmetric in $M = 0$ and $F = 0$ 163
- 6.4 (a) The variation of $M(l, t)$ and $F(l, t)$ (indicated by the solid and broken lines respectively) against time. The results include the values obtained before the recoil correction was included in the calculation. (b) A graph of $M(s, t)$ over one period at three different positions along the body: $s = 0.25, 0.5, 0.75$ 164
- 6.5 Graphs to show the variation in the bending moment distribution over one period. The system was solved using both the large amplitude equations (solid lines), and the small amplitude equations (broken lines). The order of the graphs is top to bottom, left to right. 166
- 6.6 Graphs of the bending moment $M(s, t)$ against time, at intervals of 0.1 along the body. In (a) the solid lines are for $s = 0.0, s = 0.5$, with the broken lines corresponding to $s = 0.1, 0.2, 0.3, 0.4$. In (b) the solid lines are for $s = 0.5, s = 1.0$, with the broken lines corresponding to $s = 0.6, 0.7, 0.8, 0.9$. The intermediate results in each case can be identified by the fact that the maximum amplitude increases with s for $0 < s < 0.5$, and decreases with s for $0.5 < s < 1.0$. 167
- 1 Flowchart indicating the structure of the program, in terms of the procedures that are followed at each time step. 177

List of Tables

1.1	Typical swimming speeds, approximate sizes and the resulting Reynolds number Re for a variety of swimming animals, (data from Videler, 1993, Table 1.1). . . .	3
3.1	Table of parameter values for a set of examples used to test the recoil correction. The wave parameters are set up such that one wavelength is equal to the body length, with the wave speed being 1.1 times the forward swimming speed. The amplitude envelope is set to be increasing from the minimum at the nose to the maximum at the tail.	81
3.2	Table of parameter values for the large amplitude simulation. The wave parameters are set up such that one wavelength is equal to the body length, with the wave speed being 5/4 times the forward swimming speed. The amplitude envelope is set to be increasing from the minimum at the nose to the maximum at the tail.	86
4.1	Table of parameter values for the simulations in Sections 4.6.1 and 4.6.2. The wave parameters are set up such that one wavelength is equal to the body length, with the wave speed being 5/4 times the forward swimming speed. The amplitude envelope is set to be linearly increasing from the minimum at the nose to the maximum at the tail.	109

4.2	Table of parameter values for a large amplitude test. The wave parameters are set up such that one wavelength is equal to the body length, with the wave speed being $5/4$ times the forward swimming speed. The amplitude envelope is set to be linearly increasing from the minimum at the nose to the maximum at the tail. In this case, the amplitude of the tail's motion is of the same order as that of a real fish.	117
4.3	Table of panel method parameter values for two large amplitude simulations. The parameters describing the details of the geometry are given in Table 4.2. In these two examples the time step was changed from Δt_0 to Δt_1 at time $t = t_1$	118
5.1	Table of parameter values for the geometry of the eel motion. These non dimensional values are derived from data in Videler's book.	144
6.1	Table of the kinematic parameters used in small amplitude swimming simulation to obtain a test solution for the bending moment distribution.	163

Nomenclature

General Notation:

Re	Reynolds Number
ν	kinematic viscosity
ρ	fluid density
Φ	velocity potential
Φ^\pm	velocity potential (above and below the vortex sheet)
ϕ	velocity potential (in moving frame, see calculation of pressure jump)
$O X Z$	fixed frame of reference ($2D$)
$O X Y Z$	fixed frame of reference ($3D$)
V	fluid velocity (in fixed frame of reference)
S_b	the fluid-boundary created by the body of the fish
S_w	the wake surface
ζ	transformed cross-stream variable in the boundary layer problem

Parameters relating to fish's body:

U	constant swimming speed of the fish
l, l_X	body length ($2D, 3D$ resp.)
l_Y	semi-span of the body ($3D$)
s, s_X	distance along the centreline of the body ($2D, 3D$) measured from the nose
s_Y	distance along the body in the spanwise direction, measured from $Y = 0$
V_b	velocity of the body
n	normal to the surface of the body
τ	tangent to the centreline of the body ($2D$)
τ_{sx}	chordwise tangent vector to the plate ($3D$)
τ_{sy}	spanwise tangent vector to the plate ($3D$)
M_b	total mass of the body
m_b	mass distribution along the body (ie mass per unit length)

Description of the bending wave on the body:

V	wave speed of the wave travelling backwards along the body (body-wave)
λ_b	wavelength of the body-wave
f	frequency of the body-wave
T	period of the body-wave
λ_s	swimming "stride length"
A, B	amplitude parameters in imposed swimming motion (see equation (3.2))
α, β	amplitude-growth parameters in imposed swimming motion (eqn(3.2))
b	body-wave "envelope shape" (3.2))
k	wavenumber of imposed body-wave
ω	angular frequency of imposed body-wave
ξ	phase of imposed body-wave

Panel method parameters:

N	number of panels on the body
N_X	number of chordwise panels on the body
N_Y	number of spanwise panels on the body
N_W	number of "wake-panels"
A	matrix of influence coefficients
A_{ij}	element of A
Γ_j	strength of the j 'th point vortex
$\gamma(s)$	continuous vorticity distribution on surface of a vortex sheet
Δt	time step
Δl	panel length (2D)
Δl_X	chordwise panel length (3D)
Δl_Y	spanwise panel length (3D)

Recoil:

$R(t), R_Z(t)$	sideways translation (2D, 3D)
$\Theta(t)$	rotation
$R_X(t)$	streamwise "recoil" (3D)

Forces and moments on the body:

Δp	pressure distribution
L	lift on the body
T_X	thrust on the body
T_S	suction force
C_L	lift coefficient
ΔC_p	jump in the pressure coefficient
E	shear rate
D	viscous drag per unit length of the body
F	integrated shear stress on transverse surface of cross-sectional element of body
F	integrated normal stress on transverse surface of cross-sectional element of body
$\kappa(s)$	curvature of the body as it bends
H	angular momentum per unit mass of a cross-sectional element about its centre of mass
M	bending moment distribution
M_m	“active” component of bending moment distribution
M_p	“passive” component of bending moment distribution

Chapter 1

Introduction

This thesis is concerned with the fluid mechanics, and to a lesser extent the solid mechanics, involved in the motion of certain animals through water. The aim of this first chapter is to introduce the subject, explaining what motivates the study, why it is difficult, and crucially to what subset of the aquatic animal kingdom the work is relevant. There is some discussion of the history of the study of aquatic locomotion, which is followed by an outline of earlier mathematical modelling of the mechanics of how fish swim. Finally there is an introduction to our own model for swimming and an outline of the thesis as a whole.

1.1 Introduction

The aquatic environment represents many diverse habitats. The animals that live primarily in water (and in particular some 22000 species of fish) have evolved various forms of propulsion. Understanding the factors that govern an animal's locomotion is central to understanding the animal itself because locomotion is pivotal to its existence. Factors relating, for example, an animal's anatomy, physiology, mode of life and evolution are all intrinsically linked to the way it moves and the physics that constrain its motion.

Amongst the great variety of aquatic life and its "solutions" to the problems associated with moving underwater are some compelling examples of animals being extremely well-adapted to their environment and mode of life. For example, the pike is an ambush predator, hiding in wait for

its prey. With the capability of accelerating from rest at greater than twenty times the acceleration due to gravity (Videler, 1993) it has a high ratio of successful to attempted attacks.

There is also an engineering slant to the study of aquatic locomotion. Perhaps it might become possible to imitate mechanically some of the techniques used by fish to realise better efficiency and manoeuvrability in ships, boats, and at least un-manned submersible vessels (Weihs, 1972; Triantafyllou and Triantafyllou, 1995; McGregor and Thomson, 1997). For example many species of fish are able to change direction without losing speed, and using a turning circle that is a fraction of the equivalent distance required by ships.

The great variety of aquatic animals and their modes of propulsion means that we cannot hope to cover the whole subject. The current work then relates to probably the most common general mode of propulsion: “undulatory swimming”. This involves the animal passing a bending wave backwards along its body. Other main forms of locomotion involve ciliary motion (eg in many protozoans) or propulsion by jet reaction (eg in jellyfish or squid). We further subdivide undulatory swimming on a hydromechanical basis, in terms of the Reynolds number,

$$Re = \frac{Ul}{\nu} \quad (1.1)$$

where l is the animal’s length, U its forward swimming speed, and ν the kinematic viscosity of water.

For a hydromechanics-based review of aquatic animal propulsion see Lighthill (1969). Lighthill (1975, Chapter 3) examines low Reynolds number swimming, where the motion is dominated by viscous effects. The Reynolds number represents the relative importance of inertial and viscous forces. This allows us to consider two physically distinct groups of swimmers: ie those swimming in either the high or low Reynolds number regime. Table 1.1 (Table 1.1 Videler, 1993) shows typical values for several animals.

Given the stated area of interest the obvious fluid mechanics question is: “What physical characteristics of the fish body and kinematics allow the animal to achieve such effective propulsion.?” A more fundamental point relates to the behaviour of the fish muscle. How do the forces produced by the muscles interact with the body tissue and the water to generate the undulatory motions (the “wiggles”) that we observe? Both these questions have been studied successfully to some extent (see Section 1.3). The aim of our work is to continue along these lines:

Species	Velocity (ms^{-1})	Length (m)	Re
Blue Whale	10.0	30.0	3×10^8
Tuna	10.0	3.0	3×10^7
Human	1.7	1.8	3×10^6
Mackeral	3.3	0.3	1×10^6
Herring Adult	1.0	0.2	2×10^5
Herring Larvae	0.5	0.1	5×10^4
	0.16	0.04	6×10^3
	0.06	0.02	1×10^3
	0.02	0.01	2×10^2
Copepods	0.002	0.001	2×10^0
Sea urchin sperm	0.0002	0.00015	3×10^{-2}

Table 1.1: Typical swimming speeds, approximate sizes and the resulting Reynolds number Re for a variety of swimming animals, (data from Videler, 1993, Table 1.1).

- to improve on previous hydromechanical models of high Reynolds number undulatory swimming;
- and to use the new model in conjunction with a description of the mechanics governing the deformation of the fish body.

In simple terms the problem is as follows. The animal sends an activation signal to its muscles causing them to contract and generate a force to deform the body. The resulting pattern of bending progresses backwards along the body and imparts a backwards momentum to the water. By Newton's third law this generates a forward thrust on the fish enabling it to progress. However the hydromechanics of fish swimming presents a significant problem. Lighthill (1977) stated that "although a correct mathematical expression of the laws of motion has been known for over a century, any direct numerical calculation of the motion from those laws is far beyond the capacity of any existing computer". Over the intervening twenty years there has been a revolution in the availability of computing power. Nonetheless, the nature of fluid mechanics is such that the comment remains essentially valid. The basis of the problem lies in the fact that the governing hydrodynamic equations (the Navier-Stokes equations) are nonlinear, and in four variables; and

that the ratio of the fish length to the boundary layer thickness (the shortest distance over which significant variation in the flow occurs) is so large. In fact Liu *et al.* (1996) have successfully solved the two-dimensional Navier-Stokes equations in modelling swimming tadpoles using techniques from Computational Fluid Dynamics. They are working on a three-dimensional version of the code. Any such solution is likely to remain prohibitively expensive for routine use, in terms of time and storage, for some time to come.

Finally, note that the hydrodynamic sections of this work are of relevance to any “body” that moves through water (at a high Reynolds number) by sending travelling waves of curvature backwards along itself. Throughout this thesis the term “fish” will sometimes be used in a biologically-inaccurate sense, as parts of the theory might equally be applied to certain mammals and reptiles, or even robots.

1.2 Basic fish biology

1.2.1 Neutral buoyancy

Fish are (or are close to) neutrally buoyant, and this is of relevance to their locomotion. For further details and examples see Bone and Marshall (eg see 1982). Most of the materials making up a fish’s body are more dense than water. However, most fish offset this by storing low density materials. Two distinct systems are used to this end: a gas-filled swimbladder, and/or the presence of low-density lipids (fats and oils).

The gas filled swimbladder is the more efficient source of static lift in terms of lift per unit volume, but requires complex physiological control mechanisms to deal with changes in the ambient pressure associated with changes in depth. In other words the swimbladder must obey Boyle’s law that volume is inversely proportional to pressure. Many teleosts (bony fishes) do possess a gas-filled swimbladder, and such fish may be found across a wide range of habitat-depths. However, they are prohibited from making large relative changes to their depth; and may also be forced to make any changes in depth quite slowly. It is not surprising then that some fish (eg tunas) living near the surface, but also travelling to depths of tens of metres, have no swimbladder and use other means to achieve neutral buoyancy.

Fish using lipids as a source of static lift do not have a problem with changing depth. However, lipids are less efficient at producing static lift, and may also be used by the animal for other purposes, such as food reserves. There are extreme examples of fish (eg the deep sea angler fishes) that have severely reduced skeleton and musculature, and are virtually “floating traps” (Bone and Marshall, 1982) luring their prey to come to them. Bone and Marshall (1982) suggest that in other cases the reduction of dense body components without such weakening effects could be said to be part of teleost evolution.

In certain cases, amongst those fish using stored lipids to obtain static lift, there may be insufficient lift to achieve neutral buoyancy. The result is the need to generate dynamic lift, by cruising at some minimum speed. Indeed, some sharks appear to regulate their density so as to be slightly more dense than water. Such sharks, continuously swimming and with fairly rigid pectoral fins required for manoeuvring, are bound to generate dynamic lift when moving and so do not need to achieve fully neutral buoyancy.

1.2.2 Fish muscle

Most teleost bodies are divided into two lateral halves by the median septum. This is a sheet of collagenous connective tissue supported by the axial skeleton: the skull and vertebral column. The main bulk of the swimming muscle is made up of rows of blocks of relatively short lateral muscle fibres arranged on each side of the median septum. A wave of muscle activation passes alternately down each side of the body causing the muscles to contract. The body bends (as a result of the vertebral column being longitudinally inextensible) and so a wave of body curvature follows the activation from the head to the tail.

There are essentially two types of muscle fibre: superficial red fibres running parallel to the longitudinal axis; and deeper white fibres arranged in complicated three-dimensional patterns. This complex structure allows all the white fibres to contract to a similar extent as the body bends (Alexander, 1969). The two types of muscle fibre form two separate “locomotory engines” for fish. The “slow” (aerobic) red muscle is very efficient and is used by the fish for cruising. The fast (anaerobic) white muscle is inefficient but very powerful. The weight cost of carrying an inefficient “burst engine” is insignificant for fish as they are approximately neutrally buoyant. (A terrestrial

animal could not afford such a bulky mechanism.) Note that the two systems are not in general used exclusively from one another. Part of the white muscle bulk may well be recruited for cruising in some fishes.

1.3 The study of fish swimming

We split the study of fish swimming into three broad categories: the study of swimming kinematics; the hydrodynamic modelling of swimming; and the integrated modelling of the muscle mechanics and hydrodynamics involved in swimming.

1.3.1 Description of swimming kinematics

This section briefly discusses the history of the study of fish swimming to arrive at a more precise description of what fish (at least those relevant to this thesis) are actually seen to do as they move around. (For more detail see Webb and Weihs, 1983, Chapter 1.)

Very early ideas related to aquatic locomotion date back to Aristotle who thought the animal made use of pivot points to progress forwards. The 17th century Neapolitan professor, Borelli, described the motion of the caudal fin as being the means by which fish propelled themselves. The oscillation was supposedly made up of a passive stroke from the straight position to the position of maximum bending, and an active stroke pushing water backwards as the tail returned to its centre-position. His views went unchallenged until Pettigrew (1873) concluded that the tail acted as a propellor throughout the whole stroke.

The advent of photography created an opportunity to improve on those earlier kinematic descriptions. Houssay (1912) used a time series of photographs taken and published by Marey in 1895. In particular he (Houssay) pointed out that in elongated fishes (he had pictures of dogfish and eel) the lateral wave of curvature moves from head to tail. Breder (1926) divided fish movements into two main categories with several subgroups. His classification (although slightly modified) remains useful. Firstly fishes were separated according to whether they used body and tail to propel themselves, or the movement of appendages. In the former category Breder classified the movements into three groups: anguilliform, ostraciiform, and carangiform; and in the latter he

identified seven groups: amiiform, gymnotiform, balistiform, rajiform, tetraodontiform, labriform, and diodontiform (Videler, 1993). In fact the original classification was not based on precise kinematic analyses, and has since been modified by subsequent researchers. Two of the terms are useful to us.

- Anguilliform motion (after the common eel of genus *Anguilla*) is the motion of fish with long flexible bodies. The amplitude of the bending wave on the body has discernible amplitude over the whole length of the body. Animals swimming using this mode tend to be of roughly uniform height (or span) along their whole length.
- Carangiform motion (after the family *Carangidae* including, for example, mackerel) describes fish swimming by lateral oscillations of the body for which the amplitude of the movement is only significant over roughly the last third of the body.

Gray (1933) provided quantitative analyses of the kinematics of several species, and in particular described what he observed in terms of two wave-like phenomena.

- A lateral wave of curvature with velocity V , wavelength λ_b and period T runs backwards along the body, with $V = \lambda_b T^{-1}$.
- Each point follows a sinusoidal path relative to a fixed frame of reference with forward velocity U , wavelength λ_s , period T and amplitude A . The wavelength λ_s is called the stride length, and we have $U = \lambda_s T^{-1}$.

Using more detailed techniques Videler and Wardle (1978) studied the kinematics of cod (*Gadus morhua*); and Videler and Hess (1984) studied the kinematics of saithe (*Pollachius virens*) and mackerel (*Scomber scombrus*). The aim of these studies was to quantify, as accurately as possible, Gray's kinematic parameters. Thus they were able to make a mathematical description of the fishes' motion, based on experimental data, to use as input to one of the hydrodynamic models for swimming (see below). Note that although not clear from Gray's description, the wave parameters may in fact vary along the length of the body.

Finally, these kinematic studies are fraught with difficulties. Videler (1993, Ch.5) describes the main techniques used in this field, including: methods to induce fish to swim under controlled

conditions, the cinematography, and the analyses and data processing. Undoubtedly great patience is required!

1.3.2 Mathematical modelling of swimming

We now move on to look at the mathematical modelling of high Reynolds number undulatory swimming. Traditionally this has been split into two groups: the first dealing with the flow about the whole undulating body, and the second treating the lunated tail (found in certain animals) in isolation. Our modelling is essentially related to the former.

The majority of models for swimming have concentrated on animals swimming at a constant velocity. In this so-called “steady state swimming” just enough thrust is produced to exactly balance the drag experienced by the fish due to its forward motion. A second characteristic of these models is that they quantify the fluid mechanical forces produced by some prescribed motion of the fish’s body. The work described in Section 1.3.1 illustrates how the relevant kinematic descriptions of swimming have been obtained.

Lighthill (1960) examined “what oscillatory movements a slender fish can make which will give it a high Froude efficiency”,

$$\eta = \frac{(\text{forward speed}) \times (\text{thrust available to overcome viscous drag})}{(\text{work done to produce both thrust and vortex wake})}. \quad (1.2)$$

Lighthill’s small amplitude elongated body theory for quantitative analysis of the reactive forces involved in swimming was based on “slender body” theory from aerodynamics. The assumption is that the dimensions and movements of the body at right angles to its direction of motion are small compared with its length, with “its cross-section varying only gradually” (Lighthill, 1960). This theory was based on a perturbation expansion in an amplitude parameter ϵ (Lighthill, 1960, Appendix), but was then interpreted in physical terms.

The theory is set out in a frame of reference in which the fish holds station in a uniform stream of speed U in the x -direction. The body has a “stretched straight position”, such that no resultant normal force acts on any cross-section, and swims by each cross-section S_x having a displacement $h(x, t)$ in the z -direction only. The slender body theory then allows the flow to be considered as

the sum of the steady flow around the stretched straight fish, and the flow due to the displacements $h(x, t)$. Each cross-section moves with lateral velocity

$$w = \frac{\partial h}{\partial t} + U \frac{\partial h}{\partial x} \quad (1.3)$$

relative to the free stream, giving the flow a momentum $m(x)w(x, t)$ per unit length of the body, where $m(x)$ is the added mass (virtual mass) of water per unit length associated with the motions in the z -direction.

The force in the z -direction on a cross-section S_x is equal and opposite to the rate of change of momentum of the fluid passing S_x :

$$Z(x, t) = \left(\frac{\partial}{\partial t} + U \frac{\partial}{\partial x} \right) [m(x)w(x, t)]. \quad (1.4)$$

From there Lighthill obtained the rate of work done by the fish's transverse motion and hence the mean rate of working

$$\bar{W} = m(l)U \left[\overline{\frac{\partial h}{\partial t} \left(\frac{\partial h}{\partial t} + U \frac{\partial h}{\partial x} \right)} \right]_{x=l} \quad (1.5)$$

which is seen to depend on the conditions at the tail only. By energy arguments he showed the mean thrust to be

$$\bar{P} = \frac{1}{2} m(l) \left[\overline{\left(\frac{\partial h}{\partial t} \right)^2} - U^2 \overline{\left(\frac{\partial h}{\partial x} \right)^2} \right]_{x=l}. \quad (1.6)$$

He further pointed out that in this model for steady state swimming (constant speed U in a straight line) the lateral displacements $h(x, t)$ are further restricted by the requirements that

1. the rate of change of lateral momentum must equal the resultant of the lateral (or lift) forces;
2. the rate of change of angular momentum about the y -axis must equal the moment of lateral forces about that (fixed) axis.

For an arbitrary $h(x, t)$ the motion can be made to satisfy these conditions by the addition of a rigid body motion: a lateral translation and a rotation. Lighthill called this the recoil correction.

The main conclusions (of Lighthill, 1960) were that the fish should pass a wave of increasing amplitude backwards along its body, and the bending wave having speed $\frac{5}{4}$ of the swimming speed and including a positive and negative phase to minimize angular recoil. These conclusions were

sufficiently in line with observation to warrant further investigation. A key point to note regarding this model is that the effect of the vortex wake on the fish is neglected.

Lighthill (1970) went on to discuss the use of slender body theory with some refinements to look in detail at anguilliform and carangiform swimming. In particular he examined the approximation used in calculating the virtual mass per unit length m , that for a cross-section S_x , m may be estimated as the virtual mass per unit length for an infinite cylinder C_x with the same cross-section. He found his assumptions to be a valid “rough approximation”.

Lighthill (1970, Section 2) obtained the instantaneous thrust P after extending the basic method to provide a first approximation of momentum in the x -direction associated with the body’s lateral displacement. Anguilliform motion is well suited to a model based on slender body theory. The animals in question (such as eels) tend to have continuous dorsal and anal fins towards the posterior end. The result is that whilst the cross-section is reduced to almost zero (a sharp trailing edge) the span remains fairly uniform over the whole length of the body.

Lighthill (1969) also points out that certain animals with numerous separate dorsal fins (eg cod, haddock) swim using something close to the anguilliform mode. He predicts (Lighthill, 1970, Section 3) that the vortex sheet filling the inter-fin gaps must behave much like a solid surface, and suggests the arrangement would be advantageous (over pure anguilliform swimming) in terms of efficiency.

The carangiform mode is seen as a further evolutionary “improvement” in obtaining thrust efficiently. Elongated body theory indicates that the mean thrust, equation (1.6), and the efficiency, are dependent on the conditions at the trailing edge only. In carangiform swimming the bending wave is effectively seen only over approximately the last third of the body, but has a larger amplitude in that region compared with the anguilliform mode. This may well improve efficiency since lateral acceleration of “water slices” occurs over a shorter time and is less likely to be accompanied by losses associated with vortex shedding at the dorsal and anal “edges” of the body (Lighthill, 1969). The result of the development to a different undulatory motion is that fish using the carangiform mode tend also to show certain morphological adaptations: in particular a reduction of body depth in the region just anterior to the tail fin; and a large mass in the front portion of the body that is not seen to move as part of the body’s bending wave. Lighthill (1970, Section 4) showed these

adaptations to be consistent with the reduction of (especially angular) recoil.

Lighthill (1971) developed the large amplitude elongated body theory. The original small amplitude version was derived (initially) from a complicated perturbation theory that could not be extended to large amplitude. However, Lighthill (1970, equations (13)-(15)) arrived at a physical interpretation of the theory, that did facilitate extension to large amplitude. He used a frame of reference where the fluid far from the fish is at rest and made use of the following principles (Lighthill, 1971).

1. "Water momentum near a section of fish is in a direction perpendicular to the backbone and has magnitude equal to the virtual mass per unit length, m , times the component w of the fish velocity in that direction."
2. "Thrust can be obtained by considering the rate of change of momentum within a volume enclosing the fish whose boundary at each instant includes a flat surface Π perpendicular to the caudal fin through its posterior end."
3. "In the momentum balance it is necessary to take into account the transfer of momentum across Π not only by convection but also by the action of the resultant $\frac{1}{2}mw^2$ of the pressures generated by the motions within the plane Π ."

Thus he was able to arrive at an expression for the instantaneous force on the fish

$$(P, Q) = \left[mw \left(\frac{\partial z}{\partial t}, -\frac{\partial x}{\partial t} \right) - \frac{1}{2}mw^2 \left(\frac{\partial x}{\partial a}, \frac{\partial z}{\partial a} \right) \right]_{a=0} - \frac{d}{dt} \int_0^l mw \left(-\frac{\partial z}{\partial a}, \frac{\partial x}{\partial a} \right) da, \quad (1.7)$$

where the motion occurs in the $y = 0$ plane, a is a Lagrangian coordinate along the backbone of the fish ($a = 0$ at the tail), $(x(a, t), z(a, t))$ is the position of a particular point on the fish, m is the virtual mass per unit length, and w is the velocity distribution of the body in a direction perpendicular to the backbone.

The conclusions of the small-amplitude theory are not greatly affected by the extension to large amplitude. The mean thrust can (as before) be found in terms of the conditions at the tail only. Also the recoil is still minimized by having an anterior portion of the body with large cross-sectional depth which is significantly reduced just ahead of the tail fin.

Note that in the large-amplitude elongated body theory (just as in Lighthill's earlier small-amplitude model) the effect of the vortex wake on the fish is neglected.

Weihs (1972, 1973) used the large-amplitude elongated body theory to look at fish going through the unsteady manoeuvres of starting and turning. To do this a slight change to the theory was required to separate the effect of the individual fins (sharp edges) in terms of their shedding of vorticity. Lighthill had assumed the shed wakes due to sharp edges to be absorbed into the flow around the fish, considering momentum shedding from the tail fin only. For swimming in a straight line this is probably a reasonable assumption. Weihs, however, required the momentum shedding forces at the various surfaces on the body because they follow different paths through the water (in turning) and because the point of action of the distribution of forces is also important in these unsteady motions. His equation for the instantaneous force on the body was

$$\mathbf{F} = -\frac{d}{dt} \int_0^l m w n d a - \sum_{i=1}^k \mathbf{L}_i \quad (1.8)$$

where the first term is due to the momentum of the added mass of water moved by the fish (and was in Lighthill's version, equation (1.7)); but the second term represents the sum of the momentum changes due to the shedding of vorticity at the fish's sharp edges, replacing Lighthill's equivalent term involving conditions at the trailing edge only. The \mathbf{L}_i ("lift" forces on individual fins) are calculated from "classical methods of unsteady aerodynamics".

Weihs (1972) described the turning manoeuvres in terms of three distinct stages based on the motion of the centre of mass. Initially, as the head and tail bend towards each other, the centre of mass moves along the initial straight swimming direction. At this point the head points along the final direction. During the second stage, the body curvature further increases, and the resulting forces are directed towards the centre of the turn: the centre of mass moves through a curve until in line with the head along the new direction of travel. Finally, as the body straightens, the tail flicks back producing forces that are basically parallel to the new direction, and a couple that brings the body's rotation slowly to zero.

Looking at fast starts, Weihs (1973) used Lighthill's version of elongated body theory to explain the conditions required for high thrust at high efficiency: the essential conclusion being that the rear part of the fish was required to move with high speed in a direction perpendicular to the intended direction of motion, oriented at a small positive angle of attack. He found the conclusions to be

borne out by his modified, slightly more detailed version of the theory. Weihs described both starts and turns in terms of “C-shape” bending of the body. Webb (1976) also identified an “S-shaped” body curve associated with fast starts. Harper and Blake (1990, 1991) examined Pike startle-responses and fast starts in feeding. They found different types of fast start, allowing the fish to move off at various angles to its original orientation. In particular, in feeding, the pike tends to strike along the direction of its initial orientation.

The use of elongated body theory in the context of starts and turns is not entirely satisfactory because of the requirement of small curvature. The movements associated with unsteady manoeuvres such as starts and turns are characterized by the body of the fish assuming positions involving both large lateral deformation and large curvature.

Wu (1961) set out a two-dimensional inviscid theory for swimming using “the general theory for oscillating deformable airfoils” (see also Chapter 3). He calculated time averaged thrust and power associated with two simple examples for the lateral motion $h(x, t)$: namely a travelling wave with (a) a uniform amplitude envelope, and (b) a linearly varying amplitude envelope. He went on (Wu, 1971a) to use the same basic model (two-dimensional, linearized, inviscid theory) to allow variable forward speed. This was done using a Laplace transform method.

In addition Wu (1971a, section 4) considered an elementary beam theory model describing the deformation of the swimming body. He separated the total bending moment at each point along the body into an active contribution due to muscular contractions, and a passive contribution due to the elastic nature of the body tissue. He simplified the equations by assuming tangential forces to be everywhere small, but did not actually solve the equations to study the applied bending moment distribution. He did however integrate the equations and show them to be “linked” to Lighthill’s recoil conditions. This point is important, and is considered in greater detail in Chapter 6.

Wu (1971b, 1971c) considered the “optimum shape” for the minimization of energy loss given the production of some fixed thrust. Note that “optimum shape” refers to the characteristics of the lateral deformation of the body, not its three-dimensional shape. Firstly (Wu, 1971b) this was done for the time-harmonic motion of a rigid plate. In considering the general problem of a flexible plate, Wu concluded that “the exact nature of the optimum shape could not be completely determined”. He then (Wu, 1971c) looked at the optimum shape problem in the context of the unsteady slender

body theory (Lighthill, 1960), initially for a body of zero thickness, but with the additional shedding of vorticity from sharp “trailing edges” forward of the tail fin. In this case the optimum lateral displacement was determined to be a backwards travelling wave of speed $c > U$ (where U is the forward swimming speed) with an amplitude nearly uniform from the section of maximum span to the tail. Wu (1971c, Appendix) also accounted for the effects of geometrical asymmetry, thickness and time dependent forward speed, but did not find any major changes to the conclusions regarding optimum shape.

Cheng *et al.* (1991) followed Lan (1979) in using a vortex-lattice panel method to model swimming. The three-dimensional, small-amplitude analysis of an infinitely thin waving plate was shown to be capable of producing reasonable results over a wide range of aspect ratios. They concluded that the undulatory motion served to reduce three-dimensional effects and postulated this to be a significant reason behind the fact that undulatory swimming is used by a large number of aquatic animals. Crucially, and in contrast to Lighthill’s elongated body theory, the vortex ring panel method includes the effect of the wake on the flow around the body (or plate). In this small-amplitude theory, the self-induced deformation of the wake is neglected and it is assumed that the wake is planar. Note that the model is not able to treat a thin plate of general shape, but is restricted to rectangles and simple profiles where the leading edge may have a slope, but the tail remains rectangular.

There has also been work on the propulsive effectiveness of a pitching and heaving plate. This has been done in the context of modelling the “lunate tail” arrangement of many of the fastest fish (eg tuna) and cetacean mammals (eg whales). If the carangiform mode can be seen as an evolutionary development from the anguilliform mode (Lighthill, 1969) then it could be said that certain carangiform swimmers have evolved more specialised characteristics associated with high speed and efficiency (Lighthill, 1970). There are three distinct elements to this further development. The central posterior portion of the caudal fin is “missing” (the trailing edge is concave). There is a reduction in the sweepback of the two “wing-like” surfaces that make up the caudal fin. The caudal fin acquires a large aspect ratio (the square of the span divided by the planform area) and the “lunate” form. These features are not consistent with the animal being an “elongated body”: hence the separate theory. Fig. 1.1 (taken from Lighthill, 1969) shows some examples of the lunate tail in various animals. Note that some of these forms were acquired along quite

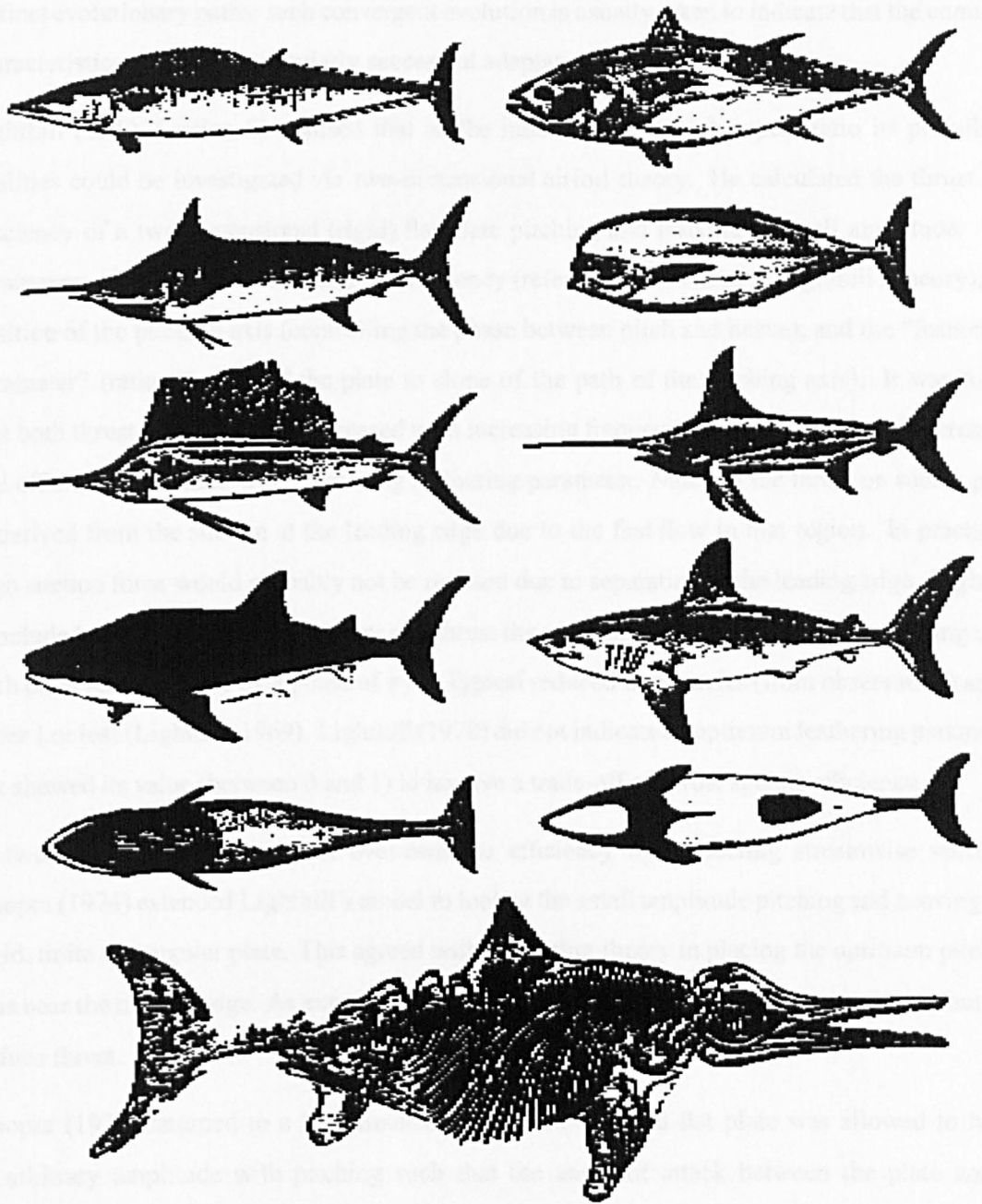


Figure 1.1: Variations of the lunate tail. Reading from left to right down the page: lateral views of wahoo, tunnyfish, striped marlin, louvar, sailfish, swordfish, whale shark, and porbeagle; ventral views of the sei whale, and a dolphin; an impression of *Ichthyosaurus* (taken from Lighthill, 1975).

distinct evolutionary paths; such convergent evolution is usually taken to indicate that the common characteristics represent particularly successful adaptations.

Lighthill (1970, Section 5) realised that as the lunate tail had high aspect ratio its propulsive qualities could be investigated via two-dimensional airfoil theory. He calculated the thrust and efficiency of a two-dimensional (rigid) flat plate pitching and heaving at small amplitude. The parameters of interest were the reduced frequency (referred to the chord in Lighthill's theory); the position of the pitching axis (controlling the phase between pitch and heave); and the "feathering parameter" (ratio of slope of the plate to slope of the path of the pitching axis). It was found that both thrust and efficiency decreased with increasing frequency; and that the thrust decreased, and efficiency increased with increasing feathering parameter. Much of the thrust on such a plate is derived from the suction at the leading edge due to the fast flow in that region. In practice a high suction force would probably not be realised due to separation at the leading edge. Lighthill concluded that for optimum efficiency and thrust the pitching axis would be near the trailing edge with pitch leading heave by a phase of $\pi/2$. Typical reduced frequencies (from observation) are of order 1 or less (Lighthill, 1969). Lighthill (1970) did not indicate an optimum feathering parameter, but showed its value (between 0 and 1) to involve a trade-off of thrust against efficiency.

A two-dimensional theory must over-estimate efficiency by neglecting streamwise vorticity. Chopra (1974) extended Lighthill's model to look at the small amplitude pitching and heaving of a rigid, finite rectangular plate. This agreed with the earlier theory in placing the optimum pitching axis near the trailing edge. As expected, finiteness (indeed, reduction in aspect ratio) was found to reduce thrust.

Chopra (1976) returned to a two-dimensional model. A rigid flat plate was allowed to heave at arbitrary amplitude with pitching such that the angle of attack between the plate and its instantaneous path remained small. (This is justified on the basis of avoiding the leading edge separation that would probably otherwise occur.) Based on the previous work the pitching axis was set at the trailing edge with pitch leading heave by $\pi/2$. Again, the conclusion was for "competition" between thrust and efficiency. High efficiency, low thrust was found at large amplitude, small angle of attack and small frequency. Increasing the angle of attack (ie increasing the feathering parameter) and the frequency improved the thrust but reduced efficiency. The

warning was repeated that high angle of attack to increase thrust would imply a high suction component that might not be realised in practice if separation occurred at the leading edge. Chopra commented that the work indicates a preference for a reduced frequency (based on chord length) of approximately 0.8 and an amplitude of roughly twice the mean chord length, agreeing with data on wavyback skipjacks (Fierstine and Walters, 1968).

Chopra and Kambe (1977) returned to a three-dimensional model of small amplitude pitching and heaving of plates with general planform. They analysed the propulsive performance in terms of aspect ratio, reduced frequency, feathering parameter and position of the pitching axis of thin plates with various curved leading and trailing edges. The general conclusions continued to agree with the previous work. They found that at low feathering parameter values (not seen in nature) the planform shape was not significant. At higher values of the feathering parameter the propulsive performance was very dependent on shape. In particular a sweptback leading edge resulted in a smaller suction contribution for the same total thrust (which is desirable because it makes performance less susceptible to thrust-loss due to separation at the leading edge). However, increasing the sweepback caused efficiency to be reduced (markedly so at sweepback angles greater than 30°).

Katz and Weihs (1978) modelled the pitching and heaving on a two-dimensional propulsor with passive chordwise flexibility. The model was extended (Katz and Weihs, 1979) to a three-dimensional calculation involving a slender flexible plate. The flexibility was found (in both cases) to reduce the total force on the plate, but in such a way that the component oriented to provide thrust was not greatly affected. On the other hand, efficiency was improved.

Liu and Bose (1997) examined the propulsive performance of a large aspect ratio lunate tail using a three-dimensional unsteady panel method. They looked at the effect of passive and active spanwise flexibility. Efficiency was reduced by passive flexibility. However, "careful" active control of the phase of the spanwise flexibility was calculated as improving propulsive efficiency over the value for an equivalent rigid foil. They concluded then, that if high propulsive efficiency was a major factor in lunate tail evolution, either high spanwise stiffness or active control of spanwise deformation would be required. They add that many bony fishes and cetaceans do possess tail fins of high spanwise stiffness; but that there is "no conclusive evidence" that such animals have active

control of any spanwise deformation of their tail fins.

Hydromechanical models of swimming have tended to concentrate on steady swimming, and the production of the thrust required to overcome viscous drag and retain a constant speed. Lighthill (1971, Section 3) estimated that the drag associated with the undulatory motion of a swimming fish was approximately four times that associated with the same fish gliding rigidly. Webb (1971a,b) obtained a factor of three for this discrepancy from experiments on trout. Weihs (1974) then estimated that at slow average speeds, fish could cover a given distance at half the energy cost needed for steady swimming by intermittently adopting periods of swimming and gliding. Videler and Weihs (1982) showed similar energetic advantages to exist for high average speeds also. They obtained high speed film of free swimming saithe and cod at high velocities in a “kick and glide” style. Lighthill comments several times in his book (Lighthill, 1975) that ultimately one requires a combined theory of swimming including both reactive and resistive forces. Liu and Bose (1997) refer to “an approximate prediction of skin friction through a two-dimensional boundary layer calculation” in their lunate tail model, but no further details are given.

1.3.3 Fish-water interactions

Hess and Videler (1984) modelled a swimming fish as an active bending beam (Wu, 1971a), obtaining a second order differential equation for the bending moment distribution $M(x, t)$:

$$\frac{\partial^2 M}{\partial x^2} = m_b \frac{\partial^2 h}{\partial t^2} - L \quad (1.9)$$

where x is the distance along the body measured from the nose, $m_b(x)$ is the body mass distribution, $h(x, t)$ is the imposed lateral displacement of the body, $L(x, t)$ is the hydrodynamic force integrated across the span (ie dorso-ventrally), acting on the body due its motion through the water, and $M(x, t)$ is the bending moment distribution along the body. They used Lighthill’s small-amplitude slender body theory to do the fluid mechanics and calculate Δp . The input body motion was taken from a study of the kinematics of swimming of saithe and mackerel (Videler and Hess, 1984). Their main result was to conclude that the bending moment behaves as a standing wave.

Cheng and Blickhan (1994) made a similar analysis using the three-dimensional waving-plate theory. They compared three descriptions of the lateral displacement: Hess & Videler’s kinematic

data (Videler and Hess, 1984); and two travelling wave functions with an exponential and parabolic amplitude envelope respectively. Both Hess and Videler (1984) and Cheng and Blickhan (1994) used a mass distribution chosen to approximate the data obtained by Videler and Hess (1984).

The main conclusion of Cheng and Blickhan (1994) of interest to us is that in comparison with the slender body theory, the vortex-ring panel method required a smaller recoil correction when applied to Hess & Videler's kinematic data. Recoil would cause lateral vortex shedding from the edges of the fish body, and thus waste energy. We assume then that evolution would favour the reduction of recoil. The fact that the vortex-ring panel method theory requires a smaller recoil correction than the slender body theory is taken as an indication that the former is the better model, at least with regards to momentum balance. This is part of the motivation for our model being based on an extension to the waving plate theory of Cheng *et al.* (1991). They also noted that recoil resulted in a non-zero amplitude at the head for a subcarangiform swimmer such as saithe.

Their model further suggested that the highest bending moment occurred near the section of the body with highest muscle mass, and that the bending moment behaved as a standing wave in that part, which "acts like the motive source". In the part of the body between this motive section and the caudal fin the bending moment varied as a travelling wave with speed close to that of the body's lateral motion.

Cheng *et al.* (1998) went on to consider a more detailed model of the fish internal mechanics. The bending moment $M(x, t)$ of equation (1.9) can be thought of as being made up of two components: the active bending moment due to muscular contractions; and a passive contribution governed by the viscoelastic properties of the body tissues. By modelling the passive properties of the body they were able to obtain an improved estimate of the bending moment M_m generated by the muscle. It is assumed that the behaviour of muscle activation corresponds to that of the muscle bending moment. They compared their results for the wave speed of the muscle bending moment travelling wave with experimental measurements of the speed of the muscle activation wave (also a travelling wave). Given the difficulties associated with the calculations and the experiments the agreement was encouraging. The next stage of development was felt to be the improvement of the hydrodynamic calculations to include the nonlinear, three-dimensional effects of a full large-amplitude model.

Carling *et al.* (1994) have looked at the problem of integrating the body and fluid mechanics slightly differently. Bowtell and Williams (1991) developed a discrete model for the mechanical structure of the lamprey. They derived a set of linearized equations to study the interaction between muscle activation and body curvature, initially neglecting the fluid mechanical constraints on a swimming body. Bowtell and Williams (1994) derived a first order continuous version of the discrete model. This was deemed to be as effective, but more practical to use. The aim of their work is to “develop a simulation in which activation of the spinal cord circuitry will lead to realistic forward swimming of the lamprey” (Carling *et al.*, 1994, p.132). The hydrodynamic component of their model involves the solution of the two-dimensional Navier-Stokes equations. At this time a model integrating the muscle activation, body curvature and fluid mechanics has not been published.

1.4 A model for large amplitude swimming

We consider only steady state swimming, although the basic method and model will be applicable to more general motions. Thus we assume that the fish swims at a constant speed in a straight line. It is further assumed to swim in a horizontal plane. The forward motion is taken to be the result of the fish sending a known (prescribed) wave of lateral displacement backwards along its body.

In terms of modelling the fluid mechanics we suppose

- that having a high Reynolds number allows us to neglect viscosity, assuming inviscid flow everywhere except in the boundary layer along the surface of the body, and in the wake;
- that the boundary layer is laminar and remains attached along the whole length of the body, with vorticity being shed into the wake from the tail fin (trailing edge);
- and that the most important input to the model is the description of the displacement wave.

The hydrodynamic calculations assume the body to be infinitely thin. However, in modelling the effect of the hydrodynamic forces, it is necessary to model the fish as having some mass distribution. This implies that the body must have density, which is taken to be uniform, and equal to the density of the surrounding water. In the examples given in this thesis, in which the fish body

form is taken to be rectangular, the mass per unit length is also taken to be uniform, although this is not a requirement of the model.

The body of the fish is modelled as an active bending beam to calculate the bending moment distribution associated with a given pattern of movement. This involves several detailed assumptions (see Chapter 6) but in particular supposes that it is sufficient to specify the internal and external forces as a function of position along the longitudinal axis only.

The fluid mechanical model, involving an infinitely thin fish, is aimed towards calculating the time-dependent pressure distribution along a swimming fish, given some imposed description of its motion. The solid mechanics model, involving a body with thickness, relates the imposed motion and the resulting external forces to the bending moment distribution along the fish. The two calculations can be done independently. Thus, it is not inconsistent to be using different simplifying assumptions regarding the geometry of the body.

The input to our model is a constant swimming speed, say U_0 , and an imposed lateral undulation wave $h(s, t)$, where s is the position along the body measured from the nose, and t is the time. Associated with the lateral motions is some distribution of thrust-producing pressure forces acting on, and in a direction normal to, the surface of the body. The relative tangential motion between the body and fluid serves to create a drag force (acting along the tangent of the surface) due to the viscosity of the fluid. Our assumption of constant forward swimming speed requires that the streamwise component of the pressure forces exactly balance that component of the drag forces. It is also of course important to consider the balance of sideforce and moment due to the large lateral component of the pressure forces. Any imbalance in the sideforce or moment would result in a change of lateral or angular momentum. This means that an arbitrary $h(s, t)$ is not in general consistent with pure translation in the swimming direction. The solution to this problem, Lighthill's recoil correction (Lighthill, 1960), is to include an additional time-dependent rigid-body lateral translation and rotation (sideslip and yaw). These additional components of the motion are not known in advance. In our model it is necessary to calculate the recoil correction iteratively at each time step (see Chapter 3).

Our hydrodynamic model also includes a calculation of the viscous drag along the body using a boundary layer model. We realised that in order to correctly describe the deformation of the

bending beam at arbitrary amplitude it is necessary to include the tangential component of the external forces acting on the beam (Wempner, 1973). However, having an estimate of the drag is useful beyond calculating the bending moment distribution. Rather than merely stating that the thrust must balance the drag, we can in principle enforce the conservation of forward momentum. In other words, we add a streamwise component to the recoil correction, thereby allowing variations in the swimming speed.

1.5 Outline of the thesis

This introductory chapter concludes by outlining the work in the remainder of the thesis.

Chapter 2 describes the method behind a basic two-dimensional hydrodynamic model of swimming. The method used is a point-vortex panel method. The work in the chapter focuses on explaining the method, and verifying that it works by comparison with examples relating to the unsteady motion of a flat plate.

Chapter 3 continues with the two-dimensional hydrodynamic theory. There is some discussion of the wave of lateral displacement on the body, and also of the recoil correction. Results are compared with Wu's two-dimensional theory (Wu, 1961).

Chapter 4 develops the large amplitude three-dimensional hydrodynamic model for swimming. This is done using a vortex lattice panel method, extending the work of Cheng *et al.* (1991). The method is tested in the context of a pitching and heaving flat plate, and for a small amplitude waving plate. Unfortunately (due to an as yet untraced bug in the code) we have been unable to force the system to satisfy the recoil correction.

Chapter 5 introduces a first attempt at the boundary layer problem along the body of a swimming fish. The aim here is to estimate the viscous drag as a function of position along the longitudinal axis. The numerical method for solving the boundary layer equations is first order accurate, and only two-dimensional as yet.

Chapter 6 deals with the solid mechanical aspects of the work. The fish is modelled as an active bending beam, and the derivation of the bending moment equations is included for both small and

large amplitude bending. In the context of fish swimming, the large amplitude equations represent a new development.

Our conclusions are presented in Chapter 7. There is an Appendix with some further information about the computer programs produced during the research.

Chapter 2

Two-dimensional panel method

2.1 Introduction

It seems natural to start with a two-dimensional version of the model. This gives an opportunity to deal with the basic principles of the method in a simpler setting than the full 3D problem. In addition there are many examples against which the results can be tested, including Wu's two-dimensional theory for a waving plate, (Wu, 1961).

To reiterate what has already been said, we are interested in the class of swimmers who move forward by passing a wave backwards along their bodies. Although this general mode of swimming is found across a very wide range of Reynolds Numbers (based on the body length), this work is related only to those situations where inertial forces dominate the motion. We assume that the flow is inviscid, except on the body and in the wake, and our problem is that of the movement of the known boundary S_b (the animal), and an unknown boundary S_w (its wake), submerged in a potential flow of an incompressible fluid. The continuity equation therefore reduces to Laplace's equation for the velocity potential Φ

$$\nabla^2 \Phi = 0. \tag{2.1}$$

The problem is solved in a frame of reference, OXZ , in which the fluid is at rest at infinity. Consequently, the boundary conditions for the problem are as follows:

1. All disturbances decay to zero at infinity.

2. There is no flow through the boundary: the normal component of the velocity relative to the body must be zero on the body.

$$(\mathbf{V} - \mathbf{V}_b) \cdot \mathbf{n} = 0 \quad (2.2)$$

where \mathbf{V} is the absolute velocity; \mathbf{V}_b is the velocity of the body; and \mathbf{n} is the unit normal at that point. Notice that for a swimming fish these quantities are all changing with time.

3. Pressure is continuous across the wake: the wake must deform according to the local fluid velocity.
4. From the Helmholtz Theorems we have that the circulation around any closed loop of material particles is constant. Thus, the total circulation around the body and the wake remains constant (zero, if the body starts from rest), and vortices in the wake will be of constant strength.
5. The Kutta Condition: this is used to force the fluid to flow smoothly off the trailing edge of the body.

Using Green's Identity one can show that a general solution may be constructed as a sum of source and doublet distributions on the surface of the body and in the wake. In fact, for an infinitely thin body a distribution of point vortices also provides a general solution to the problem. This has the advantage of being slightly simpler, and also more easily represents some of the physics of the flow in question, at least intuitively.

The point vortex is a singularity which induces a tangential velocity component whose magnitude decays like $1/r$, where r is distance from the the vortex. For the velocity field, \mathbf{q} , we have (relative to the vortex at $r = 0$)

$$q_r = 0, \quad (2.3)$$

$$q_\theta = -\frac{\Gamma}{2\pi r}, \quad (2.4)$$

where Γ is positive clockwise. The potential is

$$\begin{aligned} \Phi &= \int q_\theta r d\theta + C \\ &= -\frac{\Gamma\theta}{2\pi} + C, \end{aligned} \quad (2.5)$$

where C is an arbitrary constant that we can set to zero.

2.2 The lumped vortex element

Before describing the panel method in detail, it is necessary to explain the “Lumped Vortex Element”, (Katz and Plotkin, 1991).

Consider a flat plate airfoil at constant small angle of incidence, α , in a constant free stream U . This airfoil can be represented by a continuous vorticity distribution $\gamma(s)$, which can in turn, from a far field point of view, be replaced by a single point vortex (the Lumped Vortex Element) of strength $\Gamma = \int_0^l \gamma(s) ds$, where l is the chord length of the plate.

By the Kutta-Zhukovskii Theorem, the lift on this airfoil is known to be $\rho U \Gamma$ acting at the centre of pressure, which is at the quarter-chord. So we place the single vortex at this point and then satisfy the zero normal velocity condition at some collocation point kl , where k is unknown. Remembering the induced velocity due to a point vortex, equation (2.4), the boundary condition gives

$$\frac{-\Gamma}{2\pi(kl - \frac{1}{4}l)} + U\alpha = 0 \quad (2.6)$$

But we already know the value of the circulation around such a flat plate:

$$\Gamma = \pi l U \alpha, \quad (2.7)$$

and so substituting for Γ we can solve this equation and obtain

$$k = \frac{3}{4}. \quad (2.8)$$

This result is based on the value for Γ from equation (2.7), which is obtained from a solution which takes into account the Kutta Condition at the trailing edge. Thus, the use of a Lumped Vortex Element guarantees that the Kutta Condition has been satisfied. For a multi-element body it is therefore reasonable to place a point vortex at the quarter-chord of each element, impose the boundary condition at the three-quarter chord, and assume that the Kutta Condition is satisfied. However, this may become inaccurate as we depart further and further from a flat plate at constant, small angle of incidence. (Remember that the reason for writing a two-dimensional panel method was primarily to gain experience in the general concepts, rather than to accurately model large amplitude swimming.)

2.3 The two-dimensional panel method

This section describes the key details of the method, which is taken basically from the section on unsteady panel methods in Katz and Plotkin (1991). In contrast to the method in the book I have solved the problem in a frame of reference where the fluid is at rest at infinity.

The unsteady panel method is based on marching through time and following a number of procedures at each time step. Firstly we establish the current geometry. Then the boundary conditions are used to construct a set of linear equations for the strengths of the point vortices. The calculated strengths are used to calculate the pressure distribution along the body. Finally we must deal with the deformation of the wake, before returning to the start of the time loop.

2.3.1 Non-dimensionalisation

We are modelling the motion of a body of length \hat{l} , where the “hat” is used to denote a dimensional variable. Typically the body is moving in the negative \hat{X} -direction with a characteristic speed \hat{U}_0 . It is possible that the whole body has \hat{X} -component of velocity $-\hat{U}_0$; that a single fixed point on the body has an \hat{X} -component of velocity $-\hat{U}_0$; or that \hat{U}_0 is an approximate mean forward speed of the body, or some fixed point on the body.

We non-dimensionalise lengths with respect to \hat{l} , and velocities with respect to \hat{U}_0 . Time is non-dimensionalised such that

$$t = \hat{U}_0 \hat{t} / \hat{l}. \quad (2.9)$$

The non-dimensional pressure is taken to be

$$p = \hat{p} / (\hat{\rho} \hat{U}_0^2). \quad (2.10)$$

2.3.2 Description of the motion.

We model the body as infinitely thin, and of non-dimensional length $l = 1$. It also has some overall motion in the negative X -direction, characterized by at least one fixed point on the body moving with constant speed $U = 1$. The body is inextensible. The variable s is used as a

Lagrangian coordinate describing the distance along the body from the leading edge (nose) at $s = 0$. For consistency with the later 3D version, the lateral displacement is in the Z -direction. The displacement is given by

$$Z = h_z(s, t). \quad (2.11)$$

A consequence of requiring that the body be inextensible is that a lateral displacement $h_z(s, t)$ is accompanied by motion in the x -direction. The inextensibility condition is written:

$$\left(\frac{\partial h_x}{\partial s}\right)^2 + \left(\frac{\partial h_z}{\partial s}\right)^2 = 1, \quad (2.12)$$

so that $h_x(s, t)$ describes the body's displacement in the X -direction due to its lateral movements.

For the purposes of the current chapter we will be considering the motion of a flat plate, so both $h_x(s, t)$ and $h_z(s, t)$ can be expressed analytically. However, when $h_z(s, t)$ describes the lateral displacement of a waving plate (in order to model swimming) it is necessary to use the inextensibility condition and a numerical integration to obtain $h_x(s, t)$, see Chapter 3.

2.3.3 Discretisation of the body and the wake

The body is divided up into N lumped vortex elements, or “panels”. A point vortex is placed at the quarter chord of each panel, with an associated collocation point at the three-quarter chord of the panel. The panels may be of equal length l/N , or a variable distribution of panel lengths may be used, such as “cosine spacing”, (Katz and Plotkin, 1991, p.319). In this variable panelling of the body, it is assumed that there is a greater need for smaller panels near the leading and trailing edges.

Figure 2.1 illustrates the idea and shows why the term “semi-circle method”, (Cheng *et al.*, 1991) is also used in this context. Using equal spacings in the angle θ , (positive clockwise) provides variable length panels as required. With N panels, the i 'th panel-node is found using the angle

$$\theta_i = \frac{i\pi}{N}, \quad i = 0..N. \quad (2.13)$$

The i 'th node has s -coordinate

$$s_i = \frac{l}{2}(1 - \cos \theta_i), \quad (2.14)$$

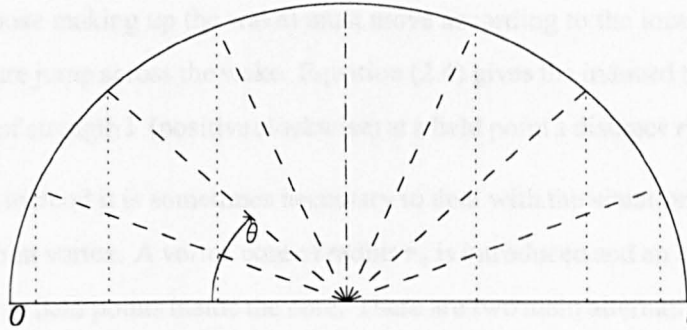


Figure 2.1: Variable length panels are produced from equally spaced angles around a semi-circle.

and the length of the j 'th panel ($j = 1..N$) is given by

$$\begin{aligned} (\Delta l)_j &= s_j - s_{j-1} \\ &= \frac{l}{2} (\cos \theta_{j-1} - \cos \theta_j). \end{aligned} \quad (2.15)$$

As the body moves, vorticity is shed continuously into the wake. We assume that there is no separation along the body, nor from the leading edge, and that vorticity is shed only from the trailing edge. The wake is a continuous vortex sheet modelled by a distribution of point vortices, with one point vortex being shed at each time step. It is necessary to decide where to place the shed vortex: approximately $1/4$ of the distance back along the path travelled by the trailing edge in the latest time step has been found to work well. Using equations (2.18) and (2.19), and by putting $s = l$ and $t = t_j - k\Delta t_{j-1}$, the shed vortex can be placed at any point along the trailing edge path. The choice of $k = 1/4$ is discussed by Katz and Plotkin (1991), and is briefly examined later in the current chapter. The determination of the strength of this shed vortex is described in Section 2.3.5.

2.3.4 The induced velocity due to a point vortex

As stated earlier the panel method models the body and wake by a distribution of point vortices. The bound vortices (those modelling the body) are constrained by the motion of the body. The free point vortices (those making up the wake) must move according to the local velocity field so that there is no pressure jump across the wake. Equation (2.4) gives the induced tangential velocity due to a point vortex of strength Γ (positive clockwise) at a field point a distance r from the point vortex.

In the numerical method it is sometimes necessary to deal with the situation where a field point is very close to a point vortex. A vortex core of radius r_c is introduced and an adjustment made to the induced velocity at field points inside the core. There are two main alternatives: to set the velocity inside the core to zero; or to have a Rankine vortex with solid body rotation inside the core. In the latter case, the tangential induced velocity is

$$q_\theta = \begin{cases} -\Gamma/2\pi r & r \geq r_c \\ \Omega r & r \leq r_c \end{cases} \quad (2.16)$$

where the value of Ω is given by

$$\Omega r_c = \frac{-\Gamma}{2\pi r_c}. \quad (2.17)$$

According to Katz and Plotkin (1991) the core radius can be as small as the machine accuracy. Note that introducing the vortex core in this manner also deals with the fact that a point vortex induces zero velocity on itself.

2.3.5 Forming the boundary condition equations

Calculating the current geometry is simple, and just involves using the displacement functions (equations (2.11) and (3.3)). An array stores the positions of the $N + 1$ panel nodes along the body. Evidently the i 'th node lies at a certain value of s_i from the nose, and so its position at time t is given by

$$X_i = -Ut + h_x(s_i, t) \quad (2.18)$$

$$Z_i = h_z(s_i, t). \quad (2.19)$$

Additionally, we must shed a point vortex of unknown strength from the trailing edge. This strength is chosen to ensure that the total circulation around the body and the wake remains constant.

The main task in the basic panel method is to form the set of linear equations for the unknown vortex strengths, that is N vortices on the body, and the latest shed vortex. Let $\Gamma_j, j = 1..N$ be the strengths of the bound vortices, with Γ_{N+1} being the strength of the shed vortex. Remember that the bound vortices are placed at the quarter-chord of each element, with the boundary condition being satisfied at the collocation points placed at the three-quarter chord of each element. We construct the so-called matrix of influence coefficients A , where the element A_{ij} is the normal component of the induced velocity at the i 'th collocation point due to the j 'th point vortex, assuming that the vortex is of strength unity. The magnitude of the induced velocity is given by equation (2.4), but we need a vector in order to find its component normal to the body. If \mathbf{r}_{ij} is the position vector of the i 'th collocation point relative to the j 'th point vortex then, temporarily making use of the 3rd dimension, we have

$$A_{ij} = \left(\hat{\mathbf{r}}_{ij} \times \hat{\mathbf{j}} \left(\frac{-1}{2\pi |\mathbf{r}_{ij}|} \right) \right) \cdot \mathbf{n}_i \quad (2.20)$$

where $\hat{\mathbf{j}}$ is the unit vector in the y-direction, and $\hat{\mathbf{r}}_{ij}$ is the unit vector in the direction of \mathbf{r}_{ij} .

The right hand sides of these N equations are the normal components of the fluid velocity at the collocation points. Initially, this is just the normal component of the velocity of the body. However, in general the wake also makes a contribution which must be included. We know the strengths and positions of the vortices in the wake so its total contribution to the velocity at the i 'th collocation point $(\mathbf{V}_w)_i$ is easily calculated.

Thus we have N equations in $N + 1$ unknowns:

$$\sum_{j=1}^{N+1} \Gamma_j A_{ij} = (\mathbf{V}_b - \mathbf{V}_w)_i \cdot \mathbf{n}_i, \quad i = 1..N, \quad (2.21)$$

where \mathbf{V}_b , \mathbf{V}_w and \mathbf{n} are the velocity of the surface, the velocity induced by the wake, and the unit normal respectively, at the i 'th collocation point. (Note also that $\mathbf{V}_w = 0$ at $t = 0$.) These equations describe how the normal fluid velocity at each collocation point on the body is equal to the normal velocity of the body itself.

We need one more equation, and this comes from the conservation of circulation. If $\sum(\Gamma_j)_{t-\Delta t}$ is the total bound vorticity at the end of the previous time step, we must have

$$\sum_{j=1}^{N+1} \Gamma_j = \left(\sum_{i=1}^N \Gamma_j \right)_{t-\Delta t} . \quad (2.22)$$

The resulting set of linear equations for the vortex strengths $\Gamma_j, j = 1..N + 1$ can be solved numerically in a straightforward manner, such as by LU Decomposition.

Having calculated the bound and shed vortex strengths we can use them to calculate the pressure distribution along the body. As things stand, it is possible to leave this calculation until later: a detailed description is given below. However, it turns out that our need to make a recoil correction will require us to calculate the pressure distribution as we go along.

2.4 The pressure distribution

The goal here is to write an expression for the pressure jump across the body at each collocation point in terms of the bound vortex strengths. Equation (2.47) below is essentially that used by Katz and Plotkin (1991, p.474). (The terms arising from the motion of the body differ in sign, but this is a consequence of using a different frame of reference.)

We start from the (dimensional) unsteady Bernoulli Equation in a frame of reference in which the fluid is at rest far from the body:

$$\frac{\hat{P}_\infty - \hat{P}}{\hat{\rho}} = \frac{1}{2} |\hat{\nabla} \hat{\Phi}|^2 + \frac{\partial \hat{\Phi}}{\partial \hat{t}}. \quad (2.23)$$

Writing superscripts + and - to denote above and below the plate respectively, the jump in non-dimensional pressure across the plate is given by $\Delta P = P^- - P^+$.

$$\Delta P = \frac{1}{2} |\nabla \Phi^+|^2 - \frac{1}{2} |\nabla \Phi^-|^2 + \frac{\partial \Phi^+}{\partial t} - \frac{\partial \Phi^-}{\partial t}. \quad (2.24)$$

There is a complication here in that the point at which we want to calculate the pressure jump is moving. So for each collocation point we make a coordinate transformation to a (non-rotating) frame of reference at which this point is the stationary origin. In what follows, capital letters denote the global frame where the fluid is at rest at infinity, and small letters are used to denote quantities in the moving frame. In this new moving frame the potential ϕ can be written as the sum of potentials

1. $\mathbf{u}(t) \cdot \mathbf{x}$, from the time dependent free stream, where $\mathbf{u}(t) = -\mathbf{V}_b(s_0, T)$, the velocity of the point $s = s_0$ as described in the global frame.

2. $\phi_b(\mathbf{x}, t)$, the potential due to the bound vortex sheet,
3. $\phi_w(\mathbf{x}, t)$, the potential due to the wake vortex sheet.

For the moment we will write $\phi_1(\mathbf{x}, t) = \phi_b + \phi_w$. The total potential is given by

$$\phi(\mathbf{x}, t) = \phi_1(\mathbf{x}, t) + \mathbf{u}(t) \cdot \mathbf{x}. \quad (2.25)$$

If $\mathbf{X}_0(s_0, 0)$ is the position vector of the current collocation point $s = s_0$ at time $t = 0$ in the original global frame, then the required transformation is given by

$$\mathbf{X} = \mathbf{x} - \int_0^t \mathbf{u}(t') dt' + \mathbf{X}_0(s_0, 0), \quad (2.26)$$

$$T = t. \quad (2.27)$$

Under this transformation the shape of the body is unchanged so that the tangent vector is identical in the two frames; and the potential Φ in the global frame is related to the potential ϕ in the moving frame by

$$\Phi(\mathbf{X}, T) = \phi_1(\mathbf{x}, t). \quad (2.28)$$

The velocities are related by

$$\nabla_{\mathbf{X}} \Phi = \nabla_{\mathbf{x}} \phi_1. \quad (2.29)$$

Re-writing the pressure jump in the global frame, equation (2.24), in terms of quantities from the moving frame (now omitting the subscript \mathbf{x} on $\nabla_{\mathbf{x}}$) gives

$$\frac{\Delta P}{\rho} = \frac{1}{2} |\nabla \phi_1^+|^2 - \frac{1}{2} |\nabla \phi_1^-|^2 + \mathbf{u} \cdot (\nabla \phi_1^+ - \nabla \phi_1^-) + \frac{\partial}{\partial t} (\phi_1^+ - \phi_1^-). \quad (2.30)$$

Now consider these terms in turn, remembering that $\phi_1 = \phi_b + \phi_w$, and $\phi_w^+ = \phi_w^-$.

Start with the time derivative term:

$$\frac{\partial}{\partial t} (\phi_1^+ - \phi_1^-) = \frac{\partial}{\partial t} (\phi_b^+ - \phi_b^-). \quad (2.31)$$

To explain how this is written in terms of the bound vortex strengths, consider a planar vortex sheet along the x -axis between the points x_1 and x_2 , of strength distribution $\gamma(x)$. The potential Ξ due to this sheet is

$$\Xi(x, z) = -\frac{1}{2\pi} \int_{x_1}^{x_2} \gamma(x_0) \tan^{-1} \left(\frac{z}{x - x_0} \right) dx_0. \quad (2.32)$$

On the sheet itself, $x = 0^\pm$, we are able to write down the potential jump

$$\begin{aligned}\Delta\Xi(x) &= \Xi(x, 0^+) - \Xi(x, 0^-) \\ &= \int_{x_1}^{x_2} \frac{\gamma(x_0)}{2} dx_0 - \int_{x_1}^{x_2} -\frac{\gamma(x_0)}{2} dx_0 \\ &= \int_{x_1}^{x_2} \gamma(x_0) dx_0,\end{aligned}\tag{2.33}$$

assuming that $\Xi = 0$ ahead of the vortex sheet.

Returning to our model, we write the integral as the sum of the point vortices representing the vortex sheet, and hence

$$\left[\frac{\partial}{\partial t} (\phi_b^+ - \phi_b^-) \right]_j = \frac{\partial}{\partial t} \left(\sum_{k=1}^j \Gamma_k \right).\tag{2.34}$$

Next, consider the term

$$\mathbf{u} \cdot (\nabla\phi_1^+ - \nabla\phi_1^-) = \mathbf{u} \cdot (\nabla\phi_b^+ - \nabla\phi_b^-).\tag{2.35}$$

We model the bound vortex sheet as having local strength (constant over the j 'th panel)

$$\gamma = \frac{\Gamma_j}{(\Delta l)_j},\tag{2.36}$$

where Γ_j is the strength of the j 'th point vortex, and $(\Delta l)_j$ is the length of the j 'th panel. Then we can write down the velocity jump due to the sheet at the point x_j (see Batchelor, 1967, p.99):

$$\nabla\phi_b^+ - \nabla\phi_b^- = \gamma\boldsymbol{\tau}\tag{2.37}$$

$$= \frac{\Gamma_j}{\Delta l_j} \boldsymbol{\tau}.\tag{2.38}$$

where $\boldsymbol{\tau}$ is the tangent vector to the vortex sheet.

Hence we have

$$\mathbf{u} \cdot (\nabla\phi_b^+ - \nabla\phi_b^-) = \frac{\Gamma_j}{(\Delta l)_j} (\mathbf{u} \cdot \boldsymbol{\tau}).\tag{2.39}$$

Finally:

$$\begin{aligned}\frac{1}{2} |\nabla\phi_1^+|^2 - \frac{1}{2} |\nabla\phi_1^-|^2 &= \frac{1}{2} |\nabla\phi_b^+ + \nabla\phi_w^+|^2 - \frac{1}{2} |\nabla\phi_b^- + \nabla\phi_w^-|^2 \\ &= \left(\frac{1}{2} |\nabla\phi_b^+|^2 + \frac{1}{2} |\nabla\phi_w^+|^2 + |\nabla\phi_b^+ \cdot \nabla\phi_w^+| \right) \\ &\quad - \left(\frac{1}{2} |\nabla\phi_b^-|^2 + \frac{1}{2} |\nabla\phi_w^-|^2 + |\nabla\phi_b^- \cdot \nabla\phi_w^-| \right).\end{aligned}\tag{2.40}$$

We have

$$\nabla\phi_w^+ = \nabla\phi_w^-, \quad (2.41)$$

and therefore also

$$|\nabla\phi_w^+|^2 = |\nabla\phi_w^-|^2. \quad (2.42)$$

Note that $\nabla\phi_w$ is the velocity at the collocation point induced by the wake, so $\nabla\phi_w = \mathbf{V}_w$.

The bound vortex terms $\nabla\phi_b^\pm$ are not so straightforward. For a general, non-uniform vortex sheet, we can specify only the velocity jump in terms of the local vortex strength, as given by equation (2.38). However, if we introduce the term \mathbf{V}_m , the velocity at a point on the vortex sheet due to that vortex sheet excluding the effect of the local velocity jump, then

$$\nabla\phi_b^\pm = \mathbf{V}_m \pm \frac{1}{2}\Delta\mathbf{V} \quad (2.43)$$

where $\Delta\mathbf{V}$ is the local velocity jump. We still have

$$\nabla\phi_b^+ - \nabla\phi_b^- = \Delta\mathbf{V} \quad (2.44)$$

as required, but can now specify the actual fluid velocity on the vortex sheet. In terms of the panel method itself, \mathbf{V}_m is taken to be the induced velocity at the collocation point due to all the bound vortices except the vortex attached to that same panel, while $\Delta\mathbf{V}$ just comes from the local panel.

Thus, from equation (2.38) we have

$$(\nabla\phi_b^\pm)_j = (\mathbf{V}_m)_j \pm \left(\frac{\Gamma_j}{\Delta l_j}\right) \boldsymbol{\tau}_j, \quad (2.45)$$

and hence, equation (2.40) reduces to

$$\frac{1}{2}(|\nabla\phi_1^+|^2 - |\nabla\phi_1^-|^2) = (\mathbf{V}_m + \mathbf{V}_w)_j \cdot \boldsymbol{\tau}_j \left(\frac{\Gamma_j}{\Delta l_j}\right). \quad (2.46)$$

Putting everything in terms of known quantities in the original global frame we finally obtain

$$(\Delta P)_j = \left\{ [\mathbf{V}_m + \mathbf{V}_w - \mathbf{V}_b] \cdot \boldsymbol{\tau}_j \left(\frac{\Gamma_j}{\Delta l_j}\right) + \frac{\partial}{\partial t} \left(\sum_{k=1}^j \Gamma_k \right) \right\}. \quad (2.47)$$

This provides us with the pressure jump distribution in terms of the bound vortex strengths. Clearly, this can now be used to calculate integrated quantities such as the lift (or sideforce), thrust and

moment. We will use these integrated forces to some extent; especially in testing the model against other work. But it is the distribution itself that we really want, in order to calculate the distribution of bending moments along the fish's body.

Taking the sideforce as the force in a direction perpendicular to the direction of swimming, and thrust in the direction of swimming, we have

$$L = \sum_{j=1}^N ((\Delta P)_j (\Delta l)_j) \mathbf{n}_j \cdot \mathbf{k}, \quad (2.48)$$

$$T_X = - \sum_{j=1}^N ((\Delta P)_j (\Delta l)_j) \mathbf{n}_j \cdot \mathbf{i}, \quad (2.49)$$

where \mathbf{i} and \mathbf{k} are unit vectors in the X and Z directions respectively. It is worth reminding oneself here that these forces are calculated per unit length in the Y -direction.

2.5 A flat plate moving with constant speed

Consider the classic problem of a flat plate of length l at a constant, small angle of incidence α , moving in the negative x -direction with constant speed U . The lift on the plate is given by the Kutta-Zhukovskii Theorem:

$$L = \rho U \Gamma, \quad (2.50)$$

acting in a direction perpendicular to the free stream. The circulation Γ is given by

$$\Gamma = \pi l U \sin \alpha. \quad (2.51)$$

From thin airfoil theory the plate may be approximated by a bound vortex sheet of strength

$$\gamma(\theta) = 2U \left[A_0 \frac{1 + \cos \theta}{\sin \theta} + \sum_{n=1}^{\infty} A_n \sin(n\theta) \right], \quad (2.52)$$

where $x = \frac{l}{2}(1 - \cos \theta)$; see for example Katz and Plotkin (1991, Section 5.3). As explained there, for a flat plate the coefficients are all zero except $A_0 = \alpha$.

This is a useful result because it allows us to test the most basic quantity calculated by the panel method, namely, the strengths of the bound vortices.

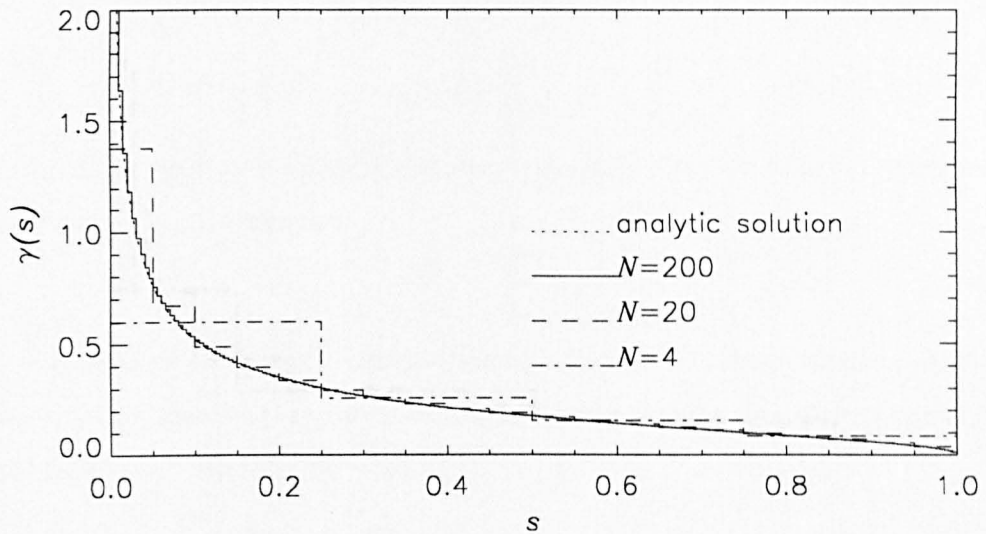


Figure 2.2: Graph of bound vortex strength for uniform panels for various values of N , the number of panels. Angle of attack is $\alpha = 5^\circ$.

Solving the steady state problem involves making some simplifications to the unsteady code. Firstly there is no variation in time. Secondly, no vorticity is shed from the trailing edge as the flow is assumed to have reached a constant, uniform steady state.

The bound vortex strengths are used to show convergence with increasing number of panels for both uniform and variable length panels. Note that for comparison with the analytic bound vorticity distribution, we plot the strength of each bound vortex divided by the associated panel's length. It is assumed that the strength is constant over each panel.

The example was tested over a wide range of values of N , both for uniform and variable panels. Figs. 2.2 and 2.3 show a small number of the results. It can be seen that the solution converges well as N is increased. It is also clear that using the cosine spacing improved accuracy with a smaller number of panels.

Furthermore it was found that for all the examples tested the sum of the bound vortex strengths agreed to at least six decimal places with the analytic value for the circulation in equation (2.51).

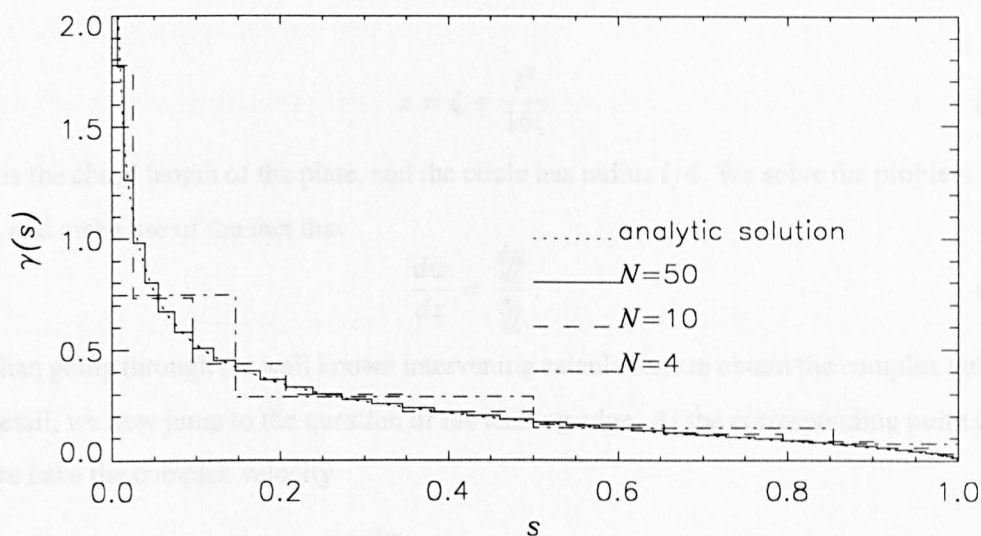


Figure 2.3: Graph of bound vortex strength for variable panels for various values of N , the number of panels. Angle of attack is $\alpha = 5^\circ$.

2.6 The suction force

For a body which is infinitely thin, it is necessary to include a suction force, as explained, for example, in Robinson and Laurmann (1956). This is a force acting at the leading edge resulting from the singularity in pressure at that point. Its existence is easily seen by considering the example in Section 2.5 above.

We know from the Kutta-Zhukovskii Theorem that the lift on the plate is $\rho U \Gamma$, in the direction perpendicular to the free stream. However, if we wanted to calculate the lift by integrating the pressure jump along the plate

$$\begin{aligned} L &= \int_0^l (\Delta P) ds, \\ &= \pi \rho l U^2 \sin \alpha \cos \alpha, \end{aligned} \quad (2.53)$$

we would obtain a force perpendicular to the plate.

To explain how we calculate the leading edge suction force, it is helpful to continue with this example (Katz and Plotkin, 1991). Using the classical complex variables method we transform

the flat plate in the $z = x + iy$ plane into a circle in the $\zeta = \xi + i\eta$ plane.

We put

$$z = \zeta + \frac{l^2}{16\zeta} \quad (2.54)$$

where l is the chord length of the plate, and the circle has radius $l/4$. We solve the problem in the ζ -plane, and make use of the fact that

$$\frac{dw}{dz} = \frac{\frac{dw}{d\zeta}}{\frac{dz}{d\zeta}}. \quad (2.55)$$

Rather than going through the well known intervening calculations to obtain the complex velocity, etc, in detail, we now jump to the question of the leading edge. At the corresponding point on the circle, we have the complex velocity

$$\frac{dw}{d\zeta} = -4iU \sin \alpha. \quad (2.56)$$

Near the leading edge, $\zeta \rightarrow -l/4$,

$$\begin{aligned} \frac{dw}{dz} &= \frac{\zeta^2 \frac{dw}{d\zeta}}{\zeta^2 - l^2/16} \\ &\approx \frac{il}{2} U \sin \alpha \frac{1}{\zeta + l/4}. \end{aligned} \quad (2.57)$$

Inverting the transformation, and letting $z \rightarrow -l/2$

$$\begin{aligned} \zeta &= \frac{1}{2} \left(z + \sqrt{z^2 - l^2/4} \right) \\ &= -\frac{l}{4} + \frac{i}{2} \sqrt{l} \sqrt{z + l/2}. \end{aligned} \quad (2.58)$$

So the complex velocity in the neighbourhood of the leading edge is given by

$$\frac{dw}{dz} = \frac{U \sin \alpha \sqrt{l}}{\sqrt{z + l/2}}. \quad (2.59)$$

Now we use the Blasius Theorem on a small circle S surrounding the leading edge, (and the residue theorem for the integral itself):

$$\begin{aligned} T_s - iT_n &= \frac{i\rho}{2} \int_S \left(\frac{dw}{dz} \right)^2 dz \\ &= \frac{1}{2} i\rho l U^2 \sin^2 \alpha \int_S \frac{dz}{z + l/2} \\ &= -\pi\rho l U^2 \sin^2 \alpha. \end{aligned} \quad (2.60)$$

where T_s and T_n are the forces tangential and normal to the plate at the leading edge respectively. Thus T_s is the leading edge suction force.

Note then that the x -component of the suction force cancels out the x -component of the force obtained by integrating the pressure jump:

$$(-\pi\rho lU^2 \sin^2 \alpha) \cos \alpha + (\pi\rho lU^2 \sin \alpha \cos \alpha) \sin \alpha = 0. \quad (2.61)$$

The z -components of the two forces sum to give $\rho U\Gamma$ as required by the Kutta-Zhukovskii theorem:

$$\begin{aligned} \pi\rho lU^2 \sin^3 \alpha + \pi\rho lU^2 \sin \alpha \cos^2 \alpha &= \pi\rho lU^2 \sin \alpha (\sin^2 \alpha + \cos^2 \alpha) \\ &= \pi\rho lU^2 \sin \alpha \end{aligned} \quad (2.62)$$

The result is then generalized in two ways: to deal with non-planar “wings”, and unsteady motion. Firstly we assume that the complex velocity can be written as

$$\frac{dw}{dz'} = f(z') + \frac{C}{\sqrt{z'}}, \quad (2.63)$$

where $f(z')$ is bounded at $z' = 0$, the leading edge, and C is a constant, given by

$$C = \lim_{z' \rightarrow 0} u\sqrt{z'} \quad (2.64)$$

where u is taken to mean the fluid velocity along the plate. In order to calculate the suction force at the leading edge we place a small circle S , radius ϵ , around $z' = 0$ and apply Blasius Theorem:

$$X - iZ = \frac{1}{2}i\rho \int_S \left(f(z') + \frac{C}{\sqrt{z'}} \right)^2 dz'. \quad (2.65)$$

Consequently, using the residue theorem,

$$T_s = -\pi\rho C^2, \quad (2.66)$$

and

$$T_n = 0. \quad (2.67)$$

Unsteady motion fortunately poses no further problem in terms of calculating the suction force, as explained by Robinson and Laurmann (1956, p.498). The complex potential associated with the

complex velocity given by equation (2.63) is bounded at the leading edge; and so is its derivative with respect to time. The calculation from steady flow therefore remains valid for unsteady flow.

To make use of this result in our numerical method it is clear that we will need to approximate C in terms of the tangential velocity $(\nabla_X \Phi) \cdot \tau$ on the body close to the leading edge. Using the transformation from the calculation of the pressure distribution, equation (2.26), we model the leading panel as a stationary, uniform planar vortex sheet of strength $\gamma = \Gamma_0 / \Delta l_0$. Then the tangential velocity on the plate is $\pm \Gamma_0 / 2\Delta l_0$. With the notation from Section 2.4

$$\phi = \phi_1 + \mathbf{u} \cdot \mathbf{x} \quad (2.68)$$

where the velocities in the two frames are related by

$$\nabla_X \Phi = \nabla_x \phi_1. \quad (2.69)$$

As with the pressure jump calculation we require the actual tangential velocity on the vortex sheet. We have

$$\phi_1 = \phi_b + \phi_w. \quad (2.70)$$

as before, with

$$(\nabla \phi_b^\pm)_j = (\mathbf{V}_m)_j \pm \frac{\Gamma_j}{2\Delta l_j}, \quad (2.71)$$

and

$$\nabla \phi_w = \mathbf{V}_w. \quad (2.72)$$

The leading panel has subscript $j = 0$, and the full expression for the tangential velocity near the leading edge is

$$\nabla_X \Phi \cdot \tau = \frac{\Gamma_0}{2\Delta l_0} + (\mathbf{V}_m + \mathbf{V}_w) \cdot \tau_0. \quad (2.73)$$

It remains to decide what value to give $\sqrt{z'}$. Assume that we can take some fraction a of the leading panel length Δl_0 . Then the suction force T_S acting along the tangent to the plate at the leading edge is

$$T_S = -\pi \rho C_s^2 \tau_0, \quad (2.74)$$

where C_s is given by

$$C_s = \left[\frac{\Gamma_0}{2\Delta l_0} + (\mathbf{V}_m(a\Delta l_0) + \mathbf{V}_w(a\Delta l_0)) \cdot \tau_0 \right] (a\Delta l_0)^{\frac{1}{2}}. \quad (2.75)$$

We return to the calculations relating to the flat plate moving with constant speed U at small angle of attack. Referring back to equation (2.75) we know that for this example, $V_w = 0$ because the starting vortex is assumed to be at infinity, and $V_m \cdot \tau_0 = 0$ because we are dealing with a flat plate.

So C_s is given by

$$C_s = \frac{\Gamma_0}{2\Delta l_0} (a\Delta l_0)^{\frac{1}{2}} \quad (2.76)$$

so that

$$T_s = \frac{\pi\rho\Gamma_0^2 a}{4\Delta l_0}. \quad (2.77)$$

Using the analytic expression for the suction force on a flat plate moving at constant speed U ,

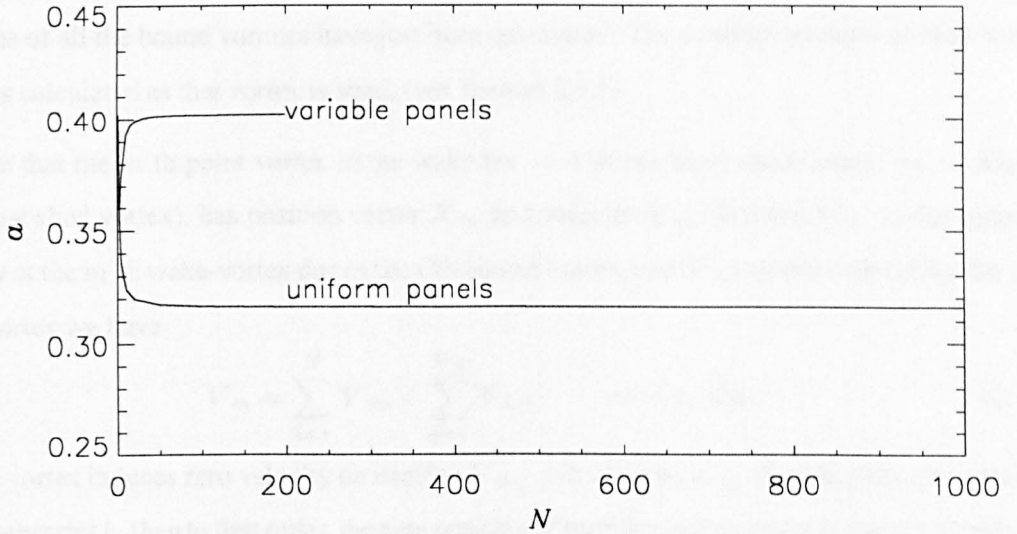


Figure 2.4: Graph showing the variation of a used in the suction approximation, as the number of panels N is increased. Both uniform and variable panels are shown and the result is significantly different for the two methods.

equation (2.60), we can obtain an expression for a once we have calculated the bound vortex strengths. We expect the value of a to change with the number of panels. Fig. 2.4 shows the variation in the calculated value of a against the number of panels N . It is clear that the choice between uniform and variable panel lengths makes a significant difference to our “ideal” value for a . However, in both cases we find that increasing N causes a to converge to a constant value. Consequently we use these values when calculating the suction force in general. That is, for

uniform panels we take $a = 0.315$, and for variable panels we take $a = 0.40$.

2.7 The wake

2.7.1 Wake rollup

An important aspect of this work is that the influence of the wake is felt by the body. Given that the model aims to deal with large-amplitude unsteady motion, a further requirement is to include the deformation of the wake. This procedure is done by calculating the total induced velocity at each wake-vortex, and then moving them all accordingly. Note that at this point in the method, the strengths of all the bound vortices have just been calculated. The constant strength of each wake-vortex is calculated as that vortex is shed, (see Section 2.3.5).

Suppose that the m 'th point vortex in the wake ($m = 1$ at the latest shed vortex, $m = N_W$ at the oldest shed vortex), has position vector \mathbf{X}_m and velocity \mathbf{V}_m . Writing \mathbf{V}_{mi} as the induced velocity at the m 'th wake-vortex due to the i 'th bound-vortex, and \mathbf{V}_{mj} as that induced by the j 'th wake-vortex we have

$$\mathbf{V}_m = \sum_{i=1}^N \mathbf{V}_{mi} + \sum_{j=1}^{N_W} \mathbf{V}_{mj}, \quad m = 1..N_W. \quad (2.78)$$

A point vortex induces zero velocity on itself so $\mathbf{V}_{mj} = 0$ when $m = j$. Denoting time increments by the subscript k , then to first order, the new position of each free point vortex is found by applying

$$\mathbf{X}_{m,k+1} = \mathbf{X}_{m,k} + (\Delta t)_k \mathbf{V}_{m,k} \quad m = 1..N_W. \quad (2.79)$$

A first order explicit method in this situation is usual for panel methods. There is some further discussion of this point in Section 2.7.3. A higher order method would require the velocity of each of the free vortices at intermediate time steps. However, to evaluate these wake-vortex velocities we must go through the full panel method calculation to first obtain the current bound vortex strengths. In other words the cost associated with knowing the flow field at any instant makes higher order methods impractical.

There are two further points to note about the wake. Firstly the number of vortices increases indefinitely, which becomes prohibitively expensive. Secondly it is widely recognised that the discretisation of a continuous vortex sheet into point vortices is numerically unstable.

2.7.2 Simplification of the wake model

Calculating the total wake-induced velocity involves finding the induced velocity due to a point vortex N_W times. Consequently any calculation that requires the total induced velocity due to the wake at a number of different points becomes expensive as N_W increases. In particular the wake deformation procedure involves N_W^2 calls to the vortex-induced-velocity calculation, and is the dominant expense associated with the wake.

At small amplitude it is common (and accurate) to assume that the wake does not roll up. In examples involving small-amplitude motion we are able to make the same simplification, so that shed vortices are left at the point where they were shed. However, in the main we are interested in large-amplitude motion where this assumption is not acceptable.

The alternatives involve the assumption that at some distance “sufficiently far” (see below) from the trailing edge of the body, the wake can be simplified in a manner that does not affect the pressure distribution along the body. The first of these methods is simply to neglect the vortices that are far from the trailing edge. We define the “truncation distance” D_T as being that distance beyond which the wake can be truncated without the pressure distribution on the body being affected. The second method is to amalgamate vortices that are further than the “amalgamation distance” D_A from the trailing edge of the body. Again, D_A is chosen so that the amalgamations do not affect the pressure distribution. In both cases, the simplification occurs after the updating of the vortex positions at each time step.

There is little to be said on the question of truncation. It relies solely on the fact that the induced velocity due to a point vortex tends to zero with distance.

The amalgamation procedure works as follows. Two vortices Γ_1, Γ_2 at positions $\mathbf{x}_1, \mathbf{x}_2$ respectively are amalgamated to form a new vortex Γ at \mathbf{x} given by

$$\Gamma = \Gamma_1 + \Gamma_2 \quad (2.80)$$

$$\mathbf{x} = \mathbf{x}_1 + \lambda(\mathbf{x}_2 - \mathbf{x}_1) \quad (2.81)$$

where λ is such that the new point vortex is placed at the centroid of vorticity of the two old point vortices (Moore, 1974), ie

$$\lambda = \frac{\Gamma_2}{\Gamma_1 + \Gamma_2}. \quad (2.82)$$

To see why the amalgamation works well consider two point vortices Γ_1 , Γ_2 at points x_1 and x_2 respectively along the x -axis. The total induced velocity due to these vortices at the origin is perpendicular to the x -axis, and given by

$$\begin{aligned} q &= \frac{-\Gamma_1}{2\pi x_1} + \frac{-\Gamma_2}{2\pi x_2} \\ &= \frac{-(\Gamma_1 x_2 + \Gamma_2 x_1)}{2\pi x_1 x_2}. \end{aligned} \quad (2.83)$$

If the vortices are amalgamated according to the above procedure to form a new vortex Γ at x , then the induced velocity at the origin is of course given by

$$q = \frac{-\Gamma}{2\pi x}. \quad (2.84)$$

Now suppose that the vortices are close together, (relative to their distance from the origin), so that

$$x_1 \approx x_2 \approx x. \quad (2.85)$$

Then

$$q \approx \frac{-x(\Gamma_1 + \Gamma_2)}{2\pi x^2} = \frac{-\Gamma}{2\pi x}. \quad (2.86)$$

Alternatively suppose that one of the two vortices is significantly stronger than the other, say $|\Gamma_2| \gg |\Gamma_1|$. The vortices do not have to be close together, but the ratio of the distances must not be comparable to the ratio of strengths. Then

$$\begin{aligned} \frac{-(\Gamma_1 x_2 + \Gamma_2 x_1)}{2\pi x_1 x_2} &= \frac{-\Gamma_2 \left(\frac{\Gamma_1 x_2}{\Gamma_2 x_1} + 1 \right)}{2\pi x_2} \\ &\approx \frac{-\Gamma_2}{2\pi x_2} \\ &\approx \frac{-\Gamma}{2\pi x}. \end{aligned} \quad (2.87)$$

For two vortices that are a distance greater than D_A from the body, the first result, equation (2.86), shows that the amalgamation is a reasonable strategy. If we add the further constraint that only vortices of the same sign are amalgamated, the second result, equation (2.87) adds to our confidence in the procedure. As the distance between amalgamating vortices increases the elder of the two must be the result of many amalgamations. Consequently it is likely to have a significantly larger strength.

2.7.3 Numerical instability in the discretisation of a continuous vortex sheet

A further potential complication due to the wake is that the representation of a continuous vortex sheet by discrete point vortices is unstable (Chorin and Bernard, 1973; Moore, 1974; Fink and Soh, 1978). The discrete approximation is adequate for calculating the induced velocity away from the sheet. However when determining the self-induced motion of the vortex sheet itself, the discrete vortex model introduces some problems.

The authors mentioned above all describe the difficulties in the context of a problem first discussed by Westwater (1935). That is, the roll-up of a two-dimensional vortex sheet initially along $y = 0$ in the interval $-a \leq x \leq a$, with vorticity distribution

$$\omega(x) = 2Ux(a^2 - x^2)^{-\frac{1}{2}}. \quad (2.88)$$

The vorticity distribution represents that which would be induced by an elliptically loaded wing moving with constant speed U . It was expected that, as seen experimentally, the edges of the vortex sheet would roll up into a spiral. Westwater's calculations (done by hand) seemed to indicate agreement in this respect. The vortex sheet was represented by $2M$ point vortices with strengths chosen to model the distribution in equation (2.88). The discretized equations of motion were numerically integrated to find the paths travelled by the point vortices. However, it was later found, eg by Takami (1964) and Moore (1971) that "the method can produce errors of arbitrarily large amplitude" (Chorin and Bernard, 1973).

Moore (1974) showed that the instability was not a numerical artefact by instantaneously reversing the vortex strengths at some time after random vortex motion had been observed. He found that the "chaotic motion would unscramble" (Moore, 1974). By using a vortex amalgamation procedure in the spiral to ensure that a full turn was always represented by some minimum number of vortices he was able to successfully model the vortex rollup at the edge of the sheet. The inner vortices were amalgamated into a single point vortex modelling the centre of the rolled up region of the sheet. We found it difficult to extend this successfully to "internal" regions of a vortex sheet similarly rolling up.

According to Fink and Soh (1978), "Examination of the finite difference approximation to the appropriate integral equation exposes not only the customary set of equivalent discrete vortices,

each carrying a correct share of the circulation, but also logarithmic and higher-order terms which relate to series expansions of the vorticity density in the neighbourhood of points on the sheet." Indeed they went on to describe a method that successfully deals with the difficulty, but the method is not applicable to the situation in the panel method where the wake vortices are all that is known about the wake vortex sheet.

Chorin and Bernard (1973) introduced a vortex core of radius r_c to reduce the induced velocity close to each point vortex. They used a velocity in the core equal to the value at the edge, ie

$$q = -\frac{\Gamma}{2\pi r_c}, \quad (2.89)$$

but noted that the exact form of the velocity distribution inside the core did not seem to be of great importance. Using a 4'th order Runge-Kutta method to integrate the vortex paths, with $\Delta t^* = 5 \times 10^{-5}$, $r_c = 6a/M^2$ ($t^* = Ut/a$), they found the rollup proceeded smoothly. However, their final conclusion, in testing the long-term evolution of the sheet, was that the use of Euler integration in conjunction with longer time steps (subject to $\Delta t^* \approx 10^{-2}$) appeared to have a smoothing effect on the vortex motion. They commented that this observation sheds some light on Westwater's apparently successful result, and further note that under these circumstances the choice of the vortex core radius actually had little effect on the result.

We ran a similar set of experiments with various values of M , Δt and the core radius r_c . Fig. 2.5 shows the result for $M = 50$, $\Delta t^* = 10^{-2}$ at $t^* = 1$. Our results appeared to bear out the conclusions of Chorin and Bernard (1973). We also found that using the distributed vorticity model of Scully (1975), where everywhere

$$q = -\frac{\Gamma}{2\pi} \frac{r}{r^2 + r_c^2}, \quad (2.90)$$

with $r_c \approx a/M$ helped to smooth the motion for slightly longer than the Rankine vortex model and the vortex core model used by Chorin and Bernard.

In terms of representing the wake in our panel method we can draw the following conclusions.

- The instability in the wake should not directly affect the pressure jump distribution on the body as the discrete approximation to the continuous vortex sheet calculates accurately the induced velocity away from the sheet, (Fink and Soh, 1978).

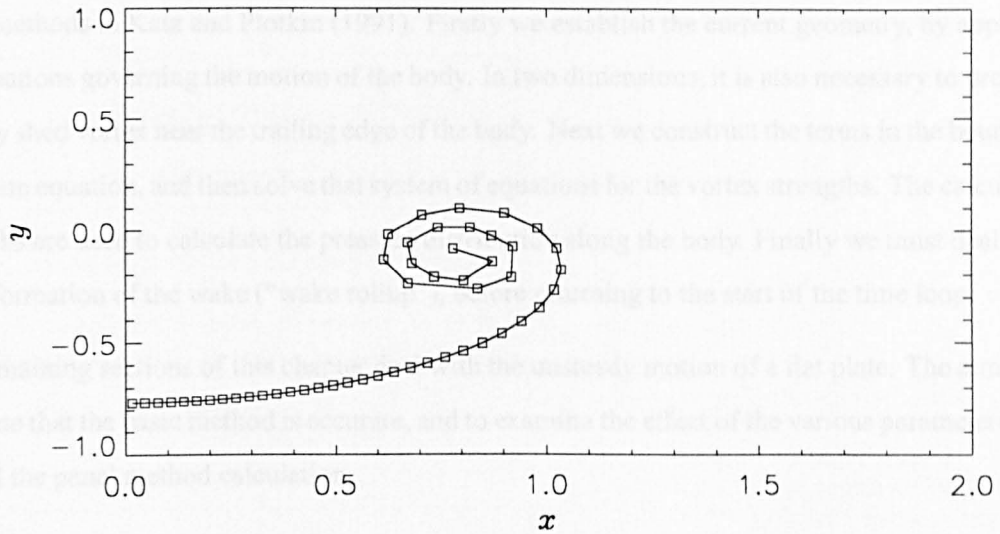


Figure 2.5: The shape of the vortex sheet at $t^* = 1.0$. In this example, $M = 50$ and $\Delta t^* = 10^{-2}$. The core radius is given by $r_c \approx a/M$.

- The use of Euler integration to calculate the motion of the wake vortices is not only ideal from an efficiency point of view, but should also serve to smooth the instability arising from the discrete model (Chorin and Bernard, 1973).
- Our use of an amalgamation procedure to reduce the expense associated with the wake (described in Section 2.7.2) should also help to reduce the effect of the instabilities in the model. We know that the chaotic motion will occur inside a portion of the sheet that is rolling up, but that initially the process will be modelled successfully. The amalgamations help by replacing the chaotic, rolled up portions of the vortex sheet by single point vortices: the “macroscopic” shape of the wake remains accurate.

2.8 Summary

We now summarise the unsteady panel method in terms of the procedures outlined above.

Starting from $t = 0$, we march through time using (not necessarily constant) time steps Δt_k , so that $t_k = t_{k-1} + \Delta t_{k-1}$. At each time increment, we follow a number of procedures as illustrated

by the flow diagram in Fig. 2.6. A similar flow diagram can be found in the section on unsteady panel methods in Katz and Plotkin (1991). Firstly we establish the current geometry, by applying the equations governing the motion of the body. In two dimensions, it is also necessary to produce a newly shed vortex near the trailing edge of the body. Next we construct the terms in the boundary condition equation, and then solve that system of equations for the vortex strengths. The calculated strengths are used to calculate the pressure distribution along the body. Finally we must deal with the deformation of the wake (“wake rollup”), before returning to the start of the time loop.

The remaining sections of this chapter deal with the unsteady motion of a flat plate. The aim is to illustrate that the basic method is accurate, and to examine the effect of the various parameters that control the panel method calculation.

2.9 A flat plate at constant small angle of incidence started impulsively from rest.

This is a classic problem to use in testing the code, initially analysed by Wagner (1925), and also later by von Karman and Sears (1938). Using the usual non-dimensionalisation, we have a plate of length $l = 1$ at a constant small angle of incidence α . At $t = 0$, the plate is started impulsively and then moves to the left with constant speed $U = 1$.

The results in this section are based on plots of the lift coefficient $C_L(t)$ at time t divided by its steady state value, where

$$C_L(t) = \frac{L(t)}{\frac{1}{2}\rho U^2 l}, \quad (2.91)$$

and

$$L(t = \infty) = \pi \rho l U^2 \sin \alpha. \quad (2.92)$$

Wagner (1925) gives values of $C_L(t)/C_L(t = \infty)$ in the table on his page 31. As a further check, the approximations given by equations (43) and (44) of von Karman and Sears (1938), were used. For values up to $t \approx 5$, their results agree. For larger t , von Karman and Sears point to an incorrect asymptote in Wagner (1925).

The test example was run many times with various values of N and Δt , using both uniform and

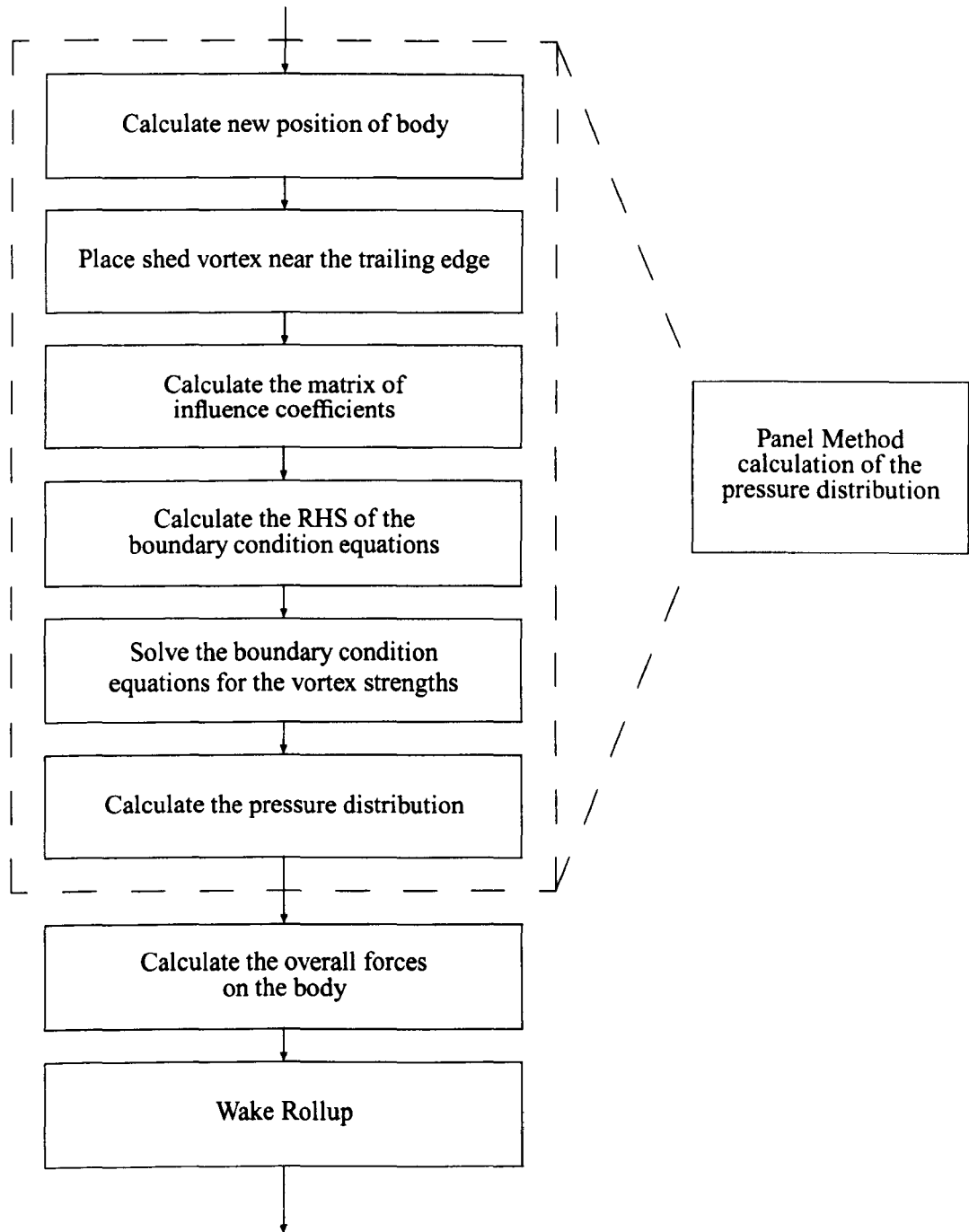


Figure 2.6: Flowchart of the basic procedures to be performed at each time step. The elements in the dashed box can be thought of as a single procedure when more complexity is added to the problem later on.

variable panel lengths. The results were judged broadly on how well they agreed with the analytic solutions over $0 \leq t \leq 5$, and in particular over the first few time steps.

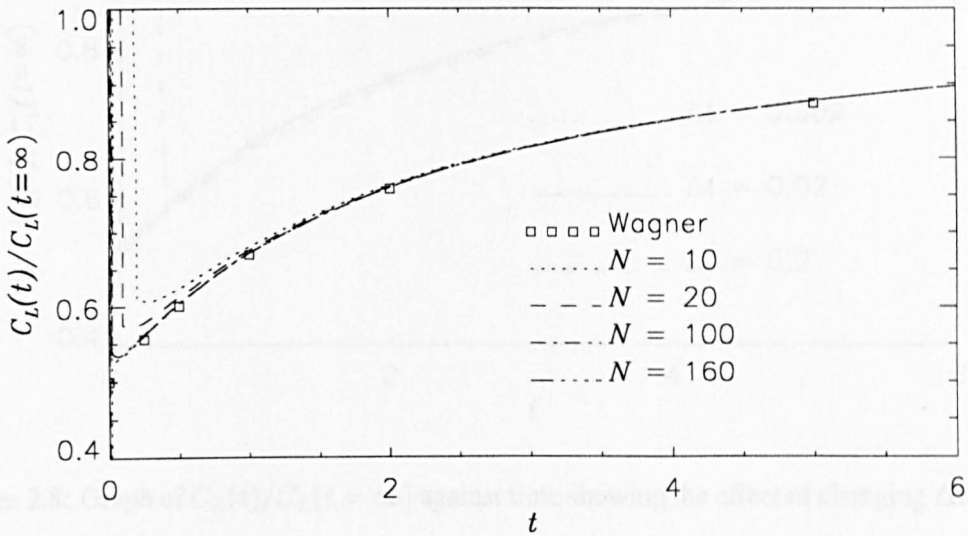


Figure 2.7: Graph of the lift coefficient divided the steady state value of the lift coefficient $C_L(t)/C_L(t = \infty)$: a comparison of Wagner's result with the numerical method for uniform panels. Using $\Delta t = l/NU$ to set the time step, the graph shows that the method converges with increasing N .

The results for uniform panels are not shown in detail here, allowing us to concentrate more on the cosine spacing method, which easily out-performs the uniform panelling on grounds of efficiency. In conducting the tests on uniform panels it was found that the choice of time step Δt altered the results for any given number of panels N . However, provided Δt was chosen well, the results were seen to improve with increasing N , as suggested by the examples in Section 2.5, and shown in Fig. 2.7. Furthermore it was found that setting

$$\Delta t = \frac{l/N}{U} \quad (2.93)$$

tended to produce an appropriate time step, which is perhaps related to this choice of time step causing the panels in the wake and on the body to be of similar lengths.

For variable panel lengths, using $\Delta t = l/NU$, the results improve with increasing N , with convergence at $N \approx 50$. However, whilst equation (2.93) proves to be a useful “rule of thumb”, at

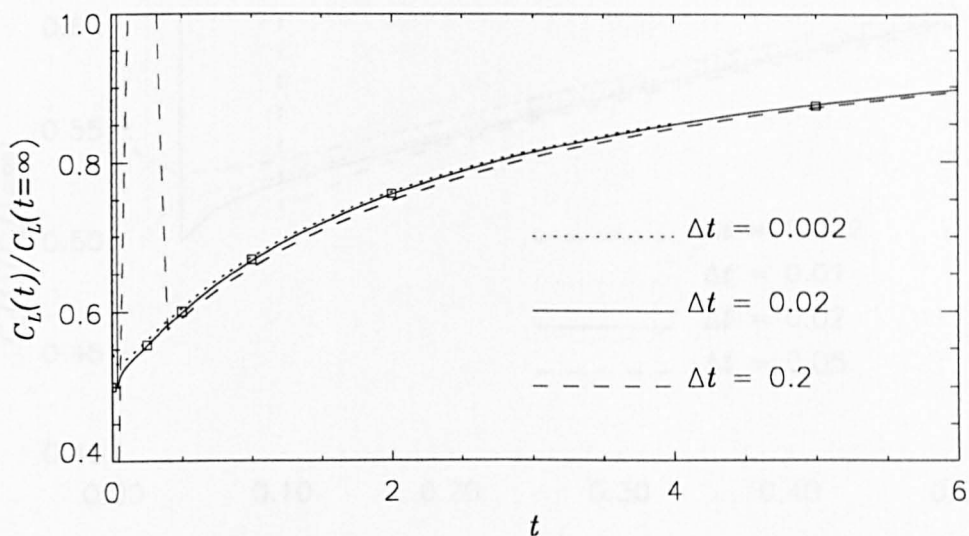


Figure 2.8: Graph of $C_L(t)/C_L(t = \infty)$ against time showing the effect of changing Δt for $N = 50$ (cosine spacing). The boxes mark the values from (Wagner, 1925).

large N the method is less sensitive to changes in Δt . Fig. 2.8 compares Wagner’s result and three runs using cosine spacing $N = 50$. For $t > 0.5$ there is reasonable agreement, although $\Delta t = 0.2$ is not appropriate for looking at the impulsive start.

To study the situation closer to $t = 0$, Fig. 2.9 plots similar results, this time for $0 \leq t \leq 0.5$, and also two new values of Δt . The analytic solution has $C_L(0+)/C_{L\infty} = 0.5$, with infinite lift at $t = 0$ due to the impulsive start. The numerical results always show a high value of C_L at the first time step for the same reason. (Although the model does not include a true impulsive start because of the finite time step, the time dependence in the Bernoulli equation still reproduces the effect to some extent.) The curve from $\Delta t = 0.002$ does not have the same sharp minimum that is seen on the other curves (and the analytic solution): which is taken to indicate that the result is less accurate than for a “more appropriate” time step. Our conclusion (from this and other results not shown here) is that using equation (2.93) is a good method for determining an appropriate time step.

Having looked at the effect of varying N and Δt , the final test on this problem relates to the position of the shed vortex at each time step. As mentioned earlier, at each time step a vortex of unknown

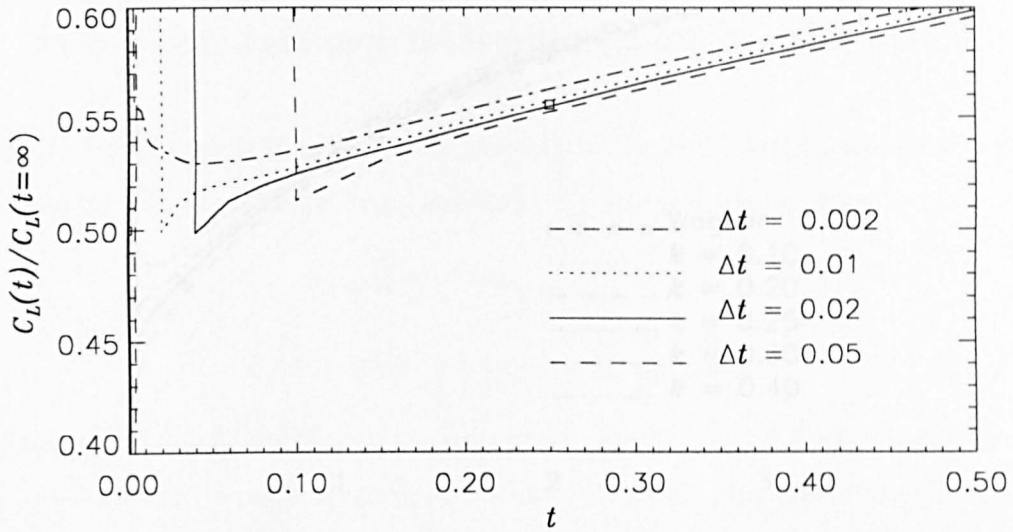


Figure 2.9: Graph of $C_L(t)/C_L(t = \infty)$ against time showing the effect of changing Δt at small t , ($N = 50$). The box at $t = 0.25$ marks a data point from (Wagner, 1925).

strength is shed from the trailing edge. This is to model the continuous vortex sheet that would be shed from the trailing edge, and so we place the vortex at some point along the path travelled by the trailing edge. Specifically, the vortex position is taken to be some fraction k back along the path travelled by the trailing edge over the latest time step. Katz and Plotkin indicate that $0.2 < k < 0.3$ is better than the more “natural” choice of $k = 0.5$ where the approximation “underestimates the induced velocity when compared with the continuous wake vortex sheet result”, (Katz and Plotkin, 1991).

Fig. 2.10 shows that $k = 0.1$, $k = 0.4$ are certainly unsatisfactory. Even $k = 0.2$ and $k = 0.3$ cause visible variations to the result, and it is clear that $0.2 < k < 0.3$ is a good choice. The impulsively started wing problem is known to be sensitive to the position of the shed vortex, and on the basis of the result in Fig. 2.10 we adopt $k = 0.25$.

At this point the method has been tested against the problem of a flat plate at constant small angle of incidence moving with constant speed U . Both the steady state problem, and the impulsive start problem have been used, and we are able to draw the following conclusions:

- the method converges with increasing N provided an appropriate time step is used;

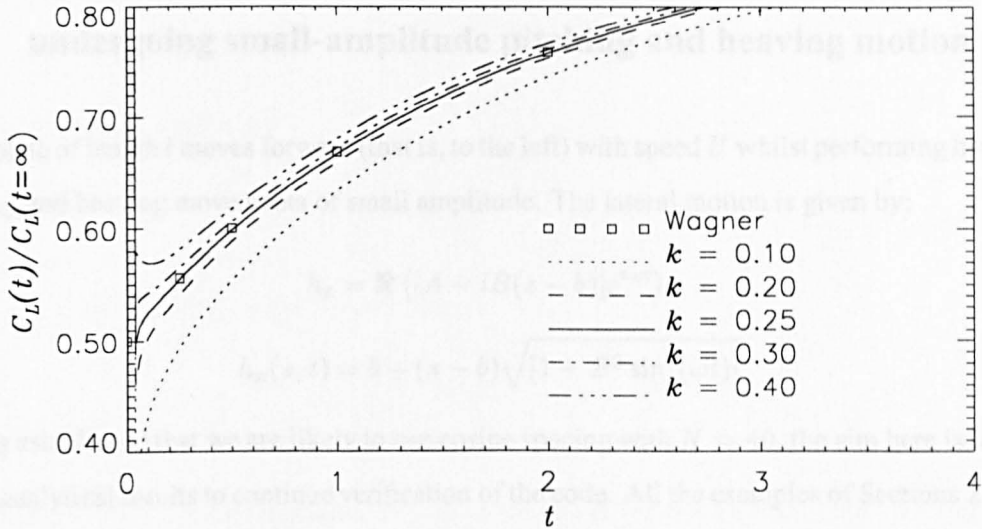


Figure 2.10: Graph of $C_L(t)/C_L(t = \infty)$ against time. The parameter k is the position of the latest shed vortex, as a fraction of the distance back along the path travelled by the trailing edge over the latest time step. This example was done using $N = 50$ (cosine spacing) and $\Delta t = 0.02$.

- our model for the suction force is adequate (bearing in mind the difference between uniform and variable panels);
- variable panels (cosine spacing) achieve a greater accuracy for smaller N ;
- we want the time step to be of the order $\Delta t = l/NU$, although at large N it is not a strict requirement;
- the fraction k along the path travelled by the trailing edge over the latest time step at which the shed vortex is placed should be in the interval $(0.2, 0.3)$. We use $k = 0.25$;

After satisfying the above conditions the numerical results compare favourably with the analytic solutions.

2.10 The sideforce and pressure distribution on a flat plate undergoing small-amplitude pitching and heaving motion.

A flat plate of length l moves forward (that is, to the left) with speed U whilst performing harmonic pitching and heaving movements of small amplitude. The lateral motion is given by:

$$h_z = \Re \left([A - iB(s - b)]e^{i\omega t} \right), \quad (2.94)$$

$$h_x(s, t) = b + (s - b)\sqrt{[1 - B^2 \sin^2(\omega t)]}. \quad (2.95)$$

Having established that we are likely to use cosine spacing with $N \approx 40$, the aim here is to make use of analytical results to continue verification of the code. All the examples of Sections 2.10 and 2.11 were done by starting the system impulsively from rest at $t = 0$ and waiting for a steady state to be reached. (That is where the results for one period are identical over two consecutive periods.) In the cases that follow a steady state was reached typically by the second or third period (one period is $T = 2\pi/\omega$).

2.10.1 Analytic solution

Johnson (1994, p.482), describes a method for calculating the sideforce on such a flat plate, including the calculation of the time dependent pressure distribution. The plate is of length l , lying between $x = -l/2$ and $x = l/2$, in a uniform stream U . It has a small amplitude heaving motion (positive downwards) $h(t) = \bar{h}e^{i\omega t}$, and a small amplitude pitching motion $\alpha(t) = -i\bar{\alpha}e^{i\omega t}$ (positive for nose upward) about the pitching axis $x = al/2$. The wake is modelled as a continuous vortex sheet along the x -axis.

The lateral position of the plate is given by

$$z = -\Re \left([\bar{h} - i\bar{\alpha}(x - ab)] e^{i\omega t} \right), \quad (2.96)$$

which is of a similar form to equation (2.94). Note that (comparing equations (2.94) and (2.96)) the descriptions are identical provided that we have

$$A = -\bar{h} \quad (2.97a)$$

$$B = -\bar{\alpha} \quad (2.97b)$$

$$a = \frac{2b}{l} - 1. \quad (2.97c)$$

The pressure jump is given by

$$-\Delta p = \rho U^2 e^{i\omega t} \sum_{n=0}^{\infty} a_n f_n(\theta) \quad (2.98)$$

where $x = \frac{l}{2} \cos \theta$, and f_n is the Glauert series

$$f_n(\theta) = \begin{cases} \tan \theta/2 & n = 0 \\ \sin n\theta & n \geq 1. \end{cases} \quad (2.99)$$

The normal velocity of the fluid relative to the plate due to the plate's motion and the free stream (Johnson calls it the "upwash" w_a) is expanded as a cosine series

$$w_a = U e^{i\omega t} \left(A_0 + 2 \sum_{n=1}^{\infty} A_n \cos n\theta \right). \quad (2.100)$$

There is also a contribution to the normal velocity on the plate due to the bound vortex sheet and the wake. The solution is written:

$$a_0 = 2(A_0 + A_1)C(\sigma) - 2A_1 \quad (2.101)$$

$$a_n = \frac{-2i\sigma}{n} (A_{n+1} - A_{n-1}) + 4A_n, \quad (2.102)$$

with the resulting lift

$$L = \rho U^2 \frac{l}{2} \pi \left(a_0 + \frac{1}{2} a_1 \right) e^{i\omega t}. \quad (2.103)$$

$C(\sigma)$ is called the Theodorsen lift deficiency function, (see, for example, Johnson, 1994; Katz and Plotkin, 1991), in terms of the reduced frequency $\sigma = \omega l/2U$. For the specific motion described by equation (2.96), the upwash is

$$\begin{aligned} w_a &= U\alpha + \dot{h} + \dot{\alpha}(x - ab) \\ &= \left[-Ui\bar{\alpha} + i\omega\bar{h} + \omega\bar{\alpha}(x - a\frac{l}{2}) \right] e^{i\omega t}. \end{aligned} \quad (2.104)$$

Comparing coefficients of x in equations (2.100) and (2.104) gives

$$A_0 = -i\bar{\alpha} + 2i\bar{h}\sigma - \bar{\alpha}a\sigma \quad (2.105a)$$

$$A_1 = \frac{\bar{\alpha}\sigma}{2} \quad (2.105b)$$

$$A_n = 0, \quad n \geq 2. \quad (2.105c)$$

Hence

$$a_0 = 2C(\sigma) \left[-i\bar{\alpha} + \frac{2\sigma}{l}(i\bar{h} - a\frac{l}{2}\bar{\alpha}) + \frac{\bar{\alpha}\sigma}{2} \right] - \bar{\alpha}k, \quad (2.106a)$$

$$a_1 = -2\sigma \left[\bar{\alpha} - \frac{2\sigma}{l}(\bar{h} + ia\frac{l}{2}\bar{\alpha}) \right] + 2\bar{\alpha}\sigma, \quad (2.106b)$$

$$a_2 = \frac{i\sigma^2\bar{\alpha}}{2}, \quad (2.106c)$$

$$a_n = 0 \quad n > 2. \quad (2.106d)$$

which can be substituted back into equation (2.98). These coefficients can also be checked by comparing the expanded version of equation (2.103) with equivalent expressions for the lift on a pitching and heaving flat plate (Katz and Plotkin, 1991; von Karman and Sears, 1938).

2.10.2 Results

Note that we use the usual non-dimensionalisation, and that we have now returned to the old notation.

For the examples set out below, the relevant parameter values were:

$$U = 3, \quad (2.107a)$$

$$A = 0.05, \quad (2.107b)$$

$$B = 0.1, \quad (2.107c)$$

$$b = 0.5, \quad (2.107d)$$

so that as well as having small amplitude, we have small reduced frequency $\sigma = \omega l/2U$. Similar tests were run on pure pitching ($A = 0$), and pure heaving ($B = 0$). In Sections 2.3.1 and 2.3.2 it was stated that lengths and velocities were non-dimensionalized with respect to the body length and forward speed respectively (thereby fixing $l = 1$ and $U = 1$). In fact the method is unchanged if a different reference length or velocity is used. Thus it possible to have values of U and l that are not unity.

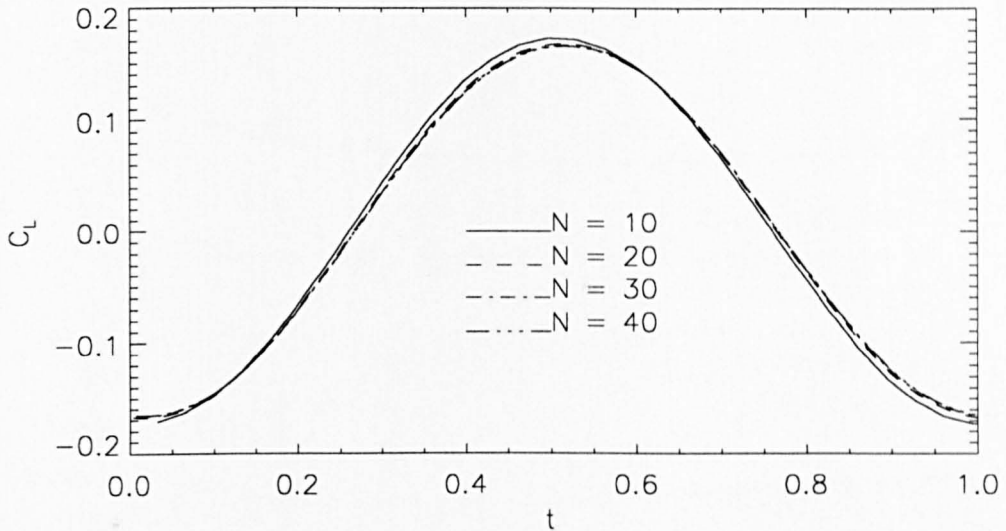


Figure 2.11: Graph of the lift coefficient against time for small amplitude pitching-heaving flat plate. Results are shown for a varying number of panels, from $N = 10$ to $N = 40$. As explained in the text the parameter values of the pitching-heaving motion were: $U = 3$, $A = 0.05$, $B = 0.1$, $b = 0.5$.

Fig. 2.11 shows the variation in the lift coefficient C_L over one period for various values of N . In each case, cosine spacing was used in conjunction with a variable time step based on the average panel length divided by the approximate tangential velocity at the trailing panel's collocation point. The method converges well, and it is difficult to see any difference between $N = 30$ and $N = 40$. Fig. 2.12 compares the result for $N = 30$ against the analytic result obtained from the method described in Section 2.10.1 above. Obviously there is excellent agreement.

The analytic result for the pressure distribution can also be used to check the results from the code. Fig. 2.13 plots the coefficient of the pressure jump across the body, ΔC_p , against position s along the body. The situation at different times is shown in separate graphs, with the time marked for each one. With the solid line giving the analytic result, and the dotted line (with diamonds marking the actual collocation points) the program results, it is clear again that the agreement is good.

This section has shown that the method produces good results for both the pressure distribution and time dependant lift on a flat plate oscillating at small-amplitude. The next section continues along

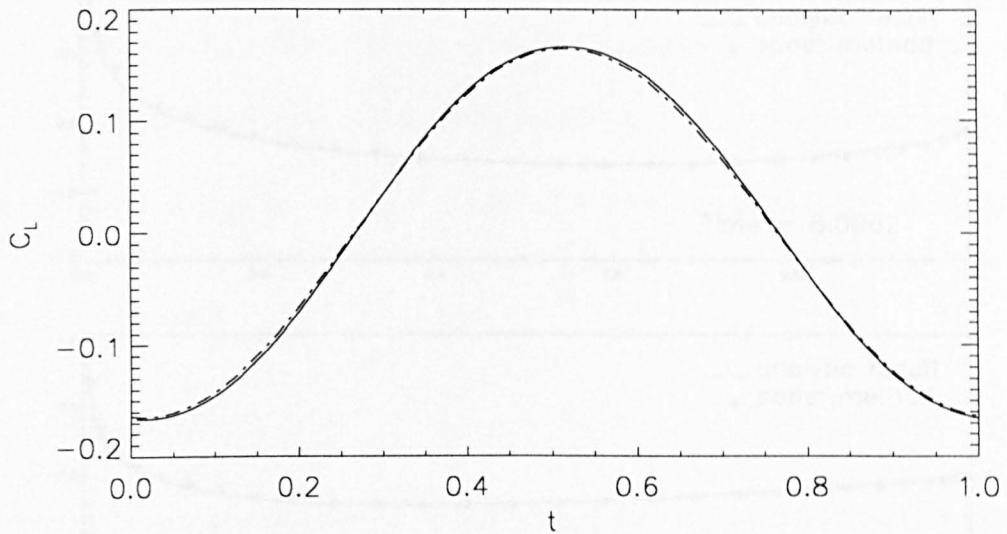


Figure 2.12: The lift coefficient against time for the same parameter values as the results in Fig. 2.11. In this case the analytic solution (solid line) is compared with the numerical result (broken line) for $N = 30$.

this line, looking at the mean thrust on a flat plate oscillating at both small and large amplitude.

2.11 Pitching and heaving flat plate model of lunate-tail propulsion

It was discussed in the introductory chapter that a two-dimensional model involving the pitching and heaving of a thin-airfoil with a rounded leading edge was used to model lunate-tail propulsion; initially by Lighthill (1975), and later by Chopra (1976). The important conclusions from the work were discussed in Chapter 1, but it is a useful exercise to run some similar tests on the panel method code. Lighthill points out that a rounded leading edge would be important on grounds of efficiency, which is why his (and Chopra's) calculations are done on a symmetric thin-airfoil with a rounded leading edge. Consequently we do not expect precise quantitative agreement with our flat plate, but it is another good test of the code.

Important points to remember are

- although the reduced frequency of the wave on a swimming fish is of order 10, the reduced

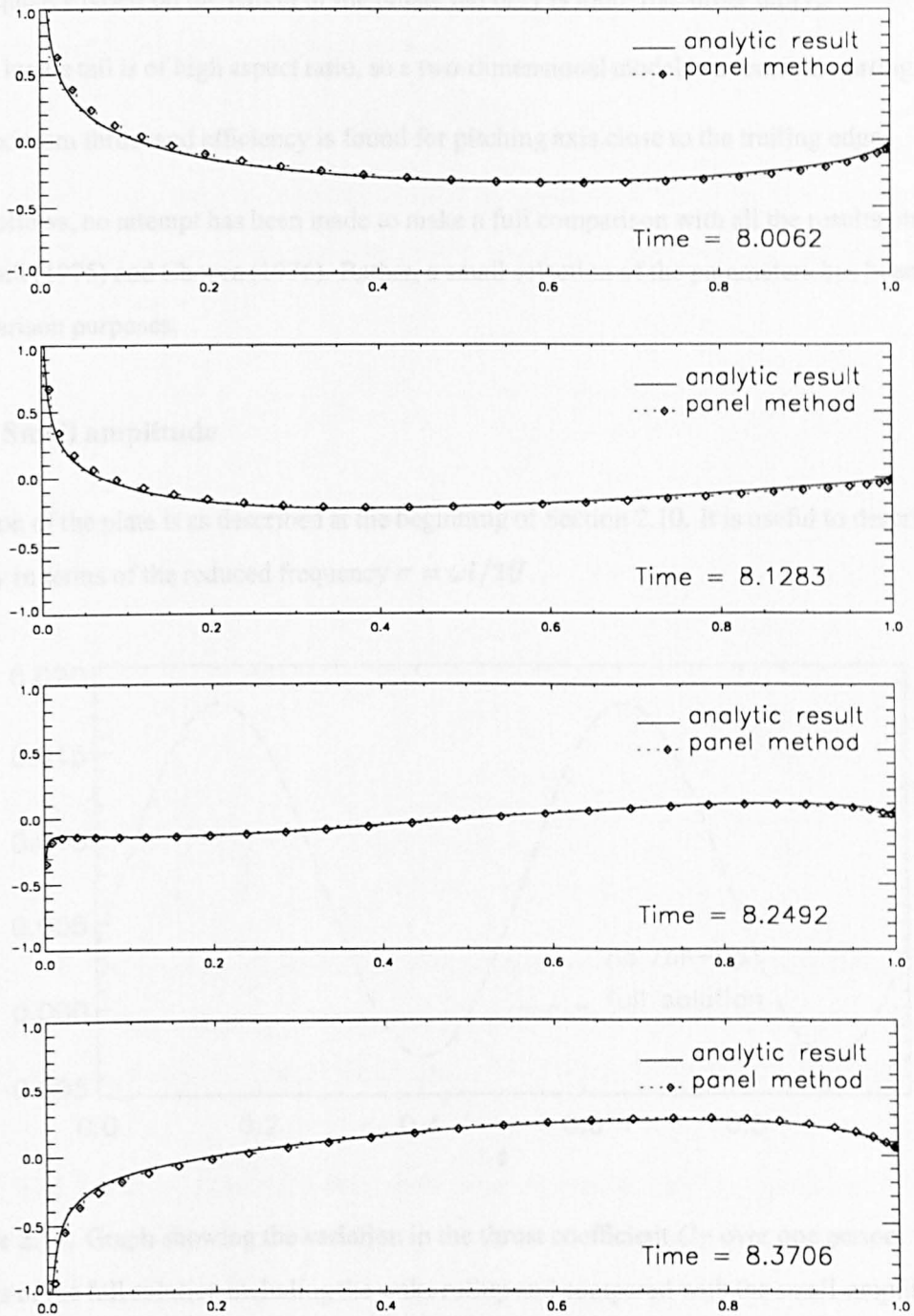


Figure 2.13: Graphs of the pressure jump coefficient against distance s along the body. The graphs come from four instances in the first half-period, ($T = 1$).

frequency based on the length of the lunate tail only is more like order unity;

- the lunate tail is of high aspect ratio, so a two-dimensional model is a sensible starting point;
- maximum thrust and efficiency is found for pitching axis close to the trailing edge.

In what follows, no attempt has been made to make a full comparison with all the results obtained by Lighthill (1975) and Chopra (1976). Rather, a small selection of the parameters has been made for comparison purposes.

2.11.1 Small amplitude

The motion of the plate is as described at the beginning of Section 2.10. It is useful to describe the frequency in terms of the reduced frequency $\sigma = \omega l/2U$.

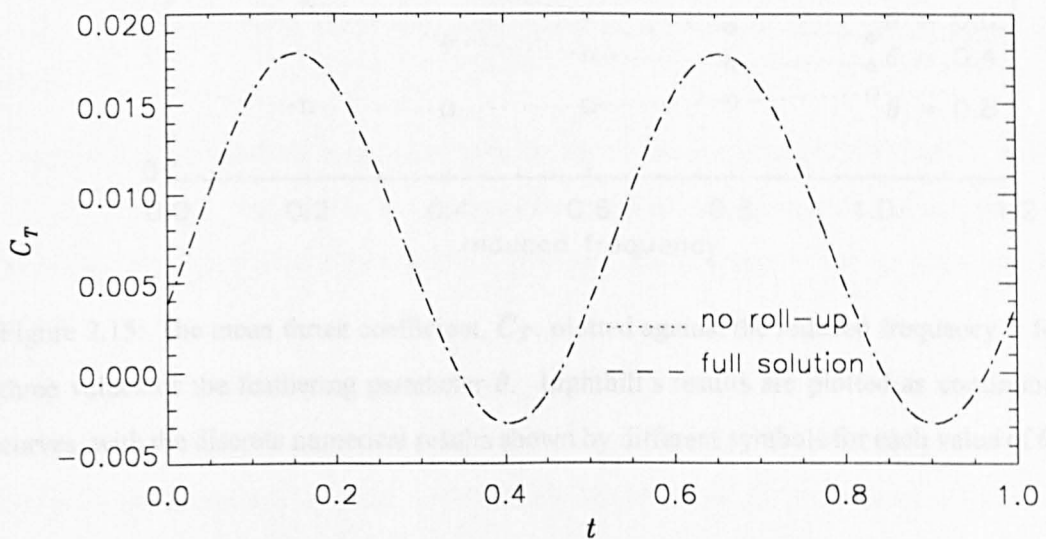


Figure 2.14: Graph showing the variation in the thrust coefficient C_T over one period. The results of the full solution including the wake rollup and compared with the small-amplitude approximation that neglects the deformation of the wake. This example is for a reduced frequency of $\sigma = 1.0$; the “feathering parameter” is $\theta = UB/\omega A = 0.4$.

Taking advantage of the fact that this is a small-amplitude model the results here were obtained without the wake-rollup procedure. However, by way of a check, the least expensive runs with

$\sigma = 1.0$ were also done using the full code. Fig 2.14 shows a comparison of the time dependent thrust coefficient C_T for the two methods, where

$$C_T = \frac{T_X}{\frac{1}{2}\rho U^2 l} \quad (2.108)$$

and the thrust T_X is the force on the plate acting in the negative X -direction. It is clear from the figure that agreement is good and there is no need to include the deformation of the wake for this small-amplitude motion.

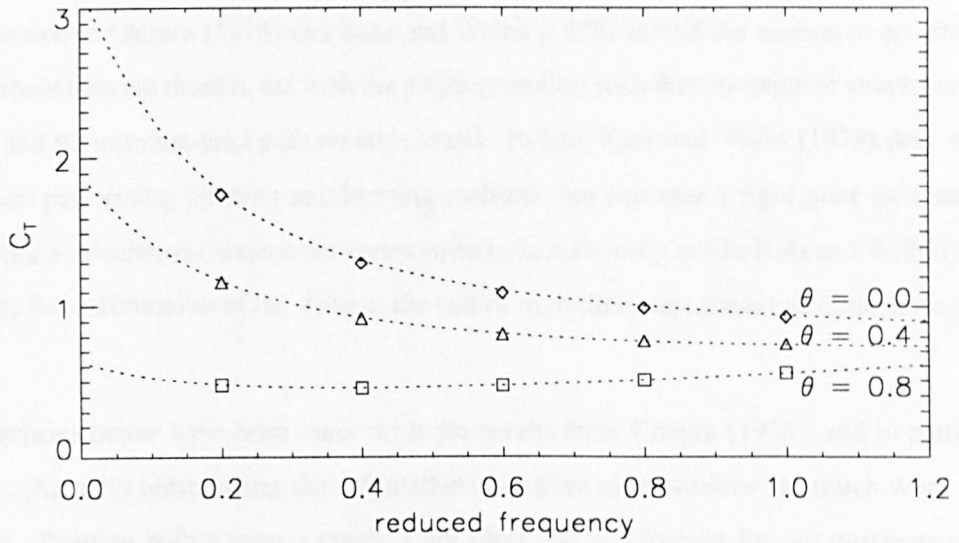


Figure 2.15: The mean thrust coefficient, \bar{C}_T , plotted against the reduced frequency σ for three values of the feathering parameter θ . Lighthill's results are plotted as continuous curves, with the discrete numerical results shown by different symbols for each value of θ .

Fig. 2.15 is the full set of results displayed in the same manner as used by Lighthill (1975, p.98). The mean thrust coefficient is the mean (dimensional) thrust per unit area divided by $\frac{1}{2}\hat{\rho}(\hat{\omega}\hat{A})^2$:

$$\bar{C}_T = \frac{\overline{(T_X)}}{\frac{1}{2}\hat{\rho}\hat{\omega}^2\hat{A}^2\hat{l}} \quad (2.109)$$

This is plotted against the reduced frequency σ for various values of the “feathering parameter”

$$\theta = \frac{UB}{\omega A}. \quad (2.110)$$

(Note that Lighthill (1975) plots the mean thrust against twice the reduced frequency.)

The fact that we have good quantitative agreement here is further vindication of the suction force approximation that we use. In all three cases most of the thrust here comes from the suction force, but in the case of $\theta = 0$, all the thrust is due to the suction.

We also found that for these oscillatory motions the number of time steps per period becomes an important consideration. At small amplitude, setting $T/\Delta t \approx 150$ worked well.

2.11.2 Large amplitude

The models due to Chopra (1976) and Katz and Weihs (1978) extend the motion to an arbitrary finite amplitude heaving motion, but with the pitching motion such that the angle of attack between the airfoil and its instantaneous path remains small. In fact, Katz and Weihs (1978) deal with a flexible plate performing pitching and heaving motions, but consider a rigid plate as a starting point. Chopra's calculations assume the vortex wake to be stationary, unlike Katz and Weihs (1978) who include the deformation of the wake at the end of each time step, (rather as done in the panel method).

The comparisons below have been made with the results from Chopra (1976), and in particular his Fig. 2. (Actually reproducing the calculations in either case involves too much work to be worthwhile. Reading points from a graph is not ideal, but is adequate for our purposes in this instance.)

In Chopra (1976) the plate is taken to be of length $2c$, with the path of the trailing edge given by $X = X_0(t)$, $Z = Z_0(t)$. The trailing edge moves in the direction $\theta(t)$ where $\tan \theta = \dot{Z}_0/\dot{X}_0$. The small angle of attack $\alpha(t)$ is the angle between the plate and the direction of motion, so that $\theta(t) - \alpha(t)$ is the angle of inclination between the plate and the X -axis. Given the description used by Chopra it is convenient to redefine the nondimensionalisation used in the panel method so that lengths are non dimensionalised with respect to the semi chord. This has no effect on the code itself, and merely means that the length of the plate is $l = 2$.

In terms of the panel method notation the position of the plate is given by

$$X(s, t) = X_0(t) + (s - l) \cos(\theta - \alpha) \quad (2.111)$$

$$Z(s, t) = Z_0(t) + (s - l) \sin(\theta - \alpha). \quad (2.112)$$

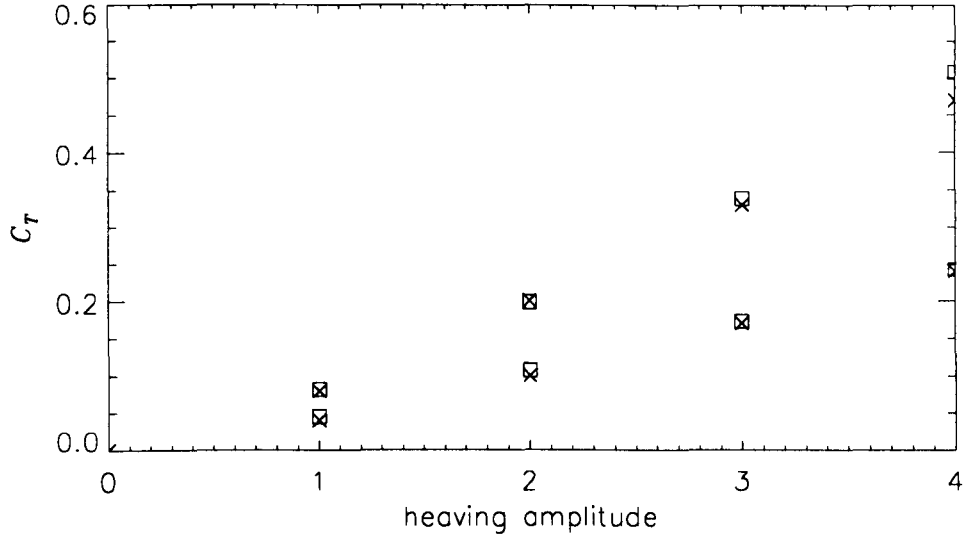


Figure 2.16: A graph of the mean thrust coefficient against the heaving amplitude. The panel method results are plotted with squares. The data read off from the graph in Chopra (1976) is plotted by crosses. The results in this case are for $\alpha_0 = 0.24$. The upper set of points is for $\sigma = 0.2$, the lower for $\sigma = 0.1$.

As used by Chopra, we put

$$X_0(t) = -Ut \quad (2.113)$$

$$Z_0(t) = h \cos \omega t \quad (2.114)$$

$$\alpha(t) = \alpha_0 \sin \omega t. \quad (2.115)$$

The reduced frequency is $\sigma = \omega l/2U$ as usual, which means that $\sigma = \omega$ under the current non-dimensionalisation.

Fig. 2.16 shows a comparison between the panel method results and those from Chopra (1976). It was noted by Katz and Weihs (1978) that for a reduced frequency $\sigma > 0.3$ it was no longer valid to ignore the deformation of the wake. Consequently the results here are for $\sigma = 0.1$ and 0.2 . We found that at higher values of the reduced frequency the agreement was not so good, but since Chopra's results are at least partly called into question by the above comment we did not examine such values in detail.

Again (as with the small-amplitude examples) it was found that the number of time steps per period was influential in obtaining a converged solution. For the large-amplitude examples seen in this section we used $T/\Delta t \approx 400$.

2.12 Conclusions

This chapter dealt with the description and validation of the two-dimensional panel method. The method was shown to converge as the number of panels N is increased, although the results can also be sensitive to the choice of time step Δt . The simplest examples suggest that some general rules can be used to link N and Δt , where $\Delta t \approx l/NU$. However, for examples involving oscillatory motion, a more important consideration is the number of time steps per period T . From experimentation, we found that for the small-amplitude motion, a number of the order 150-200 time steps per period is adequate for a good solution, whereas for the larger-amplitude motion as seen in the previous section, we require a number closer to 400-500. Unfortunately it seems that for any given example a certain amount of experimentation is required before we can be sure that we are using adequate values for N and Δt .

It was also shown that, provided parameters are chosen so as to provide a properly converged solution, that solution is accurate when compared with analytic results obtained for a variety of examples of the unsteady motion of a flat plate. In particular, the method of Section 2.6 for calculating the suction force has been found to be accurate, and robust to changes in both the method of panelling and the number of panels.

Difficulties associated with the vortex wake were also discussed. The computational expense of including the deformation of the wake is a concern. For small-amplitude motion we can neglect the deformation of the wake, but at large-amplitude it may become necessary to adopt some other simplification of the wake model. Although the amalgamation and neglect of wake vortices has been described, neither was found to be necessary for the examples in this chapter. Experimentation with both ideas suggested that the details were likely to be dependent on any particular problem, so detailed explanation of the use of the methods is postponed until they are actually required.

The next chapter continues with the two-dimensional model, but deals with the motion of a

deformable, waving plate.

Chapter 3

Two-dimensional Swimming

3.1 Introduction

Chapter 2 described the vortex panel method in detail and examined its performance in modelling the unsteady motion of a flat plate. In Chapter 3 we look specifically at the modelling of swimming using the two-dimensional panel method. Firstly we deal with the description of the motion of the body. Secondly we return to the question of the recoil correction introduced in Section 1.4 and discuss its calculation. We use the model to look at some examples relating to swimming, in particular comparing results with Wu (1961), but also examining the recoil correction, and the pressure jump distribution.

3.2 Motion of a waving plate

As described in Chapter 2, we model the body as being infinitely thin, and of (dimensional) length \hat{l} . In the model of steady state swimming the nose moves in the negative x -direction with constant speed \hat{U}_0 . Lengths are non-dimensionalised with respect to the body length \hat{l} , and velocities with respect to the swimming speed \hat{U}_0 . Time is non-dimensionalised as usual: $t = \hat{U}_0 \hat{t} / \hat{l}$. The body is inextensible with the Lagrangian variable s denoting the distance along the body from the nose at $s = 0$. There is a travelling wave with frequency \hat{f} and wavelength $\hat{\lambda}$ moving backwards along the body (see below). Consequently the wave has non-dimensional wavelength $\lambda = \hat{\lambda} / \hat{l}$, wavenumber

$k = 2\pi/\lambda$ and angular frequency $\omega = \hat{\omega}\hat{l}/\hat{U}_0$, ($\hat{\omega} = 2\pi\hat{f}$). The non-dimensional period is given by $T = 2\pi/\omega$.

To deal with the equations of motion of the body we require that the “fish” has a distribution of body mass per unit length, $m_b(s)$. For the two-dimensional model this is also the mass distribution per unit “span” (length in the Y -direction). Naturally, we have $\int_0^l m_b(s)ds = M_b$, with M_b the total non-dimensional mass of the fish (per unit span):

$$M_b = \hat{M}_b/\hat{\rho}_b\hat{l}^2(2\hat{l}_Y), \quad (3.1)$$

where $2\hat{l}_Y$ is the (uniform) span of the waving plate. (The apparently odd notation is used here for consistency with the three-dimensional notation used later.) The density of the fish is taken to be equal to the density of water: $\hat{\rho}_b = \hat{\rho}$. At this stage we use a uniform mass distribution m_b , so that $M_b = lm_b$.

There are two contributions to the motion of the body: the prescribed bending wave together with the constant forward swimming, and the additional recoil correction. We start by neglecting the recoil correction and deal with the basic motion of the body. We use a general function that describes a travelling wave moving backwards along the body (from nose to tail) with possibly varying amplitude. The lateral displacement due to the bending of the fish is given by $h_z(s, t)$. There are many possible forms for $h_z(s, t)$, but in setting up the code and initial testing we used

$$h_z = \Re \left([Ae^{\alpha s} - iB(s^\beta - b)]e^{i(ks - \omega t + \xi)} \right), \quad (3.2)$$

where α , β , A and B are real constants and ξ is a phase constant. In addition to meeting our requirements for modelling swimming (see below) this has the advantage of simplifying to the pitching and heaving of a flat plate when $\alpha = k = 0$ and $\beta = 1$, as seen in Chapter 2.

The travelling wave behaviour is governed by the $e^{i(ks - \omega t + \xi)}$ term. The terms in the square brackets provide some flexibility in the amplitude envelope of the wave. Using $Ae^{\alpha s}$ (Azuma, 1992) sets the minimum amplitude A to be at the nose $s = 0$. Cheng *et al.* (1991) used an amplitude varying as a power of s , with the nose fixed at $z = 0$, as given by using the Bs^β term in equation (3.2). Alternatively the terms can be used in conjunction to produce more complicated behaviour. For example, Videler and Hess (1984) note that in saithe (*Pollachius virens*) the minimum amplitude (which is non-zero) occurs slightly behind the head. Finally, there is no reason why different forms

for the bending wave should not be used, such as a Fourier series (Wu, 1961; Hess and Videler, 1984), and so the description below is done in terms of $h_z(s, t)$ rather than the specific form in equation (3.2).

As mentioned earlier we impose the condition that the body is inextensible, as did Lighthill (1971). Consequently a lateral displacement of the body $h_z(s, t)$ is accompanied by motion in the x -direction. We write the inextensibility condition as

$$\left(\frac{\partial h_x}{\partial s}\right)^2 + \left(\frac{\partial h_z}{\partial s}\right)^2 = 1, \quad (3.3)$$

so that $h_x(s, t)$ describes the body's displacement in the x -direction due to its lateral movements. Equation (3.3) can be re-arranged to give $h_x(s, t)$ in terms of $h_z(s, t)$:

$$h_x(s, t) = \int_0^s \left[1 - \left(\frac{\partial h_z}{\partial s'}\right)^2\right]^{\frac{1}{2}} ds'; \quad (3.4)$$

a 4th-order Runge-Kutta method is used to calculate h_x accurately and efficiently. The velocity and acceleration of the body, as functions of s and t , are also used throughout the program. In general, both \dot{h}_x and \ddot{h}_x must be found numerically from the following integrals, whose integrands can, however, be specified analytically.

From equation (3.4), we have

$$\begin{aligned} \dot{h}_x(s, t) &= \frac{\partial}{\partial t} \int_0^s \left[1 - \left(\frac{\partial h_z}{\partial s'}\right)^2\right]^{\frac{1}{2}} ds' \\ &= \int_0^s \left(-\frac{\partial h_z}{\partial s'} \frac{\partial^2 h_z}{\partial s' \partial t} \left[1 - \left(\frac{\partial h_z}{\partial s'}\right)^2\right]^{-\frac{1}{2}}\right) ds'; \end{aligned} \quad (3.5)$$

similarly,

$$\begin{aligned} \ddot{h}_x(s, t) &= \frac{\partial^2}{\partial t^2} \int_0^s \left[1 - \left(\frac{\partial h_z}{\partial s'}\right)^2\right]^{\frac{1}{2}} ds' \\ &= \int_0^s - \left[1 - \left(\frac{\partial h_z}{\partial s'}\right)^2\right]^{-\frac{1}{2}} \left[\left(\frac{\partial h_z}{\partial s'} \frac{\partial^3 h_z}{\partial s' \partial t^2}\right) \right. \\ &\quad \left. + \left(\frac{\partial^2 h_z}{\partial s' \partial t}\right)^2 \left(1 + \left(\frac{\partial h_z}{\partial s'}\right)^2 \left[1 - \left(\frac{\partial h_z}{\partial s'}\right)^2\right]^{-1}\right) \right] ds'. \end{aligned} \quad (3.6)$$

In practice the bending wave on the body of a swimming fish varies between species, and even between individuals of the same species. Equation (3.2) is a good starting point, but to draw meaningful biological conclusions from our numerical method we will need to be more careful about the correlation between the “swimming function”, equation (3.2), and the real motion of any particular fish.

3.3 The recoil correction

The nature of our model for swimming is that the motion of the fish is a prescribed input to a fluid mechanical calculation from which we can obtain quantities such as the pressure jump distribution along the body. Lighthill (1960) pointed out that in such a model we cannot know in advance that the prescribed motion satisfies the conservation of momentum and angular momentum of the fish. There are two sources of inaccuracy: firstly (as already discussed) any $h_z(s, t)$ inferred from experimental data is bound to be inaccurate; and secondly the hydrodynamic model obviously involves several approximations.

Ideally the conservation of momentum in the direction of swimming would be satisfied by including a time-dependent perturbation to the mean swimming speed U_0 . This requires the calculation of the viscous drag on the body which is not directly possible in the context of an inviscid model (see Chapter 5). We are therefore forced to assume that the fish swims at a constant velocity with the thrust exactly balanced by the drag. However, excluding a small component due to drag, we do calculate the time dependent lateral forces, and thus should ensure that the motion satisfies the conservation of lateral momentum, and of angular momentum. These conservation conditions are satisfied by adding a sideways translation $R(t)$ and rotation $\Theta(t)$ to $h_z(s, t)$ (see below). The failure to conserve longitudinal momentum may seem inconsistent, but the lateral component of the pressure jump is large compared to the thrust-producing streamwise component and, as we see later, a small recoil correction can have a marked effect on the resulting pressure distribution.

The conservation of momentum in the z -direction requires that the total hydrodynamic sideforce is equal to the rate of change of lateral momentum of the body:

$$\int_0^1 \Delta p(s) \hat{n}(s) \cdot \hat{k} - \int_0^1 m_b(s) \frac{\partial^2 Z}{\partial t^2} ds = 0. \quad (3.7)$$

In terms of the panel method this is

$$\sum_{i=1}^N \Delta l_i \Delta p_i \hat{\mathbf{n}}_i \cdot \hat{\mathbf{k}} - \int_0^1 m_b(s) \frac{\partial^2 Z}{\partial t^2} ds = 0. \quad (3.8)$$

The conservation of angular momentum requires that the moment of hydrodynamic forces is equal to the rate of change of angular momentum of the body where moments are taken about the same fixed axis. Note that the suction force \mathbf{T}_s must also be included. In order that it be applicable at large-amplitude, the condition is formulated in terms of the vector position of the element ds (rather than assuming the body lies along the X -axis). Recall that the problem is solved in a frame of reference where the fluid is at rest far from the fish, and that the motion is such that the nose of the fish has a constant speed U in the negative X -direction. The choice of axis about which to take moments then creates a problem.

- The origin of the “lab frame” is certainly fixed, but the magnitude of the moments taken about this point will increase as the fish swims away from its starting position.
- The centre of mass of the fish is accelerating (and in fact its position is not known).
- The nose of the fish has lateral acceleration.

Consider a frame of reference where the fish “holds station” in a uniform stream with velocity $(U, 0)$. We take moments about the origin of this inertial frame, which coincides with the mean position of the nose (excluding any recoil correction, see below). We continue to express the equations in terms of the original lab frame however since the transformation between the two frames is so straightforward. The position vector of the origin of the new frame is $\mathbf{X}_0(t) = (-Ut, 0)$: it is clearly not accelerating. We can now express the conservation of angular momentum of the body in the original (lab) frame of reference.

$$\begin{aligned} \int_0^1 (\mathbf{X}(s, t) - \mathbf{X}_0(t)) \wedge (\Delta p(s, t) \hat{\mathbf{n}}(s, t)) ds + (\mathbf{X}(s, t) - \mathbf{X}_0(t)) \wedge \mathbf{T}_s \\ = \int_0^1 (\mathbf{X}(s, t) - \mathbf{X}_0(t)) \wedge m_b(s) \ddot{\mathbf{X}}(s, t) ds \end{aligned} \quad (3.9)$$

which gives

$$\begin{aligned} \int_0^1 (\mathbf{X}(s, t) - \mathbf{X}_0(t)) \wedge [\Delta p(s, t) \hat{\mathbf{n}}(s, t) - m_b(s) \ddot{\mathbf{X}}(s, t)] ds \\ + (\mathbf{X}(s, t) - \mathbf{X}_0(t)) \wedge \mathbf{T}_s = 0. \end{aligned} \quad (3.10)$$

The left hand sides of equations (3.7) and (3.10) are functions of a number of variables governing the model, such as the swimming speed, amplitude of the bending wave, and the number of panels on the body. However, for a specific run, they define two functions of the recoil parameters $R(t)$ and $\Theta(t)$:

$$L_R(R, \Theta) = 0 \quad (3.11)$$

$$M_R(R, \Theta) = 0. \quad (3.12)$$

We have no analytic expression for L_R and M_R in terms of R and Θ and in general (at least for the large amplitude motion in which we are interested) the functions are nonlinear. The problem then is to solve the equations (3.11) and (3.12) for R and Θ at each time step. The evaluation of L_R and M_R for any value of R, Θ involves calculating the resulting pressure jump distribution via the panel method.

To describe in detail how the recoil correction is computed we must first specify the motion of the body, now including the unknown recoil parameters $R(t)$ and $\Theta(t)$. This is most easily explained in terms of an intermediate frame of reference, although ultimately everything is expressed in the lab frame. We consider a coordinate frame of reference (x, z) (the ‘‘body frame’’) where the nose of the fish has a fixed x -position $x = 0$, the lateral displacement of the fish is given by $z = h_z(s, t)$, and the longitudinal displacement of the fish, $x = h_x(s, t)$, is calculated via the inextensibility condition, equation (3.3). Note that in the absence of the recoil correction it is the origin of this frame about which we take moments (eg equation (3.9)). The recoil correction is the addition of a lateral translation $R(t)$ and rotation $\Theta(t)$ of the body frame. The rotation is defined about the origin of the body frame, see Fig. 3.1. Referring back to the lab frame, the position vector of a point on the body is given by

$$X = -Ut + h_x \cos \Theta - h_z \sin \Theta, \quad (3.13a)$$

$$Z = R + h_z \cos \Theta + h_x \sin \Theta. \quad (3.13b)$$

Thus it is possible to specify the derivatives with respect to time in order to write the velocity and acceleration of the body as a function of position and time. The velocity components are given by

$$\dot{X} = -U + \dot{h}_x \cos \Theta - h_x \dot{\Theta} \sin \Theta - \dot{h}_z \sin \Theta - h_z \dot{\Theta} \cos \Theta, \quad (3.14a)$$

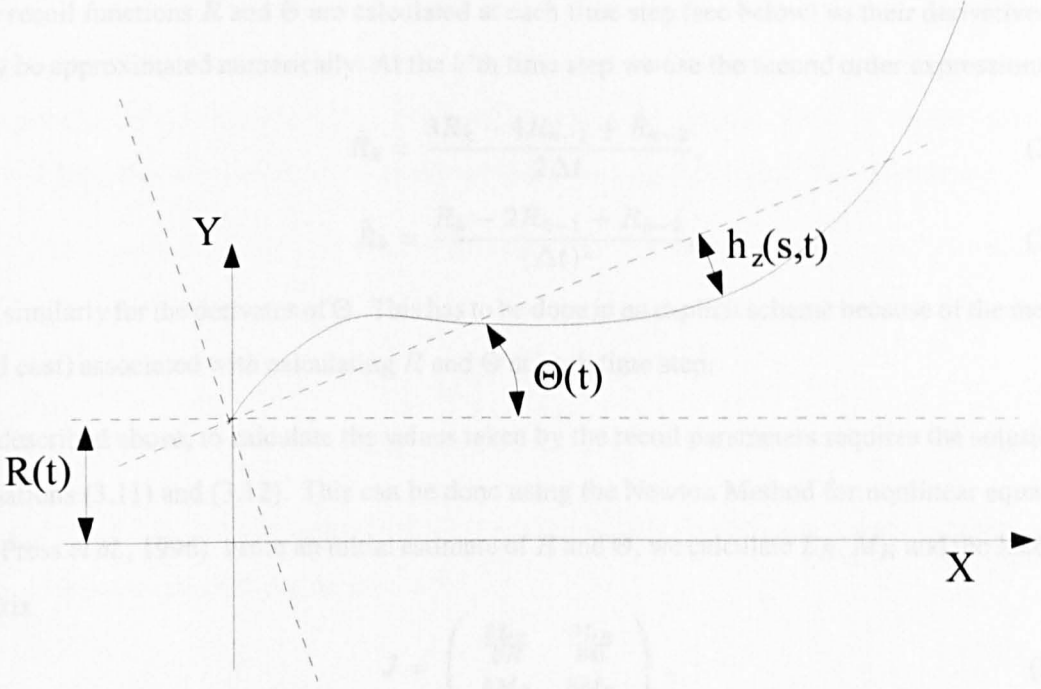


Figure 3.1: Sketch of the waving plate (the solid line) including the displacement and rotation due to the recoil parameters $R(t)$ and $\Theta(t)$. The X, Y axes represent the “lab frame”; the dashed axes represent the “body frame” in which the waving motion is defined.

$$\dot{Z} = \dot{R} + \dot{h}_z \cos \Theta - h_z \dot{\Theta} \sin \Theta + \dot{h}_x \sin \Theta + h_x \dot{\Theta} \cos \Theta \quad (3.14b)$$

and the acceleration components are given by

$$\ddot{X} = (\ddot{h}_x - h_x \dot{\Theta}^2 - 2\dot{h}_z \dot{\Theta} - h_z \ddot{\Theta}) \cos \Theta + (h_z \dot{\Theta}^2 - 2\dot{h}_x \dot{\Theta} - h_x \ddot{\Theta} - \ddot{h}_z) \sin \Theta \quad (3.15a)$$

$$\ddot{Z} = \ddot{R} + (\ddot{h}_z - h_z \dot{\Theta}^2 + 2\dot{h}_x \dot{\Theta} + h_x \ddot{\Theta}) \cos \Theta + (\ddot{h}_x - 2\dot{h}_z \dot{\Theta} - h_z \ddot{\Theta} - h_x \dot{\Theta}^2) \sin \Theta. \quad (3.15b)$$

where the dot is used to indicate differentiation with respect to time, as usual. Note that when $R \equiv \Theta \equiv 0$, these equations reduce to their required forms:

$$X = -Ut + h_x, \quad (3.16a)$$

$$Z = h_z, \quad (3.16b)$$

etc.

The recoil functions R and Θ are calculated at each time step (see below) so their derivatives can only be approximated numerically. At the k 'th time step we use the second order expressions:

$$\dot{R}_k = \frac{3R_k - 4R_{k-1} + R_{k-2}}{2\Delta t}, \quad (3.17)$$

$$\ddot{R}_k = \frac{R_k - 2R_{k-1} + R_{k-2}}{(\Delta t)^2}, \quad (3.18)$$

and similarly for the derivatives of Θ . This has to be done in an explicit scheme because of the method (and cost) associated with calculating R and Θ at each time step.

As described above, to calculate the values taken by the recoil parameters requires the solution of Equations (3.11) and (3.12). This can be done using the Newton Method for nonlinear equations (eg Press *et al.*, 1996). From an initial estimate of R and Θ , we calculate L_R , M_R and the Jacobian matrix

$$J = \begin{pmatrix} \frac{\partial L_R}{\partial R} & \frac{\partial L_R}{\partial \Theta} \\ \frac{\partial M_R}{\partial R} & \frac{\partial M_R}{\partial \Theta} \end{pmatrix}. \quad (3.19)$$

The Jacobian is calculated numerically in this case. We then solve

$$J \begin{pmatrix} \delta R \\ \delta \Theta \end{pmatrix} = - \begin{pmatrix} L_R \\ M_R \end{pmatrix} \quad (3.20)$$

to obtain an ‘‘iterate-step’’ $(\delta R_n, \delta \Theta_n)$. We move towards the final converged solution by putting

$$R_{n+1} = R_n + \delta R_n \quad (3.21)$$

$$\Theta_{n+1} = \Theta_n + \delta \Theta_n, \quad (3.22)$$

and repeating the procedure until some preset convergence condition is met. The Newton method is generally quite robust, and may be further improved by taking care over the length of each step using the method of linesearches and backtracking (Press *et al.*, 1996), which avoids taking the full Newton-step $(\delta R_n, \delta \Theta_n)$ when this step is too large.

However, the evaluation of (L_R, M_R) is expensive, and the Newton Method requires at least three function evaluations per iteration because of the need to calculate the Jacobian. We have also used Broyden's method (Press *et al.*, 1996) which essentially uses an approximation to the Jacobian and an algorithm that updates this matrix at each iteration, rather than re-evaluating the Jacobian. The method still relies on repeatedly solving for an iterate-step and using Equation (3.22) to obtain a

converged solution, but is not as robust as the Newton method. Consequently we use a combination of the two methods where the Jacobian is calculated as the initial matrix, as opposed to some other cheaper approximate starting point. In situations where the cheaper Newton-Broyden combined method fails, the calculation can be re-started using the more robust full Newton method.

Note that at each new time step we can provide an initial estimate of the recoil parameters by writing:

$$\begin{aligned} R_{k+1} &= R_k + \Delta t \left(\frac{dR}{dt} \right)_k + \frac{(\Delta t)^2}{2} \left(\frac{d^2 R}{dt^2} \right)_k \\ &= 3R_k - 3R_{k-1} + R_{k-2}, \end{aligned} \quad (3.23)$$

and likewise for Θ . See the Appendix for further details about the time and storage costs associated with different components of the program.

3.4 Small amplitude two-dimensional swimming

At this stage we continue the process of verifying that the panel method code calculates the same results as analytically based theory. Wu (1961) gave a two-dimensional theory for describing the small-amplitude swimming of a waving plate. The theory is for a deformable solid plate of zero thickness in a constant, uniform stream U , with the motion of the plate given by an arbitrary continuous function of x and t

$$y = h(x, t) \quad -1 < x < 1, \quad (3.24)$$

with h and $\partial h/\partial x$ assumed very small compared with unity. The solution is found in terms of Prandtl's acceleration potential ϕ , where the linearized Euler equations of motion for the ideal fluid give

$$\left(\frac{\partial}{\partial t} + U \frac{\partial}{\partial x} \right) \mathbf{q} = \nabla \phi \quad (3.25)$$

$$\phi(x, y, t) = \frac{p_\infty - p}{\rho} \quad (3.26)$$

where $\mathbf{q} = (U + u, v)$; (u, v) being the (assumed small) perturbation velocity due to the motion of the plate. The wake is assumed to lie along the x -axis for $x \geq 1$, with its strength being a function

of the single variable $(x - Ut)$. Wu (1961) developed expressions for the mean thrust, mean energy, and propulsive efficiency for a motion described by

$$h(x, t) = \left[\sum_{m=0}^{\infty} b_m x^m e^{i\epsilon_m} \right] e^{i(\omega t - kx)}. \quad (3.27)$$

In terms of $h(x, t)$, the small amplitude approximation in this case requires that

$$\frac{1}{U} \left| \frac{\partial h}{\partial t} \right| \ll 1 \quad (3.28)$$

and

$$\left| \frac{\partial h}{\partial x} \right| \ll 1. \quad (3.29)$$

Consequently, if we impose a wavelength approximately equal to the body length, and a non-dimensional velocity of $U = 1$, we see that the maximum amplitude of the wave (at the tail) A_l is required to be small

$$A_l \ll 1, \quad (3.30)$$

but that the wave's angular frequency ω is not so heavily constrained:

$$|A_l \omega| \ll 1. \quad (3.31)$$

In fact, for a reduced frequency $\sigma = \omega l / 2U \gtrsim 8$, the Kutta condition is probably no longer valid and the results would be adversely affected (Katz and Plotkin, 1991). (The Kutta condition is probably violated for slightly lower reduced frequencies, but without the results for the pressure being significantly affected.) So given the condition on the maximum amplitude of the bending wave (equation (3.30)) there is not a strong restriction on the angular frequency.

Wu's expressions are in terms of the reduced frequency σ and wavenumber k . In the descriptions below we compare the mean thrust coefficients for the simplest examples: namely a uniform amplitude wave where $b_m = 0$ for $m > 0$, and a linearly varying amplitude where $b_m = 0$ for $m > 1$. The non-dimensionalised lengths with respect to the semi-chord of the plate, and so for purposes of these comparisons we have done the same for the panel method model. (Such a change does not affect the formulation of the code, but it means that the length of the plate becomes $l = 2$, as opposed to $l = 1$. It is then easier to ensure that the other parameters match up between methods.) Note that in our method the waving motion of the plate is governed by equation (3.2):

$$h_z = \Re \left([Ae^{\alpha s} - iB(s^\beta - b)] e^{i(k s - \omega t + \xi)} \right). \quad (3.32)$$

To ensure that the two descriptions of the motion are equivalent, in equation (3.27) we set $\epsilon_0 = 0$, $\epsilon_1 = -\pi/2$; and in equation (3.32) we set $\alpha = 0$, $\beta = 1$, $b = 1$, $\xi = 0$. The amplitude parameters are related by $b_0 = -A$, $b_1 = -B$; with k and ω have the same sense in both equations.

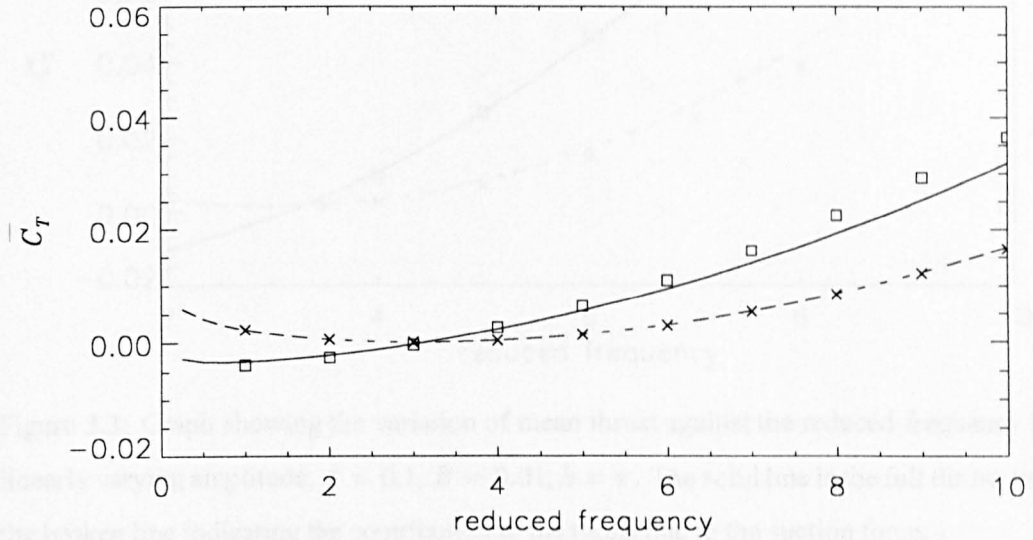


Figure 3.2: Graph showing the variation of mean thrust against the reduced frequency σ . The solid line is the full thrust, with the broken line indicating the contribution to the thrust due to the suction force. The amplitude envelope is constant, $A = 0.05$, $B = 0.0$, and the wavenumber is $k = \pi$.

As a first example, Fig. 3.2 shows a comparison of the mean thrust, $\bar{C}_T = \bar{T}_X / \frac{1}{2} \rho U^2$, against the reduced frequency for a constant-amplitude envelope with $A = 0.05$, $B = 0.0$ and a wavelength equal to the body length, so that $k = \pi$. (With $l = 2$ the reduced frequency is ω). The solid line is the full thrust, with the dotted line indicating the contribution due to the suction force. The agreement is good, but not excellent, although the suction approximation does very well. Fig. 3.3 and Fig. 3.4 show a similar situation for two linearly varying amplitude examples. Fig. 3.3 shows the variation in the mean thrust coefficient against the reduced frequency with $A = 0.1$, $B = 0.01$, $k = \pi$. Fig. 3.4 plots the mean thrust coefficient against the wavenumber k with $A = 0.0$, $B = 0.1$, $\omega = 5.0$. Note that at $k = 0$ the motion reduces to the pitching-heaving of a flat plate, which we already know to be accurately modelled by the panel method.

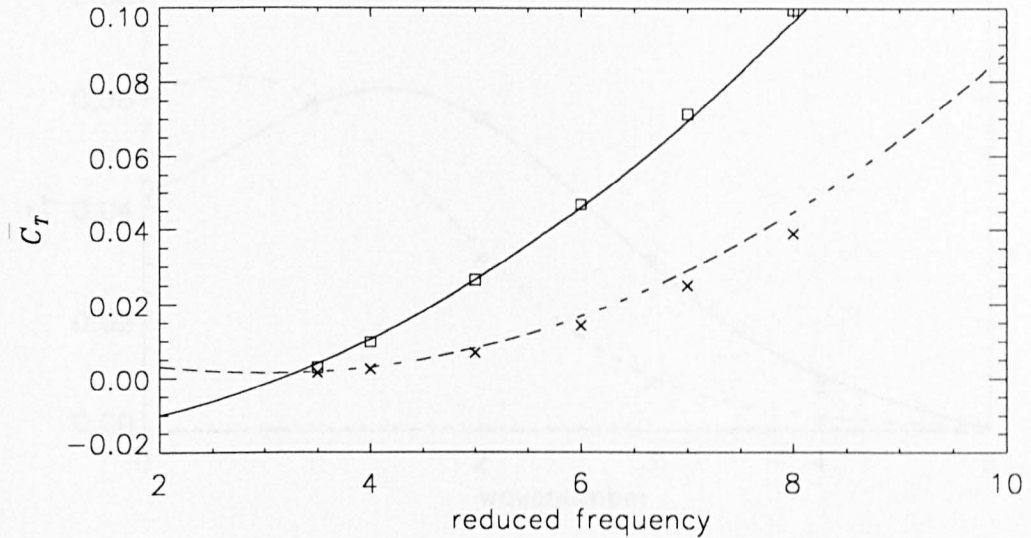


Figure 3.3: Graph showing the variation of mean thrust against the reduced frequency for linearly varying amplitude, $A = 0.1$, $B = 0.01$, $k = \pi$. The solid line is the full thrust, with the broken line indicating the contribution to the thrust due to the suction force.

The evidence presented in the graphs of Figs. 3.2-3.4 shows that it is possible to obtain satisfactory results using the panel method in this context. However, some discussion of the convergence in terms of the time step, and number and distribution of panels is required. It must be emphasized that although one can draw general conclusions about these parameters, it is necessary to check the details for any new geometry/problem.

The comments below relate to Fig. 3.5, which plots the mean thrust coefficient against number of panels, for a constant-amplitude waving motion with $\omega = 5.0$, $k = \pi$, $A = 0.05$ and $B = 0.0$ (cf Fig. 3.2). The two horizontal lines plot Wu's analytic solution for the full mean thrust (solid line) and suction force (dotted line).

The crosses mark the computed suction force for each experimental run. Evidently the method for calculating the suction is both accurate and stable to changes in N and Δt .

The plus signs and the triangles plot the mean thrust for variable and uniform panelling respectively with the time step chosen such that $U\Delta t \approx l/N$. As found in Chapter 2, for an oscillatory motion of period T , the quantity $T/\Delta t$ has a greater impact on the accuracy than the earlier requirement

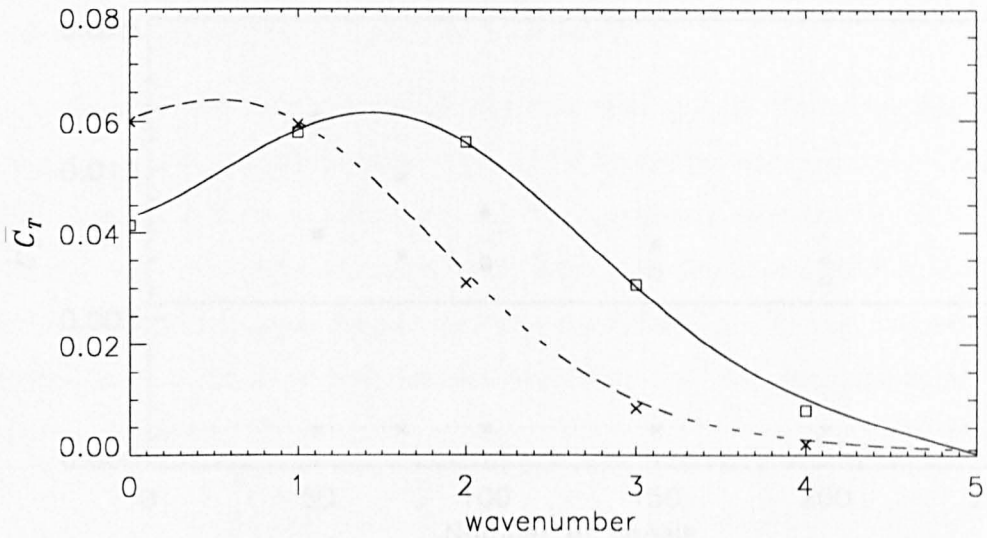


Figure 3.4: Graph showing the variation of mean thrust against the wavenumber k for linearly varying amplitude, $A = 0.0$, $B = 0.1$, $\omega = 5.0$. The solid line is the full thrust, with the broken line indicating the contribution to the thrust due to the suction force.

that $U\Delta t \approx l/N$. As expected, the solution improves with increasing N .

The asterisks and squares plot the results for variable and uniform panelling respectively, with $\Delta t = 0.0025$. For the example used in this case ($\omega = 5$) such a time step corresponds to having approximately 500 time steps per period. Again there is convergence with increasing N .

In view of the results in Chapter 2 it is surprising that apparently there is little difference between uniform and variable panelling. Note that when using cosine spacing, the leading and trailing edge panels soon become small (at $N = 100$, $(\Delta l)_0 \approx 2.5 \times 10^{-4}$). It is to be expected that very small panels will introduce numerical errors in the solution for the pressure jump distribution, and so we have not continued beyond $N = 100$ in this case.

In fact, looking at the pressure jump distribution suggests that even with $N < 100$ as in Fig. 3.5, the uniform solution is more accurate. Although the panel method does not allow us to specify it, ideally we require that the pressure jump at the trailing edge should be zero. We can only calculate the pressure jump at the collocation point (rather than the actual trailing edge), but we certainly want the pressure jump to appear to tend smoothly to zero at the tail. For uniform panelling this is indeed

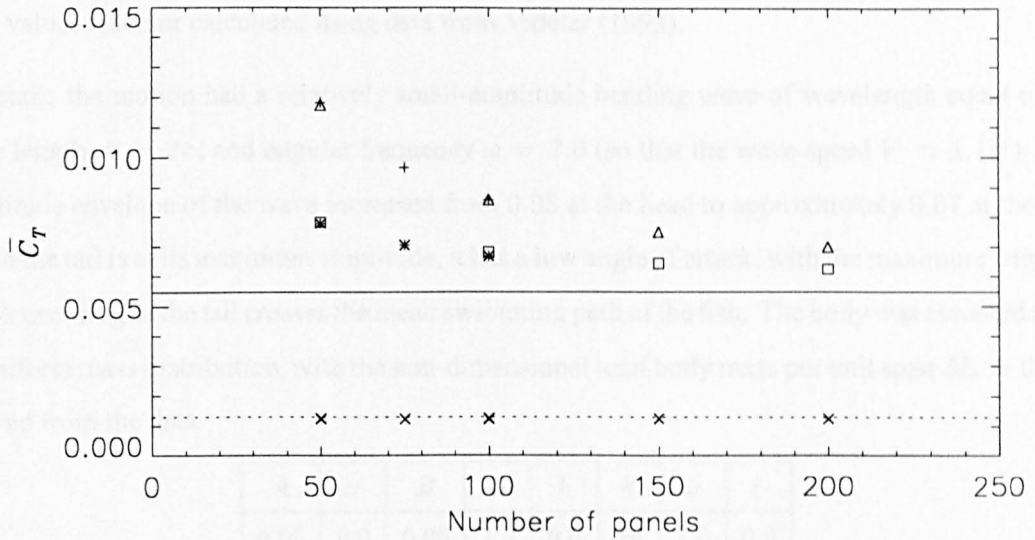


Figure 3.5: Graph showing the convergence of the panel method solution for mean thrust with varying N and Δt for both uniform and variable panelling. In this case $\omega = 5$, $k = \pi$, $A = 0.05$, $B = 0.0$. The solid line shows Wu's analytic solution, and the broken line shows the suction force. The crosses mark the computed suction force for each experimental run. The plus signs and the triangles plot the mean thrust for variable and uniform panelling respectively with the time step chosen such that $U\Delta t \approx l/N$. The asterisks and squares plot the results for variable and uniform panelling respectively, with $\Delta t = 0.0025$.

the case as N is increased, whereas for variable panelling we find typically that the pressure jump at the trailing edge panel oscillates with an amplitude which is large relative to its nearest neighbours. On this basis, coupled to the fact that the calculation of other quantities seemed equally accurate for both panel distributions we used uniform panelling for the remaining examples in this chapter. Note that this decision must be re-assessed when we move on to consider the three-dimensional calculations.

3.4.1 Testing the recoil correction

Before describing the work done to establish that the recoil correction is working, we start by describing the waving plate motion that we used in the tests. Rather than using an arbitrary motion,

the parameters were chosen such that the motion described a “simplified” anguilliform swimmer, with values taken or calculated using data from Videler (1993).

In detail: the motion had a relatively small-amplitude bending wave of wavelength equal to the body length, $k = 2\pi$, and angular frequency $\omega = 7.0$ (so that the wave speed $V \approx 1.1U$). The amplitude envelope of the wave increased from 0.05 at the head to approximately 0.07 at the tail. When the tail is at its maximum amplitude, it has a low angle of attack, with the maximum angle of attack occurring as the tail crosses the mean swimming path of the fish. The body was assumed to be of uniform mass distribution, with the non-dimensional total body mass per unit span $M_b = 0.065$ derived from the data.

A	α	B	β	b	k	ω	ξ
0.05	0.0	0.05	1.0	0.0	2π	7.0	0.0

Table 3.1: Table of parameter values for a set of examples used to test the recoil correction. The wave parameters are set up such that one wavelength is equal to the body length, with the wave speed being 1.1 times the forward swimming speed. The amplitude envelope is set to be increasing from the minimum at the nose to the maximum at the tail.

The body starts from rest at time $t = 0$. (At this time the body is not stretched out straight as might be considered ideal.) In trying to model steady state swimming we merely allow the calculation to start from rest and continue until there is no change between successive oscillations. In this case it is clear from the time dependent thrust (for example) that the motion has arrived at a steady state by $t > 2T$. Note also that the recoil correction is not included from $t = 0$, but is “switched on” at some later time $t = t_r$. Whilst it was not found necessary to wait for a fully steady state before including the recoil correction, it was found that t_r could not be too close to the non-physical impulsive start at $t = 0$.

Fig. 3.6 shows that the recoil calculation certainly works in terms of ensuring that there is no net force or moment acting on the body. However, given that the calculation is “switched on” at an arbitrary time (“sufficiently long after” $t = 0$) it is important to consider the effect on the final solution that this “switch-on time” might have.

Fig. 3.7 plots the values of the recoil parameters (R, Θ) for four different “switch-on times” $t = t_r$.

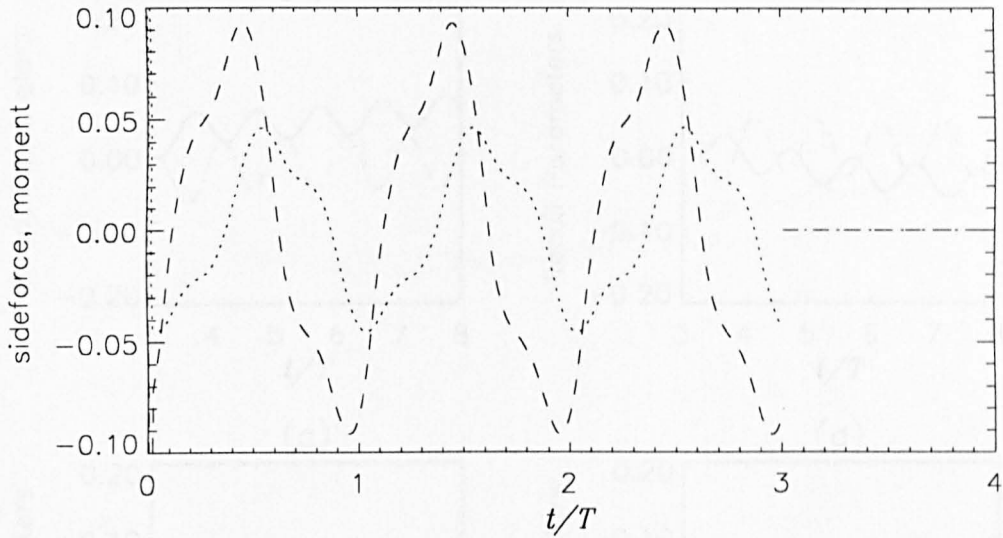


Figure 3.6: Curves plotting L_R (dotted) and M_R (dashed) over first four periods of the swimming motion. At time $t = 3T$ the recoil calculation is started, and both values go to zero.

As expected, the values of R and Θ depend on the instant in the bending wave cycle at which the recoil calculation is started. We tended to find (as suggested by the data in Fig. 3.7) that the recoil often produces some constant mean drift (that is $|R|$ increasing), with a constant non-zero mean rotation. In fact we should probably expect this from the method. It may be that there do exist in general some functions $R(t)$, $\Theta(t)$ which have zero mean and frequency ω , but we are unlikely to find these by the method of Section 3.3. We impose the condition that there is no sideforce, and hence no lateral acceleration of the body as a whole, but this does not preclude the possibility of the body having some overall sideways velocity. Hence it is hardly surprising that we frequently obtain such a mean sideways velocity. In real swimming such sideways motion would be damped by the action viscosity and the vortex shedding that would occur at the sharp “top and bottom edges” of the body.

However, having been concerned to see that the recoil may provide us with a “choice” of distinct solutions for the fish’s motion, it turns out that in practice there is no problem. In the cases that we tested here, the solutions for the pressure jump distribution (and, for example, the thrust) converge

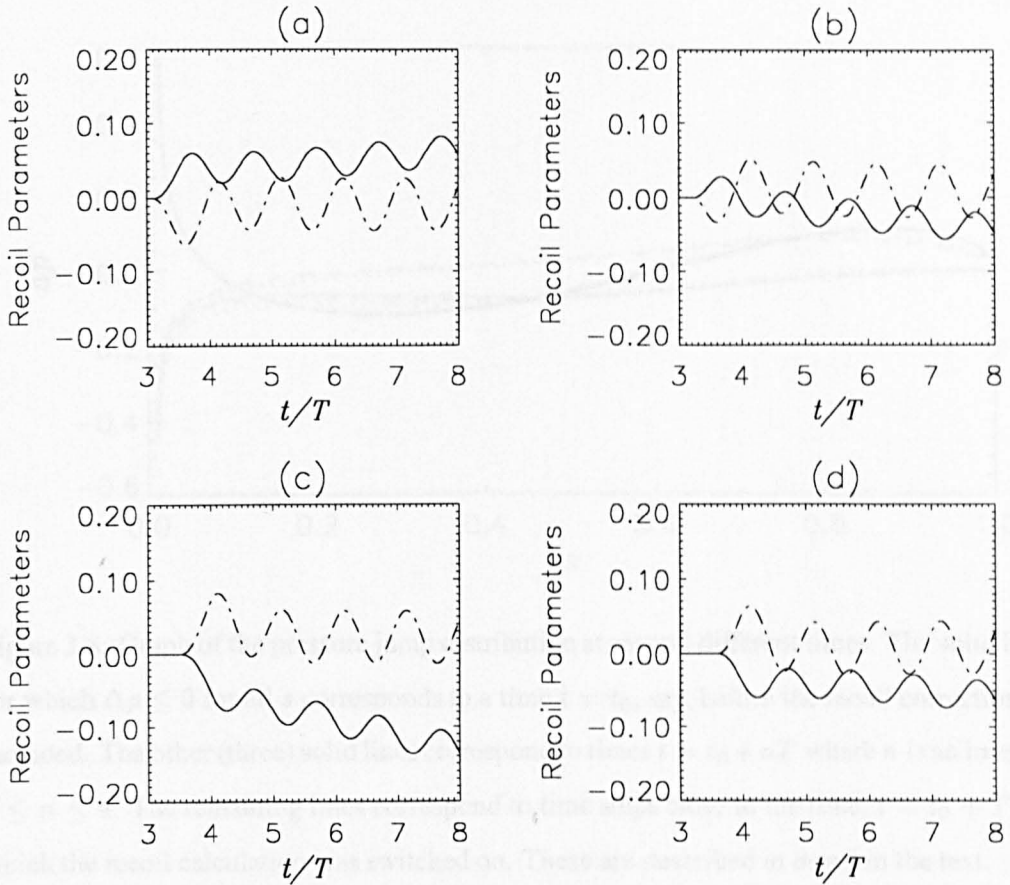


Figure 3.7: Variation in the recoil parameters depending on the time $t = t_r$ at which the recoil correction is “switched on” In each case, the solid line is R , with the dashed line being Θ which is an angle in radians. The graphs correspond to t_r as follows: (a) $t_r = 3.11T$, (b) $t_r = 3.25T$, (c) $t_r = 3.5T$, (d) $t_r = 3.61T$.

at some later time.

Firstly, Fig. 3.8 shows the effect on Δp of including the recoil calculation. The single solid line (with $\Delta p \leq 0$ for all s) corresponds to a time $t = t_0$ before the inclusion of the recoil correction. After one period, ie at $t_1 = t_0 + T$ the recoil correction was switched on. The dotted and dashed lines correspond to the time steps immediately preceding and subsequent to this moment. The lower group of three lines are for $t < t_1$, with the dashed line indicating the latest of the three $t = t_1 - \Delta t$. It can be seen that had the recoil calculation not been included at that point, the next curve would have coincided with that of $t = t_0$. However, the recoil correction then causes a

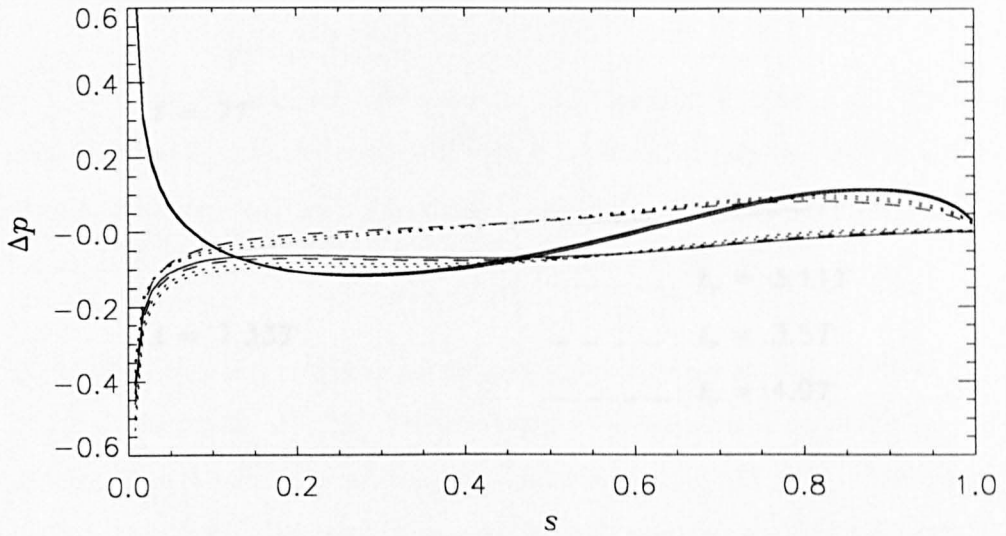


Figure 3.8: Graph of the pressure jump distribution at several different times. The solid line for which $\Delta p \leq 0$ for all s corresponds to a time $t = t_0$, say, before the recoil correction is included. The other (three) solid lines correspond to times $t = t_0 + nT$ where n is an integer $2 \leq n \leq 4$. The remaining lines correspond to time steps close to the time, $t = t_0 + T$, at which the recoil calculation was switched on. These are described in detail in the text.

discontinuity, and the pressure jump distribution at the subsequent time step $t = t_1$ is given by the dashed line in the upper group of three curves. In both cases the dotted lines are included to give some sense of the time variation of the pressure distribution at either side of the recoil switch-on time.

If we look at the solid lines, that is the results that correspond to times at which a steady state has been reached, we see that the recoil correction has a large effect on the pressure jump distribution. This backs up the philosophical decision to include the sideways and rotational recoil even though streamwise variations in the swimming velocity are assumed to be negligible. Fig. 3.8 certainly indicates that it is important to include the recoil correction.

Secondly, Fig. 3.9 shows the pressure jump distribution for three different simulations, where in each case the recoil switch-on time $t = t_r$ was different. Of course, the simulations were identical in all other senses. The curves plot the results at two different moments in the bending wave

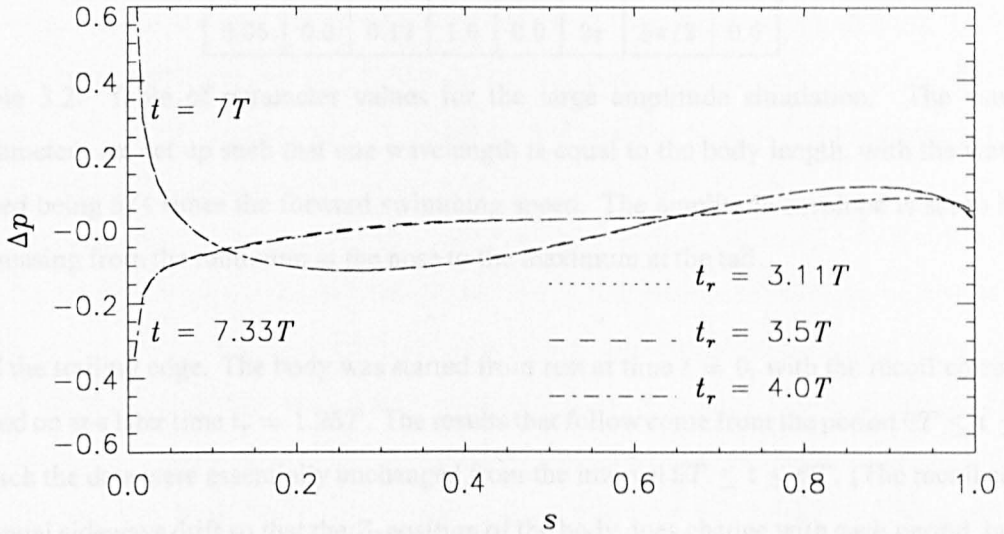


Figure 3.9: Graph of the pressure jump distribution (once a steady state has been reached) for simulations involving different recoil switch-on times $t = t_r$. The results are given at two different times, one-third of a period apart.

cycle: at the “beginning”, and then at one third of a period later. The agreement between curves is excellent (indeed it is difficult to make out three separate curves). We can apparently choose any value of t_r without affecting the resulting pressure jump distribution.

3.5 Large amplitude two-dimensional swimming

In this section we show some of the output from a specific simulation. The swimming parameters were chosen to give a reasonably large-amplitude wave on the body, and were taken broadly from data relating to saithe (*Pollachius virens*) (Table 6.1 Videler, 1993), and are given in Table 4.1 below. The non-dimensional length and speed of the fish are $l = 1$ and $U = 1$ respectively. The amplitude of the bending wave increases from nose to tail. The wavelength is equal to the body length, and the wave speed $V = \omega/k$ (ω being the angular frequency) is $V = 5/4$. We assume a uniform mass distribution, with the total mass per unit span $M_b = 0.065$.

We used $N = 200$ panels, and included the vortex amalgamation procedure at a distance of 2

A	α	B	β	b	k	ω	ξ
0.05	0.0	0.12	1.0	0.0	2π	$5\pi/2$	0.0

Table 3.2: Table of parameter values for the large amplitude simulation. The wave parameters are set up such that one wavelength is equal to the body length, with the wave speed being $5/4$ times the forward swimming speed. The amplitude envelope is set to be increasing from the minimum at the nose to the maximum at the tail.

behind the trailing edge. The body was started from rest at time $t = 0$, with the recoil correction switched on at a later time $t_r = 1.25T$. The results that follow come from the period $6T \leq t \leq 7T$ for which the data were essentially unchanged from the interval $5T \leq t \leq 6T$. (The recoil causes a continual sideways drift so that the Z -position of the body does change with each period, but the other quantities of interest remain unaffected.)

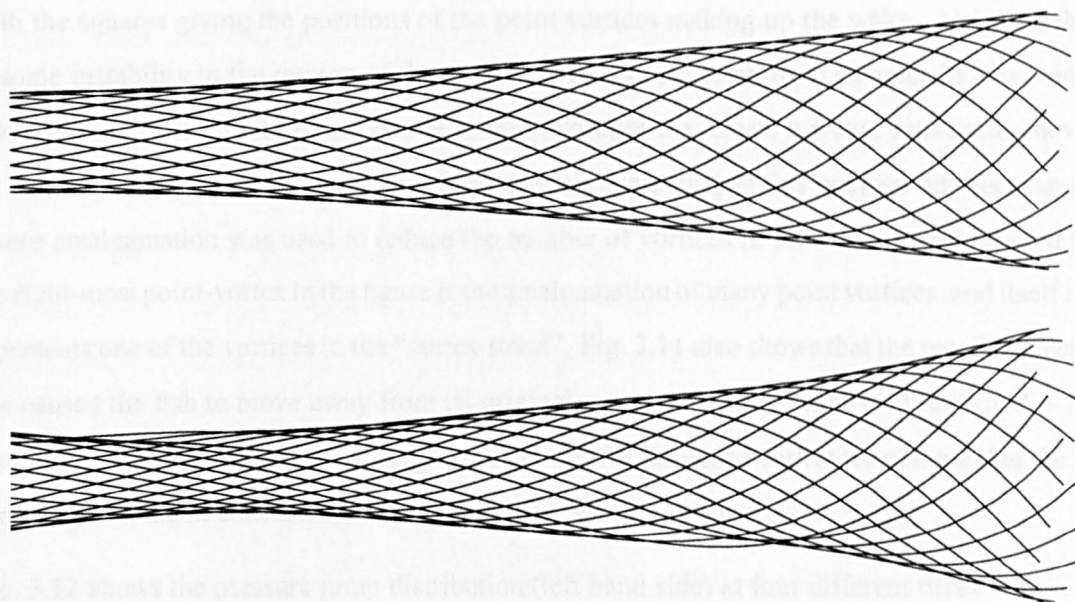


Figure 3.10: The amplitude envelope of the body, formed by plotting the body shape over one period in a frame of reference where the nose of the fish does not advance. The top picture is before the recoil correction is included; and the lower picture is after the recoil has been included, and a steady state has been reached.

Figs. 3.10 and 3.11 give some indication of the actual swimming that occurs. Fig. 3.10 plots the body shape at successive time steps over one period in a frame of reference where the body does

not advance (in the negative X -direction). The top picture shows the amplitude envelope without the recoil correction: the amplitude increases linearly from the nose to the tail, as input. The lower picture shows the amplitude envelope for the motion including the recoil correction. Note that in the lower case, the body is travelling at a slight angle to the negative X -axis. Consequently, positions separated in time by one period are not completely superimposable. It was stated above that the swimming parameters were chosen by comparison with data relating to steadily swimming saithe. In fact the bending wave on the real fish is seen to have an amplitude envelope with minimum behind the head. We found (from experimentation) that if we input a linearly increasing amplitude envelope the recoil correction caused the minimum to move to a point behind the head. The fact that the recoil-corrected version of the motion transformed the input waveform to one more closely resembling that seen in the actual fish is taken to be an indication of the model working well.

Fig. 3.11 shows an instant of the motion ($t = 7T$). The solid line gives the position of the body, with the squares giving the positions of the point vortices making up the wake. Although there is some instability in the motion of the point vortices (as expected from Chapter 2) it is evident that the wake rolls up into large counter-rotating vortices that create a wavy, backwards-moving jet behind the tail, as is broadly seen behind animals swimming in this manner. In this example, where amalgamation was used to reduce the number of vortices in the wake, it can be seen that the right-most point-vortex in the figure is the amalgamation of many point vortices, and itself now represents one of the vortices in the “vortex street”. Fig. 3.11 also shows that the recoil correction has caused the fish to move away from its original course along the negative X -axis and is now swimming at a slight angle to that original direction. As explained earlier we assume that the fish is now swimming at constant speed along this new straight line path.

Fig. 3.12 shows the pressure jump distribution (left hand side) at four different times within one period, together with the corresponding body shape (right hand side). Note that the result is symmetric about $t = \frac{1}{2}T$ so we only need plot times in the first half-period; and that the pressure distribution is close to zero at the trailing edge (as required). The pressure jump distribution appears to take the form of a travelling wave with amplitude varying in a complicated fashion with distance along the body. As was noted in the previous section, the recoil correction has a marked effect on the pressure distribution, and so it should be noted here that this result is likely to depend on parameters describing the physical characteristics of our model. The purpose of the panel method calculation

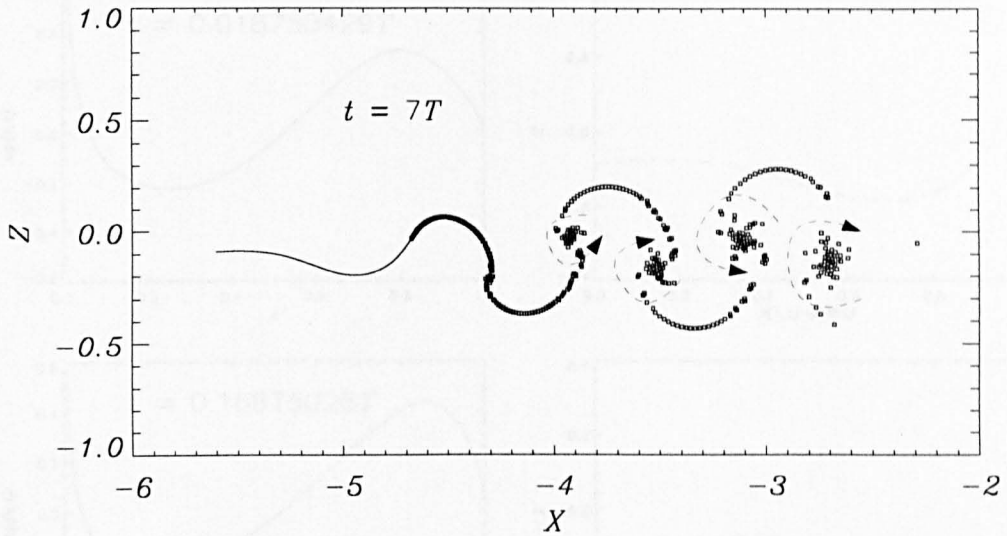


Figure 3.11: The body and wake at $t = 7T$. The solid line indicates the position of the body. The squares each represent a point vortex that has been shed from the trailing edge. The figure shows that the wake is not free of instabilities, but that the macroscopic behaviour that we expect is still in evidence. In particular we see counter-rotating, large-scale vortices (as opposed to the actual point vortices) behind the tail in a “vortex street”. The sense of the rotation in the fluid generated by these vortices is indicated by the arrows. Note that far from the body, the point vortices are amalgamated; and the furthest point vortex from the tail has resulted from many amalgamated vortices and now represents one of the vortices in the vortex street.

is to obtain the pressure jump distribution as it varies over time. However, in terms of the biology of fish, it is the quantities derived from the pressure distribution that are of most interest: in particular the bending moment distribution (see Chapter 6).

Finally, Fig. 3.13 shows the variation in the total thrust on the body over one period. The dashed line is the hydrodynamic thrust resulting from the pressure jump along the body, and the suction force at the leading edge. The solid line also includes the body inertia (with the nose moving at a fixed speed in the negative X -direction, the centre of mass must have non-zero longitudinal acceleration). Consequently, if the body is to move with constant speed, then it is the solid line that must be

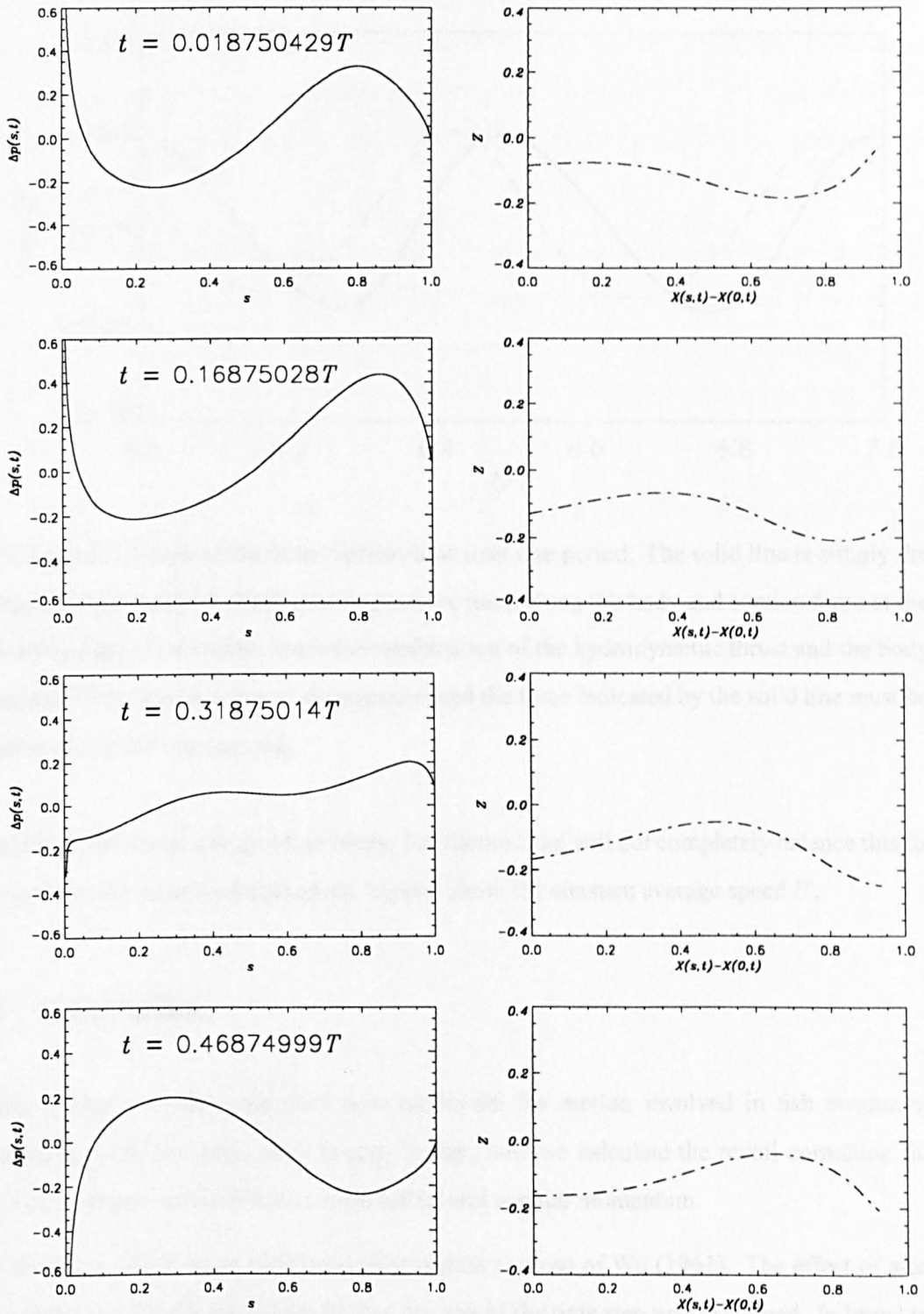


Figure 3.12: Graphs to show the pressure jump distribution against position along the body at four distinct moments in the period. The graphs on the right hand side show the body shape that corresponds to each pressure distribution.

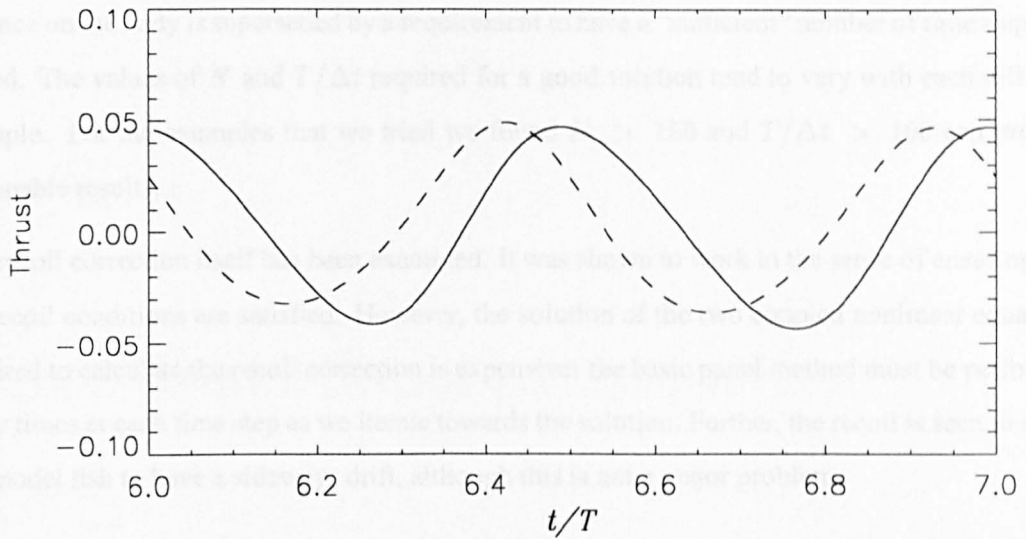


Figure 3.13: Graph of the thrust against time over one period. The solid line is simply the total hydrodynamic thrust due to the pressure jump along the body and suction force at the leading edge. The broken line is the combination of the hydrodynamic thrust and the body inertia. If the nose is to move at constant speed the force indicated by the solid line must be balanced by the viscous drag.

balanced by the viscous drag. More likely, the viscous drag will not completely balance this force, and so there will be some longitudinal “recoil” about the constant average speed U .

3.6 Conclusion

In this chapter we have described how we model the motion involved in fish swimming in combination with the panel method and, further, how we calculate the recoil correction that is required to ensure the motion conserves lateral and angular momentum.

The method was shown to produce similar results to those of Wu (1961). The effect of altering the number and distribution of panels and the size of the time step was examined. In broad terms the solution improves for increasing N and decreasing Δt with a limit on both parameters beyond which no improvement in accuracy can be obtained. The earlier conclusion that the time step should

be chosen to ensure that the distance between consecutive vortices in the wake be similar to that distance on the body is superseded by a requirement to have a “sufficient” number of time steps per period. The values of N and $T/\Delta t$ required for a good solution tend to vary with each different example. For the examples that we tried we found $N > 150$ and $T/\Delta t > 100$ can provide reasonable results.

The recoil correction itself has been examined. It was shown to work in the sense of ensuring that the recoil conditions are satisfied. However, the solution of the two coupled nonlinear equations required to calculate the recoil correction is expensive: the basic panel method must be performed many times at each time step as we iterate towards the solution. Further, the recoil is seen to cause our model fish to have a sideways drift, although this is not a major problem.

Finally we output some results from a “saithe-like” swimming example, noting in particular that the recoil correction was able to “correct” the input waveform to one more closely resembling that seen on the real fish. The input waveform was approximately correct for most of the relevant parameters, but inaccurately placed the minimum of the amplitude envelope at the nose. The recoil-corrected version had moved the minimum to a point slightly behind the head.

Chapter 4

Three-dimensional panel method

4.1 Introduction

The three-dimensional panel method is in many ways very similar to the two-dimensional version. We are looking at high Reynolds number flow, and so may treat the fluid as inviscid except on the body and in the wake. Consequently, the continuity equation again reduces to Laplace's Equation for the velocity potential Φ

$$\nabla^2 \Phi = 0. \tag{4.1}$$

Our model is of an infinitely thin body, so Green's identity leads to a general solution in terms of vortex line segments of unknown strength, which are then calculated via the boundary conditions.

The problem is solved in a frame of reference, $OXYZ$, in which the fluid is at rest at infinity. The boundary conditions are similar to those in the two-dimensional model, as given by the list in Section 2.1. The first three conditions are identical: no flow far from the body, no flow through the body, and continuous pressure across the wake. The Helmholtz Theorems still apply so that the circulation around any closed material loop is constant.

The body is divided up into a number of panels. A "bound" vortex ring of initially unknown strength is attached to each panel. The boundary conditions of the flow are used to construct a set

of equations for the unknown strengths. We are modelling an unsteady problem: the body moves through the fluid, and so the strengths of the bound vortex rings vary with time.

The Kutta Condition, which is used to force fluid to flow smoothly off the trailing edge of the body, is enforced in a different way to the method used in two dimensions: the details are deferred until Section 4.2.5. Essentially, the trailing edge vortex rings are shed into the wake. From then on, each of those (wake) vortex rings represents a given material loop, and therefore must have a constant strength. In other words, the strengths of the rings in the wake do not decay.

Having established, at each time step, the strength of all the vortex rings on the body, we are able to calculate the distribution of the pressure jump across the body, which is then used to calculate the other required quantities.

4.2 The three-dimensional panel method

This section describes the three-dimensional method in full. Again most of the detail can be found in Katz and Plotkin (1991), but the work of Konstadinopoulos *et al.* (1981) was also useful.

4.2.1 Geometry and non-dimensionalisation of the model

The body is assumed to be infinitely thin and rectangular with (dimensional) chordlength \hat{l}_X and span $2\hat{l}_Y$. The non-dimensionalisation is the same as in the two-dimensional model, as described in Section 2.3.1. Lengths are non dimensionalised with respect to \hat{l}_X , and velocities with respect to \hat{U}_0 , a characteristic speed of the overall motion of the body. The non-dimensional pressure is again given by

$$p = \hat{p} / \left(\hat{\rho} \hat{U}_0^2 \right) \quad (4.2)$$

and the time by

$$t = \hat{U}_0 \hat{t} / \hat{l}_X. \quad (4.3)$$

The aspect ratio of the plate is the square of the span divided by the surface area. For a rectangular plate then the aspect ratio is $2\hat{l}_Y / \hat{l}_X = 2l_Y$, the non-dimensional span.

The body is modelled as inextensible, and spanwise deformations are neglected. Given that we have symmetry in the $Y = 0$ plane, the problem is solved in the halfspace $Y \geq 0$. Thus, although the Lagrangian body coordinates (s_X, s_Y) lie in the ranges $(0, l_X)$ and $(-l_Y, l_Y)$ respectively, we only use $s_Y \geq 0$ in our calculations. The neglect of spanwise deformations means that the description of the motion in three dimensions is identical to the two-dimensional model. As in Chapter 3 we deal with the motion in two parts. Firstly there is an imposed motion: usually a constant forward swimming together with some transverse oscillation such that

$$Z = h_z(s_X, t). \quad (4.4)$$

We may choose any form for $h_z(s_X, t)$, and in particular have used the motion of a flat plate to test the model, and a description of a travelling wave of varying amplitude moving backwards along the body as an approximation to swimming. As the plate is inextensible there is some motion $h_x(s_X, t)$ in the X -direction resulting from the sideways motion. For a flat plate, $h_x(s_X, t)$ may be expressed analytically, whereas for a deforming plate we must rearrange the inextensibility condition

$$\left(\frac{\partial h_x}{\partial s_X}\right)^2 + \left(\frac{\partial h_z}{\partial s_X}\right)^2 = 1, \quad (4.5)$$

and integrate to obtain

$$h_x(s_X, t) = \int_0^{s_X} \left(1 - \left(\frac{\partial h_z}{\partial s'_X}\right)^2\right)^{\frac{1}{2}} ds'_X. \quad (4.6)$$

This integration is done numerically.

Secondly, in the modelling of swimming it is also necessary to include the recoil correction (R, Θ) . The description and calculation of the recoil follows that in two dimensions as described in Section 3.3. Consequently (for motion involving constant forward swimming speed U) the position of the body in the frame of reference where the fluid is at rest at infinity is given by

$$X = -Ut + h_x \cos \Theta - h_z \sin \Theta, \quad (4.7)$$

$$Z = R + h_z \cos \Theta + h_x \sin \Theta. \quad (4.8)$$

The relevant derivatives with respect to s_X and t are easily obtained (and are given by Equations (3.14) to (3.15b)). Furthermore it is clear that when $R \equiv \Theta \equiv 0$ we have the required simplified expressions

$$X = -Ut + h_x \quad (4.9)$$

$$Z = h_z, \quad (4.10)$$

etc.

4.2.2 Discretisation of the body and the wake

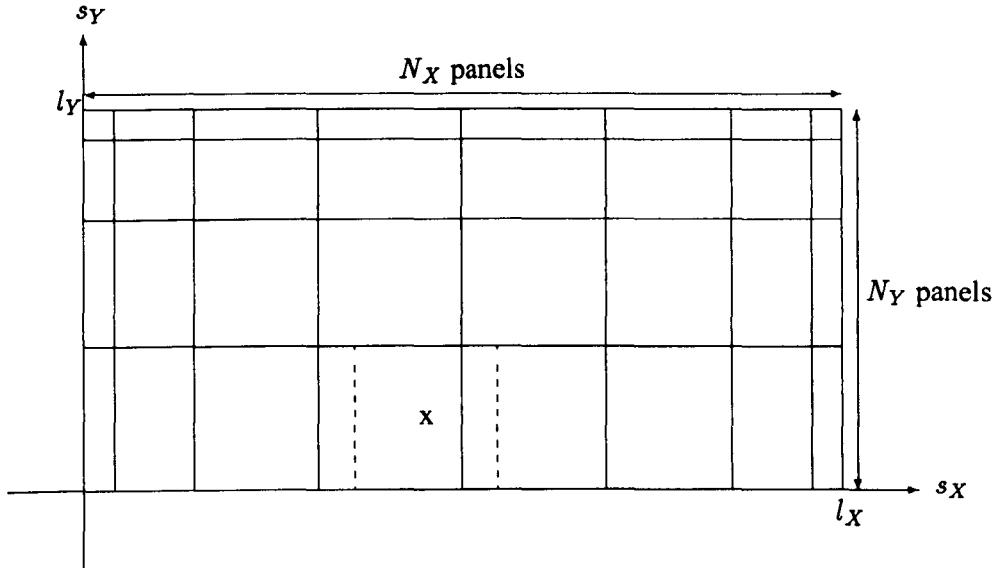


Figure 4.1: An example of variable panelling, with $N = 32$. The dashed lines show the position of a single vortex ring, with the cross marking the collocation point.

The half-body is divided up into N rectangular panels: N_X in the chordwise direction, and N_Y in the spanwise direction. It is useful to index the panels in two different ways. Firstly, we may refer to the (i, j) 'th panel, using $i = 1..N_X$ to count "rows" in the s_X -direction, and $j = 1..N_Y$ to count "columns" in the s_Y -direction. Alternatively it is sometimes appropriate to refer to the I 'th panel where a capital subscript is used to denote indexing over the whole body, with $I = 1..N$ so that

$$I = (i - 1)N_Y + j. \quad (4.11)$$

From the two-dimensional work it is expected that cosine spacing will be preferred to uniform panels, and this can easily be checked. Fig. 4.1 shows an example of variable panelling with $N = 32$. It can be seen from Fig. 4.1 that whilst the panel lengths in the chordwise direction are calculated as in the two-dimensional method, the spanwise panels must take account of the

symmetry so that the widest panels are at the centre of the body $s_Y = 0$. The i 'th chordwise panel node is given by

$$s_{X_i} = \frac{l_X}{2} \left(1 - \cos \frac{i\pi}{N_X} \right), \quad i = 0..N_X, \quad (4.12)$$

and the j 'th (spanwise) panel node by

$$s_{Y_j} = l_Y \sin \frac{j\pi}{N_Y}, \quad j = 0..N_Y. \quad (4.13)$$

The dimensions of the (i, j) 'th panel are given by

$$\begin{aligned} \Delta l_{X_i} &= s_{X_i} - s_{X_{i-1}} \\ &= \frac{l_X}{2} \left(\cos \frac{(i-1)\pi}{N_X} - \cos \frac{i\pi}{N_X} \right), \quad i = 1..N_X, \end{aligned} \quad (4.14)$$

and

$$\begin{aligned} \Delta l_{Y_j} &= s_{Y_j} - s_{Y_{j-1}} \\ &= l_Y \left(\sin \frac{j\pi}{N_Y} - \sin \frac{(j-1)\pi}{N_Y} \right), \quad j = 1..N_Y. \end{aligned} \quad (4.15)$$

A vortex ring of strength Γ_i is placed on each panel in such a way that the front segment of the vortex ring is along the quarter-chord of the panel. The associated collocation point, where the boundary condition is satisfied, is at the centre of the vortex ring; that is at the three-quarter chord of the panel, but midway between the chordwise vortex lines (which do coincide with the panel edges). This is based on the same reasoning as in the two-dimensional case, and it allows us to assume that the two-dimensional Kutta Condition is automatically satisfied. The variable panel setup shown in Fig. 4.1, includes the positioning of a vortex ring in dashed lines, and its collocation point. Konstadinopoulos *et al.* (1981) comment that the vortex ring segments should not line up with the trailing edge; nor indeed with any edge at which vorticity is being shed. Our model assumes that vorticity is shed from the trailing edge only.

4.2.3 The induced velocity due to a finite vortex line segment.

We require an expression for the velocity induced by a finite length vortex segment of constant strength. Take the vortex line segment AB as shown in Fig. 4.2, together with the field point P . Suppose the vortex line is of strength Γ with the end-points having position vectors $\mathbf{r}_1, \mathbf{r}_2$ relative

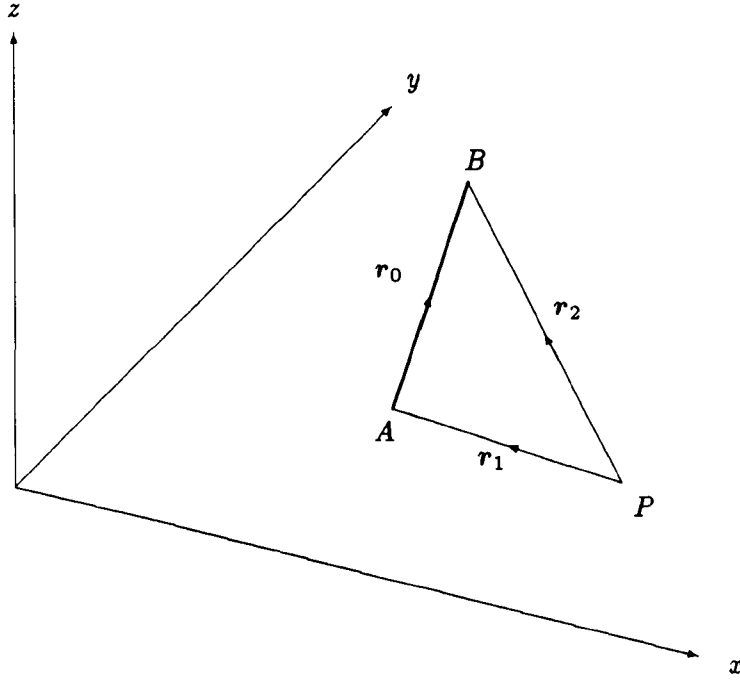


Figure 4.2: Sketch of a finite length vortex line segment, AB . In order to calculate the induced velocity at P we require the position vectors of the line segment's end-points relative to P : $\mathbf{r}_1, \mathbf{r}_2$. The vortex line segment has strength Γ , defined positive for clockwise rotations about the vector \mathbf{r}_0 .

to P . Let $\mathbf{r}_0 = \mathbf{r}_2 - \mathbf{r}_1$. Positive Γ is defined such that it generates a clockwise rotation about the vector \mathbf{r}_0 . From the Biot-Savart Law we can obtain an expression for the induced velocity at P in terms of the quantities defined above (see Katz and Plotkin, 1991, p.48):

$$\mathbf{q} = \frac{\Gamma}{4\pi} \frac{\mathbf{r}_1 \times \mathbf{r}_2}{|\mathbf{r}_1 \times \mathbf{r}_2|^2} \mathbf{r}_0 \cdot (\hat{\mathbf{r}}_1 - \hat{\mathbf{r}}_2). \quad (4.16)$$

As usual care is required if the field point P is close to the vortex line segment. More precisely, we must check if the perpendicular distance d ,

$$d = \frac{|\mathbf{r}_1 \times \mathbf{r}_2|}{|\mathbf{r}_0|}, \quad (4.17)$$

from the vortex line segment (extended to infinite length) to P is smaller than some vortex core radius, r_c . The options here are much the same as those in two dimensions. Katz and Plotkin (1991,

p.293) suggest a vortex core as small as the computer truncation error coupled to a test for r_1 , or r_2 , or $|\mathbf{r}_1 \times \mathbf{r}_2| < r_c$, with the induced velocity set to zero inside the core. We used a Rankine vortex, with solid body rotation inside the core. Following Katz and Plotkin we set a very small core radius.

There is also the question of symmetry. Occasionally the induced velocity due to a segment alone, not including its image in the X - Z plane, is required. However usually it is helpful to include the effect of a vortex line's image. Consider the same vortex line as before, with end-points

$$\mathbf{r}_a = (x_a, y_a, z_a), \quad (4.18)$$

$$\mathbf{r}_b = (x_b, y_b, z_b). \quad (4.19)$$

Using prime to denote the image quantities, the image vortex has end-points

$$\mathbf{r}'_a = (x_a, -y_a, z_a), \quad (4.20)$$

$$\mathbf{r}'_b = (x_b, -y_b, z_b), \quad (4.21)$$

and strength

$$\Gamma' = -\Gamma. \quad (4.22)$$

The corresponding velocity \mathbf{q}' is obtained from the primed version of equation (4.16), and the total induced velocity at P is the sum of \mathbf{q} and \mathbf{q}' .

4.2.4 Forming the boundary condition equations

The position of the body is found from the displacement functions, as seen in Section 4.2.1. Again, the main task of the basic panel method is to form the set of linear equations for the unknown vortex-ring strengths.

We need to construct the matrix of influence coefficients A , where the element A_{IJ} is the normal component of the induced velocity at the I 'th collocation point due to the J 'th vortex ring, assuming that the vortex ring has strength unity. To explain how this is done, it is important to point out that all the vortex-line segments on the body are part of two adjacent vortex rings, (except those around the edge of the body). So it is most efficient to calculate the induced velocity due to each vortex line segment only once and ensure that its effect is included in the correct elements of A .

We label the panel nodes (k, l) , with $k = 0..N_X$ and $l = 0..N_Y$, see Fig. 4.1. Then we let $v_{I,(k-1,l-1)}^C$ be the induced velocity at the I 'th collocation point due to the vortex segment with the end-points given by nodes $(k-1, l-1)$ and $(k, l-1)$, and its image. We let $v_{I,(k-1,l-1)}^S$ be the induced velocity at the I 'th collocation point due to vortex line segment with end-points $(k-1, l-1)$ and $(k-1, l)$, and its image. The superscripts C and S indicate that a segment has direction in the chordwise or spanwise direction respectively. Then the (I, J) 'th element of the matrix of influence coefficients A is given by

$$\begin{aligned} A_{IJ} &= A_{I,(k,l)} \\ &= \left[-v_{I,(k-1,l-1)}^C + v_{I,(k-1,l)}^C + v_{I,(k-1,l-1)}^S - v_{I,(k,l-1)}^S \right] \cdot n_I. \end{aligned} \quad (4.23)$$

Note that the term $v_{I,(k-1,l)}^C$ also appears in the equivalent expression for $A_{I,J+1}$.

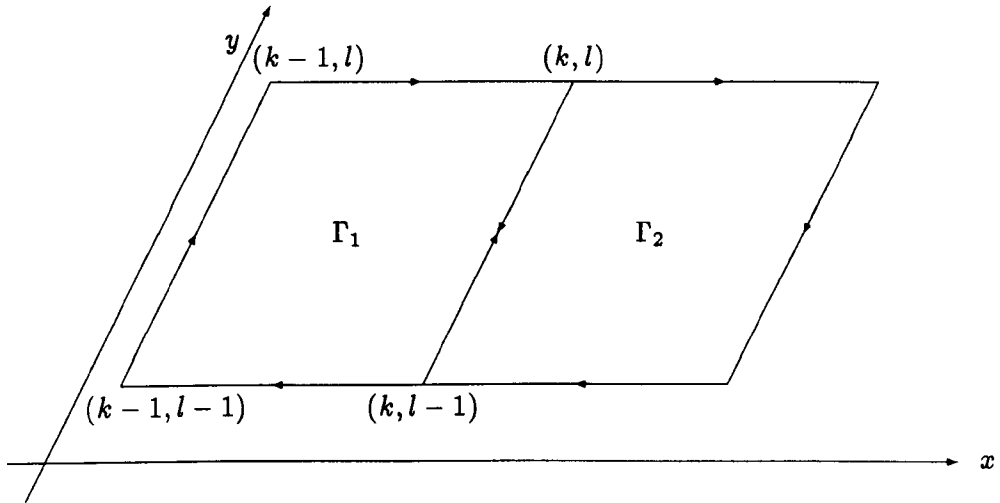


Figure 4.3: Two adjacent rings of strengths Γ_1 and Γ_2 coincide at the vortex line segment connecting the nodes $(k, l-1), (k, l)$: the strength of this segment is $\Gamma_2 - \Gamma_1$.

The right hand side of the boundary condition equations is the normal component of the fluid velocity at each collocation point. In general this is the normal component of the velocity of the body with the normal component of the velocity induced by the wake subtracted. The resulting set

of N linear equations is

$$\sum_{J=1}^N \Gamma_J A_{IJ} = (\mathbf{V}_b - \mathbf{V}_w)_I \cdot \mathbf{n}_I, \quad I = 1..N \quad (4.24)$$

where \mathbf{V}_b , \mathbf{V}_w and \mathbf{n} are the velocity of the surface, the velocity induced by the wake, and the unit normal respectively. The subscript I is to indicate that these quantities are calculated at the I 'th collocation point. (Note also that at $t = 0$, $\mathbf{V}_w = 0$.) There are no real problems associated with solving this set of equations.

4.2.5 The unsteady Kutta condition: shedding vortex rings

In two dimensions we use the Kelvin Condition to provide an extra equation that allows us to solve for the strength of the latest shed vortex at the same time as calculating the bound vortex strengths. In three dimensions the Kelvin Condition is automatically satisfied by the vortex ring formulation, and cannot be used to calculate the strength of the shed vortex rings. Instead we need an unsteady form of the Kutta Condition.

Konstadinopoulos *et al.* (1981, p.486) describe the unsteady Kutta Condition as “all the vorticity generated along the sharp edges where the steady-state Kutta Condition is enforced is shed”. Our model assumes that vorticity is shed from the trailing edge only. So, at each time step, as a new row of wake vortex rings is generated at the trailing edge, they have the strengths of the corresponding trailing edge bound vortex rings from the previous time step. Katz and Plotkin (1991) describe the same method, and also point out that in the steady case this reduces the wake model to horseshoe vortices as required because neighbouring rings (in the direction of motion) are all the same strength, causing the individual spanwise vortex segments to cancel out. Furthermore (as in two dimensions) the wake is force-free so that it must deform according to the local fluid velocity.

Fig. 4.4 shows the first three time steps as the wake is generated at the trailing edge of a flat plate moving to the left at speed U . Initially in (a), at $t = \Delta t$, there are no wake panels. The aft vortex segments of the trailing edge vortex rings represent the starting vortex.

At $t = 2\Delta t$ the new position of the body is calculated and a row of wake vortex elements produced at the trailing edge. These wake vortex rings have strengths equal to the strengths of the vortex

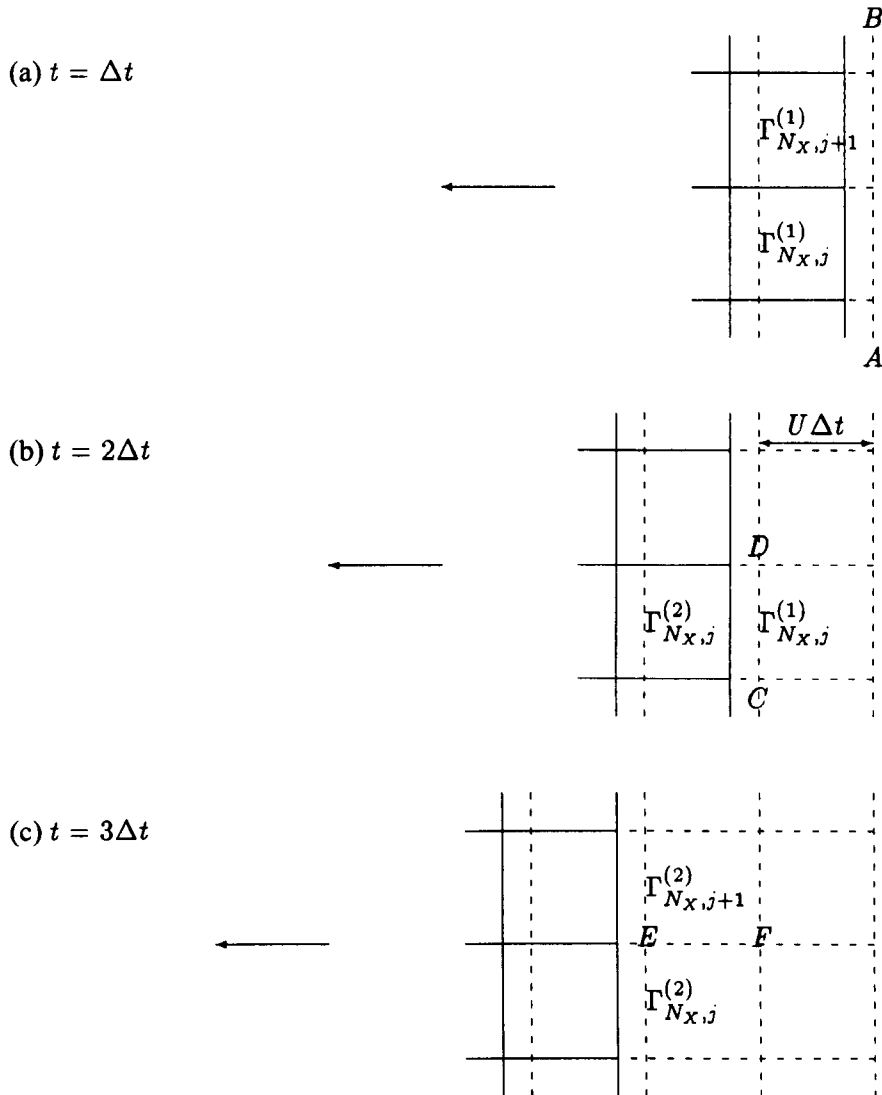


Figure 4.4: Schematic representation of vortex rings initially attached to the body and subsequently shed from the trailing edge. Solid lines represent the panels, dashed lines the actual vortex line segments. The body is moving to the left with speed U , and we assume a constant time step Δt . The line AB and its continuation represents the starting vortex. The vortex line segment CD has strength $\Gamma_{N_x, j}^{(1)} - \Gamma_{N_x, j}^{(2)}$, and the vortex line segment EF has strength $\Gamma_{N_x, j}^{(2)} - \Gamma_{N_x, j+1}^{(2)}$.

rings that were previously on the body, along the trailing edge. The strength of the vortex segment CD along the trailing edge is given by $\Gamma_{N_X,j}^{(1)} - \Gamma_{N_X,j}^{(2)}$. The last procedure of each time step is to advect all the wake vortex nodes according to the local fluid velocity. The total induced velocity at each node $\mathbf{X}_{m,j}^{(k)}$ in the wake vortex lattice is calculated: $V_{m,j}^{(k)}$, where $m = 1..N_w$ with N_w being the number of rows of wake vortex rows, and $j = 0..N_Y$ as with the nodes on the bound vortex lattice. The nodes are advected as in the two-dimensional procedure:

$$\mathbf{X}_{m,j}^{(k+1)} = \mathbf{X}_{m,j}^{(k)} + \Delta t V_{m,j}^{(k)}. \quad (4.25)$$

At the next time step, $t = 3\Delta t$, the new position is calculated and a new row of wake vortex rings shed from the trailing edge. The situation at this time is shown in Fig. 4.4(c). Note that the strength of the vortex segment EF is given by $\Gamma_{N_X,j}^{(2)} - \Gamma_{N_X,j+1}^{(2)}$. At the end of each time step the rollup procedure is repeated for the whole wake.

There are two main difficulties associated with the wake model. The shedding of vorticity at the trailing edge means that at each time step the wake increases in size. This causes wake-induced velocity calculations to become increasingly time-consuming. The solution to this difficulty is simply to truncate the wake at “some large distance” from the tail of the fish. This is done on the basis that wake elements which are sufficiently far away have a negligible effect on the flow around the fish. We have not found a satisfactory equivalent of the point vortex amalgamation procedure used in two dimensions.

The second difficulty is that the numerical approximation to the wake structure, and its motion, ultimately results in some non-physical behaviour. For example, the vortex sheet may intersect itself. However, this is not as serious as it might appear. Such problems tend to occur in the “older” portions of the wake, which are by then far from the tail of the fish. Furthermore the large-scale behaviour, and far-field influence of the wake is not greatly affected.

4.3 Calculating the pressure distribution

Again, following the two-dimensional model, we write down the unsteady Bernoulli equation and replace Φ in terms of the calculated vortex ring strengths. The final equation, Equation (4.37) is essentially the same as that found in Katz and Plotkin (1991).

Initially the argument is identical to that in two dimensions. The unsteady Bernoulli Equation in a frame of reference where the fluid is at rest far from the body is (Equation (2.23)):

$$\frac{P_\infty - P}{\rho} = \frac{1}{2} |\nabla \Phi|^2 + \frac{\partial \Phi}{\partial t}. \quad (4.26)$$

Given that we need to calculate the pressure jump at the moving collocation points we make the same coordinate transformation as described in the previous chapter. This brings us to the same equation for the pressure jump in terms of quantities in the moving frame (equation (2.30)):

$$\frac{\Delta P}{\rho} = \frac{1}{2} |\nabla \phi_1^+|^2 - \frac{1}{2} |\nabla \phi_1^-|^2 + \mathbf{u} \cdot (\nabla \phi_1^+ - \nabla \phi_1^-) + \frac{\partial}{\partial t} (\phi_1^+ - \phi_1^-) \quad (4.27)$$

where superscripts + and - are used to denote above and below the plate respectively, $\mathbf{u} = -\mathbf{V}_b$ is the velocity of the body in the global frame, and ϕ_1 is related to Φ , the potential in the global frame, by (equation (2.29)):

$$\nabla_X \Phi = \nabla_x \phi_1. \quad (4.28)$$

We need to write equation (4.27) in terms of the bound vortex strengths. To do so, we need the following results.

1.

$$\phi_1 = \phi_b + \phi_w \quad (4.29)$$

2.

$$\phi_w^+ = \phi_w^- \quad (4.30)$$

3.

$$\nabla \phi_b^\pm = \mathbf{V}_m \pm \frac{1}{2} \Delta \mathbf{V}, \quad (4.31)$$

where \mathbf{V}_m is the velocity due to the bound vortex sheet excluding the effect of the local velocity jump, so that

$$\begin{aligned} \nabla \phi_b^+ - \nabla \phi_b^- &= \left(\mathbf{V}_m + \frac{1}{2} \Delta \mathbf{V} \right) - \left(\mathbf{V}_m - \frac{1}{2} \Delta \mathbf{V} \right) \\ &= \Delta \mathbf{V}. \end{aligned} \quad (4.32)$$

4. The potential on the body is obtained by integrating the vortex strength along the body, starting from the leading edge. Representing this in terms of a summation of the vortex line strengths gives

$$\frac{\partial}{\partial t} (\phi_b^+ - \phi_b^-) = \frac{\partial \Gamma_{i,j}}{\partial t}. \quad (4.33)$$

The other vortex line segments all cancel out as we are now dealing with vortex rings.

- 5.

$$\begin{aligned} \frac{1}{2} |\nabla \phi_1^+|^2 - \frac{1}{2} |\nabla \phi_1^-|^2 &= \frac{1}{2} |\nabla \phi_b^+ + \nabla \phi_w^+|^2 - \frac{1}{2} |\nabla \phi_b^- + \nabla \phi_w^-|^2 \\ &= (\mathbf{V}_m + \mathbf{V}_w) \cdot \Delta \mathbf{V}, \end{aligned} \quad (4.34)$$

as in the two-dimensional case.

The velocity jump follows by the same argument as before but now involves components in two directions. Since the current method uses rectangular panels on a rectangular body this can be done easily in terms of components in the s_X -direction and the s_Y -direction.

Consider the (i, j) 'th panel together with the associated vortex ring, strength $\Gamma_{i,j}$. The tangent along the body in the streamwise sense is τ_{sx} , and in the spanwise sense is τ_{sy} . The collocation point is at the centre of the vortex ring, and the panel is of length Δl_{X_i} , and width Δl_{Y_j} . (In terms of the diagram in Fig. 4.1 the tangents are in the s_X - and s_Y -directions respectively, with the cross marking the collocation point.) Note that the calculation is done in terms of the dimensions of the panel, as opposed to the actual vortex ring.

The velocity jump is then given in Batchelor (1967) in terms of the vector strength density γ and the unit normal \mathbf{n} as $\gamma \times \mathbf{n}$. In terms of the tangent vectors and the vortex ring strengths we approximate the local strength as

$$\gamma = \left[\frac{\Gamma_{i,j} - \Gamma_{i-1,j}}{\Delta l_{X_i}} \right] \tau_{sy} + \left[\frac{\Gamma_{i,j-1} - \Gamma_{i,j+1}}{\Delta l_{Y_j}} \right] \tau_{sx}. \quad (4.35)$$

Hence we can write

$$\begin{aligned} \Delta \mathbf{V} &= \gamma \times \mathbf{n} \\ &= \left[\frac{\Gamma_{i,j} - \Gamma_{i-1,j}}{\Delta l_{X_i}} \right] \tau_{sx} + \left[\frac{\Gamma_{i,j-1} - \Gamma_{i,j+1}}{\Delta l_{Y_j}} \right] \tau_{sy}. \end{aligned} \quad (4.36)$$

Substituting all the relevant terms into equation (4.27) gives the final expression for the pressure jump at the (i, j) 'th collocation point:

$$\Delta P_{i,j} = \left[(\mathbf{V}_m + \mathbf{V}_w - \mathbf{V}_b) \cdot \left(\left[\frac{\Gamma_{i,j} - \Gamma_{i-1,j}}{\Delta l_{X,i,j}} \right] \boldsymbol{\tau}_{sx} + \left[\frac{\Gamma_{i,j-1} - \Gamma_{i,j+1}}{\Delta l_{Y,j}} \right] \boldsymbol{\tau}_{sy} \right) + \frac{\partial \Gamma_{i,j}}{\partial t} \right] \quad (4.37)$$

Having found the pressure distribution we can use it to calculate overall forces on the body, such as sideforce and thrust. Taking the sideforce to be in the Z -direction, and the thrust to be in the negative X -direction we have

$$L = \sum_{i=1}^{N_X} \sum_{j=1}^{N_Y} (\Delta P_{ij} \Delta l_{X_i} \Delta l_{Y_j}) \mathbf{n}_j \cdot \mathbf{k}, \quad (4.38)$$

$$T_X = - \sum_{i=1}^{N_X} \sum_{j=1}^{N_Y} (\Delta P_{ij} \Delta l_{X_i} \Delta l_{Y_j}) \mathbf{n}_j \cdot \mathbf{i}, \quad (4.39)$$

where \mathbf{i} and \mathbf{k} are unit vectors in the X and Z directions respectively.

4.4 The suction force

According to Robinson and Laurmann (1956), the spanwise component of the fluid velocity at the leading edge remains finite and so does not affect the suction force: the "velocity variation in the neighbourhood of the leading edge is effectively two-dimensional". Just as in two dimensions, moving to unsteady flow makes no difference and we retain the two-dimensional steady flow result.

We assume then that at any s_Y -station along the leading edge the flow can be thought of as two-dimensional, and the local suction force calculated accordingly. We further assume the suction at a panel to be constant over the whole of that panel.

It is then a simple matter to obtain the total suction force by summing the contribution due to each of the leading edge panels and their images.

At the j 'th spanwise panel, ($j = 1..N_Y$), the suction force is given by

$$(T_S)_j = -\pi \rho C_j^2 \quad (4.40)$$

where C_j is

$$C_j = \lim_{s_X \rightarrow 0} (\nabla \Phi \cdot \boldsymbol{\tau}) \sqrt{s_X} \quad (4.41)$$

With C_j approximated in the same way as in two dimensions, the full expression for the total suction force is

$$T_S = 2\pi\rho \sum_{j=1}^{N_Y} \Delta l_Y C_j^2, \quad (4.42)$$

with

$$C_j = \sqrt{a\Delta l_{x_0}} \left(\frac{\Gamma_{0,j}}{2\Delta l_{x_0}} + V_m + V_w \right). \quad (4.43)$$

Numerically, V_m is the induced velocity at the $(0, j)$ 'th collocation point due to all the bound vortex segments other than those making up the j 'th leading edge vortex ring. The term $a\Delta l_{x_0}$ approximates a small distance from the leading edge at which the tangential velocity is calculated. Following the results and discussion of the Section 2.6, we use $a = 0.402$ for variable panelling, and $a = 0.32$ for uniform panelling.

4.5 Motion of a flat plate

We start by testing the three-dimensional model against results for the lift and thrust on a rectangular flat plate. The aim is to show briefly that the method works. Rather than spending time detailing the effects of changes to N_X , N_Y , Δt , etc, in the context of motion of a flat plate we simply show that the method can be accurate and reliable. The reasoning behind this is that we know the choice of parameters, or even the choice between uniform and variable panelling to be affected by the geometry of a given problem. It is sufficient to note that experimentation with flat plate examples indicated that the solution improves with increasing number of panels, and that the number of time steps per period (for oscillatory motion) affects the results much as in the two-dimensional case. Additionally it appears from the pitching and heaving tests that matching the wake panel lengths to the body panel lengths (ie putting $U\Delta t \approx l_X/N$) helps in terms of producing a pressure jump distribution that tends to zero at the trailing edge. All these points are examined in more detail later.

4.5.1 Impulsively started flat plate

A rectangular flat plate (as described in Section 4.2.1) initially at rest is impulsively started at $t = 0$ so that it subsequently moves with speed $U = 1$. The plate is held at a constant angle of attack α .

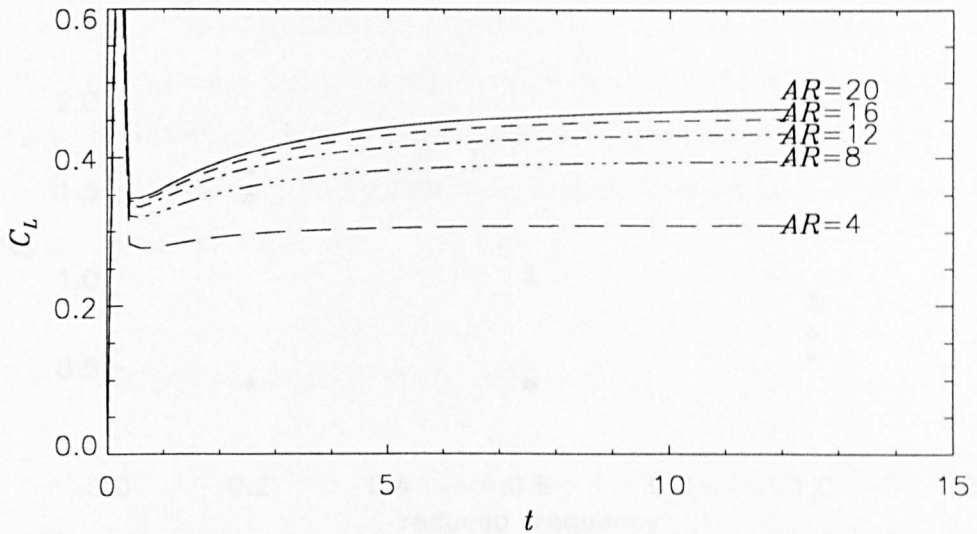


Figure 4.5: The effect of aspect ratio on the lift coefficient on an impulsively started rectangular flat plate held at a constant angle of attack $\alpha = 5^\circ$.

We are interested in the lift coefficient over early times of the motion, and in particular the effect of changing the aspect ratio $2l_Y$. Fig. 4.5 shows the variation in the lift coefficient $C_L = L/l_X l_Y$ against non-dimensional time. At large aspect ratio the graphs tend towards the two-dimensional result as required. As expected we obtain an initial drop in the lift followed by a gradual increase towards the steady state value. Comparison with a similar graph (Fig. 13.34) in Katz and Plotkin (1991, p.491) indicates that we have reasonable agreement between our method and that described in the book. We are able to conclude that in this simple case the method calculates the correct pressure distribution. Since we are looking at the lift on a plate at small angle of attack this test does not include any verification of the suction force calculation.

4.5.2 Pitching and heaving flat plate

We also briefly checked that the panel method agreed with previous work to calculate the mean thrust on a pitching and heaving flat plate moving with forward speed U . The lateral displacement of the plate is given by

$$h_z(s_X, t) = [A - iB(s - b)] e^{i\omega t}. \quad (4.44)$$

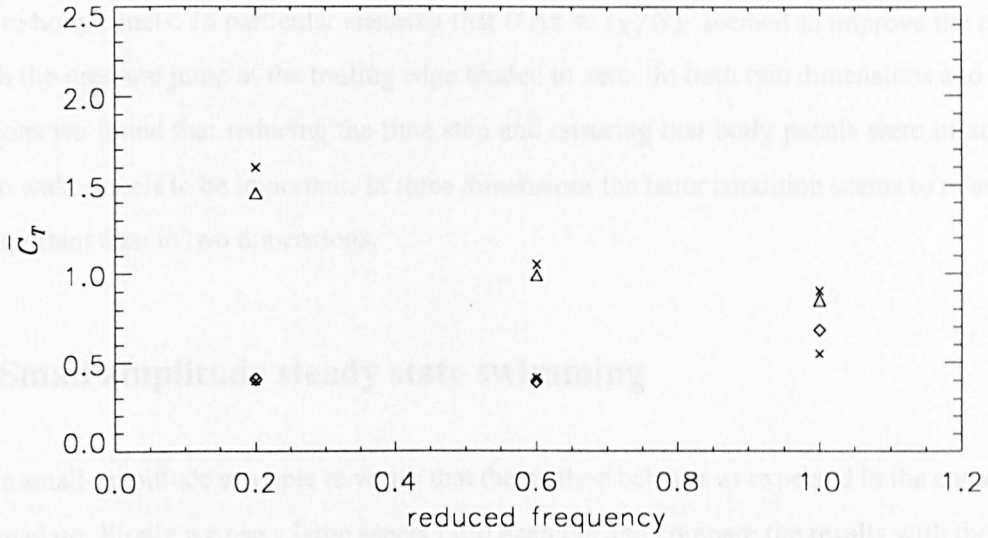


Figure 4.6: The mean thrust coefficient plotted against reduced frequency of pitching-heaving motion for a flat plate of aspect ratio 8, with pitching axis at the trailing edge. The crosses mark the data read from the graph in Fig. 6(c), Chopra (1974). The upper points (triangles) are for $\theta = 0$, with the lower points (diamonds) plotting $\theta = 0.8$.

Chopra (1974) presented both mean thrust and efficiency against the reduced frequency for aspect ratios $AR = 4$, $AR = 6$ and $AR = 8$, and with pitching axes at four different locations in each case. This was done for five different values of Lighthill's feathering parameter $\theta = UB/A\omega$.

Fig. 4.6 plots the mean thrust coefficient,

$$\bar{C}_T = \frac{\overline{(\hat{T}_X)}}{\frac{1}{2}\hat{\rho}(\hat{\omega}\hat{A})^2\hat{l}_X(2\hat{l}_Y)}, \quad (4.45)$$

against reduced frequency at $\theta = 0$ and $\theta = 0.8$ for a plate of aspect ratio $AR = 8$ and with pitching axis at the trailing edge ($b = l_X$). The crosses indicate the results from Chopra (1974). The three upper points (triangles) are for $\theta = 0$, with the three lower points (diamonds) corresponding to $\theta = 0.8$. The agreement is reasonable, and in particular confirms that the method for calculating the suction force is satisfactory. Indeed, when $\theta = 0$ the thrust is entirely due to suction. The results are of course qualitatively similar to those of Lighthill (1970) (see Fig. 2.14).

In obtaining the agreement shown in Fig. 4.6 we found (as expected) that the quantity $T/\Delta t$ was

important in achieving a good result; but that also it is important to have wake panels of similar lengths to body panels. In particular ensuring that $U\Delta t \approx l_X/N_X$ seemed to improve the extent to which the pressure jump at the trailing edge tended to zero. In both two dimensions and three dimensions we found that reducing the time step and ensuring that body panels were of similar length to wake panels to be important. In three dimensions the latter condition seems to relatively more important than in two dimensions.

4.6 Small amplitude steady state swimming

We use a small-amplitude example to verify that the method behaves as expected in the context of a waving plate. Firstly we use a large aspect ratio example and compare the results with the two-dimensional method. Secondly we examine the effect of changing the number and distribution of panels, and the time step.

In both cases that follow (Sections 4.6.1 and 4.6.2) the parameters governing the lateral deformation of the plate

$$h_z(s_X, t) = \Re \left\{ \left[A e^{\alpha s_X} - i B (s_X^\beta - b) \right] e^{i(k s_X - \omega t + \xi)} \right\} \quad (4.46)$$

are given in Table 4.1.

A	α	B	β	b	k	ω	ξ
0.005	0.0	0.012	1.0	0.0	2π	$5\pi/2$	0.0

Table 4.1: Table of parameter values for the simulations in Sections 4.6.1 and 4.6.2. The wave parameters are set up such that one wavelength is equal to the body length, with the wave speed being 5/4 times the forward swimming speed. The amplitude envelope is set to be linearly increasing from the minimum at the nose to the maximum at the tail.

4.6.1 Large aspect ratio

Using the motion parameters given in Table 4.1 we compare the three-dimensional method with the two-dimensional method. The three-dimensional simulation was for a plate of aspect ratio

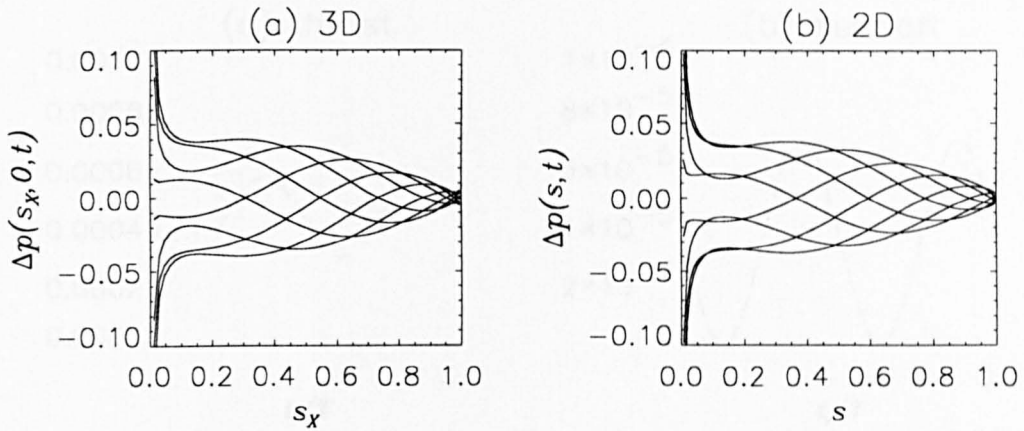


Figure 4.7: Comparison of the pressure distribution along (a) the centreline of a large aspect ratio waving plate with that on (b) a two-dimensional waving plate. In each case the variation in time is shown by overplotting the curves for various times. Exact agreement between two-dimensional and three-dimensional results is not expected.

$AR = 20$ ($l_Y = 10$) using $N_X = 60$, $N_Y = 20$ and $\Delta t = 0.02$. The two-dimensional “control” was done with $N = 100$, $\Delta t = 0.01$. We would not expect identical results because of small three-dimensional effects and because of the differences in the discretizations of the two plates. Nonetheless we should expect the results to agree qualitatively, and to be at similar orders of magnitude.

Fig. 4.7 compares the pressure distribution of the two-dimensional result with the the pressure distribution along the centreline of the three-dimensional plate. The results for the pressure distribution are directly comparable (because pressure is force per unit area). Fig. 4.7 indicates that the two methods do produce similar results.

Fig. 4.8 shows a comparison of the total hydrodynamic thrust, the suction force, the total hydrodynamic sideforce and the hydrodynamic moment taken about the mean position of the nose. In order to make a meaningful comparison between two and three dimensions the three-dimensional quantities are per unit length in the Y -direction (ie per unit span). The three dimensional results are shown with dotted lines; the two dimensional results being shown with dashed lines. Again the agreement reinforces our confidence that the three-dimensional method obtains results that agree with the two-dimensional method.

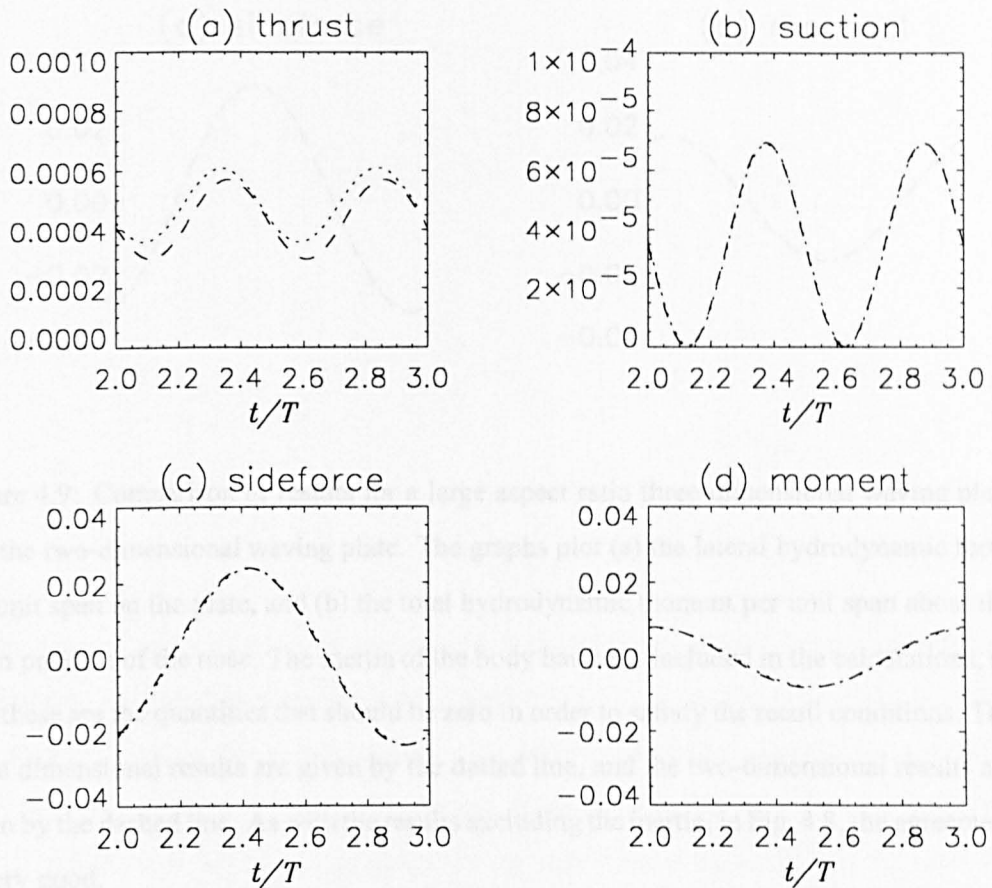


Figure 4.8: Comparison between results for large aspect ratio three-dimensional waving plate and the two-dimensional waving plate: (a) thrust, (b) suction force (c) sideforce (d) moment about mean position of the nose (“a fixed axis”). The quantities are all per unit span. The results for three dimensions are given by dotted lines, with those for two dimensions given by dashed lines. We should expect (and indeed obtain) reasonable agreement between the two methods for these quantities.

In order to compare quantities including the inertia of the body it is necessary to ensure that the total mass per unit span is the same in both examples. In the two-dimensional method this is taken to be $M_b = 0.065$ (from *saithe* data, see Chapter 3). In the three-dimensional method this requires a total mass $M_b = 1.3$. (This looks odd but is simply the results of using an aspect ratio that is unrealistically large in biological terms.) Fig. 4.9 plots the sideforce and hydrodynamic moment (both per unit span) with the body inertia included. Again we see that the results are similar. (Note

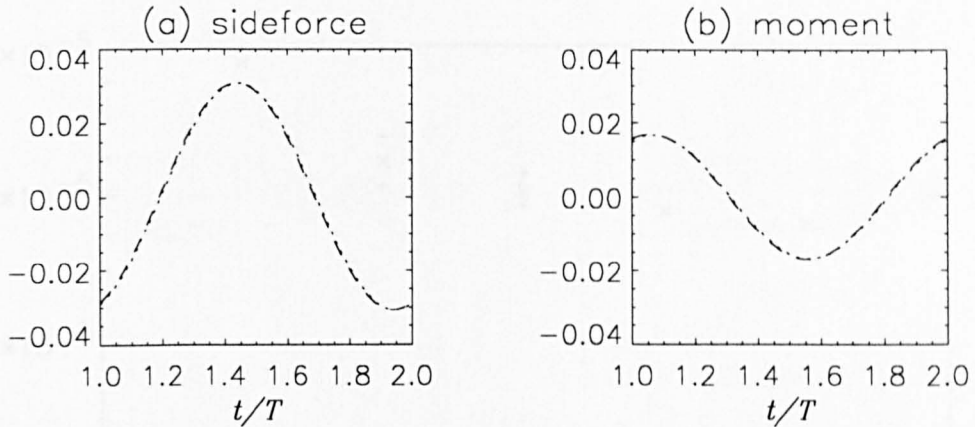


Figure 4.9: Comparison of results for a large aspect ratio three-dimensional waving plate and the two-dimensional waving plate. The graphs plot (a) the lateral hydrodynamic force per unit span on the plate, and (b) the total hydrodynamic moment per unit span about the mean position of the nose. The inertia of the body has been included in the calculations, so that these are the quantities that should be zero in order to satisfy the recoil conditions. The three dimensional results are given by the dotted line, and the two-dimensional results are given by the dashed line. As with the results excluding the inertia, in Fig. 4.8, the agreement is very good.

that no recoil correction has been included at this stage: it is the quantities plotted in Fig. 4.9 that are required to be zero by the recoil conditions.)

4.6.2 Varying the panel method parameters

Using the motion parameters listed in Table 4.1 we now look at the convergence of the method in terms of the mean thrust per unit span, and the pressure distribution along the centreline ($Y = 0$) of the body. In comparison with the previous section, the aspect ratio is smaller, and more “fish-like”, $AR = 0.2$ ($l_Y = 0.1$).

The aspect ratio is reduced from the previous example to a value of $AR = 0.2$ ($l_Y = 0.1$),

Fig. 4.10 shows the variation in $\bar{T}_X/(2l_Y)$ with an increasing number of chordwise panels (N_X). Note that the number of spanwise panels is fixed at $N_Y = 10$, with the time step Δt chosen so

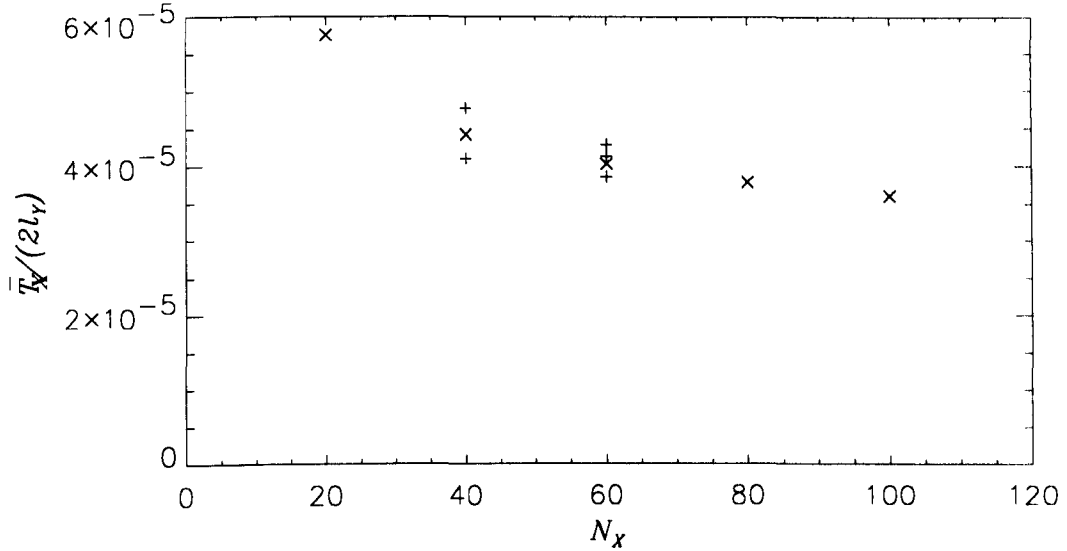


Figure 4.10: Graph of mean thrust per unit span against the number of chordwise panels used for that run. The number of spanwise panels is fixed at $N_Y = 10$. The crosses (x's) indicate the effect of increasing the number of chordwise panels with the time step chosen so that the body and wake panels are of similar dimension: $\Delta t \approx l_X / N_X$. The plus signs (at $N_X = 40$, $N_X = 60$) show the effect of changing the time step. In each case reducing Δt results in a lower mean thrust. At $N_X = 40$ we have plotted results for $\Delta t = 0.05, 0.025, 0.01$. At $N_X = 60$ we have plotted results for $\Delta t = 0.05, 0.03, 0.02, 0.01$.

that the wake panels are of similar dimension to the body panels, ie $\Delta t \approx l_X / N_X$. (These results are plotted with crosses.) There is convergence with increasing N_X . We assume that the result for $N_X = 100$ is the most accurate of those plotted. We also deduce from the graph that further increasing N_X (subject to $\Delta t \approx l_X / N_X$) would produce only marginal improvement.

Fig. 4.10 also plots results for varying the time step Δt for a fixed number of chordwise panels. This data is marked by plus-signs and was obtained for both $N_X = 40$ and $N_X = 60$. The values appear to improve with decreasing Δt (in the sense that they are closer to the result obtained for larger N_X). However, the full effect of changing Δt is not clear from this data (see below).

Fig. 4.11 shows the pressure distribution along the centreline of the plate as it varies over one period, for four different time steps (but fixed panel distribution $N_X = 60$, $N_Y = 10$). The curves for

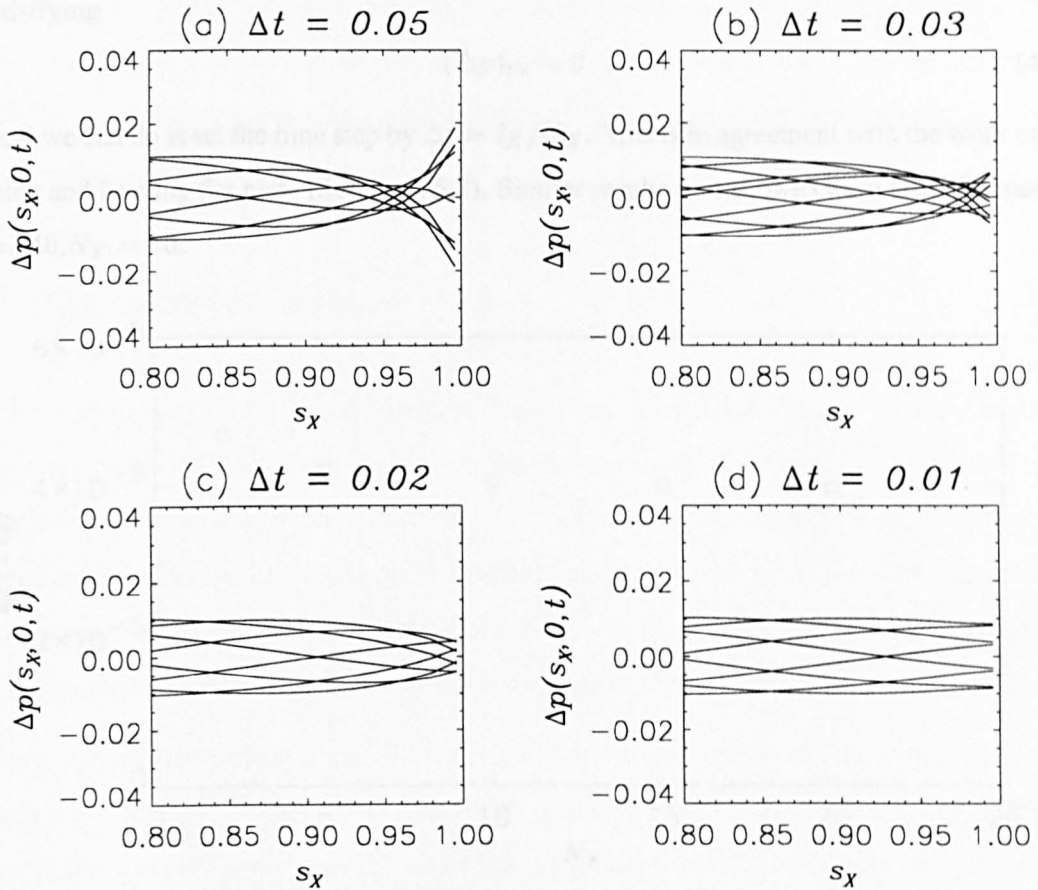


Figure 4.11: Graphs showing the pressure jump distribution along the centreline of the waving plate for four different examples; (the kinematic parameters are given by Table 4.1, $AR = 0.2$). The only parameter to be changed between the examples shown is the time step Δt . The variation in the pressure distribution over one period is indicated by superimposing results upon one another at different times. Our interest lies near the trailing edge, where the pressure jump should tend to zero. Evidently the time step size has some effect on our ability to obtain a pressure jump distribution that tends to zero near the trailing edge.

each example are superimposed on one another. We are interested in the shape of the curves near the trailing edge where we require the pressure jump to tend to zero. For “too large” a time step (Fig. 4.11(a),(b)) there is a minimum in the pressure jump before the trailing edge, with a large value actually at the trailing edge. In Fig. 4.11(d) the time step is apparently “too small” and the pressure jump does not decrease near the trailing edge. Fig. 4.11(c) seems to indicate that in terms

of satisfying

$$(\Delta p)_{t,e} = 0 \quad (4.47)$$

the best we can do is set the time step by $\Delta t \approx l_X/N_X$. This is in agreement with the work on the pitching and heaving flat plate (Section 4.5.2). Similar results (not shown) were also obtained for $N_X = 40, N_Y = 10$.

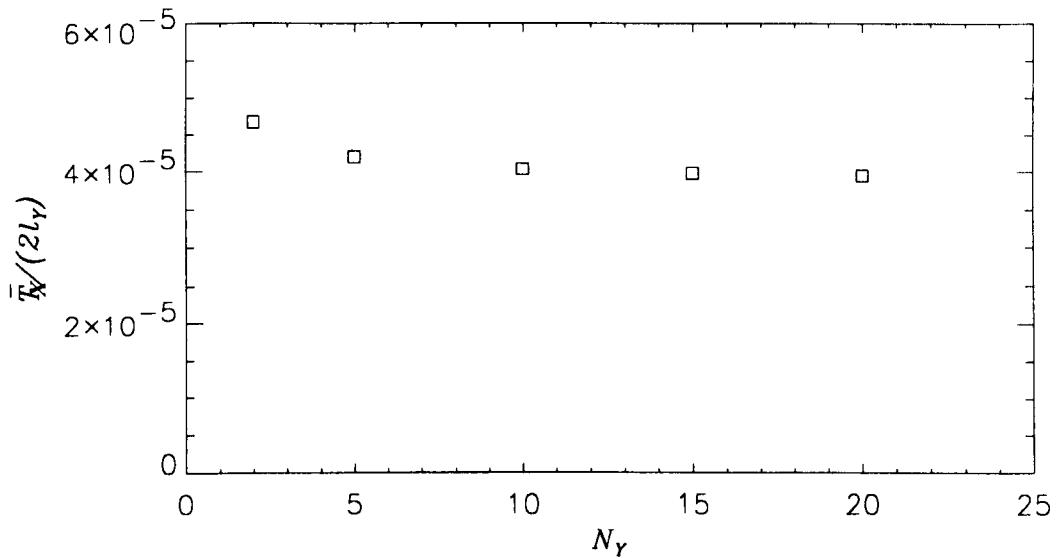


Figure 4.12: Graph of mean thrust per unit span against the number of spanwise panels. The results are for fixed $N_X = 60, \Delta t = 0.02$; kinematic parameters are given in Table 4.1, $AR = 0.2$.

Fig. 4.12 plots the variation in the mean thrust per unit span against the number of spanwise panels for the same small amplitude example. The results shown are for fixed $N_X = 60, \Delta t = 0.02$. We see that for a given number of chordwise panels the number of spanwise panels seems to have a small effect on the results. In this case, having reached $N_Y = 10$ there is seems to be little gain in further increasing the number of spanwise panels.

We also tested the effect of using variable panelling. We found that the results for the mean thrust suggested improved efficiency over uniform panelling. That is, we obtained similar results, and similar convergence with increasing N_X (the number of chordwise panels). However, the pressure jump distribution was found to have a large magnitude near the trailing edge rather than tending to

zero as required. The minimum in pressure was found to occur before the trailing edge, as in the graphs of Figs. 4.11(a),(b). Since we are able to obtain a more satisfactory result for the pressure distribution using uniform panelling we have not used variable panelling for the results that follow in the remainder of this thesis.

4.7 The recoil correction

Ideally the model should include the recoil correction (as discussed in Chapter 3), but we have not successfully integrated its calculation into our three-dimensional code. Historically speaking, it is not unusual for the recoil correction to be absent from the early stages of a hydrodynamic model of swimming. For example, Lighthill (1971) does not indicate how the recoil should be dealt with in his large-amplitude elongated body theory. Likewise Cheng *et al.* (1991) did not consider the recoil correction in their initial work on a vortex lattice panel method to study small amplitude swimming. However, in principle, the method of Section 3.3 for calculating the recoil correction in large-amplitude swimming should be independent of the details of the hydrodynamic calculation. That is, the method works in terms of the total lateral force and moment on the body, and is not “aware” of whether those quantities were obtained via a two-dimensional or three-dimensional hydrodynamic theory. It is disappointing that the three-dimensional model is not at the same stage of development as the two-dimensional model. Given the similarity between the results of the large aspect ratio example and the two-dimensional version (above) it seems likely that the problem is a practical “computing issue” (a bug). An alteration to the code that would eliminate this possibility is outlined in the Appendix.

4.8 A large amplitude example

We now move on to look at a large amplitude example. The parameters governing the motion are given in Table 4.2. The only difference between this example and the previous small-amplitude examples is that the amplitude parameters have been increased by a factor of ten.

Fig. 4.13 shows that the behaviour of the method at large amplitude is much as we have seen before.

AR	A	α	B	β	b	k	ω	ξ
0.2	0.05	0.0	0.12	1.0	0.0	2π	$5\pi/2$	0.0

Table 4.2: Table of parameter values for a large amplitude test. The wave parameters are set up such that one wavelength is equal to the body length, with the wave speed being 5/4 times the forward swimming speed. The amplitude envelope is set to be linearly increasing from the minimum at the nose to the maximum at the tail. In this case, the amplitude of the tail's motion is of the same order as that of a real fish.

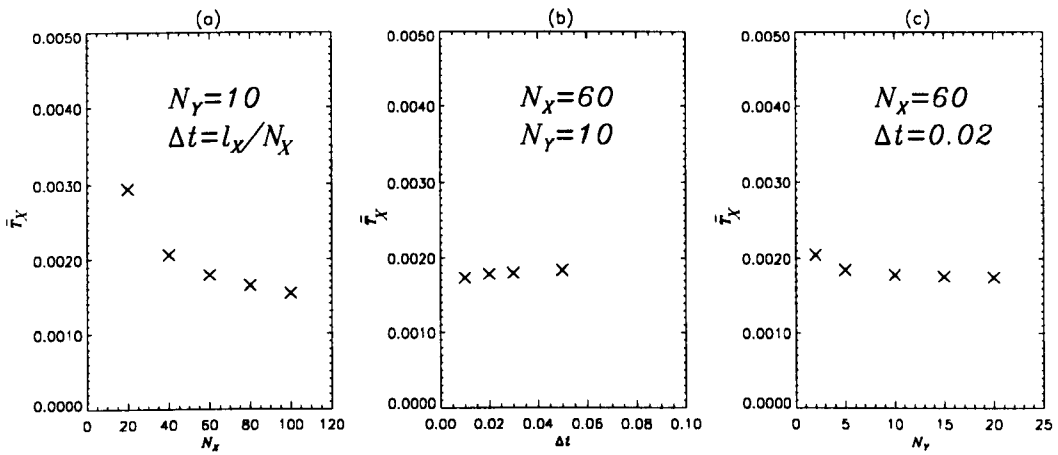


Figure 4.13: Graphs showing the mean thrust on the waving plate against variations in (a) the number of chordwise panels, (b) the time step, and (c) the number of spanwise panels.

Fig. 4.13(a) suggests that the method converges as the number of chordwise panels is increased. Note that for this result, the number of spanwise panels is held constant, whilst the time step is adjusted along the usual lines of having $\Delta t \approx l_x / N_x$. Fig. 4.13(b) shows the effect of changing the time step for a given number of panels. In terms of calculating the mean thrust it is evident that the time step does not have a great effect. However, the effect (discussed in Section 4.6.2) of the time step on the pressure jump near the trailing edge remains (data not shown). Finally Fig. 4.13(c) plots the effect of increasing the number of spanwise panels for a given number of chordwise panels and the corresponding time step. As with small amplitude it is apparent that initially some improvement is obtained with increasing N_y , but that the effect is not great.

We now move on to look at some time dependent results associated with the current example (as

described in Table 4.2). The results that follow are taken from two simulations: A and B. In these two cases the program was started using a relatively large time step, Δt_0 . This time step was retained over several periods (up to time $t = t_1$), after which it was replaced by a smaller time step Δt_1 . This small time step was chosen according to the conclusions we had previously reached regarding size of the time step (see above).

	N_X	N_Y	Δt_0	Δt_1	t_1
A	100	10	0.1	0.01	$10T$
B	40	15	0.1	0.025	$5T$

Table 4.3: Table of panel method parameter values for two large amplitude simulations. The parameters describing the details of the geometry are given in Table 4.2. In these two examples the time step was changed from Δt_0 to Δt_1 at time $t = t_1$.

Figs. 4.14 are taken from a three-dimensional animation of the swimming body and its wake. The program to create these graphics was written by Dr Mike Wilson. We thank him for allowing us to use his code, and for his further help in adapting it to suit our purposes.

Firstly, owing to the symmetry of the problem in the $Y = 0$ plane, the data shows one half of the solution. The blue surface is the fish, and the red surface represents the vortex sheet shed from the tail fin, ie the wake. We have output three different “views” of the data from simulation B (see above). “Still” frames from an animation do not really do justice to the output, but hopefully the figure gives an impression of what is happening.

In the top view the entire wake is included. Given that the time step was so large over the first five periods of the motion much of the wake surface is quite jagged. Immediately behind the tail is a much smoother portion of the wake arising from the smaller time step used after $t = 5T$. There is also a slight “glitch” in the surface associated with the change in time step. It is possible to make out some rollup of the tip vortex along the entire length of the wake. Of course the direction of rollup changes depending on whether a given portion of the vortex sheet is above or below the mean lateral position of the fish ($Z = 0$). To be more precise, the tip vortex rolls up in an alternating sense depending on the sign of the streamwise vorticity at the trailing edge at the time a given section of the vortex sheet is shed into the wake.

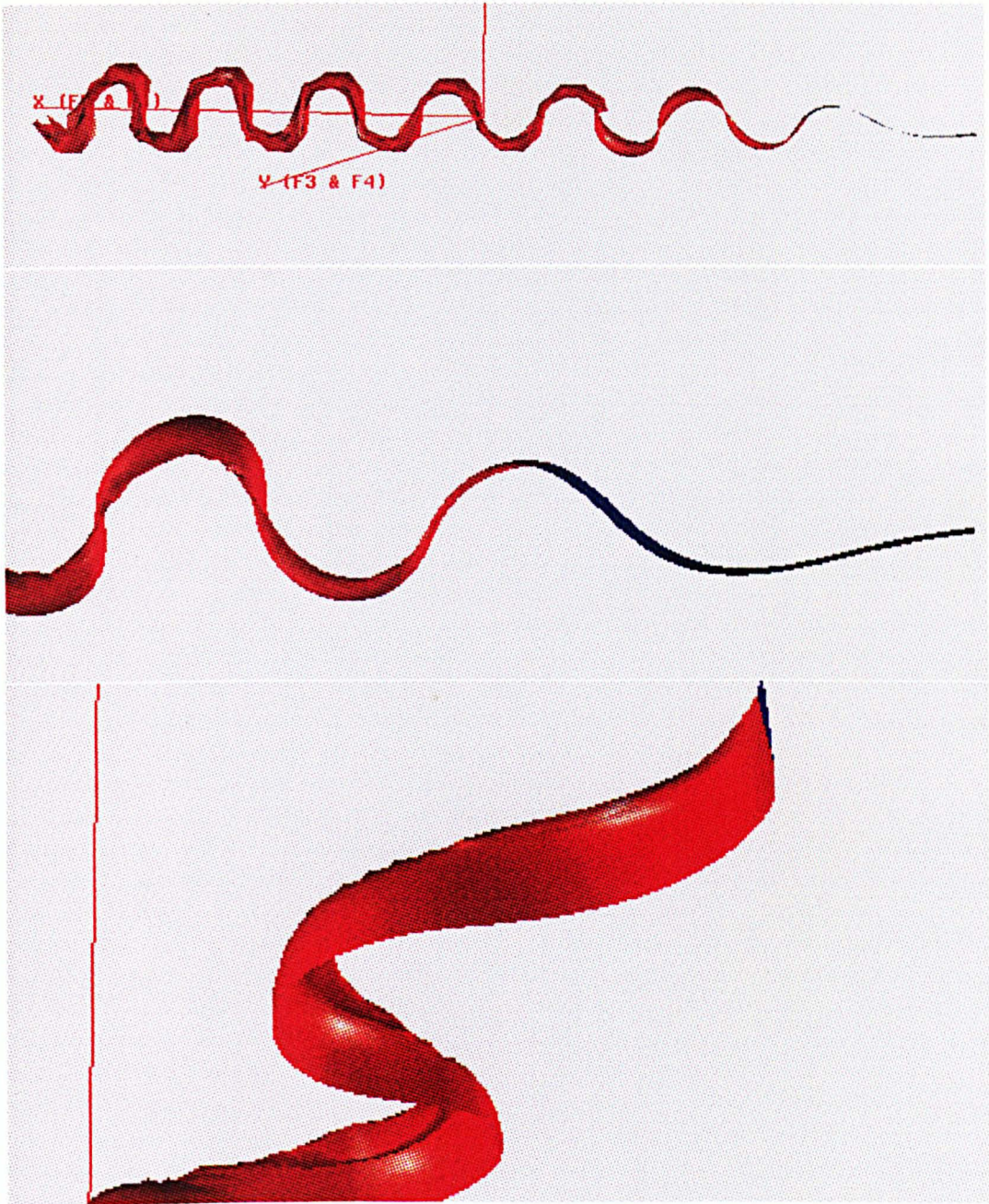


Figure 4.14: Three-dimensional surface plots of the data representing the body (shown in blue) and its wake (shown in red). Symmetry in the $Y = 0$ plane allows us to plot just half of the solution space. Three different “views” of the same run (B) are displayed. Graphics software used with permission from Dr Mike Wilson.

The trailing edge of the fish follows a sinusoidal path through the water. The induced velocity field in the neighbourhood of the wake causes it to deform. In addition to rolling up at the tip vortex we can also see that the amplitude of the wake's shape grows with time.

The middle view (in Fig. 4.14) is a close-up of the top view in the region around the tail. In the bottom view the image has been turned through 90° so that the body is vertical, and oscillates from side to side (ie like a fish, rather than a whale). The body has moved out of the field-of-view and we are looking upwards, from below the wake. These two views give a better impression of the rollup along the tip of the vortex sheet. It is difficult to make out any evidence of the vortex street (seen clearly in the two-dimensional model) creating a backwards jet along the direction of swimming.

We can also calculate the velocity field in the neighbourhood of the fish and its wake. Fig. 4.15 shows the two-dimensional velocity field in the centre-plane $Y = 0$ for the current example, (data taken from run with $N_X = 50, N_Y = 15$). The four frames are from consecutive time steps. The velocity vector at a given point is represented by an arrow starting from the point in question, with the length proportional to the magnitude of the vector. These plots are similar to the images produced by Muller (1997) using experimental flow visualisation techniques (particle image velocimetry and particle tracking velocimetry).

The motion of the body appears to generate a circulatory flow about certain points along the body, (for example at $X \approx -5.05$). Of course, the flow cannot go through the solid body: this rotation should not be called a vortex. Nonetheless, these "rotation centres" move backwards along the body with the undulation-wave, and their arrival at the trailing edge coincides with the shedding of a vortex into the wake. This seems to be in agreement with observations made by Muller (1997).

In the wake we see evidence of rollup about two perpendicular directions. Firstly, it is possible to see the counter-rotating vortices behind the tail that were not clear in Fig. 4.14. Secondly, at each "crest" and "trough" of the wake the velocity field is causing the wake to spread out (chiefly in the Z -direction). This is a three-dimensional effect and is associated with the tip vortex rollup.

It would be interesting to make more detailed comparisons between such theoretical velocity fields as calculated by the panel method, and the experimental data obtained by Muller (1997). Moreover, assuming that such comparisons were useful, the computer simulation offers certain advantages over the experimental setup. In particular we have a greater degree of flexibility regarding the space

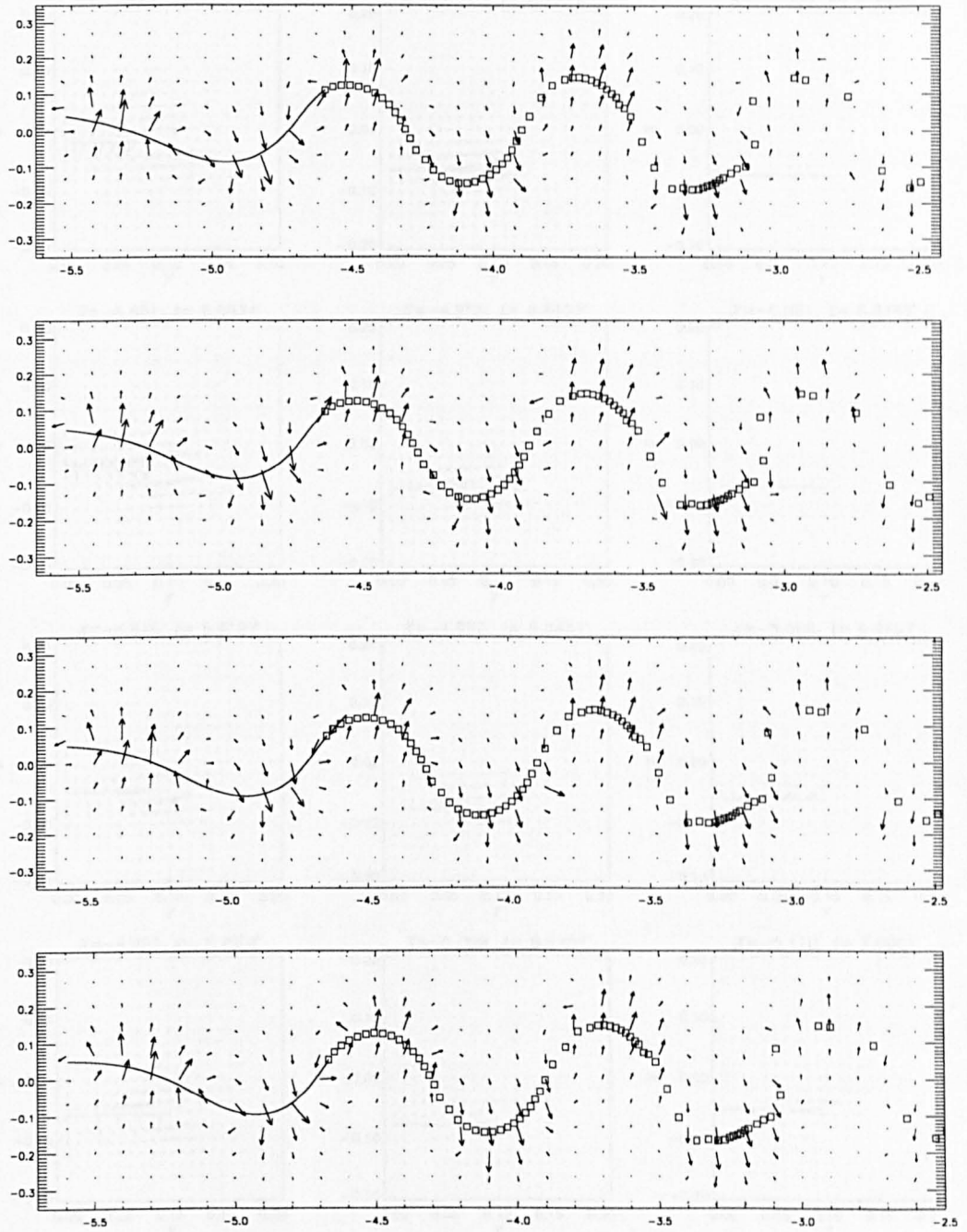


Figure 4.15: Graphs of the two-dimensional velocity field (in the plane of symmetry $Y = 0$) over four consecutive time steps. The solid line is the body; each square represents a wake-node lying along the $Y = 0$ plane; and the arrows indicate the velocity field.

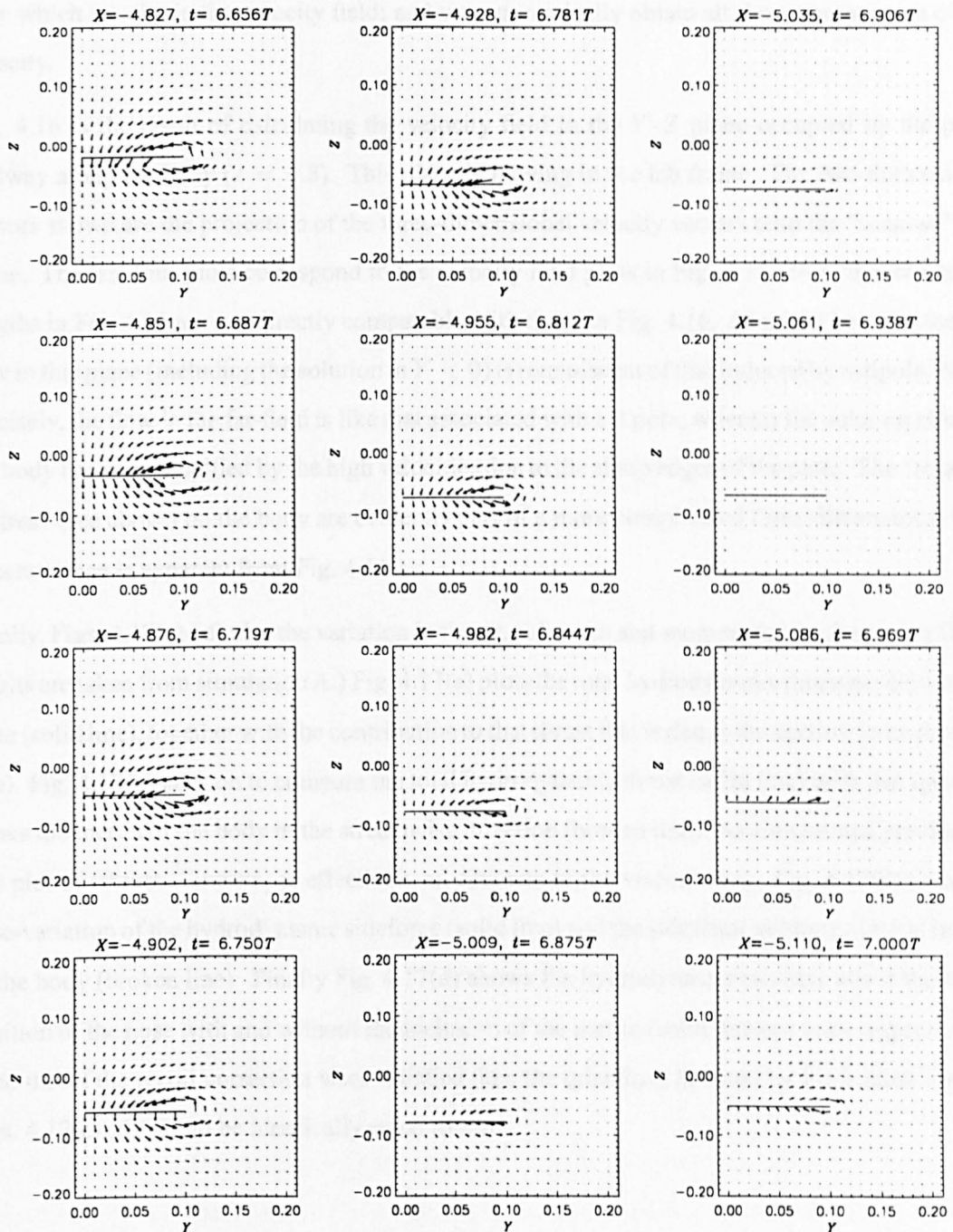


Figure 4.16: Graphs of the projection of the velocity field in the plane $X = X(s = 0.5, t)$ onto that plane. The last four plots correspond to those in Fig. 4.15. The solid line indicates the position of the "slice" of body lying in the "scanned" plane.

over which we obtain the velocity field; and we automatically obtain all three components of the velocity.

Fig. 4.16 is the result of calculating the velocity field in the Y - Z plane occupied by the point midway along the body ($s = 0.5$). This plane is moving in the lab frame. The two-dimensional vectors shown are the projection of the three-dimensional velocity vectors onto the “scanned” X -plane. The last four plots correspond to the velocity field plots in Fig. 4.15. Note that the arrow lengths in Fig. 4.15 are not directly comparable with those in Fig. 4.16. As might be expected the flow in this plane (including the solution in $Y < 0$) is reminiscent of that induced by a dipole. More precisely, the flow in the far-field is like that associated with a dipole; whereas the solution close to the body has been modified by the high velocities due to the sharp edges of the plate. The “rotation centres” (see above) on the body are evidently part of a more complicated three-dimensional flow structure than is apparent from Fig. 4.15.

Finally, Figs. 4.17(a)-(d) plot the variation in thrust, sideforce and moment (per unit span). (These results are taken from simulation A.) Fig. 4.17(a) plots the total hydrodynamic thrust on the waving plate (solid line), together with the contribution to that thrust that is due to the suction force (broken line). Fig. 4.17(b) goes on to compare the total hydrodynamic thrust (solid line) with that quantity minus the inertia of the body in the streamwise direction (broken line). As commented previously, this plot of (thrust – inertia) is effectively an estimate of the viscous drag. Fig. 4.17(c) plots the time-variation of the hydrodynamic sideforce (solid line) and the sideforce minus the lateral inertia of the body (broken line). Finally Fig. 4.17(d) shows the hydrodynamic moment about the mean position of the nose with and without the inclusion of the inertia (solid, broken lines respectively). Note that if the recoil correction were satisfied then the quantities denoted by the broken lines in Figs. 4.17(c),(d) would be identically equal to zero.

4.9 Conclusions

This chapter has dealt with the three-dimensional panel method that we have used. We have discussed results from the program relating to a pitching-heaving flat plate; a large aspect-ratio waving plate with small-amplitude lateral undulations; and an example of large-amplitude swimming.

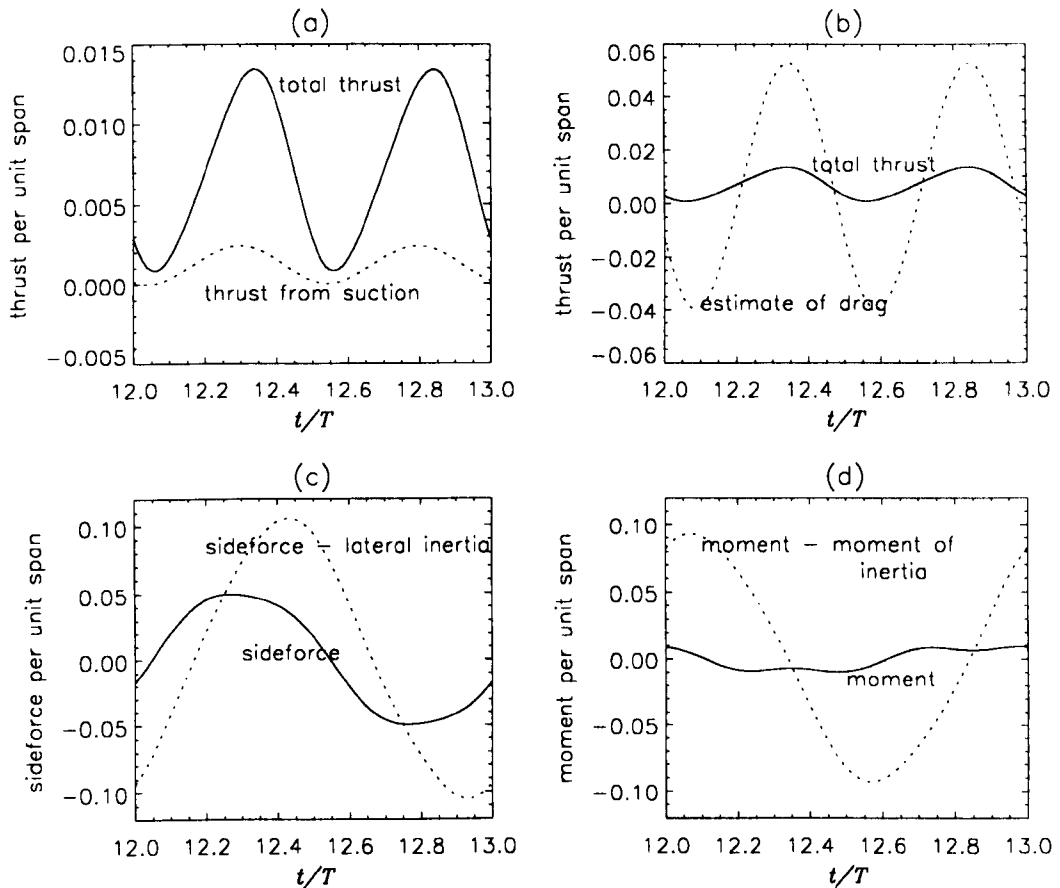


Figure 4.17: Graphs to show the variation over a single period of the thrust, sideforce and moment about the mean position of the nose. All the quantities are displayed “per unit span”. (a) compares the total hydrodynamic thrust with the contribution to thrust due to suction. In (b), the total hydrodynamic thrust is compared with the (thrust – inertia). This latter quantity gives a panel-method based estimate of the what the viscous drag would have to be to allow the fish to swim at the imposed constant speed. In (c) and (d) the solid line indicates the sideforce, and the hydrodynamic moment about the mean lateral position of the nose, respectively. In both cases the broken line plots the same quantity, but with the inclusion of body inertia.

We found we were able to produce reasonable results in comparison with earlier work and with our two-dimensional model. Further, the method is convergent with increasing N (the total number of panels): we require more chordwise than spanwise panels. In general it is best to use as small a time

step Δt as possible, subject to the constraint that $\Delta t \approx l_X/N_X$. Results indicate that matching the dimensions of the body and wake panels leads to a more satisfactory pressure jump distribution at the trailing edge. However, as N_X increases, and Δt decreases the cost of the program goes up (see Appendix). We also concluded that for the current application uniform panelling was preferable to cosine spacing.

At this stage the three-dimensional model does not include the recoil correction. In using a large aspect ratio waving plate we were able to obtain almost identical results for the sideforce and moment (including inertia) per unit span from the two-dimensional and three-dimensional models (see Fig. 4.9). Nonetheless even under these conditions the recoil for the three-dimensional version did not converge. We are confident that the temporary problem lies in the code to obtain the recoil correction, rather than in the underlying physics or model.

Finally, in the context of the large-amplitude example we have shown that in addition to the hydrodynamic quantities such as thrust, etc the method is also producing other useful output. We may examine the behaviour of the wake using a three-dimensional animation; and study the velocity field in the neighbourhood of the body and wake. This latter form of output will be useful in comparison with similar output obtained by experimental flow visualisation techniques.

Chapter 5

The boundary layer and calculation of the drag

5.1 Introduction

In this chapter we outline an approximate calculation of the distribution of the viscous drag along the swimming fish (waving plate). Lighthill (1975, Chapter 6) commented (and this remains true) that work on high Reynolds number undulatory swimming has tended to concentrate on the production of thrust by the fish's lateral movements. The viscous drag forces are associated with the tangential movement of the body, and are developed in a thin boundary layer.

By assuming "steady state swimming" it has been possible to calculate the thrust forces (via one of the methods outlined in Chapter 1) and consider them to be exactly balanced by the viscous drag. Lighthill (1971, Section 3) calculated the mean thrust associated with the motion of a dace *Leuciscus* from experimental data obtained by Bainbridge (1963). He (Lighthill) also estimated the total drag for gliding motion of a streamlined shape such as the dace in the experiments. He found that his calculated value for the mean thrust (from elongated body theory) was about four times bigger than the estimated drag on the equivalent rigid body. This discrepancy is too great to be due merely to uncertainties in the calculation of the two quantities. The conclusion then (attributed by Lighthill to Dr.Q.Bone) is that the normal movements of the body prevent the boundary layer thickness increasing to the magnitude that would normally be associated with a

body of that length, thereby increasing the viscous shear stress on the body surface. In other words, the boundary layer thickness would be the result of the balance between the diffusion of vorticity away from the surface, and the convection of vorticity towards the surface as a result of its lateral movements. Thus the undulatory motion of the fish serves to increase the drag associated with swimming compared to that associated with the rigid gliding motion of the same fish. An alternative hypothesis would be that the undulations promote flow separation, and enhance the drag that way.

Without a model of the boundary layer along the body of the swimming fish we are unable to estimate the drag on the body independently of the assumption that it is balanced by the forward thrust. The inviscid theory (the panel method) allows the calculation of the tangential fluid velocity on the body surface. This then is an opportunity to use this velocity as input to a boundary layer calculation, where the said tangential velocity is taken to be the velocity at the outer edge of the boundary layer.

In addition to asking the basic question: “What is happening in the boundary layer along the body of a swimming fish?”, there are two reasons for estimating the drag. Firstly, by calculating the total drag on the fish and comparing it with the calculated thrust we may consider a “recoil-like” oscillation in the forward swimming speed. Results obtained using the panel method (eg in Fig. 3.13, and examples not shown) indicate that the forward thrust may oscillate with an amplitude which is large compared to the mean. This makes it all the more important to provide a direct estimate of the viscous drag and to allow the velocity to vary according to Newton’s laws. Thus we will have a check on the usual assumption that the fish swims with constant velocity. Secondly, the large-amplitude equations for the bending moment distribution along the body (see Chapter 6) include the tangential forces on the surface of, and inside, the body. Thus it is necessary to include the viscous drag per unit length as a function of position along the body and time.

The boundary layer calculations outlined in this chapter are nothing more than a first attempt at this problem in the context of fish swimming. The numerical scheme is first order in time and space (see Section 5.3) and is two-dimensional. Of course the real boundary layer on a swimming fish is three-dimensional. That is, since there is a pressure gradient in the spanwise direction, there must also be some flow along that direction. In the context of the two-dimensional hydrodynamical calculations (eg in Chapter 3) it is natural to use a two-dimensional boundary layer theory. In the context of the

full, three-dimensional model we can, for a first attempt, consider the boundary layer to be quasi-two-dimensional. In other words we can solve the two-dimensional boundary layer problem at a number of discrete stations across the span of the body.

5.2 The boundary layer equations

To calculate the flow in the boundary layer we make a coordinate transformation to a frame of reference fixed in the plate. In this frame the (dimensional) streamwise coordinate is \hat{s} , and the cross-stream coordinate \hat{n} . The plate itself lies along $\hat{n} = 0$ between $\hat{s} = 0$ (the nose) and $\hat{s} = \hat{l}$ (the tail). The no-slip condition requires that the fluid velocity on the plate is $\hat{\mathbf{u}} = (\hat{u}, \hat{w}) = 0$. Far from the plate the fluid moves as a uniform free stream with speed \hat{U}_0 (ie the swimming speed in the lab-based frame of reference). At positions nearer to the plate the velocity of the fluid can be calculated as a combination of a term due to the velocity obtained from the inviscid analysis and a term due to the transformation between coordinate frames. In particular, the velocity at the outer edge of the boundary layer ($\hat{U}(\hat{s}, \hat{t}), 0$) is the tangential component of the velocity on the plate as calculated by the inviscid theory (panel method) minus the tangential component of the velocity of the plate. The pressure gradient term in the boundary layer equations (see below) must include the inertial contribution associated with the acceleration and rotation of the frame of reference. However, as in all boundary layer problems, this can be calculated by taking the limit of the s -momentum equation as the scaled normal coordinate, n , tends to infinity, because there is no variation in pressure across the boundary layer.

We now consider the boundary layer assumptions in more detail.

Flow in the spanwise direction is neglected. Consider the two-dimensional Navier-Stokes equations (in dimensional variables):

$$\frac{\partial \hat{u}}{\partial \hat{t}} + \hat{u} \frac{\partial \hat{u}}{\partial \hat{s}} + \hat{w} \frac{\partial \hat{u}}{\partial \hat{n}} = -\frac{1}{\hat{\rho}} \frac{\partial \hat{p}}{\partial \hat{s}} + \hat{\nu} \left(\frac{\partial^2 \hat{u}}{\partial \hat{s}^2} + \frac{\partial^2 \hat{u}}{\partial \hat{n}^2} \right) \quad (5.1a)$$

$$\frac{\partial \hat{w}}{\partial \hat{t}} + \hat{u} \frac{\partial \hat{w}}{\partial \hat{s}} + \hat{w} \frac{\partial \hat{w}}{\partial \hat{n}} = -\frac{1}{\hat{\rho}} \frac{\partial \hat{p}}{\partial \hat{n}} + \hat{\nu} \left(\frac{\partial^2 \hat{w}}{\partial \hat{s}^2} + \frac{\partial^2 \hat{w}}{\partial \hat{n}^2} \right) \quad (5.1b)$$

$$\frac{\partial \hat{u}}{\partial \hat{s}} + \frac{\partial \hat{w}}{\partial \hat{n}} = 0. \quad (5.1c)$$

We make the usual boundary layer assumption (Batchelor, 1967) that the boundary layer thickness, say $\hat{\delta}_0$, is small compared to the linear dimensions of the boundary over which the flow changes significantly, say \hat{l} , the length of the plate. Consequently derivatives with respect to \hat{n} of any flow quantity are much larger than those with respect to \hat{s} :

$$\left| \frac{\partial \hat{u}}{\partial \hat{s}} \right| \ll \left| \frac{\partial \hat{u}}{\partial \hat{n}} \right| \quad (5.2a)$$

$$\left| \frac{\partial^2 \hat{u}}{\partial \hat{s}^2} \right| \ll \left| \frac{\partial^2 \hat{u}}{\partial \hat{n}^2} \right|. \quad (5.2b)$$

The equation for momentum in the \hat{s} -direction (equation (5.1a)) then becomes:

$$\frac{\partial \hat{u}}{\partial \hat{t}} + \hat{u} \frac{\partial \hat{u}}{\partial \hat{s}} + \hat{w} \frac{\partial \hat{u}}{\partial \hat{n}} = -\frac{1}{\hat{\rho}} \frac{\partial \hat{p}}{\partial \hat{s}} + \hat{\nu} \frac{\partial^2 \hat{u}}{\partial \hat{n}^2}. \quad (5.3)$$

The boundary layer is that region where the viscous diffusion term $\hat{\nu} \frac{\partial^2 \hat{u}}{\partial \hat{n}^2}$ is comparable in magnitude with the inertia terms on the left hand side of equation (5.3). We suppose that $\hat{u} \frac{\partial \hat{u}}{\partial \hat{s}}$ is representative of the magnitude of the inertia terms, and say that the boundary layer is characterized by the relation

$$O \left(\hat{u} \frac{\partial \hat{u}}{\partial \hat{s}} / \hat{\nu} \frac{\partial^2 \hat{u}}{\partial \hat{n}^2} \right) = 1. \quad (5.4)$$

We take \hat{U}_0 to be representative of the magnitude of \hat{u} ; \hat{l} as a typical streamwise lengthscale for appreciable changes in \hat{u} ; and $\hat{\delta}_0$ as an average (small) length representing the boundary layer thickness. Then equation (5.4) can be re-stated as

$$\frac{\hat{\delta}_0}{\hat{l}} \sim (Re)^{-\frac{1}{2}} \text{ as } Re \rightarrow \infty, \quad (5.5)$$

where $Re = \hat{U}_0 \hat{l} / \hat{\nu}$.

Having an estimate of the magnitude of $\hat{\delta}_0$ allows us to use equation (5.1c) to show that \hat{w} is of order $\hat{U}_0 Re^{-\frac{1}{2}}$. We can then use equation (5.1b) to show that

$$\frac{\partial \hat{p}}{\partial \hat{n}} \approx 0. \quad (5.6)$$

Consequently, we have the second characteristic of boundary layer theory: that the pressure is approximately uniform across the boundary layer, and is a function of \hat{s} and \hat{t} only.

We make the following non-dimensionalization, which is different to that used in the panel method calculations:

$$s = \frac{\hat{s}}{\hat{l}}, \quad (5.7a)$$

$$n = \hat{n} \left(\frac{\hat{U}_0}{\hat{\nu} \hat{l}} \right)^{\frac{1}{2}}, \quad (5.7b)$$

$$t = \hat{t} \frac{\hat{U}_0}{\hat{l}}, \quad (5.7c)$$

$$u = \frac{\hat{u}}{\hat{U}_0}, \quad (5.7d)$$

$$w = \hat{w} \left(\frac{\hat{l}}{\hat{\nu} \hat{U}_0} \right)^{\frac{1}{2}}, \quad (5.7e)$$

$$p = \frac{\hat{p}}{\hat{\rho} \hat{U}_0^2}. \quad (5.7f)$$

The full equations of motion (equations (5.1)) then become:

$$\frac{\partial u}{\partial s} + \frac{\partial w}{\partial n} = 0 \quad (5.8a)$$

$$\frac{\partial u}{\partial t} + u \frac{\partial u}{\partial s} + w \frac{\partial u}{\partial n} = -\frac{\partial p}{\partial s} + \frac{\partial^2 u}{\partial n^2}. \quad (5.8b)$$

subject to the boundary conditions

$$u = w = 0 \text{ at } n = 0 \quad (5.9a)$$

$$u \rightarrow U(s, t) \text{ as } n \rightarrow \infty, \quad (5.9b)$$

where $U(s, t) = \hat{U}(\hat{s}, \hat{t})/\hat{U}_0$. Further, by considering the limit of the s -momentum equation as $n \rightarrow \infty$, and noting that equation (5.6) shows the pressure gradient to be uniform across the boundary layer, we have

$$\frac{\partial U}{\partial t} + U \frac{\partial U}{\partial s} = -\frac{1}{\rho} \frac{\partial p}{\partial s}. \quad (5.10)$$

5.3 The numerical method

The code used to solve the boundary layer equations is only slightly modified from one kindly provided by Dr.O.R.Tutty, and follows the methods of Keller and Cebeci (see Keller, 1971; Cebeci, 1977b; Keller, 1978; Cebeci and Bradshaw, 1977). The first version that we tried, involving a Crank-Nicholson implicit scheme, suffered from sawtooth oscillations on the length scale of the grid due to an instability in the calculation. It was replaced with a simpler first order scheme. Dr

Tutty's help in deciding that the problems in the Crank-Nicholson scheme could be overcome by switching to an alternative differencing scheme (again written by him) was invaluable. He has suggested that if the current first order scheme is reasonably successful it should be replaced by a second order version.

In order to set equations (5.8) and their boundary conditions (5.9) in a form suitable for calculating a numerical solution we make the further transformation:

$$\zeta = n/\sqrt{s}. \quad (5.11)$$

We introduce the non-dimensional stream function ψ , so that

$$u = \left. \frac{\partial \psi}{\partial n} \right|_s = \frac{1}{\sqrt{s}} \left. \frac{\partial \psi}{\partial \zeta} \right|_s, \quad (5.12a)$$

$$w = - \left. \frac{\partial \psi}{\partial s} \right|_n \quad (5.12b)$$

$$= - \left. \frac{\partial \psi}{\partial s} \right|_{\zeta} + \frac{\zeta}{2s} \left. \frac{\partial \psi}{\partial \zeta} \right|_s, \quad (5.12c)$$

and the shear rate E is

$$E = \left. \frac{\partial u}{\partial n} \right|_s = \frac{1}{\sqrt{s}} \left. \frac{\partial u}{\partial \zeta} \right|_s. \quad (5.13)$$

After some algebra the equations (5.8) become

$$u = \frac{1}{\sqrt{s}} \frac{\partial \psi}{\partial \zeta} \quad (5.14a)$$

$$E = \frac{1}{\sqrt{s}} \frac{\partial u}{\partial \zeta} \quad (5.14b)$$

$$\frac{\partial u}{\partial t} + u \frac{\partial u}{\partial s} - E \frac{\partial \psi}{\partial s} = \left(\frac{\partial U}{\partial t} + U \frac{\partial U}{\partial s} \right) + \frac{1}{\sqrt{s}} \frac{\partial E}{\partial \zeta}, \quad (5.14c)$$

subject to the boundary conditions

$$u(0) = 0 \quad (5.15a)$$

$$u \rightarrow U(s, t) \text{ as } \zeta \rightarrow \infty \quad (5.15b)$$

$$\psi(0) = 0. \quad (5.15c)$$

The method used to solve this system is described in the next section. The aim is to calculate the shear rate along the boundary $\zeta = n = 0$, so as to have an estimate of the viscous drag on the

swimming fish. In other words we need to relate E to the non-dimensional drag per unit length in the non-dimensionalization used in the panel method calculations:

$$\bar{D} = \frac{\hat{D}}{\hat{\rho}\hat{U}_0^2}. \quad (5.16)$$

(Here we use the “overbar” to indicate a non-dimensional variable in the panel method non-dimensionalization.) Now the dimensional drag per unit length is

$$\hat{D} = \hat{\mu} \left. \frac{\partial \hat{u}}{\partial \hat{n}} \right|_{\hat{n}=0}, \quad (5.17)$$

and so by equation (5.16)

$$\bar{D} = \left(\frac{\hat{\nu}}{\hat{U}_0 \hat{l}} \right) \left. \frac{\partial \bar{u}}{\partial \bar{n}} \right|_{\bar{n}=0} \quad (5.18)$$

$$= \frac{1}{Re} \left. \frac{\partial \bar{u}}{\partial \bar{n}} \right|_{\bar{n}=0}. \quad (5.19)$$

If we also express E in dimensional terms:

$$E = \frac{1}{\hat{U}_0} \left(\frac{\hat{\nu} \hat{l}}{\hat{U}_0} \right)^{\frac{1}{2}} \frac{\partial \hat{u}}{\partial \hat{n}}, \quad (5.20)$$

and use the panel method non-dimensionalization, we obtain

$$E = \frac{1}{\sqrt{Re}} \frac{\partial \bar{u}}{\partial \bar{n}}. \quad (5.21)$$

Then, comparing equations (5.19) and (5.21),

$$\bar{D} = \frac{E|_{\zeta=0}}{\sqrt{Re}}. \quad (5.22)$$

5.3.1 The finite difference equations and Newton method

We now consider the finite difference form of the transformed equations (5.14). The method described below is a first order backwards difference scheme in space and time. Essentially this scheme is the simplest option, which is the reason for using it to give a first approximation to the results. However, the method may well introduce inaccuracy in the solution through the large truncation error associated with first order finite differences. Given that we have shown (see below) that the calculation of the viscous drag works reasonably well, the method should now be improved to a second order scheme.

Consider the three-dimensional grid in (s, ζ, t) as shown in Fig. 5.1. The grid spacing (l_i, h_j, k_n) may be variable. The s, ζ -index variables are considered to run $i = 0..I$ and $j = 0..J$. There is no need to put a limit on the t -index, although we do have $n = 0$ at $t = t_0$. (The subscript n is not to be confused with the boundary layer cross-stream variable n , which has now been transformed to ζ .) In this first order backwards difference scheme we average about the point $(i, j - \frac{1}{2}, n)$ where this notation is taken to mean “halfway between the points (i, j, n) and $(i, j - 1, n)$ ”. For example we write $u_{j-\frac{1}{2}}^{i,n}$ to mean the average of the values $u_j^{i,n}$ and $u_{j-1}^{i,n}$:

$$u_{j-\frac{1}{2}}^{i,n} = \frac{1}{2}(u_j^{i,n} + u_{j-1}^{i,n}). \quad (5.23)$$

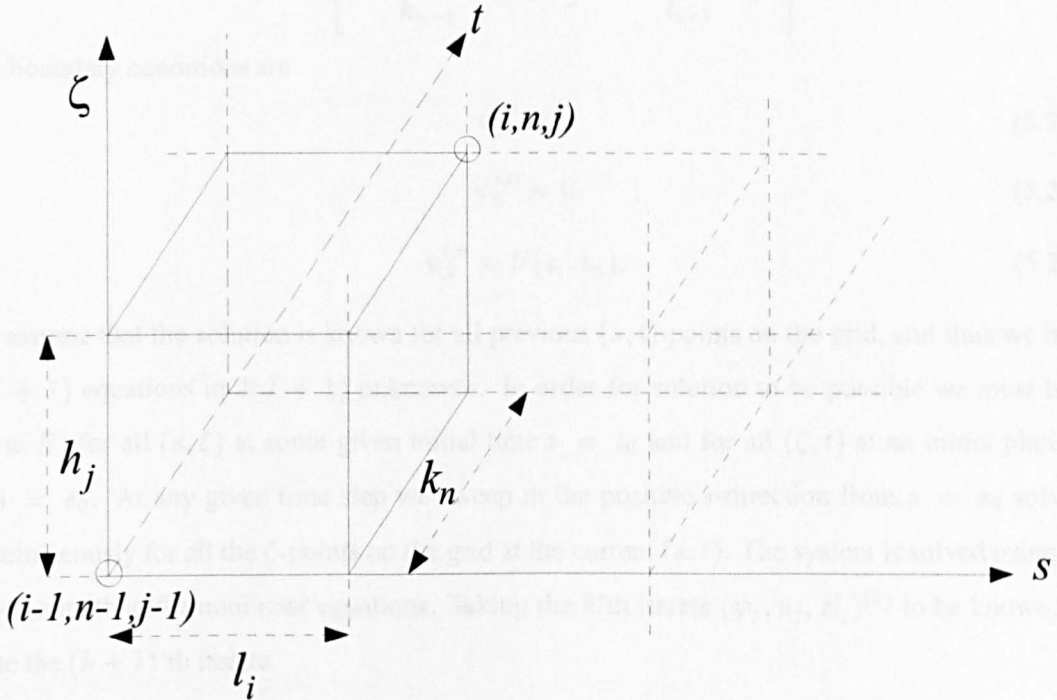


Figure 5.1: Sketch of the three-dimensional grid used for the finite difference equations in the boundary layer solver. The grid spacing is not necessarily uniform in the s and ζ directions.

Under this finite difference form, the equations (5.14) are written:

$$u_{j-\frac{1}{2}}^{i,n} = \frac{1}{\sqrt{s_i}} \left(\frac{\psi_j^{i,n} - \psi_{j-1}^{i,n}}{h_{j-1}} \right), \quad j = 1..J \quad (5.24a)$$

$$E_{j-\frac{1}{2}}^{i,n} = \frac{1}{\sqrt{s_i}} \left(\frac{u_j^{i,n} - u_{j-1}^{i,n}}{h_{j-1}} \right), \quad j = 1..J \quad (5.24b)$$

$$\begin{aligned} & \left(\frac{u_{j-\frac{1}{2}}^{i,n} - u_{j-\frac{1}{2}}^{i,n-1}}{k_{n-1}} \right) + u_{j-\frac{1}{2}}^{i,n} \left(\frac{u_{j-\frac{1}{2}}^{i,n} - u_{j-\frac{1}{2}}^{i-1,n}}{l_{i-1}} \right) \\ & - E_{j-\frac{1}{2}}^{i,n} \left(\frac{\psi_{j-\frac{1}{2}}^{i,n} - \psi_{j-\frac{1}{2}}^{i-1,n}}{l_{i-1}} \right) + P \\ & - \frac{1}{\sqrt{s_i}} \left(\frac{E_j^{i,n} - E_{j-1}^{i,n}}{h_{j-1}} \right) = 0, \quad j = 1..J \end{aligned} \quad (5.24c)$$

where

$$P = - \left[\frac{(u_J^{i,n} - u_{J-1}^{i,n})}{k_{n-1}} + u_J^{i,n} \frac{(u_J^{i,n} - u_J^{i-1,n})}{l_{i-1}} \right]. \quad (5.24d)$$

The boundary conditions are

$$u_0^{i,n} = 0 \quad (5.25a)$$

$$\psi_0^{i,n} = 0 \quad (5.25b)$$

$$u_j^{i,n} = U(s_i, t_n). \quad (5.25c)$$

We assume that the solution is known for all previous (s, t) -points on the grid, and thus we have $3(J + 1)$ equations in $3(J + 1)$ unknowns. In order for solution to be possible we must have (ψ, u, E) for all (s, ζ) at some given initial time $t = t_0$ and for all (ζ, t) at an initial plane in $s: s = s_0$. At any given time step we sweep in the positive s -direction from $s = s_0$ solving simultaneously for all the ζ -points on the grid at the current (s, t) . The system is solved using the Newton method for nonlinear equations. Taking the k 'th iterate $(\psi_j, u_j, E_j)^{(k)}$ to be known, we write the $(k + 1)$ 'th iterate

$$(\psi_j, u_j, E_j)^{(k+1)} = (\psi_j, u_j, E_j)^{(k)} + (\delta\psi_j, \delta u_j, \delta E_j). \quad (5.26)$$

So, in the finite difference equations (5.24) we replace $(\psi^{i,n}, u^{i,n}, E^{i,n})$ by $(\psi^{i,n}, u^{i,n}, E^{i,n}) + (\delta\psi_j, \delta u_j, \delta E_j)$ and linearise. The resulting three equations are

$$\left(\frac{-h_{j-1}\sqrt{s_i}}{2} \right) (\delta u_j + \delta u_{j-1}) + (\delta\psi_j - \delta\psi_{j-1}) = (r_1)_j \quad (5.27a)$$

$$\left(\frac{-h_{j-1}\sqrt{s_i}}{2} \right) (\delta E_j + \delta E_{j-1}) + (\delta u_j - \delta u_{j-1}) = (r_2)_j \quad (5.27b)$$

$$b_{21}\delta\psi_{j-1} + b_{22}\delta u_{j-1} + b_{23}\delta E_{j-1} + d_{21}\delta\psi_j + d_{22}\delta u_j + d_{23}\delta E_j = (r_3)_j \quad (5.27c)$$

where

$$b_{21} = \frac{k_{n-1}}{l_{i-1}}(E_j^{i,n} + E_{j-1}^{i,n}) \quad (5.28a)$$

$$d_{21} = b_{21} \quad (5.28b)$$

$$b_{22} = -2 - \frac{k_{n-1}}{l_{i-1}} \left(2(u_j^{i,n} + u_{j-1}^{i,n}) - (u_j^{i-1,n} + u_{j-1}^{i-1,n}) \right) \quad (5.28c)$$

$$d_{22} = b_{22} \quad (5.28d)$$

$$b_{23} = k_{n-1} \left[\left(\frac{(\psi_j^{i,n} + \psi_{j-1}^{i,n}) - (\psi_j^{i-1,n} + \psi_{j-1}^{i-1,n})}{l_{i-1}} \right) - \frac{4}{\sqrt{s_i}h_{j-1}} \right] \quad (5.28e)$$

$$d_{23} = k_{n-1} \left[\left(\frac{(\psi_j^{i,n} + \psi_{j-1}^{i,n}) - (\psi_j^{i-1,n} + \psi_{j-1}^{i-1,n})}{l_{i-1}} \right) + \frac{4}{\sqrt{s_i}h_{j-1}} \right] \quad (5.28f)$$

and

$$(r_1)_j = (u_j^{i,n} + u_{j-1}^{i,n}) \left(\frac{h_{j-1}\sqrt{s_i}}{2} \right) - (\psi_j^{i,n} - \psi_{j-1}^{i,n}) \quad (5.29a)$$

$$(r_2)_j = (E_j^{i,n} + E_{j-1}^{i,n}) \left(\frac{h_{j-1}\sqrt{s_i}}{2} \right) - (u_j^{i,n} - u_{j-1}^{i,n}) \quad (5.29b)$$

$$\begin{aligned} (r_3)_j &= 2 \left[(u_j^{i,n} + u_{j-1}^{i,n}) - (u_j^{i,n-1} + u_{j-1}^{i,n-1}) \right] \\ &+ k_{n-1} \left((u_j^{i,n} + u_{j-1}^{i,n}) \left[\frac{(u_j^{i,n} + u_{j-1}^{i,n}) - (u_j^{i-1,n} + u_{j-1}^{i-1,n})}{l_{i-1}} \right] \right. \\ &- (E_j^{i,n} + E_{j-1}^{i,n}) \left[\frac{(\psi_j^{i,n} + \psi_{j-1}^{i,n}) - (\psi_j^{i-1,n} + \psi_{j-1}^{i-1,n})}{l_{i-1}} \right] \\ &\left. + 4P - \frac{(E_j^{i,n} - E_{j-1}^{i,n})}{\sqrt{s_i}h_{j-1}} \right). \end{aligned} \quad (5.29c)$$

The boundary conditions reduce to

$$\delta u_0 = 0, \quad (5.30a)$$

$$\delta \psi_0 = 0, \quad (5.30b)$$

$$\delta u_J = 0. \quad (5.30c)$$

This set of equations is better expressed as follows. We write the equation to be solved as:

$$A\delta = r. \quad (5.31)$$

The solution vector on the right hand side of equation (5.31) is

$$\mathbf{r} = \begin{pmatrix} 0 \\ 0 \\ \mathbf{r}_1 \\ \mathbf{r}_2 \\ \vdots \\ \mathbf{r}_J \\ 0 \end{pmatrix} \quad \text{where} \quad \mathbf{r}_j = \begin{pmatrix} (r_1)_j \\ (r_2)_j \\ (r_3)_j \end{pmatrix}, \quad (5.32)$$

and the zero elements of the vector \mathbf{r} are real numbers (as opposed to three-component vectors like the \mathbf{r}_j). The terms on the left hand side of equation (5.31) give a block tridiagonal structure:

$$\boldsymbol{\delta} = \begin{pmatrix} \delta_0 \\ \delta_1 \\ \vdots \\ \delta_J \end{pmatrix} \quad \text{where} \quad \delta_j = \begin{pmatrix} \delta\psi_j \\ \delta u_j \\ \delta E_j \end{pmatrix} \quad (5.33)$$

$$A = \begin{pmatrix} D_0 & C_0 & & & \\ B_1 & D_1 & C_1 & & \\ & \ddots & \ddots & \ddots & \\ & & & B_{J-1} & D_{J-1} & C_{J-1} \\ & & & & B_J & D_J \end{pmatrix} \quad (5.34a)$$

where

$$D_j = \begin{pmatrix} 0 & 1 & -\frac{h_{j-1}\sqrt{s_i}}{2} \\ d_{21} & d_{22} & d_{23} \\ -1 & -\frac{h_{j-1}\sqrt{s_i}}{2} & 0 \end{pmatrix} \quad (5.34b)$$

$$B_j = \begin{pmatrix} 0 & -1 & -\frac{h_{j-1}\sqrt{s_i}}{2} \\ b_{21} & b_{22} & b_{23} \\ 0 & 0 & 0 \end{pmatrix} \quad (5.34c)$$

$$C_j = \begin{pmatrix} 0 & 0 & 0 \\ 0 & 0 & 0 \\ 1 & -\frac{h_{j-1}\sqrt{s_i}}{2} & 0 \end{pmatrix}, \quad (5.34d)$$

with the boundary condition requiring that

$$D_0 = \begin{pmatrix} 1 & 0 & 0 \\ 0 & 1 & 0 \\ -1 & -\frac{h_0\sqrt{s_1}}{2} & 0 \end{pmatrix}, \quad D_J = \begin{pmatrix} 0 & 1 & -\frac{h_{J-1}\sqrt{s_1}}{2} \\ d_{21} & d_{22} & d_{23} \\ 0 & 1 & 0 \end{pmatrix} \quad (5.34e)$$

The equations are solved for the iterate steps δ and the process is repeated until some preset convergence condition on the magnitude of δ is reached.

5.3.2 The initial conditions

As mentioned earlier, the process described above deals with the calculation of (ψ, u, E) at all the ζ -grid points at some fixed (s, t) point given that the solution is already known for all previous (s, t) -points. Clearly then, we also need an initial condition for all (s, ζ) at $t = t_0$, and also for all (ζ, t) at $s = s_0$. Cebeci (1977a) details a similar method based on constructing a set of equations to be solved using Newton's method to calculate the solution along these "initial planes" given an initial condition for all ζ at $s = s_0, t = t_0$. However, we have used a simpler method, imposing the steady Blasius solution for all s at $t = t_0$ (based on the imposed swimming speed), and using the quasi-steady Blasius solution as an approximate initial condition in s for all t .

The Blasius solution is the well known similarity solution for the boundary layer due to steady flow U over a semi-infinite flat plate. The steady, two-dimensional boundary layer equations are:

$$u \frac{\partial u}{\partial s} + w \frac{\partial u}{\partial n} = \nu \frac{\partial^2 u}{\partial n^2} \quad (5.35a)$$

$$\frac{\partial u}{\partial s} + \frac{\partial w}{\partial n} = 0. \quad (5.35b)$$

The cross-stream coordinate n is transformed to η :

$$\eta = \left(\frac{U}{\nu s} \right)^{\frac{1}{2}} n, \quad (5.36)$$

and the stream function is written

$$\psi(s, n) = (\nu U s)^{\frac{1}{2}} f(\eta). \quad (5.37)$$

The solution then is independent of position s along the plate (except in a small region near the nose where the boundary layer assumptions are not valid anyway) and is found by numerically solving

$$f''' + \frac{1}{2} f f'' = 0 \quad (5.38a)$$

$$f = f' = 0 \text{ at } \eta = 0 \quad (5.38b)$$

$$f' \rightarrow 1 \text{ as } \eta \rightarrow \infty. \quad (5.38c)$$

The solution is well known (see Rosenhead, 1963, p.224).

If the uniform stream is varying with time, $U = U(t)$, making a transformation that includes the time variation in U yields the quasi-steady Blasius solution. We put

$$\eta^* = \left(\frac{U(t)}{\nu s} \right)^{\frac{1}{2}} \eta \quad (5.39)$$

and

$$\psi = (\nu U(t) s)^{\frac{1}{2}} f(\eta^*). \quad (5.40)$$

This leads to the same differential equation (equation (5.38)), this time in terms of η^* .

We use the steady Blasius solution as an initial condition in t , because it is a simple approximate starting point for the Newton method. As we step through time we expect that the solution near the leading edge of the plate will be similar to the quasi-steady Blasius solution. Thus it makes sense to use this as an initial condition in s . Until now we have chosen the initial value of s , $s = s_0$, by trial and error. That is, for a given example, we use roughly the lowest value of s for which the code converges. Note that the solution in $s < s_0$ is the quasi-steady Blasius solution based on the time varying outer velocity at $s = s_0$.

5.3.3 The outer velocity condition

Finally, note that the method requires the velocity at the outer edge of the boundary layer as input. For a problem where the outer velocity can be expressed analytically this presents no difficulty. For the current application the outer velocity is found from the panel method, where we take the tangential fluid velocity on the body minus the tangential velocity of the body itself as being the velocity at the edge of the boundary layer. The nature of the panel method means that the induced

velocity on the body can only be determined (with any hope of accuracy) at the collocation points. Consequently we have two non-coincident grids: the panel method collocation points providing the input velocity data, and the s -spacing of the boundary layer solver's grid on which we need the outer velocity to form one of the boundary conditions at each (s, t) -station. It is therefore necessary to use an interpolation scheme to transform the panel method data into a form suitable for the boundary layer calculation. We use a cubic-spline method (Press *et al.*, 1996) to do this interpolation.

5.4 Oscillating free stream example

To test the code we follow Cebeci (1977a). Consider the boundary layer on a flat plate in an oscillating free stream with external velocity given by

$$U(t) = U_0 (1 + B \cos \omega t). \quad (5.41)$$

The problem was first considered by Lighthill (1954) for small amplitude oscillations, at small and large values of the reduced frequency $\omega s/U_0$. That work was further developed by, for example, Ackerberg and Phillips (1972) ($B \ll 1$); Pedley (1972) and Duck (1980) ($0 \leq B < 1$). Cebeci (1977a) gives Lighthill's result for the reduced skin friction coefficient $\frac{c_f}{2} \sqrt{Re_x}$ to be

$$\frac{c_f}{2} \sqrt{Re_x} = 0.332 + B \left(0.498 \cos \omega t - 0.849 \left(\frac{\omega s}{U_0} \right) \sin \omega t \right) \quad (5.42a)$$

for small reduced frequency, $\omega s/U_0 \ll 1$, and

$$\frac{c_f}{2} \sqrt{Re_x} = 0.332 + B \left(\frac{\omega s}{U_0} \right)^{\frac{1}{2}} \cos \left(\omega t + \frac{\pi}{4} \right) \quad (5.42b)$$

for large reduced frequency, $\omega s/U_0 \gg 1$. The skin friction coefficient c_f is

$$c_f = \frac{\hat{D}}{\frac{1}{2} \hat{\rho} \hat{U}_0^2}, \quad (5.43)$$

and Re_x is

$$Re_x = \left(\frac{\hat{U}_0 \hat{x}}{\hat{\nu}} \right). \quad (5.44)$$

In our notation then (referring back to the equations at the end of Section 5.2):

$$\frac{c_f}{2} \sqrt{Re_x} = E \sqrt{s}. \quad (5.45)$$

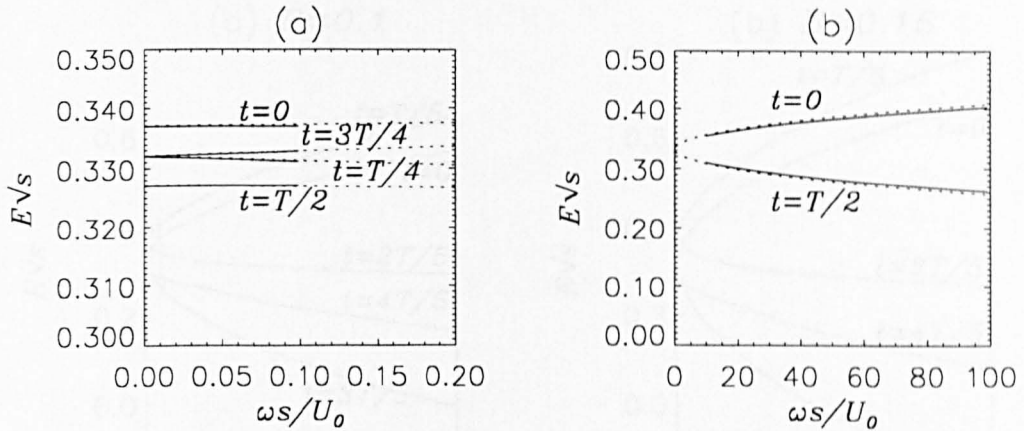


Figure 5.2: Graphs of the reduced skin friction coefficient ($E\sqrt{s}$ in our notation) against the reduced frequency, $\omega s/U_0$, for (a) small reduced frequency, and (b) large reduced frequency; $B = 0.01$. The solid lines denote the analytic solution; the dotted lines denote the numerical solution (which is valid for intermediate values of the reduced frequency).

Fig. 5.2(a),(b) shows a comparison of the analytic solution (equations (5.42)) with the numerical results at small and large reduced frequency respectively. The variation in time is included by superimposing the results over one another. Fig. 5.2(a) presents the data at four quarter-period intervals: $t = 0, T/4, T/2, 3T/4$; and Fig. 5.2(b) presents the data at half-period intervals: $t = 0, T/2$. In each case the solid lines denote the analytic solution and the dotted lines denote the numerical solution. The solid line is included only over the range for which the analytic solution could be said to be valid. The numerical solution on the other hand is valid over the intermediate values of the reduced frequency, $\omega s/U_0$. These examples were for a small amplitude oscillation, $B = 0.01$, in the free stream velocity.

Strictly speaking, our method is only applicable over values of B and $\omega s/U_0$ for which the assumption of a laminar, non-reversing boundary layer is valid. As these two parameters increase the flow in the boundary layer must eventually be reversed, and ultimately become turbulent. The present method is not capable of dealing with either situation: the code reports an error if backflow occurs. (In practice some backflow is “tolerated”, but eventually the method fails to converge as the backflow increases.) Fig. 5.3 plots the reduced skin friction coefficient $E\sqrt{s}$ against the reduced

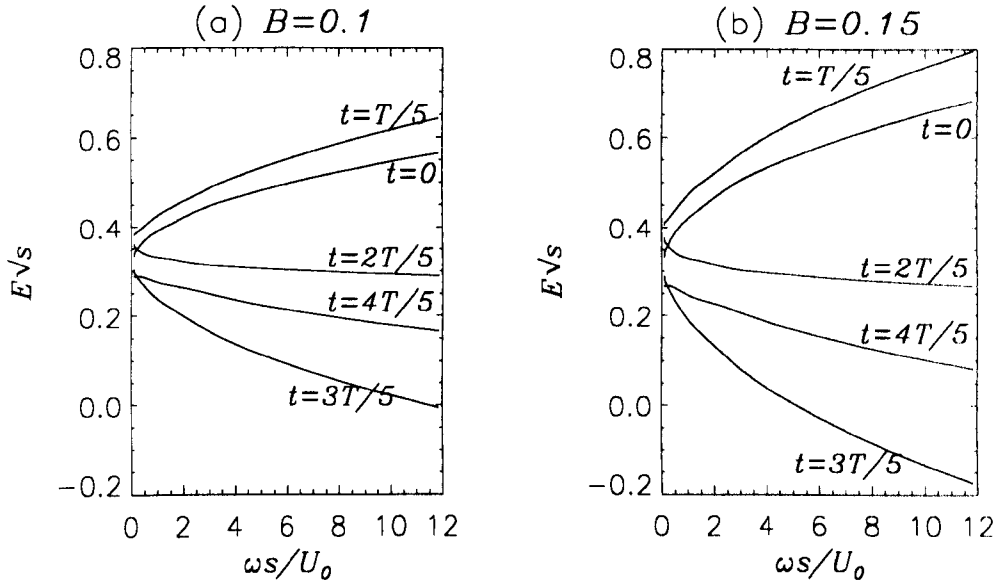


Figure 5.3: Graphs of the reduced skin friction coefficient, $E\sqrt{s}$, against the reduced frequency, $\omega s/U_0$, for (a) $B = 0.1$, (b) $B = 0.15$. The range of the reduced frequency was chosen on the basis of being relevant to fish swimming.

frequency $\omega s/U_0$ for two examples involving a larger amplitude of oscillation in the free stream: (a) $B = 0.1$, (b) $B = 0.15$. For these results we considered a range of reduced frequency up to $\omega s/U_0 \approx 12$. In the context of fish swimming we would expect this parameter to lie well within the range $6 \leq \omega s/U_0 \leq 12$. Both of the examples shown in Fig. 5.3 did converge over the whole period; but they also reported backflow. Our model is assumed to break down (ie there is at least some flow reversal) in regions where the shear rate E goes negative. In Fig. 5.3(a) ($B = 0.1$) this occurs briefly in the region $\omega s/U_0 > 11$ around $t = 3T/5$. In Fig. 5.3(b) ($B = 0.15$) the shear rate is negative for a considerable proportion of the period over most of the reduced frequency range with which we are concerned.

Fig. 5.4 shows the velocity profiles at $\omega s/U_0 \approx 3.5, 9.8, 11.9$ (solid lines) at times corresponding to the curves in Fig. 5.3(a), $t = 0, T/5, 2T/5, 3T/5, 4T/5$. As a reference, the broken line indicates the velocity profile at $s = s_0$, the assumed quasi-steady Blasius solution near the leading edge. As expected from Fig. 5.3(a), the curve corresponding to $\omega s/U_0 = 11.860$, $t = 3T/5$ includes a small negative velocity near the plate.

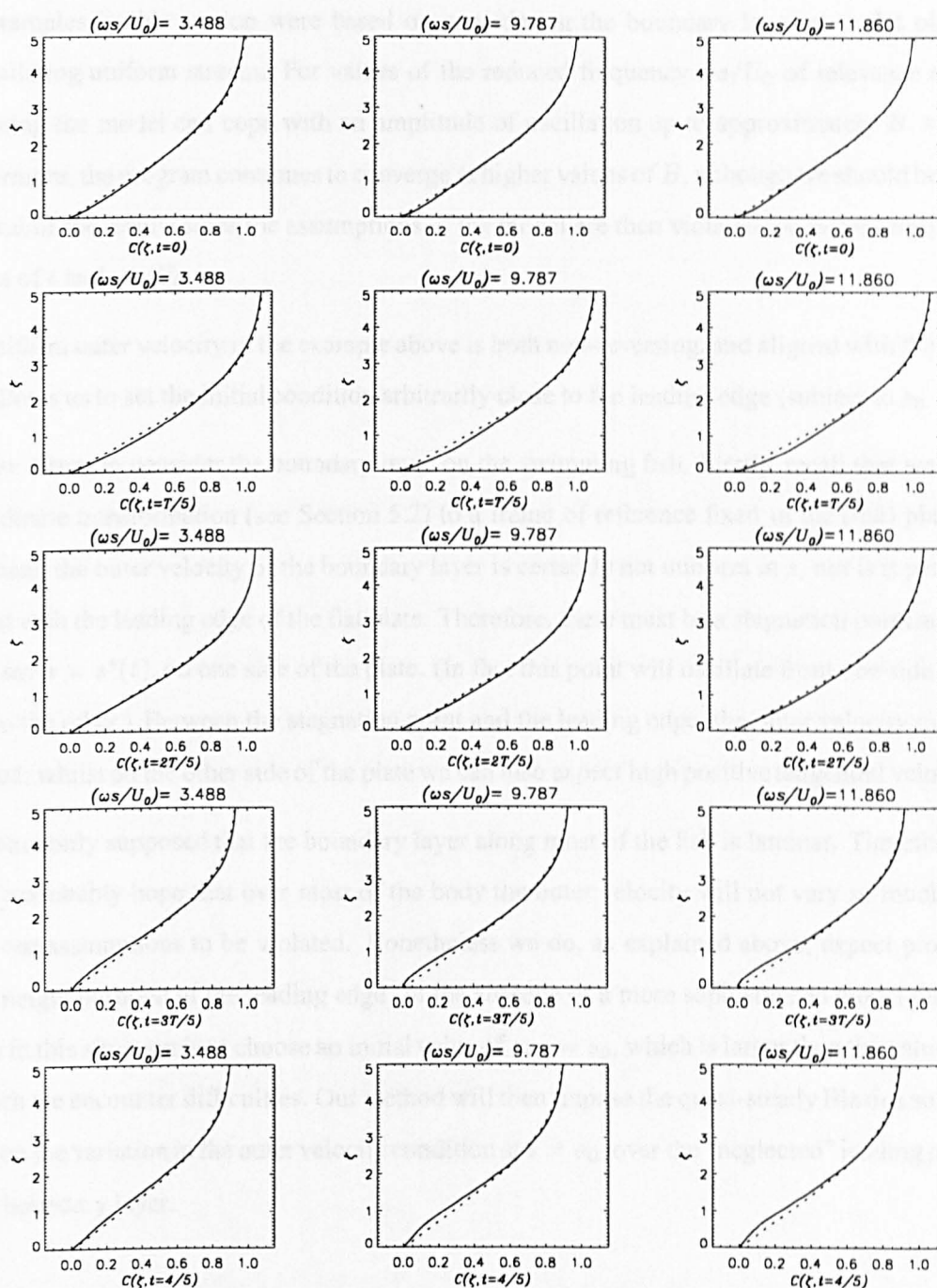


Figure 5.4: Velocity profiles of the boundary layer at three different values of $\omega s/U_0$. The quasi-steady Blasius solution is included (broken curves) to act as a reference. The variation in time is shown using times corresponding to the curves in Fig. 5.3(a).

The examples in this section were based on considering the boundary layer on a flat plate in an oscillating uniform stream. For values of the reduced frequency $\omega s/U_0$ of relevance to fish swimming the model can cope with an amplitude of oscillation up to approximately $B \approx 0.1$. Furthermore, the program continues to converge at higher values of B , although we should be more sceptical of the results since the assumptions of the model are then violated for increasingly large regions of t and $\omega s/U_0$.

The uniform outer velocity in the example above is both non-reversing, and aligned with the plate. This allows us to set the initial condition arbitrarily close to the leading edge (subject to $s_0 > 0$).

We now return to consider the boundary layer on the swimming fish. Firstly, recall that we make a coordinate transformation (see Section 5.2) to a frame of reference fixed in the (flat) plate. In this frame, the outer velocity of the boundary layer is certainly not uniform in s ; nor is it perfectly aligned with the leading edge of the flat plate. Therefore, there must be a stagnation point at some point, say $s = s^*(t)$, on one side of the plate. (In fact this point will oscillate from one side of the plate to the other.) Between the stagnation point and the leading edge, the outer velocity must be reversed; whilst on the other side of the plate we can also expect high positive tangential velocities.

It is commonly supposed that the boundary layer along most of the fish is laminar. Therefore, we might reasonably hope that over most of the body the outer velocity will not vary so much as to cause our assumptions to be violated. Nonetheless we do, as explained above, expect problems in the neighbourhood of the leading edge. In the absence of a more sophisticated model our only option in this situation is to choose an initial value of s , $s = s_0$, which is larger than the values of s at which we encounter difficulties. Our method will then impose the quasi-steady Blasius solution, based on the variation in the outer velocity condition at $s = s_0$, over the “neglected” leading portion of the boundary layer.

5.5 An example involving large amplitude swimming

In this section we use parameters derived from biological data relating to the eel (*Anguilla anguilla*). We used the combined panel method and boundary layer solver to obtain the results. There is no attempt to satisfy the recoil correction. The fish is assumed to swim at a constant speed,

and the resulting hydrodynamic forces are obtained. A non-zero time dependent resultant force acts on the fish, but no adjustment is made to its imposed motion. The data comes from Tables 6.1 and 8.1 of (Videler, 1993). The non dimensional parameter values that we calculated from the data are shown in Table 5.1.

l	U_0	M_b	A	α	B	β	b	k	ω	ξ
1	1	0.018	0.01	2.3	0.0	0.0	0.0	7.95	11.35	0.0

Table 5.1: Table of parameter values for the geometry of the eel motion. These non dimensional values are derived from data in Videler's book.

We used an exponentially increasing amplitude envelope with values of 0.01 at the nose, and 0.1 at the tail. The speed of the wave relative to the swimming speed is $V = \omega/k = 1.43$. The mass parameter is the non dimensional mass per unit span. The data gives the span of the tail as $0.1\hat{l}$. We assume the body to be of uniform span ($2l_y = 0.1$) and uniform mass distribution. The volume of the body is $0.0018\hat{l}^3$. Mass is non dimensionalised with respect to $\hat{\rho}_b\hat{l}^3$, giving $M_b = 0.018$. Note that the dimensional values of length and swimming speed are $0.14m$ and $0.28ms^{-1}$ respectively giving a Reynolds number of

$$Re = \frac{\hat{U}_0\hat{l}}{\hat{\nu}} \approx 3.3 \times 10^4. \quad (5.46)$$

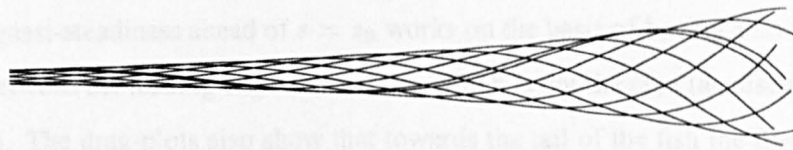


Figure 5.5: Figure to show the shape of the swimming motion of the eel, using a frame of reference in which the x -coordinate of the nose remains fixed.

The “eel” was impulsively started from rest at time $t = 0$. The boundary layer calculation was started at $t = T$. The system reaches a steady-state quickly (by $t = 3T$). Fig. 5.5 plots the position of the body at various times over one period in a frame of reference where the fish “holds station”

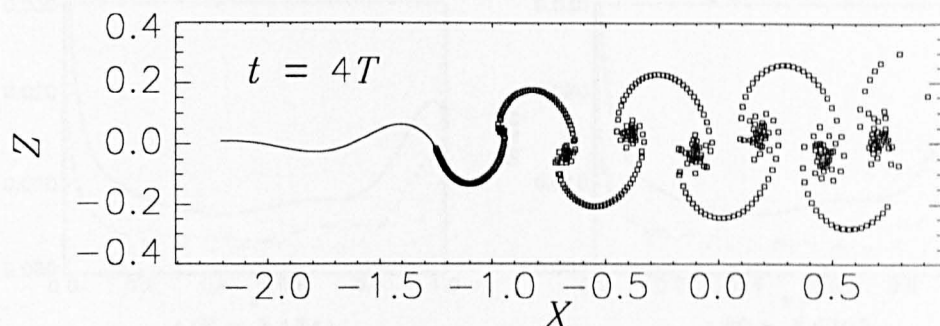


Figure 5.6: Plot of the swimming body (solid line) and its vortex wake. Each square indicates the position of a point vortex that was previously shed from the trailing edge (tail fin). As we expect, the wake rolls up into an arrangement of counter-rotating vortices.

in a uniform free stream, giving an impression of the shape of the animal as it swims. Fig. 5.6 is a plot of the body and the wake at time $t = 4T$. The solid line represents the body, with the squares indicating the positions of the point vortices making up the vortex wake.

Fig. 5.7 is a series of frames plotting the drag per unit length along the body as it varies with time. The broken lines indicate the value on the two sides of the body; the solid line is the sum of these two. In the region near the leading edge the flow is assumed to be quasi-steady Blasius, as described earlier. For this simulation we used $s_0 = 0.1$. The graphs here are quite smooth in the region of $s = 0.1$ which lends some weight to the quasi-steady assumption (for this case at least). However, the assumption of quasi-steadiness ahead of $s = s_0$ works on the basis of having a uniform outer velocity $U(s_0, t)$ between the leading edge and $s = s_0$, which is not the case (as discussed at the end of Section 5.4). The drag-plots also show that towards the tail of the fish the flow becomes rather different to the quasi-steady Blasius solution. It is reassuring to see that the solutions on either side of the plate are identical given a phase difference of $T/2$.

Fig. 5.8 plots the variation in the streamwise forces on the eel over one period. The solid line is the hydrodynamic thrust as calculated by the inviscid theory (panel method). The dotted line is the thrust minus the body inertia. In terms of the panel method calculation alone, this latter quantity represents an estimate of the viscous drag, if the fish is to move at the constant imposed swimming speed. The dashed line is the viscous drag as calculated by the boundary layer method. It is not

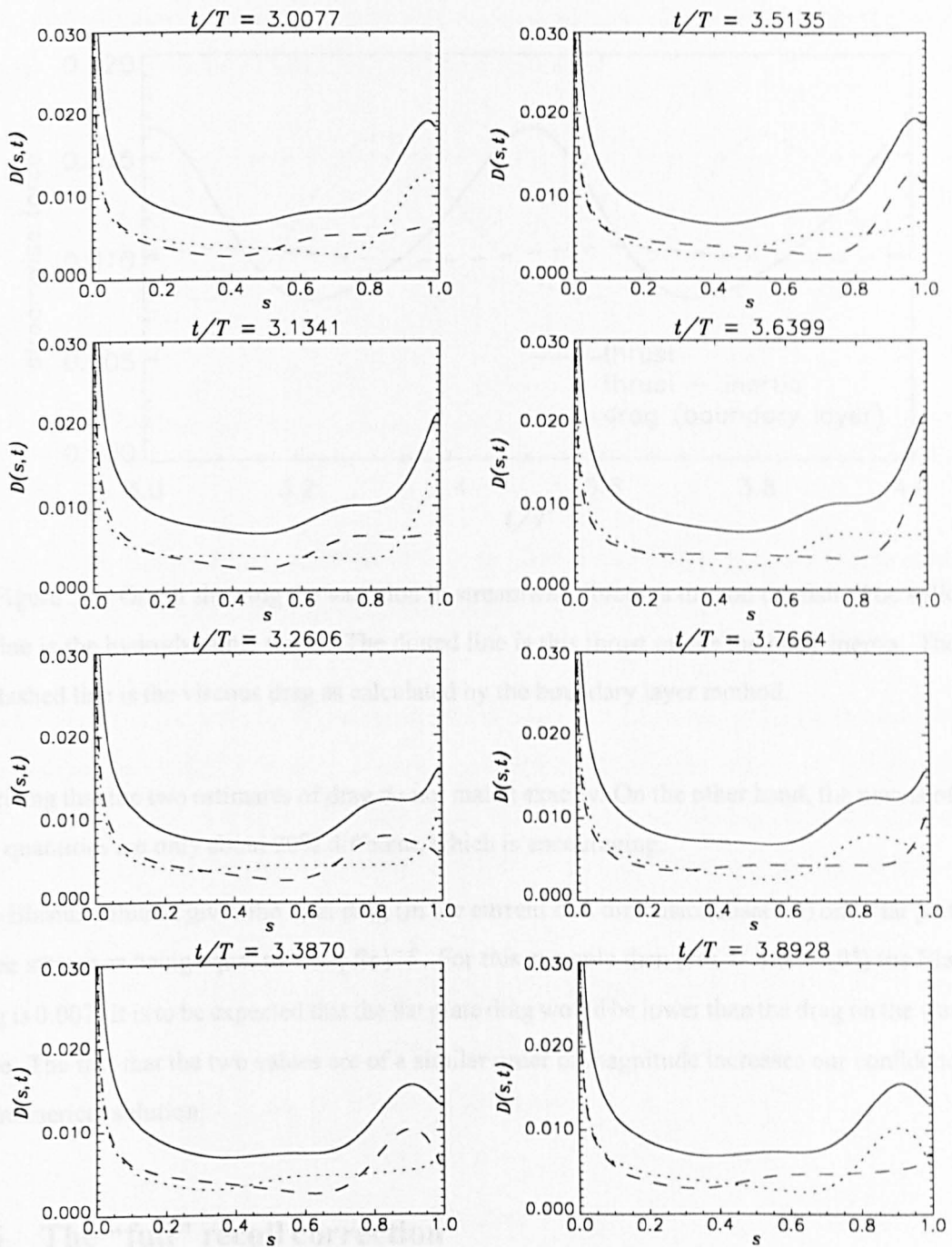


Figure 5.7: Series of graphs plotting the non dimensional drag per unit length along the body. The broken lines give the value on each side of the body, with the solid line being the sum of these two. The graphs should be read top to bottom, then left to right.

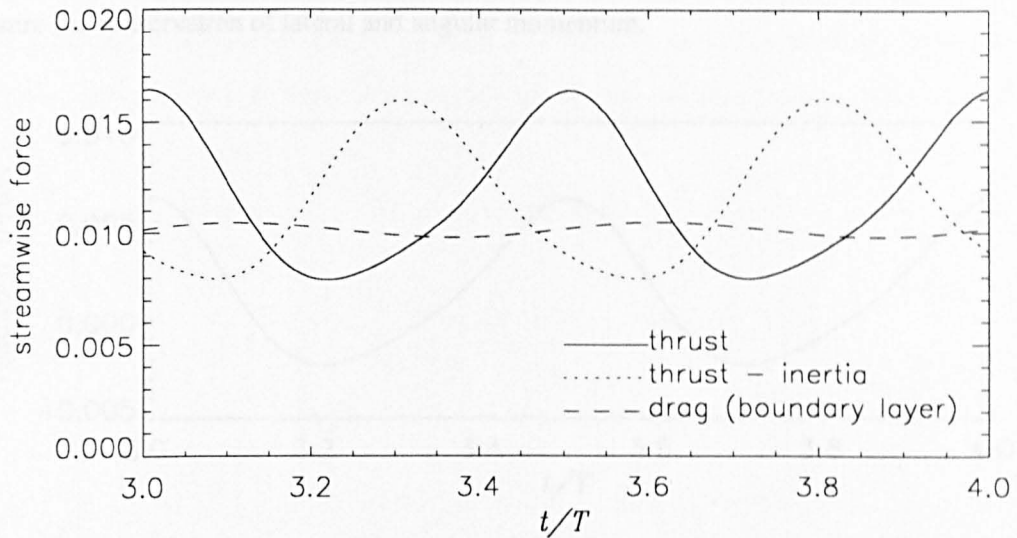


Figure 5.8: Graph showing the variation in streamwise forces acting on the fish. The solid line is the hydrodynamic thrust. The dotted line is this thrust minus the body inertia. The dashed line is the viscous drag as calculated by the boundary layer method.

surprising that the two estimates of drag do not match exactly. On the other hand, the means of the two quantities are only about 20% different, which is encouraging.

The Blasius solution gives the total drag (in the current non dimensionalisation) on a flat plate in a free stream as being equal to $1.33(Re)^{-\frac{1}{2}}$. For this example then ($Re \approx 3.3 \times 10^4$) the Blasius drag is 0.007. It is to be expected that the flat plate drag would be lower than the drag on the waving plate. The fact that the two values are of a similar order of magnitude increases our confidence in the numerical solution.

5.6 The “full” recoil correction

Until now we have not had a direct estimate of the drag on a swimming fish. Thus our model has assumed either that the drag must cancel the thrust, or that the drag must almost cancel the thrust resulting in oscillatory changes to the forward momentum that are small enough to neglect. On the other hand, by assuming that the viscous drag makes a negligible contribution to the

lateral hydrodynamic force and hydrodynamic moment we have used Lighthill's recoil correction to ensure the conservation of lateral and angular momentum.

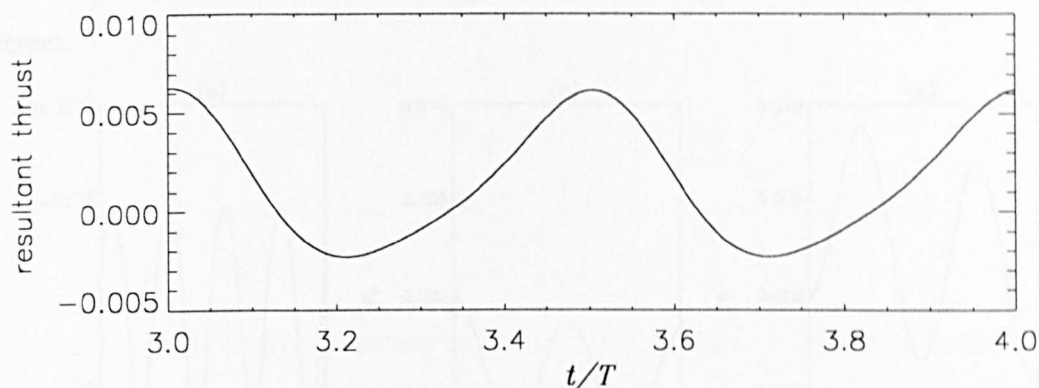


Figure 5.9: Graph of the total streamwise force (ie thrust minus drag) on the body against time. In this example conservation of momentum was not enforced.

Fig. 5.9 plots the variation in the resultant streamwise force (thrust – drag) on the fish, which suggests that there ought to be some change to the forward momentum of the fish. We implement this change to the motion as an extension to the recoil correction. That is, we add a rigid-body motion (translation $R_X(t), R_Z(t)$, rotation $\Theta(t)$) to the initially prescribed motion. Much as in Section 3.3 we define the “recoil functions”

$$T_R(R_X, R_Z, \Theta) = \text{streamwise hydrodynamic force} \quad (5.47a)$$

–rate of change of forward momentum,

$$L_R(R_X, R_Z, \Theta) = \text{lateral hydrodynamic force} \quad (5.47b)$$

–rate of change of lateral momentum,

$$M_R(R_X, R_Z, \Theta) = \text{hydrodynamic moment} \quad (5.47c)$$

–rate of change of angular momentum.

The recoil correction (R_X, R_Z, Θ) is the solution to the set of nonlinear equations:

$$T_R = 0, \quad (5.48a)$$

$$L_R = 0, \quad (5.48b)$$

$$M_R = 0. \quad (5.48c)$$

We solve this set of equations using the Newton method. Previously the recoil correction involved just two equations. Now we have three equations; but the implementation of the method is no different.

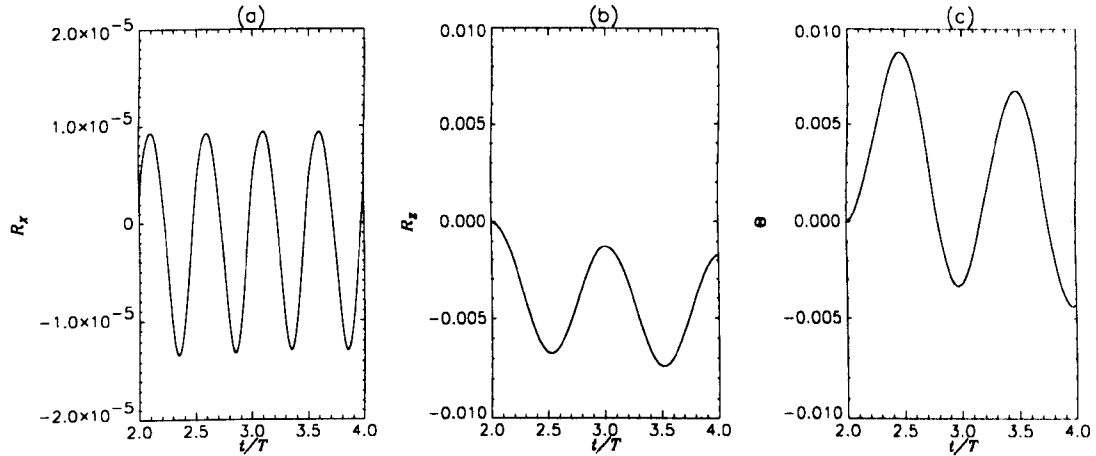


Figure 5.10: Graph to indicate the variation of the recoil parameters for the eel example including the full recoil correction (switched on at $t = 2T$). Note in particular that the streamwise recoil parameter is extremely small relative to the body length 1.

We used this full recoil correction with the large amplitude swimming example (“eel”) of the previous section. Fig. 5.10 plots the variation in the recoil parameters (a) $R_X(t)$, (b) $R_Z(t)$, (c) $\Theta(t)$ against time. As with previous results from the recoil correction (Section 3.4.1) there is some sideways drift, and some change to the direction of swimming. The important result in this case is that the variation in the streamwise motion is very small, providing evidence that the “old assumption” of constant swimming speed was a good one. Furthermore, re-plotting 5.9 with the new data, Fig. 5.11, we find that the adjustment to the streamwise momentum means that we have a resultant streamwise force (thrust – drag) on the fish with zero mean.

5.7 Conclusions

This chapter has been concerned with the boundary layer along the fish in the two-dimensional model. We have outlined a method for directly estimating the viscous drag per unit length along

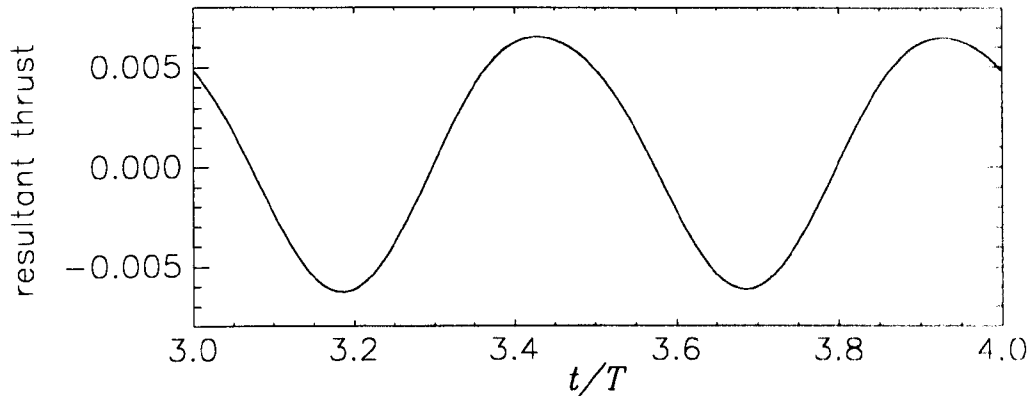


Figure 5.11: Graph of the resultant streamwise force (ie thrust minus drag) on the body against time. In contrast to Fig.5.9, for this example conservation of momentum was enforced.

the body as a function of position on the body, and time. The method used to calculate the recoil correction has been extended by making use of the viscous drag estimate to force the system to conserve momentum in the direction of swimming. Thus, the fish now has a variable forward speed calculated using the time dependent hydrodynamic forces acting upon its body.

The program to calculate the flow in the boundary layer was verified using a test case involving the boundary layer on a flat plate in an oscillating uniform stream. The results compared well with the previous work on this example problem. We also considered values of the amplitude of oscillation that would, in combination with values of the reduced frequency applicable to fish swimming, cause the model to break down.

The boundary layer solver was then used in conjunction with the panel method in an example of large-amplitude swimming. Initially the recoil correction was not included. We found the thrust and drag to ^{be} of a similar order of magnitude. Finally, using the same example, the full recoil correction was included in the calculation. The variation in the streamwise recoil parameter was found to be extremely small. The mean thrust on the fish was found to equal the mean drag, which means that the “recoiling” fish had a mean swimming speed close to the original, imposed swimming speed.

The boundary layer calculation described in this chapter could be improved in various ways.

- The differencing scheme should be improved so as to be second order in space and time.
- It would be preferable to be able to evaluate the quantities describing the flow at positions nearer to the leading edge.
- Ideally the theory should be developed to take account of the fact that the real boundary layer on the fish is three dimensional.
- We have not considered turbulence, other than to prescribe that the boundary layer be laminar. This point merits further study.

Chapter 6

The bending moment distribution

6.1 Introduction

We are now in a position to consider the internal mechanics; and the interaction between the internal mechanics and the hydrodynamics. This involves setting up a model for the fish body that is slightly different from that used in the fluid mechanical model. We start by outlining this model, and defining the problem with reference to the relevant terminology and assumptions from solid mechanics theory. It is possible to obtain a full “large-amplitude” description of the bending of the fish, from which we can consider certain simplifications as made by Wu (1971a); Cheng and Blickhan (1994); Hess and Videler (1984).

The calculations in this chapter are essentially independent of whether the hydrodynamics is done using a two-dimensional or three-dimensional theory. This is because the resulting hydrodynamic forces are expressed in terms of position along the body in the longitudinal sense only. That is, in the three-dimensional theory, the forces are integrated in the spanwise direction so as to be a function of s_X only. Given this point, we write $s = s_X$ to have a less cumbersome notation, (although in expressions involving s_Y, s_Z we retain the subscript X for clarity).

The description of the body deformations takes the form of a set of two or three coupled first order ordinary differential equations. There is a link between the boundary conditions of these equations and the recoil correction considered in earlier chapters. This connection is also discussed.

6.2 Derivation of the bending moment equations

To ensure that our model embodies the correct description of the solid mechanics we have referred to Wempner (1973). The first difficulty in describing the deformation of solids is to recognise and deal with the deformation of the coordinate system. In general this means using a notation that describes the geometry of the stresses and strains involved in the solid's deformation. Our model is simple enough to allow us to get the description right with the coordinate notation that we have already been using.

For the purposes of the internal mechanics we need to think in terms of the body, which is assumed to be an active bending "beam", having a non-zero thickness. We now go over the details of this "new geometry" and its non-dimensionalisation.

In dimensional variables the body is of length \hat{l}_X , uniform span $2\hat{l}_Y$, and has a total mass \hat{M}_b . For consistency, the inclusion of mass requires the inclusion of volume. We assume that the body density is uniform, and equal to the density of water, $\hat{\rho}_b = \hat{\rho}$. Consequently we have a body thickness, or depth distribution $\hat{l}_Z(\hat{s})$ such that

$$2\hat{l}_Y\hat{l}_Z(\hat{s})\hat{\rho} = \hat{m}_b(\hat{s}), \quad (6.1)$$

where $\hat{m}_b(\hat{s})$ is the mass per unit length and is related to the total mass \hat{M}_b by

$$\hat{M}_b = \int_0^{\hat{l}_X} \hat{m}_b(\hat{s}) d\hat{s}. \quad (6.2)$$

We non-dimensionalise lengths with respect to the body length \hat{l}_X , and mass with respect to density times volume:

$$M_b = \frac{\hat{M}_b}{\hat{\rho}\hat{l}_X^3}. \quad (6.3)$$

Note that in the two-dimensional model, quantities are thought of as being "per unit span". Thus, given the dimensional data, the two-dimensional model uses the non-dimensional mass per unit span:

$$M_b = \left(\frac{1}{2\hat{l}_Y} \right) \frac{\hat{M}_b}{\hat{\rho}\hat{l}_X^3}. \quad (6.4)$$

The mass distribution is defined in a manner consistent with equation (6.2):

$$M_b = \int_0^{\hat{l}_X} m_b(s) ds. \quad (6.5)$$

In other words $m_b(s)$ is the mass per unit length, per unit span. Thus, the depth distribution $l_Z(s)$ becomes

$$l_Z(s) = m_b(s). \quad (6.6)$$

The examples in this thesis assume a uniform mass distribution. However, the method is not actually limited in this sense, and so we retain the s -dependence in the theory.

A position vector of a point in the body is given by either

$$\mathbf{r}(s_X, s_Y, s_Z) = X\hat{\mathbf{i}} + Y\hat{\mathbf{j}} + Z\hat{\mathbf{k}} \quad (6.7)$$

where $\hat{\mathbf{i}}, \hat{\mathbf{j}}, \hat{\mathbf{k}}$ are the usual unit vectors in the global rectangular cartesian coordinate system; or

$$\mathbf{r}(s_X, s_Y, s_Z) = s_X\hat{\mathbf{t}} + s_Y\hat{\mathbf{b}} + s_Z\hat{\mathbf{n}}. \quad (6.8)$$

The unit vectors $\hat{\mathbf{t}}, \hat{\mathbf{b}}$ and $\hat{\mathbf{n}}$ give the directions of the so-called ‘‘convected lines’’, (which might otherwise be labelled $\hat{\mathbf{e}}_1, \hat{\mathbf{e}}_2, \hat{\mathbf{e}}_3$). We work in terms of the coordinate system defined by these three directions (which vary with s_X). The displacement is a function of s_X and t . For a given material point, the longitudinal position s_X is constant: the motion is represented by the change in the base vectors $\hat{\mathbf{t}}, \hat{\mathbf{b}}$ and $\hat{\mathbf{n}}$. The nature of our model means that $\hat{\mathbf{b}} = \hat{\mathbf{j}}$.

We assume the body can be modelled using the Bernoulli-Euler Theory of beams. As is common in beam and shell theory this requires that cross-sections of the beam are assumed to remain plane and normal to the bending axis. We neglect deformations of the cross-sections and so the only non-zero (or non-negligible) strains are in the s_X -direction. These strains (extensional outside the reference line s_X -axis, compressive inside) are assumed small, requiring that $\kappa l_Z \ll 1$ where κ is the curvature of the s_X -axis. The assumptions inherent in modelling the fish as a Bernoulli-Euler beam do not preclude large-amplitude bending (‘‘finite rotations’’), or geometric nonlinearity.

Note also that (from differential geometry) the curvature $\kappa(s)$ relates the normal and tangent vectors:

$$\frac{\partial \hat{\mathbf{t}}}{\partial s} = \kappa \hat{\mathbf{n}}, \quad (6.9a)$$

$$\frac{\partial \hat{\mathbf{n}}}{\partial s} = -\kappa \hat{\mathbf{t}}. \quad (6.9b)$$

We consider an element δs of the beam, as shown in Fig. 6.1. F and G are respectively the components perpendicular and parallel to the centreline; they are also the integrated shear and

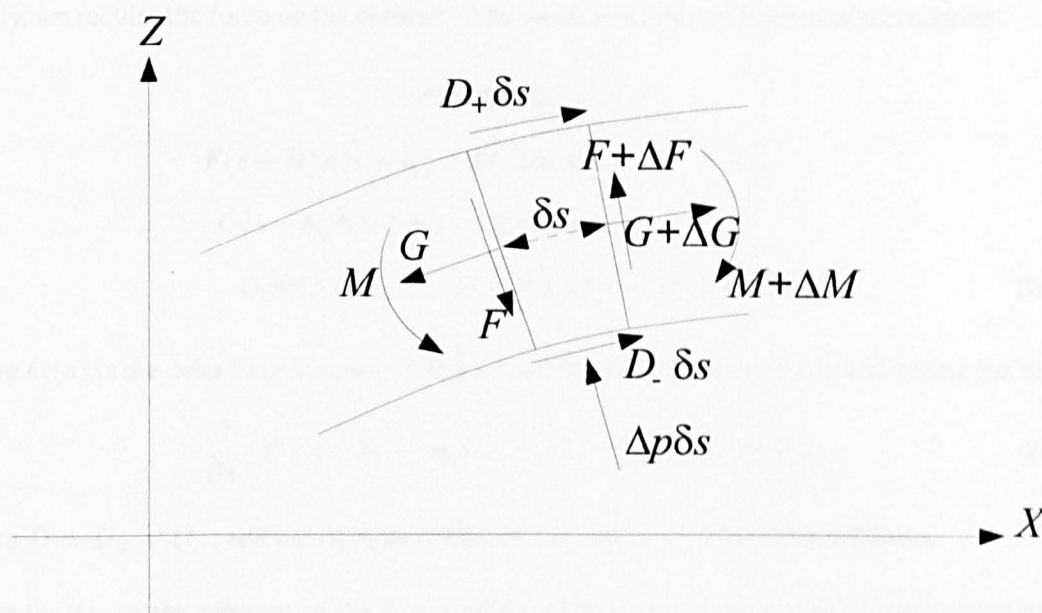


Figure 6.1: Sketch of forces and moments acting on element δs of the bending fish, modelled using the Bernoulli-Euler beam theory. F and G are the components of the internal force, with M being the bending moment. Δp and D_{\pm} are the normal and tangential components of the hydrodynamic force per unit length (as functions of s_X only, having been integrated across the span).

normal stresses on the transverse surface of the cross-sectional element δs . Δp and D_{\pm} are the normal and tangential components of the hydrodynamic force per unit length. Δp is due to the pressure jump, and D to the viscous drag (which is different on each side of the body). M is the total bending moment which is made up of the active bending due to muscular contractions along the fish's body, and the passive bending due to the elastic properties of the body tissues. The suction force must also be included at the nose $s = 0$.

The position, velocity and acceleration of the element are described in terms of the position vector $\mathbf{r}(s, t)$ of the point at the centre of the beam element. (That is the centre of the element in the longitudinal sense, and the centroid of the element when viewed as a cross-section.) The cross-section itself, a rigid-body with mass $\delta s m_b(s)$ has angular velocity ω , which is a vector in the Y -direction. That is

$$\omega = \omega_2 \hat{j}. \quad (6.10)$$

Firstly, we require the force on the element to be equal to its rate of change of momentum:

$$\begin{aligned}
 & -\delta^*(s)T_s\hat{t}(0)\delta s + \\
 & F(s + \delta s)\hat{n}(s + \delta s) - F(s)\hat{n}(s) + \\
 & G(s + \delta s)\hat{t}(s + \delta s) - G(s)\hat{t}(s) + \\
 & \Delta p\hat{n}(s)\delta s + (D_- + D_+)\hat{t}(s)\delta s = m_b(s)\delta s\ddot{\mathbf{r}}(s, t).
 \end{aligned} \tag{6.11}$$

where $\delta^*(s)$ is the delta function, and T_s is the suction force. Dividing by δs and taking the limit:

$$\frac{\partial}{\partial s} [F\hat{n} + G\hat{t}] = m_b\ddot{\mathbf{r}} - \Delta p\hat{n} - D\hat{t} + \delta^*(s)T_s\hat{t}(0), \tag{6.12}$$

where $D = D_+ + D_-$; and the right hand side of this equation is considered known.

Secondly we set the moment of the forces on the element about its centre of mass equal to the element's rate of change of angular momentum about its centre of mass. We let \mathbf{H} be the angular momentum per unit mass about the centre of mass, so the cross-section has angular momentum $\delta s m_b \mathbf{H}$ about its centre of mass.

Thus we have

$$M(s + \delta s) - M(s) - F\delta s + \delta s(D_+ - D_-)l_Z = \delta s m_b(s)\dot{\mathbf{H}}_2, \tag{6.13}$$

$$\frac{\partial M}{\partial s} - F + (D_+ - D_-)l_Z = m_b\dot{\mathbf{H}}_2. \tag{6.14}$$

Taking normal and tangential components of the force balance equation (6.12), the full set of three coupled first order ordinary differential equations is:

$$\frac{\partial F}{\partial s} = -G\kappa + m_b\ddot{\mathbf{r}} \cdot \hat{n} - \Delta p \tag{6.15a}$$

$$\frac{\partial G}{\partial s} = F\kappa + m_b\ddot{\mathbf{r}} \cdot \hat{t} - D + \delta^*(s)T_s \tag{6.15b}$$

$$\frac{\partial M}{\partial s} = F - (D_+ - D_-)l_Z + m_b\dot{\mathbf{H}}_2. \tag{6.15c}$$

Since the two ends of the body are free (ie not attached to anything) we can state on physical grounds that the equations (6.15) are subject to the boundary conditions that F, G and M are all zero at the end points $s = 0$ and $s = l$. Equations (6.15) are the non-trivial components of the full vector

equations (6.91) in Wempner (1973): the equations of motion for finite rotations in a Bernoulli-Euler beam.

Wempner, equations(6.92), goes on to give linear approximations of equations(6.15) for small rotations (effectively small curvature in our case):

$$\frac{\partial F}{\partial s} = m_b \frac{\partial^2 Z}{\partial t^2} - \Delta p \quad (6.16a)$$

$$\frac{\partial G}{\partial s} = -D + \delta^*(s)T_s \quad (6.16b)$$

$$\frac{\partial M}{\partial s} - F + (D_+ - D_-)l_Z = m_b \dot{H}_2. \quad (6.16c)$$

Therefore, assuming the hydrodynamic couple and the mass-element's angular momentum to be negligible, equation(6.16b) is decoupled, and we obtain

$$\frac{\partial M}{\partial s} = F \quad (6.17a)$$

$$\frac{\partial F}{\partial s} = m_b \frac{\partial^2 Z}{\partial t^2} - \Delta p, \quad (6.17b)$$

as given by Cheng and Blickhan (1994) and Hess and Videler (1984) with boundary conditions $F(0) = F(l) = M(0) = M(l) = 0$.

Cheng (following Wu (1971a)) and Hess and Videler neglected both the rotational inertia and the hydrodynamic couple from the outset. Hess and Videler started from the assumption that the longitudinal forces could be neglected. Wu (and hence Cheng) explicitly stated that the thrust and drag would be approximately uniformly distributed along the body so that G and D would be small everywhere. Regardless of the derivation, the final system of equations and boundary conditions is the same in each case.

6.2.1 The boundary conditions and recoil correction

The sets of equations derived in the previous section (both the simplified model with two equations, and the full model with three equations) appear to have twice as many boundary conditions as equations. To explain why this does not pose a real problem, we look first at equations (6.17).

In this case we integrate equation (6.17b):

$$F(l, t) - F(0, t) = \int_0^l \left(m_b \frac{\partial^2 Z}{\partial t^2} - \Delta p \right) ds. \quad (6.18)$$

According to the first recoil condition (that the lateral force be equal to the lateral rate of change of momentum) the right hand side of equation (6.18) is zero. Hence we have

$$F(l, t) = F(0, t). \quad (6.19)$$

Similarly, integrating equation (6.17a),

$$\begin{aligned} M(l, t) - M(0, t) &= \int_0^l F ds \\ &= [sF]_0^l - \int_0^l s \frac{\partial F}{\partial s} ds, \end{aligned} \quad (6.20)$$

(by parts), so that

$$\begin{aligned} -M(l, t) + M(0, t) - lF(l, t) &= \int_0^l s \frac{\partial F}{\partial s} ds \\ &= \int_0^l s \left(m_b \frac{\partial^2 Z}{\partial t^2} - \Delta p \right) ds. \end{aligned} \quad (6.21)$$

The right hand side of equation (6.21) is zero by the second recoil condition (that the total moment on the body be equal to the rate of change of angular momentum about some fixed axis), giving

$$M(l, t) - M(0, t) + lF(l, t) = 0 \quad (6.22)$$

Setting the conditions at the nose to be $F(0, t) = M(0, t) = 0$, equation (6.19) gives us $F(l, t) = 0$, and so consequently by equation (6.22) we also have $M(l, t) = 0$.

So the system is entirely described by two equations and two boundary conditions provided the recoil conditions are satisfied. In our calculations, the recoil correction is made before any attempt is made to solve for the bending moment distribution. Hence, enforcing the boundary conditions at the nose means, in principle, that the boundary conditions at the tail are satisfied automatically. The problem then is routine, and $M(s, t)$ can be found by a two-dimensional Runge-Kutta method (Press *et al.*, 1996).

We can obtain a similar result in the case of the full equations. This is best explained by putting the equations in vector form. Consequently, equations (6.15) become

$$\frac{\partial \mathbf{F}}{\partial s} = m_b \ddot{\mathbf{r}} - \mathbf{P} \quad (6.23a)$$

$$\frac{\partial \mathbf{M}}{\partial s} + \dot{\mathbf{i}} \wedge \mathbf{F} + \mathbf{C} = m_b \dot{\mathbf{H}}. \quad (6.23b)$$

Note that \mathbf{P} is the total external (hydrodynamic) force (resulting from the pressure, drag and suction forces), \mathbf{F} is the internal force (the resultant of components F and G), \mathbf{C} is the external couple on the cross-section about its centre of mass (due to the difference in drag on each side of the body), and \mathbf{H} is the cross-section's angular momentum per unit mass about its centre of mass. In our case, there are only three non-trivial components of equations (6.23): equation (6.23a) can be split into its tangential and normal components (equations (6.15a) and (6.15b)), and equation (6.23b) reduces to a single component in the Y -direction (equation (6.15c)).

We must also extend the original recoil conditions to a full vector description of the recoil:

- the rate of change of momentum of the fish must equal the total force with which the water acts upon it;
- the rate of change of angular momentum of the fish about a fixed axis must equal the total moment of forces about the fixed axis with which the water acts upon it.

In the notation of equations (6.23) these conditions are expressed as follows:

$$\int_0^l m_b \ddot{\mathbf{r}} ds = \int_0^l \mathbf{P} ds \quad (6.24a)$$

$$\int_0^l (\mathbf{r} \wedge m_b \ddot{\mathbf{r}} + m_b \dot{\mathbf{H}}) ds = \int_0^l (\mathbf{r} \wedge \mathbf{P} + \mathbf{C}) ds \quad (6.24b)$$

Integrating equation (6.23a):

$$[\mathbf{F}]_0^l = \int_0^l (m_b \ddot{\mathbf{r}} - \mathbf{P}) ds \quad (6.25)$$

which, by equation (6.24a) gives

$$\mathbf{F}(0, t) = \mathbf{F}(l, t). \quad (6.26)$$

If we now take the cross product of \mathbf{r} with equation (6.23a) and integrate along the body, we obtain

$$[\mathbf{r} \wedge \mathbf{F}]_0^l - \int_0^l \frac{\partial \mathbf{r}}{\partial s} \wedge \mathbf{F} ds = \int_0^l \mathbf{r} \wedge (m_b \ddot{\mathbf{r}} - \mathbf{P}) ds. \quad (6.27)$$

Note that (since s is the arc length)

$$\frac{\partial \mathbf{r}}{\partial s} = \hat{\mathbf{i}}. \quad (6.28)$$

Integrating equation (6.23b)

$$\int_0^l \hat{\mathbf{i}} \wedge \mathbf{F} ds = -[\mathbf{M}]_0^l + \int_0^l (m_b \dot{\mathbf{H}} - \mathbf{C}) ds, \quad (6.29)$$

so that, substituting into equation (6.27),

$$[\mathbf{r} \wedge \mathbf{F}]_0^l + [\mathbf{M}]_0^l - \int_0^l (m_b \dot{\mathbf{H}} - \mathbf{C}) ds = \int_0^l \mathbf{r} \wedge (m_b \ddot{\mathbf{r}} - \mathbf{P}) ds, \quad (6.30)$$

and hence

$$[\mathbf{r} \wedge \mathbf{F}]_0^l + [\mathbf{M}]_0^l = \int_0^l [\mathbf{r} \wedge (m_b \ddot{\mathbf{r}} - \mathbf{P}) + (m_b \dot{\mathbf{H}} - \mathbf{C})] ds. \quad (6.31)$$

But by the second recoil condition, equation (6.24b), the right hand side of equation (6.31) is zero:

$$[\mathbf{r} \wedge \mathbf{F}]_0^l + [\mathbf{M}]_0^l = 0. \quad (6.32)$$

As in the simpler case we note that the boundary conditions allow us to specify the values of \mathbf{F} and \mathbf{M} at the nose: $\mathbf{F}(0, t) = \mathbf{M}(0, t) = 0$, so that by equation (6.26) we have $\mathbf{F}(l, t) = 0$, and consequently (equation (6.32)) $\mathbf{M}(l, t) = 0$.

Thus we have shown that for the full vector system of equations we have the same number of boundary conditions as equations because satisfying the recoil conditions causes the values of the internal force and bending moment to be equal at the two free ends of the body.

6.2.2 The angular momentum

The expression for the angular momentum of a cross-sectional element in terms of the position vector of its centroid is not obvious, and so we now derive the relevant expressions.

In the current model the angular velocity, and hence angular momentum, are vectors for which the only non-zero component is in the Y -direction. The angular momentum per unit mass of the cross section about its centre of mass is therefore given by

$$H_2 = I_{33}\omega_2, \quad (6.33)$$

where

$$I_{33} = \int \int s_Z^2 dA, \quad (6.34)$$

dA being an element of area of the cross section.

In Fig. 6.2, let the tangent at O be $\hat{\mathbf{t}}_0$, with the velocity there $\dot{\mathbf{r}}_0$. If the angular velocity is ω , then the velocity at s and $s + \delta s$ is given by

$$\dot{\mathbf{r}}(s + \delta s) = \dot{\mathbf{r}}_0 + \omega \wedge \hat{\mathbf{t}}_0 \left(\frac{\delta s}{2} \right), \quad (6.35)$$

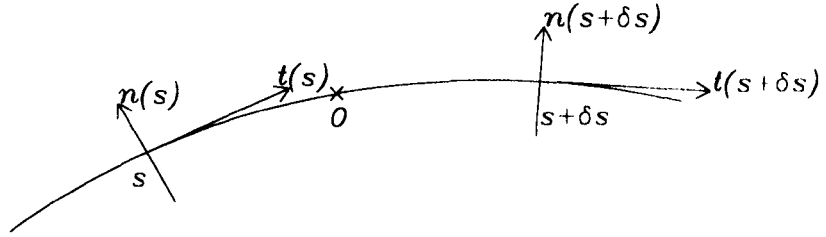


Figure 6.2: Sketch of an element of the body's bending centreline. We require an expression for the angular velocity ω at O .

$$\dot{\mathbf{r}}(s) = \dot{\mathbf{r}}_0 - \omega \wedge \hat{\mathbf{t}}_0 \left(\frac{\delta s}{2} \right). \quad (6.36)$$

Hence

$$\frac{\partial \dot{\mathbf{r}}}{\partial s} = \omega \wedge \hat{\mathbf{t}}. \quad (6.37)$$

Taking the vector product of $\hat{\mathbf{t}}$ with equation (6.37)

$$\omega = \hat{\mathbf{t}} \wedge \frac{\partial \dot{\mathbf{r}}}{\partial s}. \quad (6.38)$$

We need to write the velocity vector in terms of its components normal and tangential to the body:

$$\dot{\mathbf{r}} = (\dot{\mathbf{r}} \cdot \hat{\mathbf{t}}) \hat{\mathbf{t}} + (\dot{\mathbf{r}} \cdot \hat{\mathbf{n}}) \hat{\mathbf{n}}, \quad (6.39)$$

and noting that

$$\frac{\partial \hat{\mathbf{t}}}{\partial s} = \kappa \hat{\mathbf{n}}, \quad (6.40)$$

$$\frac{\partial \hat{\mathbf{n}}}{\partial s} = -\kappa \hat{\mathbf{t}}, \quad (6.41)$$

then

$$\frac{\partial \dot{\mathbf{r}}}{\partial s} = \left[\frac{\partial}{\partial s} (\dot{\mathbf{r}} \cdot \hat{\mathbf{t}}) - \kappa (\dot{\mathbf{r}} \cdot \hat{\mathbf{n}}) \right] \hat{\mathbf{t}} + \left[\kappa (\dot{\mathbf{r}} \cdot \hat{\mathbf{t}}) + \frac{\partial}{\partial s} (\dot{\mathbf{r}} \cdot \hat{\mathbf{n}}) \right] \hat{\mathbf{n}}. \quad (6.42)$$

Thus by equation (6.38)

$$\omega = - \left(\frac{\partial \dot{\mathbf{r}}}{\partial s} \cdot \hat{\mathbf{n}} \right) \hat{\mathbf{b}}, \quad (6.43)$$

and so

$$\begin{aligned} \dot{\omega} &= - \frac{\partial}{\partial t} \left(\frac{\partial \dot{\mathbf{r}}}{\partial s} \cdot \hat{\mathbf{n}} \right) \hat{\mathbf{b}} \\ &= - \left(\frac{\partial \ddot{\mathbf{r}}}{\partial s} \cdot \hat{\mathbf{n}} + \frac{\partial \dot{\mathbf{r}}}{\partial s} \cdot \dot{\hat{\mathbf{n}}} \right) \hat{\mathbf{b}} \\ &= - \left(\frac{\partial \ddot{\mathbf{r}}}{\partial s} \cdot \hat{\mathbf{n}} + \omega \frac{\partial \dot{\mathbf{r}}}{\partial s} \cdot \hat{\mathbf{t}} \right) \hat{\mathbf{b}}. \end{aligned} \quad (6.44)$$

Substituting for ω from equation (6.43):

$$\dot{\omega} = \left[- \left(\frac{\partial \ddot{\mathbf{r}}}{\partial s} \cdot \hat{\mathbf{n}} \right) + \left(\frac{\partial \dot{\mathbf{r}}}{\partial s} \cdot \hat{\mathbf{n}} \right) \left(\frac{\partial \dot{\mathbf{r}}}{\partial s} \cdot \hat{\mathbf{t}} \right) \right] \hat{\mathbf{b}}. \quad (6.45)$$

In order to compute this quantity we must realise that the position vector \mathbf{r} is the position vector of a material point of the body expressed in the inertial frame of reference where the fluid is at rest far from the fish. In other words, returning to the notation of the previous chapters:

$$\mathbf{r}(s_X, s_Y, s_Z) = X(s_X, t)\hat{\mathbf{i}} + Z(s_X, t)\hat{\mathbf{k}}. \quad (6.46)$$

Furthermore, these terms include not only the deformation and imposed constant forward swimming of the fish, but also the recoil correction. Equations (3.14) and (3.15) give the cartesian coordinates of $\dot{\mathbf{r}}$ and $\ddot{\mathbf{r}}$.

It is straightforward to obtain their derivatives with respect to s_X :

$$\frac{\partial \dot{X}}{\partial s} = \frac{\partial \dot{h}_x}{\partial s} \cos \Theta - \frac{\partial h_x}{\partial s} \dot{\Theta} \sin \Theta - \frac{\partial \dot{h}_z}{\partial s} \sin \Theta - \frac{\partial h_z}{\partial s} \dot{\Theta} \cos \Theta, \quad (6.47a)$$

$$\frac{\partial \dot{Z}}{\partial s} = \frac{\partial \dot{h}_z}{\partial s} \cos \Theta - \frac{\partial h_z}{\partial s} \dot{\Theta} \sin \Theta + \frac{\partial \dot{h}_x}{\partial s} \sin \Theta + \frac{\partial h_x}{\partial s} \dot{\Theta} \cos \Theta \quad (6.47b)$$

$$\frac{\partial \ddot{X}}{\partial s} = \left(\frac{\partial \ddot{h}_x}{\partial s} - \frac{\partial h_x}{\partial s} \dot{\Theta}^2 - 2 \frac{\partial \dot{h}_z}{\partial s} \dot{\Theta} - \frac{\partial h_z}{\partial s} \ddot{\Theta} \right) \cos \Theta + \left(\frac{\partial h_z}{\partial s} \dot{\Theta}^2 - 2 \frac{\partial \dot{h}_x}{\partial s} \dot{\Theta} - \frac{\partial h_x}{\partial s} \ddot{\Theta} - \frac{\partial \ddot{h}_z}{\partial s} \right) \sin \Theta \quad (6.48a)$$

$$\frac{\partial \ddot{Z}}{\partial s} = \left(\frac{\partial \ddot{h}_z}{\partial s} - \frac{\partial h_z}{\partial s} \dot{\Theta}^2 + 2 \frac{\partial \dot{h}_x}{\partial s} \dot{\Theta} + \frac{\partial h_x}{\partial s} \ddot{\Theta} \right) \cos \Theta + \left(\frac{\partial \ddot{h}_x}{\partial s} - 2 \frac{\partial \dot{h}_z}{\partial s} \dot{\Theta} - \frac{\partial h_z}{\partial s} \ddot{\Theta} - \frac{\partial h_x}{\partial s} \dot{\Theta}^2 \right) \sin \Theta. \quad (6.48b)$$

but note that the recoil terms are calculated numerically, and in particular the time derivatives involve backward differences.

Thus, we have all the quantities that we require in order to calculate $m_b \dot{H}_2$, the term due to the angular momentum of a cross-sectional element of the beam.

6.3 Small amplitude swimming

As a simple check we use a small amplitude swimming example: the parameters are given in Table 6.1. This is of little biological significance and we use it simply to illustrate the resulting

A	α	B	β	b	k	ω	ξ
0.005	0.0	0.012	1.0	0.0	2π	$5\pi/2$	0.0

Table 6.1: Table of the kinematic parameters used in small amplitude swimming simulation to obtain a test solution for the bending moment distribution.

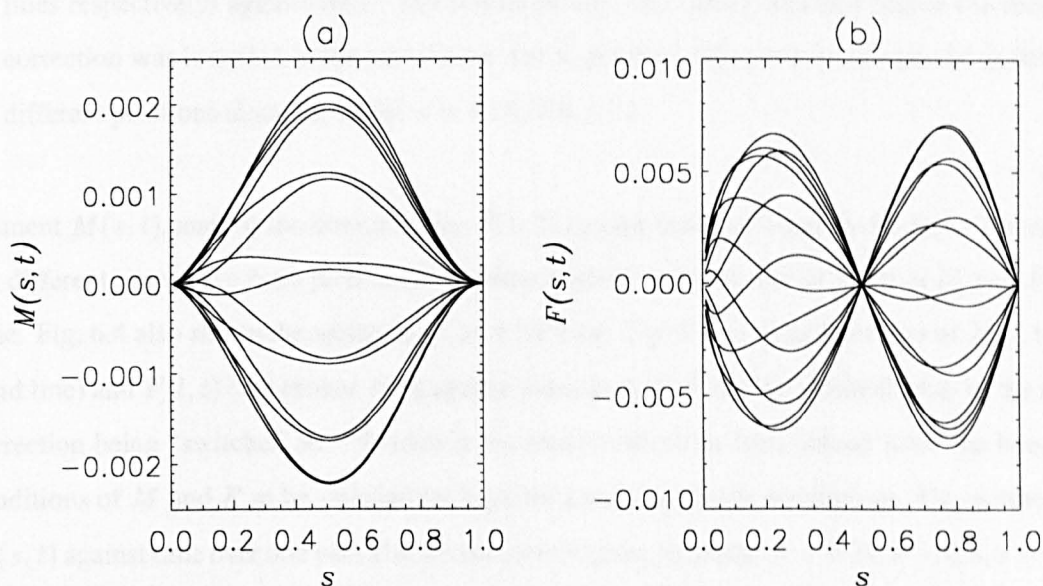


Figure 6.3: Graphs to show (a) the bending moment $M(s, t)$, and (b) the internal force $F(s, t)$ against position along the body. The curves are plotted for a number of equally spaced time steps. The time-interval between the plotted curves has been arranged so that the graphs are not simply symmetric in $M = 0$ and $F = 0$.

distributions of the bending moment, M , and internal force F . Fig. 6.3 shows (a) the bending

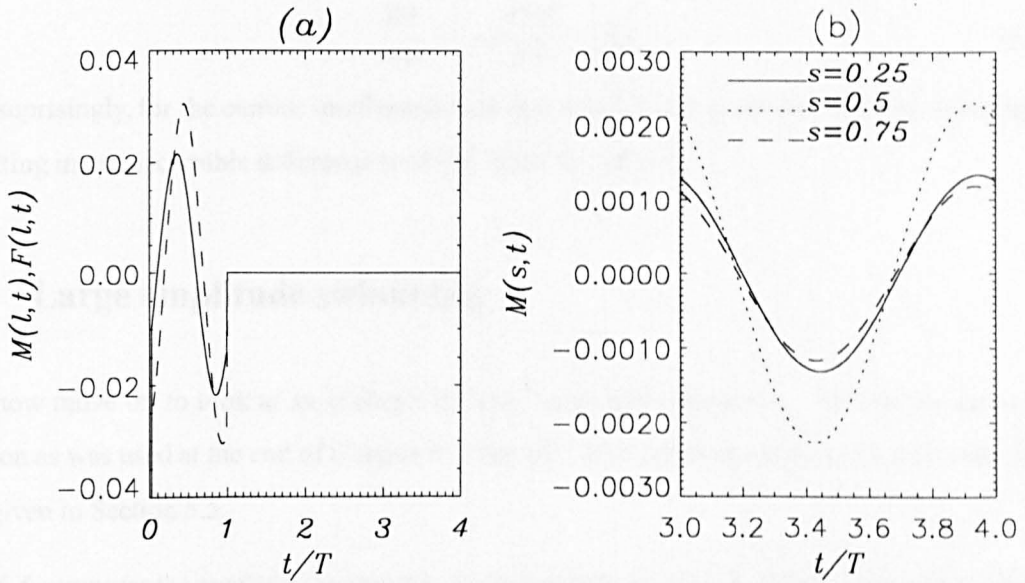


Figure 6.4: (a) The variation of $M(l,t)$ and $F(l,t)$ (indicated by the solid and broken lines respectively) against time. The results include the values obtained before the recoil correction was included in the calculation. (b) A graph of $M(s,t)$ over one period at three different positions along the body: $s = 0.25, 0.5, 0.75$.

moment $M(s,t)$, and (b) the internal force $F(s,t)$ against position along the body, s . The results for different times have been plotted on the same graph to indicate the variation in M and F with time. Fig. 6.4 also shows the variation of M with time. Fig. 6.4(a) plots the value of $M(l,t)$ (the solid line) and $F(l,t)$ (the broken line) against time, including results obtained prior to the recoil correction being “switched on”. Evidently the recoil correction does indeed force the boundary conditions of M and F to be satisfied (at least for small amplitude swimming). Fig. 6.4(b) plots $M(s,t)$ against time over one period at several points along the body: $s = 0.25, s = 0.5, s = 0.75$. It seems then that for this example M is almost a standing wave.

We have also considered the inclusion of a term associated with the moment of inertia of each cross-sectional element of the beam. This term has previously been neglected (Hess and Videler, 1984; Cheng and Blickhan, 1994). Its inclusion alters equations (6.17):

$$\frac{\partial M}{\partial s} = F + m_b \dot{H}_2 \quad (6.49a)$$

$$\frac{\partial F}{\partial s} = m_b \frac{\partial^2 Z}{\partial t^2} - \Delta p, \quad (6.49b)$$

Not suprisingly, for the current small-amplitude example the new term was found to be negligible, resulting in no discernible difference to the solution for $M(s, t)$.

6.4 Large amplitude swimming

We now move on to look at an example of large amplitude swimming. We use the same input motion as was used at the end of Chapter 5: “the eel”. The kinematic parameters and other details are given in Section 5.5.

Fig. 6.5 compares the result for the variation in the bending moment distribution over time, obtained via the large amplitude equations (solid curves) and the small amplitude equations (broken lines). The two sets of curves are quite similar. For the current example this is probably to be expected, since the body of our “steadily swimming eel” does not have a large curvature. Indeed, the main difference between the two sets of results seems to stem from the varying extent to which the models violate the boundary condition $M(l, t) = 0$. (An explanation of this is given below.)

We assume for the moment that the small curvature equations represents the “better solution” as the error in $M(l, t)$ is smaller. Fig.6.6 plots $M(s, t)$ against time at intervals of 0.1 along the body. In Fig.6.6(a) the solid lines indicate the variation in the bending moment at $s = 0$ and $s = 0.5$. The broken lines show the situation for $s = 0.1, 0.2, 0.3, 0.4$ (the maximum amplitude increases with s up to $s = 0.5$). Fig.6.6(b) plots the results between $s = 0.5$ and $s = 1.0$. The solid lines are for $s = 0.5$ and $s = 1.0$ (the maximum amplitude decreases between $s = 0.5$ and $s = 1.0$).

The results suggest that for the current example the bending moment behaves as a travelling wave; at least over the middle portion of the body. Fig.6.6(b) also indicates that the behaviour becomes more nonlinear towards the tail of the fish, although this may be an artefact of the error at $s = l$.

It is assumed that the wave of maximum bending moment can be thought of as corresponding to the wave of muscle activation; a positive bending moment implying muscle contractions on one side of the body, and a negative bending moment implying contractions on the other side of the body. Strictly speaking the bending moment distribution that we have calculated is the

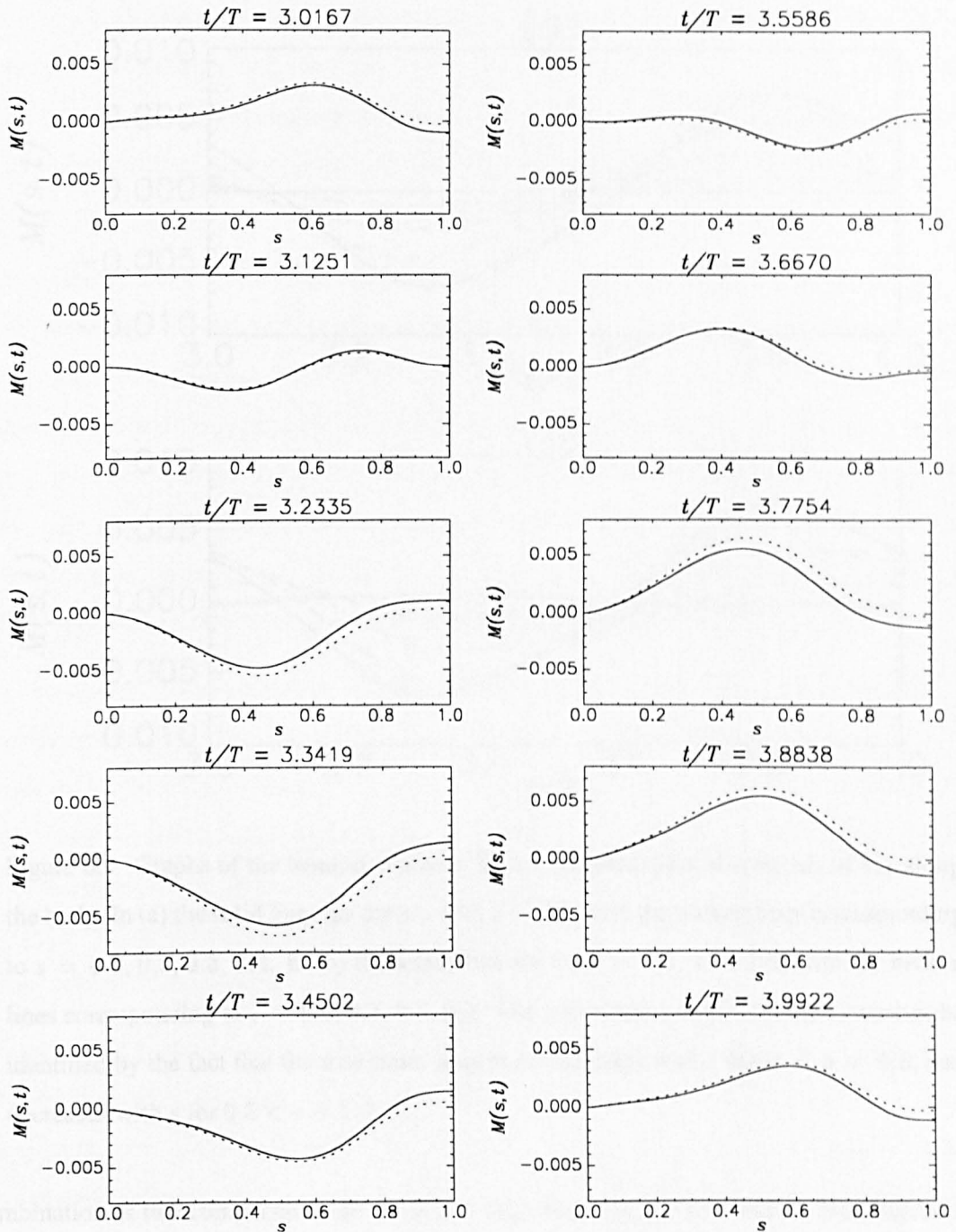


Figure 6.5: Graphs to show the variation in the bending moment distribution over one period. The system was solved using both the large amplitude equations (solid lines), and the small amplitude equations (broken lines). The order of the graphs is top to bottom, left to right.

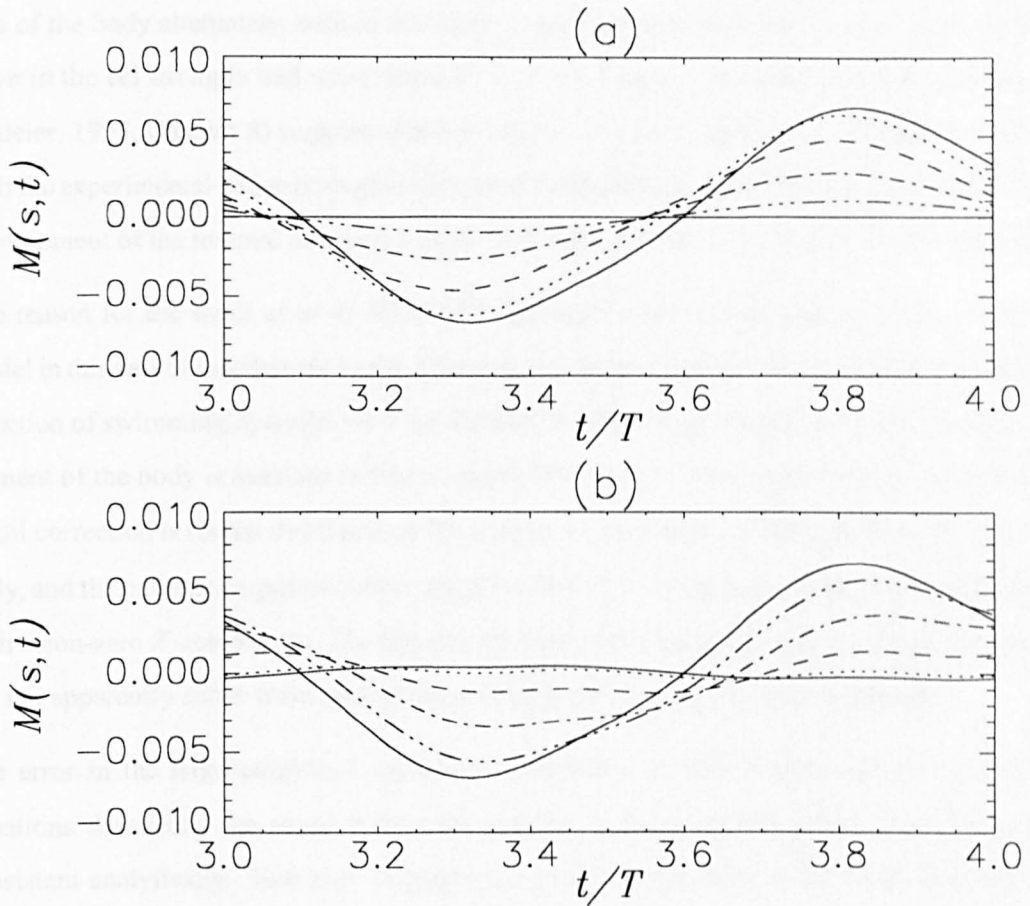


Figure 6.6: Graphs of the bending moment $M(s, t)$ against time, at intervals of 0.1 along the body. In (a) the solid lines are for $s = 0.0, s = 0.5$, with the broken lines corresponding to $s = 0.1, 0.2, 0.3, 0.4$. In (b) the solid lines are for $s = 0.5, s = 1.0$, with the broken lines corresponding to $s = 0.6, 0.7, 0.8, 0.9$. The intermediate results in each case can be identified by the fact that the maximum amplitude increases with s for $0 < s < 0.5$, and decreases with s for $0.5 < s < 1.0$.

combination of two components: $M = M_m + M_p$, where M_m is the “active” bending moment due to muscle contractions, and M_p the “passive” contribution associated with the mechanical properties of the other body tissues (Cheng *et al.*, 1998). Experimental measurements of the wave of muscle activation in swimming fish suggest that such a wave travels alternately down each side of the body, with a wave speed that is greater than that of the undulation wave, (eg Videler, 1993). From Fig. 6.6 we conclude that the maximum bending moment does indeed travel down each

side of the body alternately, with in this case, a wave speed of approximately 6. (The undulation wave in the eel example had wave speed $V \approx 1.4$). Data on the muscle activation wave in eel (Videler, 1993, Chapter 8) suggests that our results are in the “right area”. A proper comparison with the experimental data will require the use of a more realistic mass distribution, and the further development of the internal mechanics model following Cheng *et al.* (1998), as discussed above.

The reason for the small error in $M(l, t)$ for the small amplitude equations is easy to see. The model in this case is based on the normal forces being directed along a direction perpendicular to the direction of swimming, (parallel with the Z -axis). Further, the position vector of a cross-sectional element of the body is assumed to have a negligibly small Z -component. On the other hand, the recoil correction is (correctly) based on the pressure force acting normally to the centreline of the body, and the collocation points (where the pressure forces are said to act) having a position vector with a non-zero Z -component. The fact that the small amplitude swimming example (Section 6.3) did not apparently suffer from such errors at the tail lends weight to this explanation.

The error in the large amplitude equations is probably associated with numerical error. The equations describing the recoil correction and the bending moment distribution are certainly consistent analytically. However, in practice, the recoil correction is split into streamwise and lateral components, whilst the equations for the internal forces, F and G , are along the normal and tangential directions respectively. This leaves our conclusion, that the recoil correction guarantees $M(l, t) = 0$ (Section 6.2.1), at the mercy of numerical error. In particular, the body-acceleration terms involve numerical differentiation of the recoil parameters.

Finally we make a brief comment about the rotational inertia term $m_b \dot{H}_2$. In the eel example shown here, we found this “new term” to be negligible, resulting in no change to the solution for $M(s, t)$. We came to a similar conclusion for other examples that we tested (results not presented). However, there is no doubt that theoretically the rotational inertia of the cross-sectional elements of the beam should be included. Furthermore, our examples have used a simplified geometric representation of the fish, and a uniform mass distribution. Given the virtually negligible cost of calculating this extra term it seems sensible to retain it until its contribution has been considered for examples involving a more realistic body geometry. Likewise, the hydrodynamic couple due to the difference in the drag on each side of the body could also be retained on the grounds that it is cheap to calculate,

and might become more influential as we move to a model where the body has a more realistic geometry.

6.5 Conclusions

This chapter has described our model of the internal mechanics of the fish. The body is modelled as an active bending beam: an assumption that allows us to consider the bending as a function of position along the centreline of the body. The aim is to have a set of differential equations that can be solved in order to obtain the bending moment distribution.

We have derived a set of equations for the bending moment distribution that does not preclude large amplitude undulations of the body. (The “limiting assumption” is that of “beam theory”: essentially requiring $|\kappa l_Z| \ll 1$, where κ is the curvature, and l_Z is the nondimensional depth, or thickness, of the body.) Consequently it becomes necessary to retain the external and internal forces that act in a direction tangential to the centreline. Previously, these forces had been neglected. Thus we have had to calculate the viscous drag on the body as a function of position and time, as described in Chapter 5.

The boundary conditions of the beam model state that the internal stresses, F and G , and the bending moment, M , must be zero at the two free ends: $s = 0$, $s = l$. It then appears that there are twice as many boundary conditions as there are equations. In the context of the small amplitude bending moment equations Cheng *et al.* (1998) commented that the boundary conditions at the tail are equivalent to satisfying the recoil correction. This is also the case for the large amplitude system of equations. Thus, this new formulation of the bending moment equations requires not only that we calculate the viscous drag as a function of position along the body, but also that we ensure that the motion of the fish satisfies the conservation of momentum along the direction of swimming. This latter point was also discussed in Chapter 5. In practice we have found that numerical errors result in a small violation of the beam boundary conditions at $s = l$.

There is plenty of scope for further work in this area of modelling fish swimming. Firstly, an alternative numerical scheme for the bending moment distribution should be considered in order to minimize the error in $M(l, t)$. Secondly, the current model could be used to consider examples

involving non-uniform (more realistic) volume distributions. Thirdly, and most importantly, it is necessary to relate the total bending moment, $M(s, t)$, as calculated by the current theory, to quantities in real fish that can be measured (Cheng *et al.*, 1998). Thus we will begin to fully couple the internal and external mechanics: including not only the physical properties of the fish's environment, but also the physiological properties of its body that may constrain its ability to realise hydrodynamically optimal propulsion.

Chapter 7

Conclusions

The research described in this thesis has been concerned with the fluid and solid mechanics associated with fish propulsion. The study is limited to those fish (and other animals) swimming by passing a wave of lateral undulations backwards along the body. A wide range of animals propel themselves by moving their bodies in this way; we further restrict our attention to those swimming at high Reynolds number.

In terms of the hydrodynamics we have achieved our primary aim of producing an inviscid model for large amplitude swimming. In particular the model includes both the effect on the body of the vortex wake, and the self-induced deformation of the wake itself. Both the two-dimensional and three-dimensional methods produce satisfactory results for the pressure distribution on the body, and for other quantities derived from the pressure, such as the thrust or sideforce. The method behaves as expected (ie there is convergence) as the number of panels is increased. However, care must be taken in choosing the time step. The body of the fish is modelled as being infinitely thin requiring the calculation of the “suction force” at the leading edge.

The method includes a model of the vortex wake shed from the tail fin of the fish. In both two and three dimensions the wake model is seen to roll-up broadly as expected. On close examination, it is clear that elements of the wake become “entangled” after some time. The fact that we obtain good overall results suggests that whilst not strictly correct, this breakdown in the wake model is not catastrophic.

An interesting “option” of the panel method is the calculation^{of} the velocity field in the

neighbourhood of the fish and its wake. Muller (1997) has recently used experimental flow visualisation techniques to look at the velocity and vorticity fields for eel and mullet in a horizontal plane where the vertical flow should be minimal. In our model this corresponds to the plane of symmetry, across which (by definition) there is no flow. We can now compare the results of the two methods. Moreover, the computer model can just as easily calculate the results for another (arbitrary) plane, or even the entire three-dimensional domain (possibly subject to computing resources).

The two-dimensional model includes the calculation of Lighthill's recoil correction. Previous work calculating the recoil correction has relied on the linearity of the small amplitude swimming model (eg Hess and Videler, 1984; Cheng and Blickhan, 1994). We have had to use a method appropriate to the nonlinear aspects of large amplitude swimming.

In studying the internal mechanics of the fish we model it as an active bending beam. The equations of motion of cross-sectional elements of the beam lead to a set of coupled differential equations for the bending moment distribution along the body. For large amplitude deformations it is necessary to retain the tangential forces acting on the beam-element. Consequently we obtain a different set of equations to that previously used at small-amplitude (Hess and Videler, 1984; Cheng and Blickhan, 1994).

A consequence of using the large-amplitude equations for the bending moment distribution is the need to directly estimate the viscous drag as a function of position along the body. We have used a simple, first-order finite difference method to calculate the flow in a two-dimensional boundary layer along the swimming fish. Having an estimate of the viscous drag allows us to balance not only the sideforce and moment (as in Lighthill's recoil), but also to balance the streamwise component of the resultant force on the body. Indeed, this "full recoil correction" is a necessary step in setting the boundary conditions of the large amplitude bending moment equations.

The "full recoil correction" is merely the proper application of Newton's laws of motion. It is of interest regardless of considerations of the bending moment distribution. Models of steady state swimming have been forced to assume that the fish swims at a constant mean forward speed, with any periodic variations to that mean being small. Our "eel example" at the end of Chapter 5 provides direct evidence that the assumption of constant speed was a good one, as the "streamwise

recoil” is seen to be very small indeed. Of course, we must now conduct similar experiments for a range of input kinematic parameters.

We had hoped that the three-dimensional model would be at the same stage in development as the two-dimensional model. Without the recoil correction, the boundary conditions of the bending moment equations cannot yet be satisfied.

We have not had time to look at unsteady movements such as starts and turns. That said, few changes are required to allow the current program to deal with unsteady motion. The code was developed with this end in mind. The fact that we now, in principle, have the “full recoil correction” opens up two alternative routes into studying unsteady swimming movements. The first, “classical” route would be to prescribe the details of, say a fast start, in terms of the measured position of the centreline, and calculate the hydrodynamic forces associated with the motion. In this case, any recoil correction is due to inaccurate measurements of the body motion, or assumptions in the model that limit its accuracy. An alternative method would be to specify a variety of bending wave parameters, and then calculate the resulting motion. In this case the “recoil correction” is the “resulting motion”, which could then be compared with film of real fast starts in fish.

The question of whether it is cost-effective to include the deformation of the vortex wake would benefit from more detailed study. In particular, this question should be examined in the context of a range of example “input motions” obtained directly with biological data.

Developments of the current model would take the form of improvements to the hydrodynamic model and to the description of the internal mechanics.

Firstly, the input geometry should move closer to the biological data. The panel method is commonly used for complex geometries, so extending the model to include both thickness and variable “profile” should not present major difficulties. It would certainly be interesting to be able to examine the effect of vortex shedding from fins forward of the caudal fin. Currently the geometry of the body is not consistent across the entire model. The fluid mechanics is done for an infinitely thin body; whilst the solid mechanics necessarily includes thickness. It should be emphasized that this is not a major discrepancy, but evidently developing the panel method to allow a true three-dimensional fish-shape would be an improvement.

Secondly, the calculation of the flow inside the boundary layer could be improved. Ultimately one

would like an accurate method for dealing with the full three-dimensional boundary layer along the swimming fish. Before then, the current method could be replaced by a second-order method; and the three dimensional problem could be approximated by a quasi-two-dimensional approach as suggested in Chapter 5.

Research into aquatic locomotion has in the past tended to concentrate on one of several apparently distinct aspects of the problem. In particular work has focused on the hydrodynamics; the properties of either muscle actively involved in swimming, or the passive tissue resisting the bending; and the neural control mechanisms responsible for activating and deactivating the musculature in order to achieve the desired motion. In reality these aspects are linked together, and researchers now aim to include in their work the interaction between two or more components of the whole (see Wardle *et al.*, 1995).

As argued by Daniel (1995), in order to make biologically meaningful arguments based on our models of fish locomotion we must consider not only the hydrodynamic constraints described by the Navier-Stokes equations, but also the physiological constraints imposed by the “force-velocity relationships” for specific muscles as they contract; and the mechanics of the passive tissue involved in bending. Moreover, there will ^{be} further constraints imposed by the need to control the muscles (the neural control), including feedback from sensory responses to the outside world.

We can phrase this slightly differently. Most hydrodynamic models (including our own) require, as input, some specification of the body’s lateral deformations, and its swimming speed. Lighthill (1960) realised the importance of ensuring that the imposed motion satisfied the conservation of momentum (the recoil correction). But just as fundamental a consideration (albeit more difficult to implement in a model) is the question of whether the prescribed motion is physiologically realistic, or even possible. This question can only be answered by careful inclusion of the physiological constraints by coupling the description of the external mechanics to that of the internal mechanics.

Currently our model merely calculates the bending moment $M(s, t)$. However, this total bending moment can be thought ^{of} as a combination of two components: M_m , M_p , where M_m is an “active bending moment” associated with muscle contractions, resisted by the “passive bending moment” M_p governed by the mechanical properties of the enclosed tissue (Cheng *et al.*, 1998). Further development of a model for large amplitude fish swimming requires greater consideration of

the coupling between the internal and external mechanics of the problem. In particular, such developments must include a much improved description of the internal mechanics.

Appendix

A The computer program

A.1 Introduction

The software that performs the calculations described in this thesis takes the form of two main programs and a large group of library classes. The two programs deal with the two-dimensional and three-dimensional models respectively. Most of the code was written in the object-oriented language C++. The boundary layer section was written in Fortran 77. We also used the linear algebra package LAPACK++ and some functions from “Numerical Recipes” (Press *et al.*, 1996).

In this section we briefly describe the structure of the problem in “programming terms”. At the highest level the problem can be thought of as a small number of procedures that occur at each time step. The question of how many time steps are required; or how to establish whether a steady state has been reached is not considered here.

Fig. 1 shows the structure of the program in the form of a flowchart. The procedures in the flowchart naturally hide a good deal of complexity: each one has already been described in detail earlier in the thesis.

A.2 Program costs

This section discusses the elements of the problem that have a direct impact on the cost of executing the program in terms of time and storage. The aim is to broadly indicate the main points to be borne in mind, rather than go through a detailed analysis of the various algorithms.

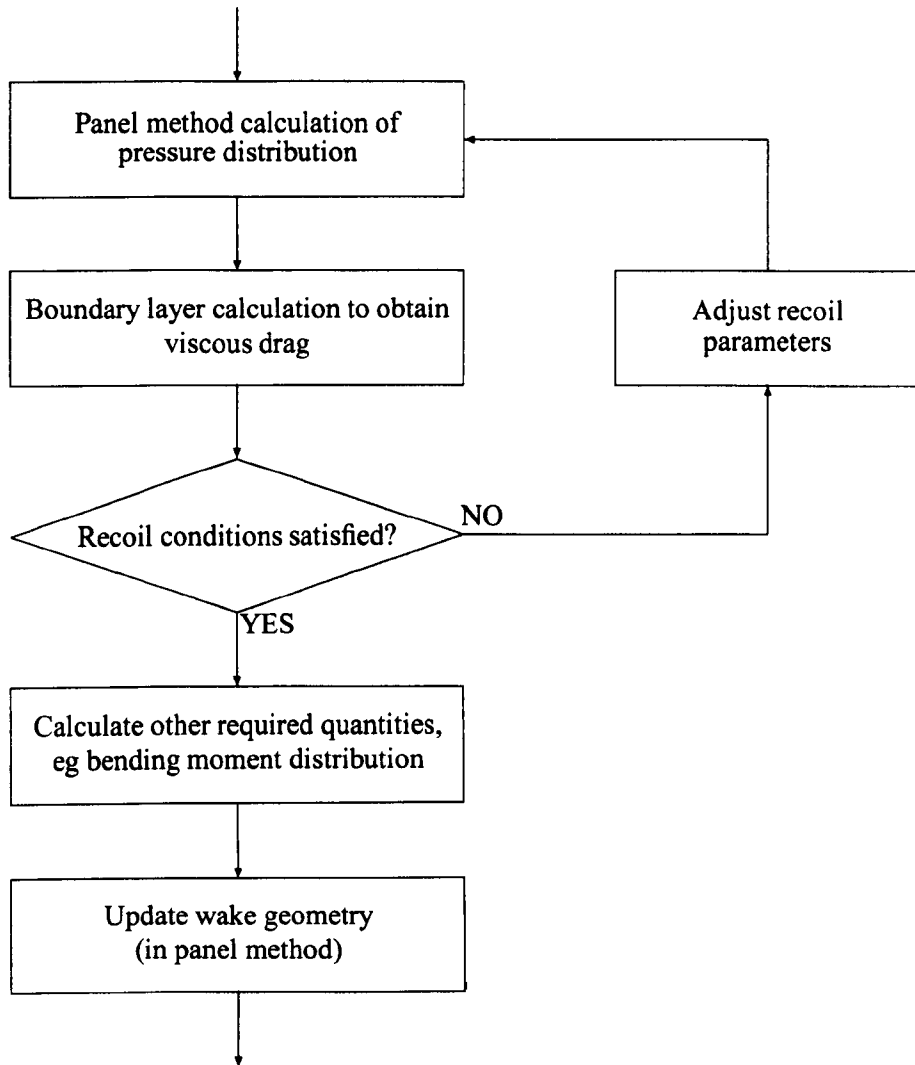


Figure 1: Flowchart indicating the structure of the program, in terms of the procedures that are followed at each time step.

There are five main parameters: the number of panels on the body N ; the number of panels/elements in the wake N_W ; the number of time steps per period $T/\Delta t$; and the number of grid points in the boundary layer solver N_X^{BL}, N_Z^{BL} . The size of the wake is related to the number of time steps since the wake increases its “chordwise length” at each time step.

For the panel method the largest arrays are associated with calculating the matrix of influence coefficients, A . A itself requires the storage of $N \times N$ real numbers. But in calculating A we also need an array of velocity vectors of the same size. The remaining arrays are of order N or N_W .

The boundary layer requires the storage of six arrays of size $N_X^{BL} \times N_Z^{BL}$. For typical values of these parameters, as seen throughout this thesis, the program is not particularly memory intensive.

In terms of computation-time there are three main sections of the panel method to consider:

- the formation and inversion of the matrix of influence coefficients;
- the updating of the wake geometry;
- the iteration on the hydrodynamic calculations to obtain the recoil correction.

The first two revolve around the cost of calculating the induced velocity at any point by summing the contribution of all the body and wake point vortex/vortex line elements. In particular, to update the wake geometry it is necessary to calculate the total induced velocity at each wake node requiring $N_W(N + N_W)$ “calls” to the induced velocity calculation. For typical parameter values, the cost of inverting the matrix of influence coefficients (order N^3) remains small compared to the wake update procedure.

The recoil calculation is potentially very expensive. Calculating the Jacobian involves at least three calls to the panel method (excluding the wake-update procedure). The Newton method converges quickly provided the initial estimate is close to the required solution. We found in practice that often only one or two iterations was necessary. In this case the additional cost of the recoil is not prohibitive.

The boundary layer calculations could become a major component of the time-cost of the program. At each s -station of the grid we use the Newton method on a set of $3 \times N_Z^{BL}$ equations. Each iteration involves the formation and solution of a tri-diagonal system of order $3 \times N_Z^{BL}$: a problem said to be of order N_Z^{BL} (Press *et al.*, 1996). Hence the total time cost associated with the boundary layer solution at each time step is of order $N_X^{BL} N_Z^{BL}$.

The three-dimensional program is typically more expensive than the two-dimensional version. It is not hard to see why. It is reasonable to assume that the two-dimensional parameter N (the number of panels) is basically equivalent to the three-dimensional parameter N_X (the number of chordwise panels). The actual number of panels (an important parameter in the discussion above) in three dimensions is $N = N_X N_Y$. Likewise, in two-dimensions, a single “element” (a point vortex) is

added to the wake at each time step, whereas in three-dimensions, N_Y “wake-elements” (a row of N_Y vortex line segments) is shed from the trailing edge at each time step. In other words, whilst the arguments on storage and time costs applies equally to both versions of the program, the parameter values are typically much larger in three dimensions.

B Improving the code

The programs that we have work well (apart from the recoil correction in the three-dimensional hydrodynamics), but could be improved in terms of being easier to use; and in being easier to maintain, develop and debug.

Firstly, the implementation of the fish body (its geometry and its motion) should be “hidden” from the hydrodynamic (and other) calculations. In other words, the panel method should not “know” anything about the fish, other than being able to “ask for” quantities such as mass, position, velocity, etc. Thus we might describe the motion of the body using a function for the lateral undulations (as in this thesis), or work directly from data, without any need to consider updating or modifying any code. Moreover, any alternative hydrodynamic model (such as Lighthill’s elongated body theory) could be “plugged in” in place of the panel method.

Equally, the method for calculating the recoil correction is independent of both the hydrodynamic model, and the method for describing the input body geometry. We believe that successfully “hiding” the implementation of the recoil correction from the hydrodynamic method would eliminate the problem currently associated with calculating the recoil for the three-dimensional program. There are certainly one or two other (less substantial) areas of the code that would benefit from a similar treatment, but the two mentioned here would have the most significant impact.

It is important to realise that such changes do not bring more efficient execution (they may even slow execution times); nor do they enhance the functionality of the code. The purpose of improving the design of such a complicated system is simply to make it easier to use, and consequently more reliable.

Bibliography

- Ackerberg, R. C. and Phillips, J. H. (1972). The unsteady laminar boundary layer on a semi-infinite flat plate due to small fluctuations in the magnitude of the free-stream velocity. *Journal of Fluid Mechanics* **51**, 137–157.
- Alexander, R. M. (1969). Orientation of muscle fibres in the myomeres of fishes. *Journal of Marine Biol. Assoc. UK* **49**, 263–290.
- Azuma, A. (1992). *The Biokinetics of Flying and Swimming*. Springer-Verlag.
- Bainbridge, R. (1963). *Journal of Experimental Biology* **40**, 23.
- Batchelor, G. K. (1967). *An Introduction to Fluid Dynamics*. Cambridge University Press.
- Bone, Q. and Marshall, N. B. (1982). *Biology of Fishes*. Blackie.
- Bowtell, G. and Williams, T. L. (1991). Anguilliform body dynamics: modelling the interaction between muscle activation and body curvature. *Phil. Trans. R. Soc. Lond. B* **334**, 385–390.
- Bowtell, G. and Williams, T. L. (1994). Anguilliform body dynamics: a continuum model for the interaction between muscle activation and body curvature. *Journal of Mathematical Biology* **32**, 83–91.
- Breder, C. M. (1926). The locomotion of fishes. *Zoologica (N.Y.)* **4**(5), 159–297.
- Carling, J. C., Bowtell, G., and Williams, T. L. (1994). Swimming in the lamprey: modelling the neural pattern generation, the body dynamics and the fluid mechanics. In L. Maddock, Q. Bone, and J. M. V. Rayner (Eds.), *Mechanics and physiology of animal swimming*, Chapter 9, pp. 119–132. Cambridge University Press.

- Cebeci, T. (1977a). Calculation of laminar and turbulent boundary layers for two-dimensional time dependent flows. Contractor Report CR-2820, NASA.
- Cebeci, T. (1977b). Calculation of unsteady two-dimensional laminar and turbulent boundary layers with fluctuations in external velocity. *Proc. Roy. Soc. Lond. A* **355**, 225–238.
- Cebeci, T. and Bradshaw, P. (1977). *Momentum transfer in boundary layers*. McGraw-Hill.
- Cheng, J., Zhuang, L., and Tong, B. (1991). Analysis of swimming three-dimensional waving plates. *Journal of Fluid Mechanics* **232**, 341–355.
- Cheng, J. Y. and Blickhan, R. (1994). Bending moment distribution along swimming fish. *Journal of Theoretical Biology* **168**, 337–348.
- Cheng, J. Y., Pedley, T. J., and Altringham, J. D. (1998). A continuous dynamic beam model for swimming fish. *Phil. Trans. Roy. Soc. Lond. B* **353**, 981–997.
- Chopra, M. G. (1974). Hydromechanics of lunate-tail swimming propulsion. *Journal of Fluid Mechanics* **64**(2), 375–391.
- Chopra, M. G. (1976). Large amplitude lunate-tail theory of fish locomotion. *Journal of Fluid Mechanics* **74**, 161–182.
- Chopra, M. G. and Kambe, T. (1977). Hydromechanics of lunate-tail swimming propulsion. *Journal of Fluid Mechanics* **79**(1), 49–69.
- Chorin, A. J. and Bernard, P. S. (1973). Discretization of a vortex sheet with an example of roll-up. *Journal of Computational Physics* **13**, 423–429.
- Daniel, T. L. (1995). Invertebrate swimming: integrating internal and external mechanics. In C. P. Ellington and T. J. Pedley (Eds.), *Biological Fluid Dynamics*, pp. 61–89. The Company of Biologists Ltd.
- Duck, P. W. (1980). A numerical method for treating time-periodic boundary layers. *Journal of Fluid Mechanics* **204**, 249–561.
- Fierstine, H. L. and Walters, V. (1968). Mem. S. Calif. Acad. Sci., Vol. 6, 1-31.

- Fink, P. T. and Soh, W. K. (1978). A new approach to roll-up calculations of vortex sheets. *Proc. Roy. Soc. Lond. A* **362**, 195–209.
- Gray, J. (1933). Studies in animal locomotion i: the movement of fish with special reference to the eel. *Journal of Experimental Biology* **10**(4), 88–104.
- Harper, D. G. and Blake, R. W. (1990). Fast-start performance of rainbow trout *salmo gairdneri* and northern pike *exos lucius*. *Journal of Experimental Biology* **150**, 321–42.
- Harper, D. G. and Blake, R. W. (1991). Prey capture and the fast-start performance of northern pike *exos lucius*. *Journal of Experimental Biology* **155**, 175–92.
- Hess, F. and Videler, J. J. (1984). Fast continuous swimming of saithe (*pollachius virens*): a dynamic analysis of bending moments and muscle power. *Journal of Experimental Biology* **109**, 229–251.
- Houssay, S. F. (1912). *Forme, Puissance et Stabilité des Poissons*. A. Hermann et fils, Paris.
- Johnson, W. (1994). *Helicopter Theory*. Dover.
- von Karman, T. and Sears, W. R. (1938, August). Airfoil theory for non-uniform motion. *Journal of the Aeronautical Sciences* **5**(10), 379–390.
- Katz, J. and Plotkin, A. (1991). *Low Speed Aerodynamics : From Wing Theory to Panel Methods*. McGraw-Hill.
- Katz, J. and Weihs, D. (1978). Hydrodynamic propulsion by large amplitude oscillation of an airfoil with chordwise flexibility. *Journal of Fluid Mechanics* **88**, 485–497.
- Katz, J. and Weihs, D. (1979). Large amplitude unsteady motion of a flexible slender propulsor. *Journal of Fluid Mechanics* **90**, 713–23.
- Keller, H. B. (1971). A new difference scheme for parabolic problems. In B. Hubbard (Ed.), *Numerical Solutions of Partial Differential Equations*, pp. 327–350. New York: Academic.
- Keller, H. B. (1978). Numerical methods in boundary-layer theory. *Ann. Rev. Fluid. Mech.* **10**, 417–433.

- Konstadinopoulos, P., Mook, D. T., and Nayfeh, A. H. (1981). A numerical method for general aerodynamics. *AIAA Paper* (81-1877).
- Lan, C. E. (1979). The unsteady quasi-vortex-lattice method with applications to animal propulsion. *Journal of Fluid Mechanics* **93**, 747–765.
- Lighthill, M. J. (1954). The response of laminar skin friction and heat transfer to fluctuations in the stream velocity. *Proc. Roy. Soc. A* **224**, 1–23.
- Lighthill, M. J. (1960). Note on the swimming of slender fish. *Journal of Fluid Mechanics* **9**, 305–317.
- Lighthill, M. J. (1969). Hydromechanics of aquatic animal locomotion. *Ann. Rev. Fluid Mech.* **1**, 413–46.
- Lighthill, M. J. (1970). Aquatic animal propulsion of high hydromechanical efficiency. *Journal of Fluid Mechanics* **44**, 265–301. Check the details on the paper.
- Lighthill, M. J. (1971). Large-amplitude elongated-body theory of fish locomotion. *Proc. Roy. Soc. B* **179**, 125–138.
- Lighthill, M. J. (1975). *Mathematical Biofluidynamics*. SIAM.
- Lighthill, M. J. (1977). Mathematical theories of fish swimming. In J. H. Steele (Ed.), *Fisheries Mathematics*, Chapter 9, pp. 131–144. New York: Academic Press.
- Liu, H., Wassersug, R. J., and Kawachi, K. (1996). A computational fluid dynamics study of tadpole swimming. *Journal of Experimental Biology* **199**, 1245–1260.
- Liu, P. and Bose, N. (1997). Propulsive performance from oscillating propulsors with spanwise flexibility. *Proc. Roy. Soc. Lond. A* **453**, 1763–1770.
- McGregor, R. C. and Thomson, G. R. (1997). Sea trials of wave propulsion of a yacht using a flexible fin propellor. *Renewable Energy* **10**(2/3), 335–338.
- Moore, D. W. (1971). The discrete vortex approximation of a vortex sheet. AFOSR 1084-69, California Inst. of Tech. Rep.

- Moore, D. W. (1974). A numerical study of the roll-up of a finite vortex sheet. *Journal of Fluid Mechanics* **63**, 225–235.
- Muller, U. K. (1997). *In the wake of fish: on the hydrodynamic interactions between swimming fish and water, the effects of ontogenetic stages and swimming kinematics*. Ph. D. thesis.
- Pedley, T. J. (1972). Two-dimensional boundary layers in a free stream which oscillates without reversing. *Journal of Fluid Mechanics* **55**, 359–383.
- Pettigrew, J. B. (1873). *Animal locomotion, or walking, swimming, and flying with a dissertation on aeronautics*. Henry S. King.
- Press, W. H., Saul, A. T., Vetterling, W. T., and Flannery, B. P. (1996). *Numerical Recipes - The art of scientific programming* (2 ed.). Cambridge.
- Robinson, A. and Laurmann, J. A. (1956). *Wing Theory*. Cambridge University Press.
- Rosenhead, L. (Ed.) (1963). *Laminar Boundary Layers*. Oxford University Press.
- Scully, M. P. (1975, March). Computation of helicopter rotor wake geometry and its influence on rotor harmonic airloads. Technical Report ASRL TR 178-1, Massachusetts Institute of Technology.
- Takami, H. (1964). A numerical experiment with the discrete vortex approximation with reference to the rolling up of a vortex sheet. SUDAER 202, Dept. of Aeron. & Astron., Stanford University.
- Triantafyllou, M. S. and Triantafyllou, G. S. (1995, March). An efficient swimming machine. *Scientific American*, 40–48.
- Videler, J. J. (1993). *Fish Swimming*. Fish and Fisheries. Chapman & Hall.
- Videler, J. J. and Hess, F. (1984). Fast continuous swimming of two pelagic predators, saithe (*Pollachius virens*) and mackerel (*Scomber scombrus*): a kinematic analysis. *Journal of Experimental Biology* **109**, 209–228.
- Videler, J. J. and Wardle, C. S. (1978). New kinematic data from high speed cine film recordings of swimming cod (*Gadus morhua*). *Netherlands Journal of Zoology* **28**(3-4), 465–484.

- Videler, J. J. and Weihs, D. (1982). Energetic advantage of burst-and-coast swimming of fish at high speeds. *Journal of Experimental Biology* **97**, 169–178.
- Wagner, H. (1925). Über die entstehung des dynamischen auftriebes von tragflugeln. *Zeitschrift für Angewandte und Mechanik* **5**, 17–35.
- Wardle, C. S., Videler, J. J., and Altringham, J. D. (1995). Tuning in to fish swimming waves: body form, swimming mode and muscle function. *Journal of Experimental Biology* **198**, 1629–1636.
- Webb, P. W. (1971a). The swimming energetics of trout: I thrust and power output at cruising speeds. *Journal of Experimental Biology* **55**, 489–520.
- Webb, P. W. (1971b). The swimming energetics of trout: II oxygen consumption and swimming efficiency. *Journal of Experimental Biology* **55**, 521–40.
- Webb, P. W. (1976). The effect of size on the fast-start performance of rainbow trout, *salmo gairdneri*, and a consideration of piscivorous predators. *Journal of Experimental Biology* **74**, 211–26.
- Webb, P. W. and Weihs, D. (Eds.) (1983). *Fish Biomechanics*. Praeger.
- Weihs, D. (1972). A hydrodynamic analysis of fish turning manoeuvres. *Proc. Roy. Soc. B* **182**, 59–72.
- Weihs, D. (1973). The mechanism of rapid starting of a slender fish. *Biorheology* **10**, 343–350.
- Weihs, D. (1974). Energetic advantages of burst swimming of fish. *Journal of Theoretical Biology* **48**, 215–229.
- Wempner (1973). *Mechanics of Solids*. McGraw-Hill.
- Westwater, F. L. (1935, August). The rolling up of the surface of discontinuity behind an aerofoil of finite span. *Aeronautical Research Committee Reports and Memoranda* (1692).
- Wu, T. Y. (1961). Swimming of a waving plate. *Journal of Fluid Mechanics* **10**, 321–344.
- Wu, T. Y. (1971a). Hydromechanics of swimming propulsion. part 1. swimming of a two-dimensional flexible plate at variable forward speeds in an inviscid fluid. *Journal of Fluid Mechanics* **46**, 337–355.

-
- Wu, T. Y. (1971b). Hydromechanics of swimming propulsion, part 2: some optimum shape problems. *Journal of Fluid Mechanics* **46**, 521–544.
- Wu, T. Y. (1971c). Hydromechanics of swimming propulsion, part 3: swimming and optimum movements of slender fish with side fins. *Journal of Fluid Mechanics* **46**, 545–568.